



Gisele Góes Cintra

**Delamination and Multi-crack Behavior of
Pultruded Glass Fiber-Polymer Web-flange
Junctions**

Tese de Doutorado

Thesis presented to the Programa de Pós-graduação
em Engenharia Civil of PUC-Rio in partial fulfillments
of the requirements for the degree of Doutor em
Ciência – Engenharia Civil.

Advisor: Prof. Daniel Carlos Taissum Cardoso

Co-advisor: Prof. Thomas Keller

Co-advisor: Prof^a. Janine Domingos Vieira

Rio de Janeiro

April 2023



Gisele Góes Cintra

Delamination and Multi-crack Behavior of Pultruded Glass Fiber-Polymer Web-flange Junctions

Thesis presented to the Programa de Pós-graduação em Engenharia Civil of PUC-Rio in partial fulfillment of the requirements for the degree of Doutor em Engenharia Civil. Approved by the Examination Committee:

Prof. Daniel Carlos Taissum Cardoso - Advisor
Departamento de Engenharia Civil e Ambiental – PUC-Rio

Prof^a. Janine Domingos Vieira - Co-Advisor
UFF

Prof. Thomas Keller - Co-Advisor
École Polytechnique Fédérale de Lausanne

Prof. Tianqiao Liu
Beijing University of Technology

Prof. Evandro Parente Junior
UFC

Prof. Lucas Lisbôa Vignoli
UFRJ

Prof. Renato Bichara Vieira
Departamento de Engenharia Mecânica – PUC-Rio

Rio de Janeiro, April 28th, 2023.

All rights reserved.

Gisele Góes Cintra

Graduated in Civil Engineering at Universidade Federal Fluminense, in 2013 and obtained her M.Sc. Degree in Civil Engineering from the Pontifical Catholic University of Rio de Janeiro in 2017. Experience with planning and management of projects, as well as retrofit and design of structures. Her area of interest encompasses structural design of both traditional and composite materials.

Bibliographic data

Cintra, Gisele Góes

Delamination and multi-crack behavior of pultruded glass fiber-polymer web-flange junctions / Gisele Góes Cintra ; advisor: Daniel Carlos Taissum Cardoso ; co-advisor: Thomas Keller, Janine Domingos Vieira. – 2023.

221 f. : il. color. ; 30 cm

Tese (doutorado)–Pontifícia Universidade Católica do Rio de Janeiro, Departamento de Engenharia Civil e Ambiental, 2023.

Inclui bibliografia

1. Engenharia Civil e Ambiental - Teses. 2. Dano. 3. Múltipla fissuração. 4. Junções alma-mesa. 5. Pultrudados de polímero com fibras. 6. Elementos coesivos. I. Cardoso, Carlos Taissum. II. Keller, Thomas. III. Vieira, Janine Domingos. IV. Pontifícia Universidade Católica do Rio de Janeiro. Departamento de Engenharia Civil e Ambiental. V. Título.

CDD: 624

*To my mother, Corina, who raised
me to be whoever I wanted to.*

Acknowledgements

My PhD was, truly, one of the most difficult processes that I have ever faced. Maybe all the doctorates are. It has been many challenging years, intensified, in the middle of the course, by the COVID. In this scenario, finishing this work would not have been possible without my faith in God and without the support of so many incredible people. These acknowledgments are an attempt to tell you how much I am grateful for your life. You made all the difference.

Firstly, I thank the Pontifical Catholic University of Rio de Janeiro (PUC-Rio), for letting me try to contribute scientifically to the Engineering advance.

To CAPES, for the financial support and to the internalization program CAPES-PrInt, for the amazing opportunity of conducting part of my research outside Brazil. This study was financed in part by the Coordenação de Aperfeiçoamento de Pessoal de Nível Superior – Brasil (CAPES) – Finance Code 001.

To my co-advisor Janine Vieira, for all your availability, support, dedication and mainly, for the attention to the smallest details, that made all the difference for the final result of this thesis. It was a great pleasure to work with you during all these years.

To my co-advisor, Thomas Keller, who gave me one of the biggest opportunities of my life: studying in one of the best universities of Switzerland and of the world. There is nothing I could say to express all my gratitude for all your technical support, your patience, and your trust during all this process. The opportunity you gave me changed my life, professionally and personally. Thank you.

To my advisor Daniel Cardoso, who was, during the last almost seven years, since the beginning of my Master's, my greatest mentor. I could say that you have opened

many doors for me. However, the right metaphor would be saying that you taught me how to get the keys to open them. Thank you for the immense support and for all your geniality. You were the booster for all the great achievements that I had during this journey.

To all the staff of Structures and Material Laboratory (LEMDEC) of PUC-Rio, with whom I shared incredible and happy moments, which certainly outperformed all experiments that went wrong. Special thanks to the dear Euclides, Marques, Rogerio, Bruno and Jhansen, who helped me so proactively for so many years.

To Julia de Castro and Saira Mohamed-Kanani, for all your technical support and kindness during my stay in Lausanne.

To the technical team of the Structural Engineering Platform (GIS-ENAC) at the *École Polytechnique Fédérale de Lausanne* (EPFL), with whom I learned so much. To Sylvain, Gilles, Armin, François, Gérald, Frédérique and Serge, *je vous remercie énormément*.

To the unforgettable and multicultural CCLab team, which I truly loved being a part of. To Lulu, Ghazaleh, Niloufar, Tara, Dharun, Schengchen, Guangjian, Yuntong, Lingfeng, Ting and Shayan, it was amazing to share special moments and to have work discussions with you. Special thanks to Congzhe, who taught me so much about Abaqus and the modelling of cohesive elements.

To my former partners Filipe Sá and Victor Nogueira, with whom I am proud of having co-founded the company Braver Engineering, where I was able to improve my knowledge of pultruded profiles and which represented, for more than two years, the fulfillment of a dream.

To Marra Projects, a company that I am proud to be part of. Without your understanding of what this research means to me, I would never have gotten here. Thank you so much for all the support, so I could finish it.

To my dearest and beloved friends, in and outside of PUC-Rio. Your motivation and unconditional support transformed very difficult moments in light memories, which I intend to carry with me forever. Thank you for everything.

To my wonderful family, who made the incessant search for knowledge guide my steps. It is not possible to describe all my love and gratitude for your existence. Thank you for all the kindness and support. All I am, I owe you.

To the Sardinha family, who not only hosted me in Lausanne, but also gave me a home, full of love, affection, and unforgettable moments. I am grateful to have found my way to your home.

To my dear father and beloved brothers. You were, in countless moments, my greatest source of strength, hope and joy.

To my dear mother, Corina, you were and still is the reason of everything. Thank you.

Abstract

Cintra, Gisele Góes; Cardoso, Daniel Carlos Taissum (Advisor); Vieira, Janine Domingos (Co-advisor). Keller, Thomas (Co-advisor). **Delamination and Multi-crack Behavior of Pultruded Glass Fiber-Polymer Web-flange Junctions**. Rio de Janeiro, 2023. 221 p. Tese de Doutorado – Departamento de Engenharia Civil e Ambiental. Pontifícia Universidade Católica do Rio de Janeiro.

This work aims to discuss the behavior of pultruded glass fiber-polymer composites related to issues not fully understood, comprising the damage and failure mechanisms, as well as the multi-crack composites response. Experimental and numerical investigations are conducted mainly on web-flange junctions (WFJ) extracted from varied profiles and bridge decks systems. Factors that favor the composites' delamination, such as the influence of local defects/imperfections and the consequent modification on the junctions' stresses trajectories are addressed. Theoretical equations were proposed to determine the WFJs rotational stiffness, resulting in maximum differences of 24% and 38% for I-sections and channels, respectively. To complement the scarcity of fracture parameter data related to the material, adaptations of classical fracture mechanic experiments for both Modes I and II were proposed and conducted. Nine data reduction methods were analyzed and compared with finite element models. The Modified Beam Theory method presented the best results for crack propagation in Mode I, whereas for Mode II, the Corrected Beam Theory using effective crack length and the Experimental Compliance Methods presented the closest results to numerical models. Finally, a novel approach for the multi-crack assessment is proposed. Compliance and R-curves are obtained based on the sum of the crack lengths and the strain energy release rate for each crack is evaluated separately. The results of this novel approach were compared with numerical analyses developed with the use of cohesive elements and a good agreement was found in terms of load vs. displacement response.

Keywords

Damage, Multiple crack behavior, Web-flange junctions, Pultruded fiber-polymers, Cohesive elements.

Resumo

Cintra, Gisele Góes; Cardoso, Daniel Carlos Taissum (Orientador); Vieira, Janine Domingos (Coorientadora). Keller, Thomas (Coorientador). **Delaminação e Comportamento de Múltipla Fissuração de Junções Alma-Mesa Pultrudadas de Polímero-Fibra de Vidro.** Rio de Janeiro, 2023. 221 p. Tese de Doutorado – Departamento de Engenharia Civil e Ambiental. Pontifícia Universidade Católica do Rio de Janeiro.

Este trabalho visa discutir tópicos ainda não totalmente compreendidos a respeito do comportamento de compósitos pultrudados de polímero reforçado com fibras de vidro, englobando os mecanismos de falha e danos, bem como a resposta à múltipla fissuração dos compósitos. Investigações experimentais e numéricas foram conduzidas, com foco nas junções mesa-alma extraídas de variados tipos de perfis e decks de pontes. Fatores que propiciam a delaminação, como a influência de defeitos e imperfeições locais e a consequente modificação das trajetórias de tensão são discutidas. Equações teóricas foram propostas para a determinação da rigidez rotacional das junções mesa-alma, resultando em máximas diferenças de 24% e 38% para seções I e C, respectivamente. Para contribuir para um banco de dados de parâmetros da fratura relacionados a esse material, adaptações de clássicos experimentos da mecânica da fratura, para ambos os Modos I e II, foram propostos e conduzidos. Nove métodos de regressão de dados foram analisados e comparados com modelos de elementos finitos. O método “*Modified Beam Theory*” (MBT_{ASTM}) apresentou os melhores resultados para propagação de fissuras no Modo I, enquanto para o Modo II, os métodos “*Corrected beam theory using effective crack length (CBTE)*” e “*Experimental compliance method (EMC)*” apresentaram os resultados mais próximos dos modelos numéricos. Finalmente, uma nova abordagem para a análise de múltipla fissuração é proposta. Curvas R e curvas compliance foram obtidas com base na soma dos comprimentos de fissuras e as respectivas taxas de liberação de energia elástica foram avaliadas separadamente. Os resultados da abordagem proposta foram comparados com modelo numérico desenvolvido com o auxílio de elementos coesivos e boas correlações em termos da resposta *carga x deslocamento* foram encontradas.

Palavras-chave

Dano, Múltipla fissuração, Junções alma-mesa, Pultrudados de polímero com fibras, Elementos coesivos.

Table of Contents

| | |
|--|----|
| 1. Introduction | 29 |
| 1.1. Motivation | 34 |
| 1.2. Objectives | 36 |
| 1.3. Organization of the dissertation | 37 |
| 1.4. References | 39 |
| | |
| 2. Experimental investigation on the moment-rotation performance of pultruded fiber-polymer web-flange junctions | 43 |
| 2.1. Introduction | 43 |
| 2.2. Materials and Methods | 46 |
| 2.2.1. Materials | 46 |
| 2.2.2. Specimens' imperfections | 48 |
| 2.2.3. Test set-up and DIC technique | 50 |
| 2.3. Results and Discussion | 53 |
| 2.3.1. Rotational stiffness | 53 |
| 2.3.2. Crack pattern | 56 |
| 2.4. Complementary analyses | 63 |
| 2.4.1. Stress analysis | 63 |
| 2.4.2. Stiffness retention function | 69 |
| 2.4.3. Theoretical and experimental k_r comparison | 73 |
| 2.5. Conclusions | 77 |
| 2.6. References | 79 |
| | |
| 3. Mode I and Mode II Fracture Behavior in Pultruded Glass Fiber-Polymer Bridge Decks – Experimental Investigation | 82 |
| 3.1. Introduction | 82 |
| 3.2. Theoretical background | 88 |
| 3.2.1. SERR in Mode I | 88 |

| | | |
|--------|---|-----|
| 3.2.2. | SERR in Mode II | 91 |
| 3.3. | Experimental Program | 93 |
| 3.3.1. | Materials | 93 |
| 3.3.2. | DCB tests | 94 |
| 3.3.3. | ELS tests | 97 |
| 3.4. | DCB experimental results | 100 |
| 3.4.1. | Failure modes | 100 |
| 3.4.2. | Asymmetry assessment | 102 |
| 3.4.3. | Load-displacement and compliance responses | 103 |
| 3.4.4. | Crack initiation points | 104 |
| 3.4.5. | R-curves and SERR values for Mode I | 105 |
| 3.4.6. | Fiber bridging length | 111 |
| 3.4.7. | Comparison with previous works | 111 |
| 3.5. | ELS experimental results | 112 |
| 3.5.1. | Failure modes | 112 |
| 3.5.2. | Asymmetry assessment | 113 |
| 3.5.3. | Load-displacement and compliance responses | 114 |
| 3.5.4. | Crack initiation points | 115 |
| 3.5.5. | R-curves and SERR values for Mode II | 116 |
| 3.5.6. | Comparison with previous works | 119 |
| 3.6. | Comparison between G_I and G_{II} | 120 |
| 3.7. | Conclusions | 120 |
| 3.8. | References | 122 |
| 4. | Mode I and Mode II Fracture Behavior in Pultruded Glass Fiber-Polymers Bridge Decks – Numerical Investigation | 126 |
| 4.1. | Introduction | 126 |
| 4.2. | CZM - theoretical background | 129 |
| 4.2.1. | Traction separation laws | 129 |
| 4.2.2. | R-curve responses and CZM length | 132 |
| 4.3. | Numerical Investigation | 134 |
| 4.3.1. | Traction separation laws | 134 |
| 4.3.2. | Fitting procedure | 136 |

| | | |
|--------|---|-----|
| 4.3.3. | DCB model | 138 |
| 4.3.4. | ELS model | 140 |
| 4.4. | Results of preliminary numerical analyses | 141 |
| 4.5. | Results and discussion for DCB models | 143 |
| 4.5.1. | Adopted cohesive laws | 143 |
| 4.5.2. | General behavior | 143 |
| 4.5.3. | R-curve and SERR values | 146 |
| 4.6. | Results and discussion for ELS models | 149 |
| 4.6.1. | Adopted cohesive laws | 149 |
| 4.6.2. | General behavior | 150 |
| 4.6.3. | R-curves and SERR values | 153 |
| 4.7. | Parametric study of the cohesive law | 156 |
| 4.7.1. | Effect of the interfacial strength (σ_c) | 156 |
| 4.7.2. | Effect of the maximum fiber bridge traction (σ_{max}) | 158 |
| 4.7.3. | Effect of the SERR due to crack initiation (G_{tip}) | 159 |
| 4.7.4. | Effect of the SERR due to fiber bridging (G_{tot}) | 160 |
| 4.7.5. | Effect of the parameter γ | 161 |
| 4.8. | Conclusions | 162 |
| 4.9. | References | 164 |
| 5. | Novel Multi-crack Damage Approach for Pultruded Fiber-Polymer Web-flange Junctions | 168 |
| 5.1. | Introduction | 168 |
| 5.2. | Experimental program | 171 |
| 5.2.1. | <i>DS</i> decks tests | 171 |
| 5.2.2. | Cracks measurement methodology | 173 |
| 5.2.3. | Novel approach to multi-crack assessment | 175 |
| 5.2.4. | <i>AS</i> decks tests | 177 |
| 5.3. | Numerical investigation | 179 |
| 5.3.1. | Properties and boundary conditions | 179 |
| 5.3.2. | Mesh elements and size | 182 |
| 5.3.3. | Traction separation laws | 183 |
| 5.3.4. | Adopted fracture parameters | 184 |

| | | |
|--------|---|-----|
| 5.4. | Results and discussion | 186 |
| 5.4.1. | Cracks assessment and measurement | 186 |
| 5.4.2. | Novel multi-crack approach | 188 |
| 5.4.3. | Numerical results for <i>DS</i> decks multi-crack behavior | 196 |
| 5.4.4. | <i>AS</i> decks results and the benefits of multiple layers | 200 |
| 5.5. | Conclusions | 203 |
| 5.6. | References | 205 |
| 6. | Conclusions and suggestions for future works | 210 |
| 6.1. | Conclusions | 210 |
| 6.1.1. | Experimental investigation on the moment-rotation performance of pultruded fiber-polymer web-flange junctions | 210 |
| 6.1.2. | Mode I and Mode II Fracture Behavior in Pultruded Glass Fiber-Polymer Bridge Decks – Experimental Investigation | 211 |
| 6.1.3. | Mode I and Mode II Fracture Behavior in Pultruded Glass Fiber-Polymers Bridge Decks – Numerical Investigation | 212 |
| 6.1.4. | Novel approach for multi-crack assessment of pultruded fiber-polymer web-flange junctions | 213 |
| 6.2. | Major contributions of the Thesis | 214 |
| 6.3. | Suggestions for future works | 215 |
| 7. | Appendix A – Novel approach for multi-crack assessment | 218 |

List of Figures

| | |
|--|----|
| Figure 1.1 - Applications in structural systems: (a) <i>Pontresina</i> Bridge, Switzerland [10,11]; (b) <i>Fasano</i> Hotel, Brazil [12]; (c) Salt Storage Unit of <i>Tortuga</i> , Brazil [13]; (d) <i>Eyecatcher</i> Building [10]; (e) Glass fiber-polymer balsa sandwich bridge deck, Switzerland [14] (f) Staircase Tower [15]; (g) <i>Kolding</i> Bridge, Denmark [16] | 30 |
| Figure 1.2 - Pultrusion process [19] | 32 |
| Figure 1.3 – Typical fiber architecture for pultruded fiber-polymer profiles (Adapted from Azo Materials [23]) | 33 |
| Figure 2.1 - Studied cross-sections: (a) I ₁ -section; (b) I ₂ -section; (c) C ₁ -channel; (d) C ₂ -channel. | 47 |
| Figure 2.2. Images taken from the microscope: (a) specimen extracted from C ₂ ; (b) specimen extracted from I ₂ . | 48 |
| Figure 2.3. Images of specimen extracted from I ₂ obtained by microtomography. | 49 |
| Figure 2.4. Specimens extracted from profiles: (a) from I-section profiles; (b) from channels. | 50 |
| Figure 2.5. Test set-up: (a) Overview; (b) detail of the test configuration. | 51 |
| Figure 2.6. Channel section tests: (a) close-mode; (b) open-mode. | 51 |
| Figure 2.7. Angle of rotation measurement through software GOM: (a) undeformed shape and (b) deformed shape. | 52 |
| Figure 2.8. $M/b \times \theta$ curves from: (a) I ₁ -section; (b) I ₂ -section; (c) C ₁ -channel; (d) C ₂ -channel. | 54 |
| Figure 2.9. Typical cracks, radial and tangential stresses: (a) open-mode; (b) close-mode. | 57 |
| Figure 2.10. Specimens' major strain extracted from DIC measurements. | 58 |
| Figure 2.11. I-sections' imperfections and respective crack patterns. | 59 |
| Figure 2.12. Channels' imperfections and respective crack patterns. | 60 |

| | |
|--|-----|
| Figure 2.13. Cracks' location in specimens extracted from I-sections. | 61 |
| Figure 2.14. Cracks' location in specimens extracted from channels. | 62 |
| Figure 2.15. Superposition of tensile stresses in I-sections' junctions. | 66 |
| Figure 2.16. Tangential and radial stresses corresponding to radial of C ₂ .04-op. | 69 |
| Figure 2.17. Curves of I-sections stiffness degradation: (a) I ₁ -section; (b) I ₂ -section. | 70 |
| Figure 2.18. Curves of C ₁ -channels stiffness degradation. | 70 |
| Figure 2.19. Curves of C ₂ -channels stiffness degradation: (a) open-mode; (b) close-mode. | 71 |
| Figure 2.20. Retention curves derived from literature and proposed lower bound function. | 72 |
| Figure 2.21. Comparison between theoretical and experimental rotational stiffness. | 75 |
| Figure 3.1. Delamination on a bridge deck system (adapted from [2]). | 83 |
| Figure 3.2. Mode I and Mode II of loading. | 84 |
| Figure 3.3. Determination of parameter Δ according to MBT method. | 89 |
| Figure 3.4. Unit section of DS deck (dimensions in mm). | 93 |
| Figure 3.5. Fiber architecture: (a) flange (t=16.8 mm); (b) flange (t=20.3 mm); (c) web. | 94 |
| Figure 3.6. Specimens extracted from the DS bridge deck system. | 95 |
| Figure 3.7. DCB test fixture: (a) scheme (dimensions in mm); (b) picture taken with video-extensometer technique. | 96 |
| Figure 3.8. ELS specimens extracted from the DS deck. | 97 |
| Figure 3.9. ELS test fixture scheme. | 98 |
| Figure 3.10. ELS test fixture: (a) front view; (b) clamping. | 99 |
| Figure 3.11. Detail of pair of black dots on the ELS.05 specimen. | 99 |
| Figure 3.12. Failure mode of DCB specimens: (a) DCB.01; (b) DCB.02; (c) DCB.03; (d) DCB.04; (e) DCB.05. | 100 |
| Figure 3.13. Delamination growth between fabric layers at the midplane DCB.01 specimen. | 101 |
| Figure 3.14. Fiber bridging observed in DCB.05. | 101 |
| Figure 3.15. Points definition for the assessment of the asymmetry | |

| | |
|--|-----|
| effect. | 102 |
| Figure 3.16. Fracture modes assessment for DCB.01. | 103 |
| Figure 3.17. Curves obtained experimentally: a) load vs. displacement curves with fracture SERR initiation points; b) compliance vs. crack length curves. | 104 |
| Figure 3.18. R-curves derived from MBT methods: (a) MBT_{ASTM} ; (b) $MBT-EI_{eq}$ | 106 |
| Figure 3.19. R-curves derived from CC methods: (a) CC_{ASTM} ; (b) CC-f [27] | 106 |
| Figure 3.20. R-curves derived from MCC methods: (a) MCC_{ASTM} ; (b) $MCC-a_{eff}$ | 107 |
| Figure 3.21. Comparison between MBT, CC and MCC method (DCB.02) | 107 |
| Figure 3.22. R-curves of DCB.02 for CC_{ASTM} and MBT_{ASTM} methods with and without the addition of the parameter Δ . | 109 |
| Figure 3.23. Failure mode of ELS specimens: (a) ELS.01; (b) ELS.02; (c) ELS.03; (d) ELS.04; (e) ELS.05. | 112 |
| Figure 3.24. Maximum deflection of ELS.01 ($P_{max} = 467.6$ N). | 113 |
| Figure 3.25. Fracture modes assessment for ELS.01: distance between $d1$ and $d2$ vs. crack length. | 114 |
| Figure 3.26. (a) load vs displacement curves of ELS specimens with fracture SERR initiation points; (b) compliance vs. crack length curves. | 115 |
| Figure 3.27. Decrease in compliance in the ELS.01 specimen. | 116 |
| Figure 3.28 - R-curve obtained from different methods: (a) CBTE method; (b) SBT method; (c) EMC method; (d) comparison between the three methods (ELS.05). | 118 |
| Figure 4.1. Typical traction separation law with linear softening. | 129 |
| Figure 4.2. Traction separation law that accounts for fiber bridging mechanism. | 131 |
| Figure 4.3. Fracture process zone of Mode I delamination with fiber bridging (adapted from [22]). | 132 |
| Figure 4.4. Typical shape of R-curve for DCB tests. | 133 |
| Figure 4.5. Cohesive laws' shape assessed: a) bilinear-exponential | |

| | |
|---|-----|
| law; b) trilinear law; c) bilinear law. | 134 |
| Figure 4.6. Preliminary cohesive laws used for the DCB model. | 138 |
| Figure 4.7. Preliminary cohesive laws used for the ELS model. | 138 |
| Figure 4.8. Scheme of DCB experiments modelling: (a) distribution of layers and adopted boundary conditions; (b) adopted mesh of 1 mm. | 139 |
| Figure 4.9. Scheme of ELS experiments modelling: (a) layers' distribution and adopted boundary conditions; (b) Adopted mesh of 1 mm. | 141 |
| Figure 4.10. Load vs. displacement curves: (a) DCB models; (b) ELS models. | 142 |
| Figure 4.11. Cohesive laws used for the simulation of DCB experiments: (a) bilinear-exponential law; (b) trilinear law; (c) bilinear law. | 143 |
| Figure 4.12. Comparison between the use of different traction-separation laws. | 144 |
| Figure 4.13. Deformed shape of DCB specimens. | 145 |
| Figure 4.14. Comparison between the DCB experimental and numerical compliance curves. | 145 |
| Figure 4.15. Comparison between numerical and experimental curves: (a) crack length vs. displacement; (b) crack opening displacement (COD) vs. displacement (δ). | 146 |
| Figure 4.16. Comparison between R-curves obtained numerically and from MBTs methods: a) MBT_{ASTM} method; b) $MBT-EI_{eq}$ method. | 148 |
| Figure 4.17. Comparison between R-curves obtained numerically and from CC methods: a) CC_{ASTM} method; b) CC-f method. | 148 |
| Figure 4.18. Comparison between R-curves obtained numerically and from MCCs methods: a) MCC_{ASTM} method; b) $MCC-a_{eff}$ method. | 149 |
| Figure 4.19. Cohesive laws used for the simulation of ELS experiments: (a) bilinear-exponential law; (b) trilinear law; (c) bilinear law. | 150 |
| Figure 4.20. Typical deformed shape of ELS specimens. | 150 |
| Figure 4.21. Comparison between ELS numerical and experimental results: load vs. displacement curves. | 152 |

| | |
|--|-----|
| Figure 4.22. Comparison between the ELS experimental and numerical compliance curves. | 152 |
| Figure 4.23. Comparison between numerical and experimental curves: (a) crack length vs. displacement; (b) shear displacement vs. displacement (δ). | 153 |
| Figure 4.24. Comparison of R-curves from ELS numerical models and experimental tests: (a) CBTE method; (b) EMC method; (c) SBT method. | 155 |
| Figure 4.25. Influence of σ_c parameter: (a) in DCB tests; (b) in ELS tests. | 157 |
| Figure 4.26. Influence of σ_{max} parameter: (a) in DCB tests; (b) in ELS tests. | 159 |
| Figure 4.27. Influence of σ_{max} parameter: (a) in DCB tests; (b) in ELS tests. | 160 |
| Figure 4.28. Influence of σ_{max} parameter: (a) in DCB tests; (b) in ELS tests. | 161 |
| Figure 4.29. Influence of the parameter γ : (a) in DCB tests; (b) in ELS tests. | 162 |
| Figure 5.1. WFJs experiments in DS decks: (a) specimens' dimensions; (b) test fixture [7]. | 171 |
| Figure 5.2. Assessment of the triangular core constituent: (a) junction before burn-off; (b) junction after burn-off. | 172 |
| Figure 5.3. Load vs. displacement curves: (a) until the final displacement applied; (b) until a displacement applied of 4 mm. | 173 |
| Figure 5.4. Crack pattern with three main cracks: (a) $lf-o_1$ at $\delta = 11.4$ mm; (b) $lf-o_2$ at $\delta = 11.1$ mm; (c) $lf-o_3$ at $\delta = 11.0$ mm. | 174 |
| Figure 5.5. Main cracks definition | 175 |
| Figure 5.6. Major and minor cracks nomenclature: (a) $lf-o_1$ specimen at $P = 0.71$ kN; $\delta = 4.0$ mm; (b) $lf-o_2$ specimen at $P = 0.66$ kN; $\delta = 4.2$ mm; (c) $lf-o_3$ specimen at $P = 0.76$ kN; $\delta = 4.1$ m. | 175 |
| Figure 5.7. Fiber architecture of AS decks [41]. | 178 |
| Figure 5.8. WFJs specimens' dimensions extracted from AS decks. | 178 |
| Figure 5.9. Used test fixture. | 179 |

| | |
|--|-----|
| Figure 5.10. Scheme of the WFJs model. | 181 |
| Figure 5.11. Local axis corresponding to the adopted properties (see Table 5.2). | 182 |
| Figure 5.12. Traction separations laws shape adopted. | 183 |
| Figure 5.13. Traction separation laws used in the Model 1. | 185 |
| Figure 5.14. Traction separation laws used in Model 2. | 186 |
| Figure 5.15. <i>If-o-1</i> experimental curves: (a) load and crack lengths vs. displacement; (b) load vs. individual crack lengths. | 187 |
| Figure 5.16. <i>If-o-2</i> experimental curves: (a) load and crack lengths vs. displacement; (b) load P vs. individual crack lengths. | 188 |
| Figure 5.17. <i>If-o-3</i> experimental curves: (a) load and crack lengths vs. displacement; (b) load P vs. individual crack lengths. | 188 |
| Figure 5.18. Proposed multi-crack approach for <i>If-o-1</i> : (a) P vs. δ and total crack length at vs. displacement applied δ ; (b) load P vs. total crack length at . | 189 |
| Figure 5.19. Proposed multi-crack approach for <i>If-o-2</i> : (a) P vs. δ and total crack length at vs. displacement applied δ ; (b) load P vs. total crack length at . | 189 |
| Figure 5.20. Proposed multi-crack approach for <i>If-o-3</i> : (a) P vs. δ and total crack length at vs. displacement applied δ ; (b) load P vs. total crack length at . | 190 |
| Figure 5.21. Compliance calibration for calculation of critical SERR: (a) specimen <i>If-o-1</i> ; (b) specimen <i>If-o-2</i> ; (c) specimen <i>If-o-3</i> and (d) comparison between the three specimens. | 191 |
| Figure 5.22. R-curve for <i>If-o-1</i> specimen. | 192 |
| Figure 5.23. R-curve for <i>If-o-2</i> specimen. | 193 |
| Figure 5.24. R-curve for <i>If-o-3</i> specimen. | 194 |
| Figure 5.25. R-curves comparison. | 195 |
| Figure 5.26. SERR values adopted for Model 2. | 197 |
| Figure 5.27. Numerical P vs. δ curves: (a) Model 1 – based on DCB and ELS results; (b) Model 2 – Based on the proposed multi-crack assessment approach. | 198 |
| Figure 5.28. Cracks' opening displacements. | 200 |

| | |
|--|-----|
| Figure 5.29. Load vs. displacements curves of AS decks. | 201 |
| Figure 5.30. AS decks cracks: (a) specimen loaded on the acute angle side (AS.01); (b) specimen loaded in the obtuse angle side (AS.05). | 202 |
| Figure 5.31. Normalized P vs. δ curves for AS and DS decks. | 203 |

List of Tables

| | |
|---|-----|
| Table 1.1 - Properties of glass fibers [17] | 31 |
| Table 1.2 - Properties of thermosetting resins (Adapted from Bank [17]) | 31 |
| Table 2.1. Sections' specifications. | 47 |
| Table 2.2. Fiber architecture of the studied sections. | 48 |
| Table 2.3. Average rotational stiffness per unit of width k_r for I-section (CoV in parenthesis). | 55 |
| Table 2.4. Average rotational stiffness per unit of width k_r for channels (CoV in parenthesis). | 55 |
| Table 2.5. Tangential and radial moduli adopted. | 65 |
| Table 2.6. Principal stresses at cracking for I-sections. | 67 |
| Table 2.7. Radial and tangential stresses at cracking for channels. | 67 |
| Table 2.8. Comparison between experimental and predict results. | 76 |
| Table 3.1. Average SERR in J/m ² reported in literature for Mode I. | 86 |
| Table 3.2. Average SERR in J/m ² values reported in literature for Mode II. | 87 |
| Table 3.3. Fiber volume ratio. | 94 |
| Table 3.4. Values of the load P in kN at the crack initiation points. | 105 |
| Table 3.5. Fitting constants for data reduction methods. | 105 |
| Table 3.6. Initiation values for SERR from different methods. | 108 |
| Table 3.7. Propagation SERR values from different methods. | 108 |
| Table 3.8. Fiber bridging length and correspondent COD. | 111 |
| Table 3.9. Values of the load P at the crack initiation points. | 115 |
| Table 3.10. Initiation values for SERR from different methods. | 119 |
| Table 3.11. Propagation SERR values from different methods. | 119 |
| Table 4.1. Traction separation laws implemented via VUMAT. | 135 |
| Table 4.2. Elastic properties adopted for the DCB model. | 139 |
| Table 4.3. SERR values obtained experimentally and in FEM models. | 147 |

| | |
|--|-----|
| Table 4.4. Values of G_{IIC} obtained experimentally and in FEM models. | 154 |
| Table 4.5. Adopted parameters for cohesive laws to assess the σ_c influence. | 156 |
| Table 4.6. Adopted parameters for cohesive laws to assess the σ_{max} influence. | 158 |
| Table 4.7. Adopted parameters for cohesive laws to assess the G_{tip} influence. | 160 |
| Table 4.8. Adopted parameters for cohesive laws to assess the G_{tot} influence. | 161 |
| Table 4.9. Adopted parameters for cohesive laws to assess the γ influence. | 162 |
| Table 5.1. AS tests information. | 179 |
| Table 5.2. Materials properties used in the numerical model. | 180 |
| Table 5.3. Parameters adopted in the cohesive laws. | 196 |
| Table 7.1. Fracture parameters of I_f-o_1 calculated with basis on the novel approach proposed for multi-crack assessment. | 219 |
| Table 7.2. Fracture parameters of I_f-o_2 calculated with basis on the novel approach proposed for multi-crack assessment. | 220 |
| Table 7.3. Fracture parameters of I_f-o_3 calculated with basis on the novel approach proposed for multi-crack assessment. | 221 |

List of Symbols

Chapter 2

| | |
|---------------------------------|---|
| b | specimen's width |
| c | constant |
| d_l | distance between applied load and junction axis |
| g | constant |
| h | specimen's height |
| k | constant |
| k_r | experimental rotational stiffness per unit of width |
| k_{th} | theoretical rotational stiffness per unit of width |
| r | radial crack position |
| $r_{m\acute{a}x}$ | radial position of maximum radial stress |
| t | specimen's thickness |
| t_l | layer's thickness |
| A, B, C constants | |
| E_r | transverse modulus in radial direction |
| E_θ | transverse modulus in tangential direction |
| M | bending moment applied |
| M_{crk} | cracking moment |
| P | applied load |
| R_i | junction's internal radius |
| R_{kr} | rotational stiffness retention |
| R_o | junction's external radius |
| δ measured displacements | |
| σ_r | radial stress |
| σ_θ | tangential stress |

| | |
|----------------------|--|
| σ_1 | maximum principal stress |
| σ_2 | minimum principal stress |
| $\tau_{m\acute{a}x}$ | maximum shear stresses |
| θ | free leg's angle of rotation |
| θ_p | principal plane direction |
| $\Delta\theta$ | variation of the increase rotation angle |

Chapter 3

| | |
|-----------------------|--|
| a | crack length |
| a_e | effective crack length of MCC method |
| a_{eff} | effective crack length of CBTE method |
| b | specimen's width |
| d_1, d_2 | distances between video-extensometer targets |
| m | constant |
| t | specimen's thickness |
| t_s | half of the specimen's thickness |
| C | compliance |
| C_o | constant |
| E_I | flexural modulus |
| G_c | critical strain energy release rate/fracture toughness |
| G_{tip} | strain energy release rate for crack initiation |
| G_{tot} | strain energy release rate for crack propagation |
| G_I | strain energy release in Mode I |
| G_{II} | strain energy release rate in Mode II |
| L | specimen's length |
| L_f | specimen's free length |
| P | applied load |
| α_s | slope of the curve $C^{1/3}$ vs. L_f |
| α, β, χ | constants |

| | |
|------------------|--|
| δ | applied displacement |
| Δ_{clamp} | clamp correction |
| Δ | parameter accounting for rotations at the delamination front |

Chapter 4

| | |
|-----------------------|--|
| a | crack length |
| a_m | critical crack length |
| b | specimen's width |
| l_{czm} | cohesive zone length |
| t | specimen's thickness |
| C | compliance |
| E_{11} | longitudinal modulus of elasticity |
| E_{22} | in-plane transverse modulus of elasticity |
| E_{33} | out-of-plane transverse modulus of elasticity |
| G_{12} | in-plane shear modulus of elasticity |
| G_{13} | out-of-plane shear modulus of elasticity (plane 1-3) |
| G_{23} | out-of-plane shear modulus of elasticity (plane 2-3) |
| G_c | critical strain energy release rate/fracture toughness |
| G_{br} | strain energy release rate due to fiber bridging |
| G_{tip} | strain energy release rate for crack initiation |
| G_{tot} | strain energy release rate for crack propagation |
| G_I | strain energy release in Mode I |
| G_{II} | strain energy release rate in Mode II |
| L | specimen's length |
| M | parameter dependent on the cohesive zone theory |
| P | applied load |
| α, β, χ | constants |
| δ | applied displacement |
| δ_{cod} | crack opening displacement |

| | |
|------------------------|--|
| δ_c | crack opening displacement correspondent to σ_c |
| δ_1 | crack opening displacement correspondent to $\sigma_{m\acute{a}x}$ |
| δ_f | final crack opening displacement |
| σ_{br} | fiber bridging tractions |
| σ_c | interface strength |
| $\sigma_{m\acute{a}x}$ | maximum fiber bridge traction |
| ν_{12} | in-plane Poisson's ratio |
| ν_{13} | out-of-plane Poisson's ratio |
| ν_{23} | out-of-plane Poisson's ratio |
| Δ_{clamp} | clamp correction |
| Ψ | crack shape parameter |

Chapter 5

| | |
|----------|--|
| a | crack length |
| a_1 | crack length of the first crack |
| a_2 | crack length of the second crack |
| a_3 | crack length of the third crack |
| a_t | sum of the length of main cracks |
| a_s | sum of the length of minor cracks |
| b | specimen's width |
| t | specimen's thickness |
| C | compliance |
| E_{11} | longitudinal modulus of elasticity |
| E_{22} | in-plane transverse modulus of elasticity |
| E_{33} | out-of-plane transverse modulus of elasticity |
| G_{12} | in-plane shear modulus of elasticity |
| G_{13} | out-of-plane shear modulus of elasticity (plane 1-3) |
| G_{23} | out-of-plane shear modulus of elasticity (plane 2-3) |
| G_c | critical strain energy release rate/fracture toughness |
| G_{br} | strain energy release rate due to fiber bridging |

| | |
|-----------|--|
| G_{ip} | strain energy release rate for crack initiation |
| G_{tot} | strain energy release rate for crack propagation |
| G_I | strain energy release in Mode I |
| G_{II} | strain energy release rate in Mode II |
| L_v | Lever arm |
| P | applied load |

| | |
|------------------------|--|
| α, β, χ | constants |
| δ | applied displacement |
| δ_{cod} | crack opening displacement |
| δ_c | crack opening displacement correspondent to σ_c |
| δ_I | crack opening displacement correspondent to $\sigma_{m\acute{a}x}$ |
| δ_f | final crack opening displacement |
| σ_{br} | fiber bridging tractions |
| σ_c | interface strength |
| $\sigma_{m\acute{a}x}$ | maximum fiber bridge traction |
| ν_{12} | in-plane Poisson's ratio |
| ν_{13} | out-of-plane Poisson's ratio |
| ν_{23} | out-of-plane Poisson's ratio |

*“E que a minha loucura seja perdoada
Pois metade de mim é amor
E a outra metade também”*

Oswaldo Montenegro

1. Introduction

Glass fiber-polymer composites are materials constituted of high strength glass fibers embedded in a resin matrix. The combination between the two materials allows achieving particular properties and a favorable behavior for structural applications. The glass fibers are responsible for the load-bearing capacity and stiffness, whereas the main role of the polymeric matrix is holding the fibers together, while protecting them against aggressive agents and deterioration, besides helping to transfer external loads to fiber [1].

In the 1940's, glass fiber-polymer composites have drawn the attention of marine and aerospace industries due to their several advantages for military applications, including lightweight and corrosion resistance. Nevertheless, the high manufacturing costs prevented these products from being an attractive alternative for the construction market. To allow fast and economical method of producing fiber-polymer profiles, an automate continuous molding process, called pultrusion, was invented in 1950's and gained place in industry. Ever since, the significant number of researches, supported by industries and governments worldwide, have contributed to develop standard provisions [2–7] and better understanding of the material in several areas of knowledge. In 1990's, the pultruded composites started being used in primary load-bearing structural systems, finding applications in pedestrian bridges, cooling towers, bridges decks, buildings, *off-shore* structures, as well as in the rehabilitation and retrofit of existing buildings [8,9]. Figure 1.1 shows examples of structural systems.



(a) *Pontresina Bridge*, Switzerland (1997)



(b) *Fasano Hotel*, Brazil (2007)



(c) *Salt Storage Unit of Tortuga*, Brazil (2014)



(d) *Eyecatcher Building*, (1999)



(e) *Avançon bridge deck*, Switzerland (2012)



(f) *Staircase Tower*



(g) *Kolding Bridge*, Denmark (1997)

Figure 1.1 - Applications in structural systems: (a) *Pontresina Bridge*, Switzerland [10,11]; (b) *Fasano Hotel*, Brazil [12]; (c) *Salt Storage Unit of Tortuga*, Brazil [13]; (d) *Eyecatcher Building* [10]; (e) *Glass fiber-polymer balsa sandwich bridge deck*, Switzerland [14] (f) *Staircase Tower* [15]; (g) *Kolding Bridge*, Denmark [16]

Glass fiber-polymer composites are anisotropic materials and may be constituted of different types of glass-fiber and resins, depending on the desired application. Four typical fibers are commonly used: *E-glass (electrical glass)*,

which consists in a borosilicate glass with high electrical resistivity, is the most used for structural applications due to its lower cost; *A-glass* (*window glass*) and *C-glass* (*corrosion resistant glass*) are good alternatives when chemical resistance is highly desirable; finally, *S-glass* (*structural or high-strength glass*) is used to improve strength and stiffness [17]. Glass fibers are usually embedded in a thermosetting resin, which undergoes a curing process during polymerization and does not liquefy when heated. The matrix can be chosen to obtain particular properties, such as chemical resistance and fire retardation. The most common thermosetting resins are polyester, epoxy, vinyl ester and phenolic. Table 1.1 and 1.2 present the physical and mechanical properties of glass fibers and thermosetting matrices, respectively.

Table 1.1 - Properties of glass fibers [17]

| <i>Glass Fiber</i> | <i>Density (g/cm³)</i> | <i>Tensile Modulus (MPa)</i> | <i>Tensile Strength (MPa)</i> | <i>Max. Elongation (%)</i> |
|---------------------------|--|-------------------------------------|--------------------------------------|-----------------------------------|
| <i>E</i> | 2.57 | 72.5 | 3400 | 2.5 |
| <i>A</i> | 2.46 | 73 | 2760 | 2.5 |
| <i>C</i> | 2.46 | 74 | 2350 | 2.5 |
| <i>S</i> | 2.47 | 88 | 4600 | 3.0 |

Table 1.2 - Properties of thermosetting resins (Adapted from Bank [17])

| <i>Resins</i> | <i>Density (g/cm³)</i> | <i>Tensile Modulus (MPa)</i> | <i>Tensile Strength (MPa)</i> | <i>Max. Elongation (%)</i> |
|----------------------|--|-------------------------------------|--------------------------------------|-----------------------------------|
| <i>Polyester</i> | 1.2 | 4.0 | 65 | 2.5 |
| <i>Epoxy</i> | 1.2 | 3.0 | 90 | 8.0 |
| <i>Vinyl ester</i> | 1.12 | 3.5 | 82 | 6.0 |
| <i>Phenolic</i> | 1.24 | 2.5 | 40 | 1.8 |

These composites can be manufactured by pultrusion process, which consists in pulling the fibers through a resin tank in order to impregnate them with liquid resin, as shown in Figure 1.2. The wet fibers continue to be pulled into a heated steel die, where resin is cured at elevated temperatures. When solidified, the profile assumes exactly the cavity shape of the die [18].

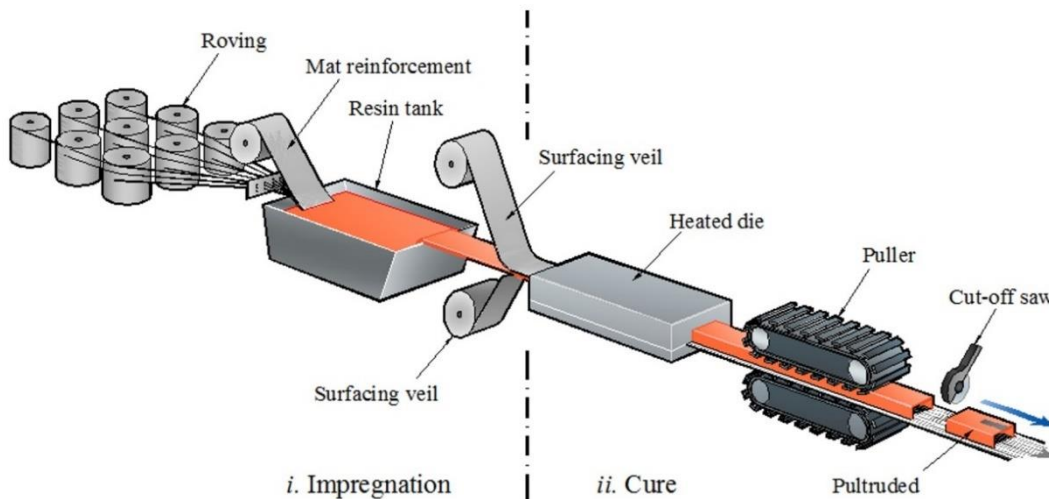


Figure 1.2 - Pultrusion process [19]

Pultrusion process enables versatility in properties and cross-section geometry, allowing the fabrication of a wide variety of shapes, although usual sections mimic those used in steel industry such as angles, channels and I-sections. Moreover, the pultrusion is an eco-friendlier process when compared to other materials manufacturing, such as steel and aluminum, due to, for instance, the energy efficiency, less pollution, and the profiles longer life cycle [20,21]. The profiles present inhomogeneous and orthotropic fiber distribution throughout cross section, which results in a significant variability of properties [22]. Usually, the fiber volume content ranges from 30 to 60%.

Three main types of fibers are used in a pultruded fiber-polymer composite: i) *rovings*; ii) *continuous strand mats (CSM)* and/or *fabrics* and iii) *surface veils*. The rovings are unidirectional continuous fibers aligned in pultrusion direction and responsible for the high longitudinal material strength, whereas the fabrics are structural mats comprised of randomly orientated strands responsible for the transverse mechanical properties of the composite. Finally, veils are usually added to external surfaces to improve weather resistance and to protect material from ultraviolet (UV) degradation. The typical fiber arrangement of this type of composite is illustrated in Figure 1.3.

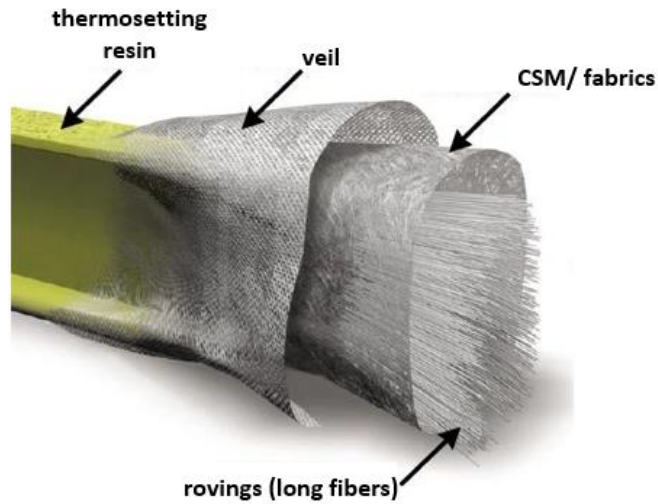


Figure 1.3 – Typical fiber architecture for pultruded fiber-polymer profiles (Adapted from Azo Materials [23])

Pultruded glass fiber-polymer composites present several advantages over conventional construction materials, among which one may cite its lightweight, resistance to a broad range of chemicals, low thermal and electrical conductivity, corrosion and fatigue resistance, besides the low maintenance costs and easy installation. However, to spread the composites use in structural systems, it is necessary to fully understanding certain issues affecting their failure and damage mechanisms, as it will be discussed in detail hereafter.

1.1. Motivation

In recent decades, a considerable number of studies – including experimental, numerical and analytical analyses – have been carried out to develop a solid comprehension about the pultruded fiber-polymers weaknesses. However, there remain topics not fully known or understood, especially when concerning their failure mechanisms and multi-crack behavior. Despite all the previously mentioned advantages over traditional construction materials, the fiber-polymer composite's load bearing capacity, global stiffness and serviceability may be strongly affected by interlaminar delamination [24], usually initiated at the web-flange junctions (WFJs) region. Due to their particular fiber architecture, with more incidence of defects, imperfections, mat wrinkling and resin-rich zones, the junctions are considered the weakest zone of the cross-section, being a potential area for the onset failure [25–28]. The premature failure generated by the separation of web and flange is a matter of concern for pultruded fiber-polymer structure's integrity and safety.

Although the WFJs are usually considered to be rigid, including in the existing design codes, studies in literature have shown that they are characterized by a non-linear semi-rigid behavior, which could be considered a weakness that affect the local buckling capacity [29–34]. Moreover, the local behavior of the junctions may also affect the composite's overall buckling response [35]. In this context, the characterization of the WFJs and its rotational stiffness is a topic of interest in order to develop reliable numerical models able to accurately predict both linear and nonlinear composite's behavior, taking it account the junctions' limitation. Therefore, the study of the rotational stiffness of the WFJs is a relevant key point to understand how exactly they affect pultruded fiber-polymer members and thus, providing fundamental information for the establishment of reliable design guidelines. This topic is addressed in Chapter 2.

In parallel, fracture mechanics data, such as normal interface strength and fracture toughness, are also needed to properly simulate the pultruded fiber-polymers response, reducing the necessity for costly and time-consuming experiments. Nevertheless, the investigations on damage mechanisms and failure

of these composites are usually hampered by the scarcity of studies available, especially addressed to interlaminar fracture and to Mode II. Moreover, the complexity in obtaining fracture parameters and the well-known high variability in general properties of this type of material are aggravating factors that increase the need of reliable guidelines for the accurate determination of their fracture characteristics. Besides that, pultruded elements are manufactured through an automatic continuous process in factories, which is an obstacle for the application of existing standardized methods adopted for polymer matrix composites, such as the Double Cantilever Beam (DCB) and the End-Loaded-Split (ELS). These standards recommend introducing a very thin initial separation (or starter crack) in the specimens during fabrication, which is not possible for pultruded elements. Therefore, new techniques and methodologies need to be developed and assessed to decrease the difficulty in determining the fracture parameters of these composites. In the numerical field, more challenges to determine these parameters are encountered. The R-curve dependence on specimens' geometry in particular cases, added to the influence of traction-separation cohesive laws shape, increase the complexity in performing reliable simulations [36–38]. Fitting procedures are usually adopted to calibrate the fracture parameters with load vs. displacement curves. To contribute to the development of future research, it is fundamental to complement this fracture mechanics data scarcity and also investigate the parameters affecting numerical reliable responses, such as the cohesive laws shape. These topics are addressed in Chapters 3 and 4.

Finally, most of the available numerical models intending to assess the composites' failure are focused on the fracture assessment due to a single crack, in contrast to the actual failure behavior of multilayered composites. Very few works in literature are focused on the multi-crack behavior of fiber-polymer composites and, to the best of the author's knowledge, none of them focused on pultruded components. In this context, a multi-crack damage approach makes itself valuable for fiber composites structural design, since its actual failure is often related, for instance, to several small imperfections and interface issues, which results in multiple layered delamination. Moreover, multiple local cracks at the junctions may allow the composites to undergo important damage mechanisms and might also enable a pseudo-ductile behavior. This is relevant, in view of the fact that pultruded

fiber-polymers are composites with linear-elastic behavior when loaded in longitudinal direction (*i.e.* parallel to pultrusion direction), exhibiting brittle rupture. This behavior ends up restricting the material use in structural applications, once the lack of warning in case of sudden failure and the ability to redistribute stresses are usual concerns for structural engineers. Strategies are needed to obtain an inelastic non-linear behavior, which may be achieved through dissipation or storage of energy, resulted from multiple damages and progressive failure. This topic is addressed in Chapter 5.

1.2. Objectives

The aim of this research is to investigate the delamination and multi-crack behavior of pultruded fiber-polymer composites (bridge decks and different shapes of profiles), seeking for a better comprehension about web-flange junctions' (WFJs) behavior and the progressive failure of these composites. The following objectives can be cited:

- Propose the characterization of the rotational stiffness by a direct method, where the relative rotation between web and flange is measured directly during test using Digital Image Correlation technique [39]. This procedure allows a simple setup to be used - without the need of a special apparatus – and simplifies issues related to the gap between the clamp tips and the junction that arise when using elastic curve approaches.
- Discuss the influence of imperfections on the WFJ's performance and to fill existing gaps in literature by proposing three complementary analyses for WFJs' behavior: *i)* a simple methodology to determine the stresses on crack onset region based on the curved beam theory for anisotropic material [40]; *ii)* a lower-bound function to model stiffness retention based on experimental results; and *iii)* a theoretical expression for prediction of the rotational stiffness of WFJs;
- Present a testing methodology to obtain interlaminar fracture mechanics parameters of pultruded glass fiber-polymers, based on

classical and standardized experiments, and assess different data reduction methods to determine the strain energy release rate (SERR) for both Fracture Modes I and II;

- Complement the scarcity on the numerical interlaminar fracture data, especially for Mode II, and evaluate the use of different shapes of traction-separation cohesive laws to simulate standardized tests, such as the DCB and ELS;
- Contribute to the development of a methodology that allows to reproduce properly the failure generated through multiple cracks in WFJ's, proposing a novel approach for the multi-crack assessment. Besides promoting the understanding on the multiple delamination growth, the multi-crack analysis could help to reduce time-consuming experiments and improve the existing design codes.
- Discuss the benefits and structural behavior improvement due to the existence of multiple interspersed layers.

1.3. Organization of the dissertation

This PhD dissertation is divided into four core chapters, presented in the form of extended and complete articles – each one with its own literature review, research methodology and results presentation. The results of Chapter 2 were published in *Composites Part B* journal as the paper entitled “*Experimental investigation on the moment-rotation performance of pultruded FRP web-flange junctions*” (<https://doi.org/10.1016/j.compositesb.2021.109087>).

A summary of each chapter is presented in the following:

- Chapter 2 presents an experimental investigation on the behavior of web-flange junctions (WFJs) rotational stiffness of pultruded fiber- polymer composites. Channels and I-sections were tested using a simple set-up, which was developed in order to experimentally characterize the junctions in a direct manner by using the Digital Image Correlation (DIC) technique. The WFJs' imperfections are analyzed, and damage thresholds are

identified in order to propose lower bound functions to simulate the junction stiffness retention. Moreover, two Equations are proposed to analytically predict pultruded junctions' rotational stiffness per unit of width.

- Chapter 3 describes the results of an experimental program conducted on interlaminar fracture of pultruded glass fiber-polymer specimens extracted from a composite bridge deck system. Both Modes I and II were investigated, through Double Cantilever Beam (DCB) and End-Loaded-Split (ELS) tests, respectively. Six data reduction methods used to determine the critical strain energy release rate (SERR) were assessed for Mode I, while other three methods were evaluated for Mode II.
- Chapter 4 presents the results of 2D finite-element analyses conducted to simulate the DCB and ELS experiments presented in Chapter 3. The cohesive zone model (CZM) approach was adopted in the modelling and the use of three different shapes of traction separation laws are investigated. The experimental and numerical results are discussed and compared. A parametric study on the different parameters of three-part cohesive laws was conducted to assess how they affect pultruded glass fiber-polymers progressive failure and their load *vs.* displacement curves.
- Chapter 5 aims to contribute to the development of a methodology and numerical models that allow to reproduce properly the failure generated through interlaminar multiple cracks in WFJ's. A cohesive damage model taking into account the junctions' heterogeneity is performed, implementing bilinear and bilinear-exponential traction separation laws in order to simulate three curved and parallel cracks on the WFJs. A novel approach is proposed to assess the composites multiple delamination and the structural behavior improvement due to the existence of multiple interspersed layers is discussed.
- Chapter 6 presents the conclusions, major contributions of the thesis, along with suggestions for future works.

1.4. References

- [1] MALLICK, P. K. **Fiber-reinforced composites: materials, manufacturing, and design.** [s.l: s.n.].
- [2] AMERICAN SOCIETY OF CIVIL ENGINEERS ASCE. **ASCE - Structural Plastic Design Manual**, 1984.
- [3] AMERICAN SOCIETY OF CIVIL ENGINEERS ASCE. **ASCE - Pre-Standard for Load and Resistance Factor Design (LRFD) of Pultruded Fiber Reinforced Polymer (FRP) Structures (Final)**, 2010.
- [4] NATIONAL RESEARCH COUNCIL OF ITALY. **Guide for the Design and Construction of Structures made of FRP Pultruded Elements**CNR-DT 205, , 2007.
- [5] ASCIONE, LUIGI, ET AL. **Prospect for new guidance in the design of FRP: Support to the implementation, harmonization and further development of the Eurocodes.** [s.l: s.n.].
- [6] NORMA BRASILEIRA NBR 15708. **Indústria do petróleo e gás natural - Perfis Pultrudados**Associação Brasileira de Normas Técnicas (ABNT), , 2011.
- [7] **European Technical Specification CEN/TS19101:2023 - Design of fibre-polymer composite structures.** , 2023.
- [8] BAKIS, C.E.; BANK, L.C.; BROWN, V.L.; COSENZA, E.; DAVALOS, J.F.; LESKO, J.J.; RISKALLA, S.H AND TRIANTAFILLOU, T. C. Fiber-Reinforced Polymer Composites for Construction—State-of-the-Art Review. **Journal of Composites for Construction**, v. 6, n. 2, p. 73–87, 2002.
- [9] CORREIA, J. R.; BAI, Y.; KELLER, T. A review of the fire behaviour of pultruded GFRP structural profiles for civil engineering applications. **Composite Structures**, v. 127, p. 267–287, 2015.
- [10] KELLER, T. et al. Effect of atural Weathering on Durability of Pultruded Glass Fiber – Reinforced Bridge and Building Structures. **Journal of Composites for Construction**, v. 20, n. 1, p. 1–9, 2015.
- [11] **Fiberline Composites (2017a).** Disponível em: <<https://fiberline.com/pontresina-bridge>>. Acesso em: 15 jun. 2017.
- [12] **Cogumelo.** Disponível em: <http://www.cogumelo.com.br/images/linha-industrial/downloads/Catalogo_Geral_Produtos.pdf>. Acesso em: 16 jun. 2017.

- [13] **Pultrusão do Brasil.**
- [14] **École Polytechnique Fédérale de Lausanne - Composite Construction Laboratory - Projects.** Disponível em: <<https://www.epfl.ch/labs/cclab/projects/avancon/>>. Acesso em: 22 apr. 2023.
- [15] COGUMELO. **Produtos Pultrudados e injetados em fibra de vidro.** Disponível em: <http://www.cogumelo.com.br/images/linha-industrial/downloads/Catalogo_Geral_Produtos.pdf>. Acesso em: 16 jun. 2017.
- [16] **Fiberline Composites (2017b).** Disponível em: <<https://fiberline.com/fiberline-bridge>>. Acesso em: 15 jun. 2017.
- [17] BANK, L. C. **Composites for construction: structural design with FRP materials.** [s.l: s.n.].
- [18] PULTRUSIONS, C. **The Pultex Pultrusion Design Manual of Standard and Custom Fiber Reinforced Polymer Structural Profiles** Alum Bank, PA, , 2017.
- [19] LANDESMANN, A.; SERUTI, C. A.; BATISTA, E. DE M. Mechanical Properties of Glass Fiber Reinforced Polymers Members for Structural Applications. **Materials Research**, v. 18, n. 6, p. 1372–1383, 2015.
- [20] SONG, Y. S.; YOUN, J. R.; GUTOWSKI, T. G. Life cycle energy analysis of fiber-reinforced composites. **Composites Part A: Applied Science and Manufacturing**, v. 40, n. 8, p. 1257–1265, 2009.
- [21] VOLK, M. et al. Cost-efficient, automated, and sustainable composite profile manufacture: A review of the state of the art, innovations, and future of pultrusion technologies. **Composites Part B: Engineering**, v. 246, n. March, p. 110135, 2022.
- [22] L., M. J. M. AND; BANK, C. Sensitivity Studies on Local Flange Buckling Equations for Pultruded Beams and Columns. **CICE 2010 - The 5th International Conference on FRP Composites in Civil Engineering**, p. 27–29, 2011.
- [23] **Fiber architecture of pultruded profiles.** Disponível em: <<https://www.azom.com/article.aspx?ArticleID=12913>>.
- [24] CAMESELLE-MOLARES, A. **Two-dimensional crack growth in FRP laminates and sandwich panels.** 2019. École Polytechnique Fédérale de Lausanne (EPFL). 2019.
- [25] FEO, L.; MOSALLAM, A. S.; PENNA, R. Mechanical behavior of web-flange junctions of thin-walled pultruded I-profiles: An experimental and numerical evaluation. **Composites Part B: Engineering**, v. 48, p. 18–39, 2013.

- [26] XIN, H. et al. Impact of hygrothermal aging on rotational behavior of web-flange junctions of structural pultruded composite members for bridge applications. **Composites Part B: Engineering**, v. 110, n. February, p. 279–297, 2017.
- [27] MOSALLAM, B. A. S.; MEMBER, A.; BANK, L. C. Short-term behavior of pultruded fiber-reinforced plastic frame. v. 118, n. 7, p. 1937–1954, 1992.
- [28] MOSALLAM, A. S. et al. Structural evaluation of axial and rotational flexibility and strength of web-flange junctions of open-web pultruded composites. **Composites Part B: Engineering**, v. 66, p. 311–327, 2014.
- [29] YANES-ARMAS, S.; CASTRO, J. DE; KELLER, T. Rotational stiffness of web-flange junctions of pultruded GFRP decks. **Engineering Structures**, v. 140, p. 373–389, 2017.
- [30] TURVEY, G. J.; ZHANG, Y. A computational and experimental analysis of the buckling, postbuckling and initial failure of pultruded GRP columns. **Computers and Structures**, v. 84, n. 22–23, p. 1527–1537, 2006.
- [31] ASCIONE, L. et al. Local buckling behavior of FRP thin-walled beams: A mechanical model. **Composite Structures**, v. 98, p. 111–120, 2013.
- [32] CINTRA, G. G.; CARDOSO, D. C. T.; VIEIRA, J. D. Parameters affecting local buckling response of pultruded GFRP I-columns: Experimental and numerical investigation. **Composite Structures**, v. 222, n. January, p. 110897, 2019.
- [33] LIU, T.; HARRIES, K. A. Flange local buckling of pultruded GFRP box beams. **Composite Structures**, v. 189, n. January, p. 463–472, 2018.
- [34] LIU, T. Q. et al. Determining rotational stiffness of flange-web junction of pultruded GFRP I-sections. **Composite Structures**, v. 236, n. January, p. 111843, 2020.
- [35] YANES-ARMAS, S.; CASTRO, J. DE; KELLER, T. Rotational stiffness of web-flange junctions of pultruded GFRP decks. **Engineering Structures**, v. 140, p. 373–389, 2017.
- [36] GUTKIN, R. et al. Modelling the R-curve effect and its specimen-dependence. **International Journal of Solids and Structures**, v. 48, n. 11–12, p. 1767–1777, 2011.
- [37] SUO, Z.; BAO, G.; FAN, B. **Delamination R-curve phenomena due to damage** *Journal of the Mechanics and Physics of Solids*, 1992.
- [38] GHADIRDOKHT, A.; HEIDARI-RARANI, M. Delamination R-curve

behavior of curved composite laminates. **Composites Part B: Engineering**, v. 175, n. June, p. 107139, 2019.

[39] GOM CORRELATE. **Evaluation Software for 3D Testing**. Disponível em: <<https://www.gom.com/3d-software/gom-correlate.html>>. Acesso em: 20 dec. 2020.

[40] LEKHNITSKII, S. G. Anisotropic plates No. FTD-HT-23-608-67. **Foreign Technology Div Wright-Patterson Afb Oh**, 1968.

2. Experimental investigation on the moment-rotation performance of pultruded fiber-polymer web-flange junctions

2.1. Introduction

The use of pultruded fiber-polymer composites in structural applications has greatly increased in recent decades, due to their several advantages over traditional materials, such as its lightweight, corrosion resistance and ability to tailor geometry. Researchers worldwide have dedicated significant efforts to better understand the performance of pultruded fiber-polymer members, especially related to instability problems. In this context, the behavior of the junctions between adjacent plates comprising the cross section became a matter of interest due to its influence on the buckling response of pultruded members. Moreover, the local failure at these regions affects the overall structure behavior, having influence on its stiffness and strength [1,2].

Previous works [3–5] have shown that web-flange junctions (WFJs) are characterized by a non-linear semi-rigid constitutive law, which affects the local buckling capacity. Cintra *et al.* [6] compared the critical loads for pultruded glass fiber-polymer columns having semi-rigid and rigid junctions between web and flange, reporting reductions up to 9.4% for the former. Liu and Harries [7] investigated the flange local buckling behavior of pultruded box beams and found out that the experimental results were less than one-third of the theoretical predictions using rigid-junction expressions available in fiber-polymers design codes [8]. The authors observed that analytical equations considering constituent plates simply supported along edges between adjacent plates lead to better predictions, ratifying the fact that junctions do not present a rigid behavior. Mosallam and Bank [2] also reported results that have indicated that the web-flange intersection could only offer a partial restraint to the compressed flange.

The composites failure is often related to the junctions, which are an important point of weakness [4,7,9,10] due to their curved shape and particular fiber architecture with incidence of mat wrinkling and presence of resin-rich areas [1,11]. Such defects are cited in literature as some of main factors that lead to premature failure of web-flange junctions [12]. The junction is, thus, a potential area for the onset of failure that might lead to separation of web and flange, controlling the overall behavior of the composite until its premature rupture [2,12,13]. Bank and Yin [14] stated that this specific failure mode is a matter of concern, once it affects the geometry integrity of the member cross-section, which will behave “*as a collection of individual and separate plates*” [14] that can no longer bear the applied load. The authors cited the geometry, fiber architecture and material properties of junctions’ region as elements that play an important role in determining the dominating failure mode. In this context, the junctions’ characterization became a matter of great relevance.

Many authors have devoted attention to develop appropriate techniques to determine the moment-rotation relations ($M - \theta$) and to obtain the WFJs rotational stiffness [2,3,9-13]. Bank *et al.* [15] have conducted four-point bending tests to characterize the junctions indirectly, through the measurements of the half-wave lengths. Values of 5.04 and 3.29 kN/rad were reported for the rotational stiffness per unit of width, considering properties obtained from characterization tests and from the lay-up information provided by manufacturer, respectively. Turvey and Zhang [16] developed three-point bending apparatus to characterize WFJs rotational stiffness of an I-section. Analytical models were used to obtain transverse bending modulus, as well as the relation between moments M and web rotations θ . The same behavior was assumed for both junctions of cross-section and values of 6.83kN/rad and 6.57 kN/rad were found for rotational stiffness. The authors reported “*a relative lack of consistency*” [16] in the results and attributed it to the fact that fiber architecture in web-flange junctions are much less ordered than other parts of the profile. In addition, the failure process was observed to initiate through a delamination at the triangular core rovings. Mosallam *et al.* [1] also developed a test apparatus to evaluate rotational stiffness of web-flange junctions of H-sections and angles. The bottom flange and web were clamped using thick steel angles, while rotation was applied to the upper flange. However, according to Yanes-Armas *et al.*

[3], this test fixture may not have represented the actual boundary conditions, due to pre-compression in specimens through thickness direction, affecting results and failure mode. Xin *et al.* [12] developed a test apparatus to obtain the moment-rotation relation. The test fixture consisted in clamping the specimen flanges with screws on a base, while a load P is applied on the web from a distance d of the junction. The set-up prevented the web's flexure, simplifying issues related to the obtaining of deflections due to bending, however demanding a more elaborate test configuration. The authors also evaluated the influence of critical parameters on the WFJs behavior, concluding that greater values of flange/web thickness and fillet radius result in higher junction's rotational stiffness. Yanes-Armas *et al.* [3] conducted an experimental study on WFJs of a bridge deck system and determined the $M-\theta$ relation through two analytical models. Results ranging from 178 to 628 kN/rad were found for junction's rotational stiffness, reaching significantly higher values in some cases. These high values were attributed to the different decks' fiber architecture, which includes triaxial multi-ply fabrics besides rovings and non-structural mats. On the other hand, some lower values were attributed to nonlinearities due to existing pre-cracks.

Based on researches available on literature, the angle of rotation θ , needed for the construction of the $M-\theta$ relation, is usually obtained through indirect manners, *i.e.*, using the elastic curve equation to previously determine additional parameters – such as the transverse modulus E_t – through specific characterization tests [16,18]. Test setups using an especial apparatus to avoid influence of flexural deformation in the measurement of θ can also be found in literature [1,13]. Therefore, the present work proposes the characterization of the rotational stiffness by a direct method, where the relative rotation between web and flange is measured directly during test using Digital Image Correlation technique [17]. This procedure allows a simple setup to be used - without the need of a special apparatus – and simplifies issues related to the gap between the clamp tips and the junction that arise when using elastic curve approaches.

Moreover, this paper aims to discuss the influence of imperfections on the WFJ's performance and to fill existing gaps in literature by proposing three complementary analyses for WFJs' behavior: *i)* a simple methodology to determine the stresses on crack onset region based on the curved beam theory for anisotropic

material [18]; *ii*) a lower-bound function to model stiffness retention based on experimental results; and *iii*) a theoretical expression for prediction of the rotational stiffness of WFJs.

2.2. Materials and Methods

An experimental investigation addressing the WFJ's rotational stiffness has been conducted. A simple set-up is proposed, and the junctions are characterized with the aid of the Digital Image Correlation (DIC) [19], defined as a non-contact optical technique that consists in tracking blocks of pixels from taken photographs during the tests. This technology allows the direct measurement of displacements, rotations and the built up of deformation vector fields and strain maps [20], as will be shown further. The WFJs experiments were conducted at the *Laboratory of Structures and Materials (LEM-DEC) of Pontifical Catholic University of Rio de Janeiro (PUC-Rio)*.

2.2.1. Materials

In all, eighteen specimens 35-mm wide were extracted from four different profiles, indicated in Figure 2.1 for testing. Two types of I-sections with dimensions of 152.4 x 76.2 x 9.5-mm (I_1) and 101.6 x 101.6 x 6.4-mm (I_2) and two different channels having 50.8 x 230.2 x 9.5-mm (C_1) and 41.28 x 152.4 x 5-mm (C_2) were analyzed. Four specimens were extracted from each I-section and eight specimens were extracted from C_2 -channel profiles, while only two were taken from C_1 -channel. Table 2.1 presents the specifications of each studied section, indicating the nominal dimensions, constituent matrices, respective nominal fillet radius, and total fiber volume ratio (V_f), as well as both of continuous strand mat (V_{csm}) and roving (V_{rov}) volume fraction. Unfortunately, it was not possible to measure individually the roving and CSM volume content of the C_1 -profile. The fiber volume ratios were obtained through burn-off tests conducted at the *Fernando Lobo Carneiro Material Structure Laboratory (LABEST) of Federal University of Rio de Janeiro (UFRJ)* and at the *Laboratory of Structures and Materials (LEM-DEC) of Pontifical Catholic University of Rio de Janeiro (PUC-Rio)*, following the recommendations of *ISO 1172:1996* [21] and the methodology presented in [22].

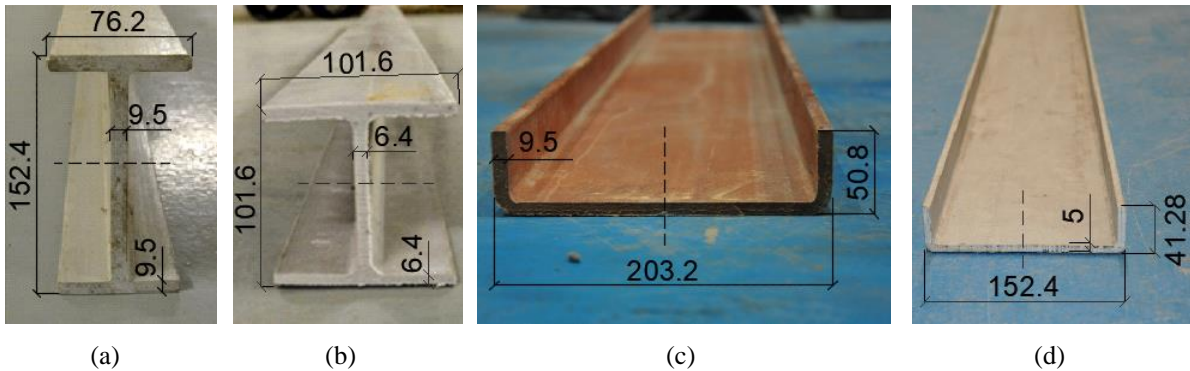


Figure 2.1 - Studied cross-sections: (a) I₁-section; (b) I₂-section; (c) C₁-channel; (d) C₂-channel.

Table 2.1. Sections' specifications.

| <i>Section</i> | <i>Nominal dimensions (mm)</i> | <i>Matrix</i> | <i>Nominal fillet radius (mm)</i> | <i>V_f (%)</i> | <i>V_{rov} (%)</i> | <i>V_{csm} (%)</i> |
|----------------|------------------------------------|---------------|---------------------------------------|------------------------------|--------------------------------|--------------------------------|
| I ₁ | 152.4 x 76.2 x 9.5 (t) | Polyester | 5.0 | 50.8 | 43.6 | 7.2 |
| I ₂ | 101.6 x 101.6 x 6.4 (t) | Vinyl Ester | 5.0 | 49.8 | 42.8 | 7.0 |
| C ₁ | 50.8 x 230.2 x 9.5 (t) | Phenolic | 7.5* | 56.5 | - | - |
| C ₂ | 41.28 x 152.4 x 5.0 (t) | Vinyl Ester | 5.0 | 48.8 | 40.8 | 8.0 |

* curve geometry is not well-defined for this cross-section and a nominal radius is informed only for reference.

The fiber architecture of the studied profiles is composed by rovings and continuous strand mats (CSM). Table 2.2 presents the number (n) of mat and roving layers of each profile and their respective thickness (t_i) in flat regions, which were measured visually through high quality pictures. The I₂-sections have shown the highest variability in terms of number of layers, presenting different number of mat/roving layers on each flange of the same profile. The web, for instance, presented three mat layers, among which two of them are distributed to the flanges - one for each side. The third web's mat layer also turns to one of the flanges, leading to the existence of two mats in one of the flanges and three in the other one. On the other hand, I₁-sections are composed by four mat layers in the web, which are distributed equally to each flange. Finally, the channels presented the same number of mat and roving layers, both in web and in flange, interspersed throughout the specimens' thickness and having mats as the outermost layers. The profiles used

in this study meet geometric tolerances required by *ASTM D3917*. These global imperfections have minor influence on the junction's performance and, therefore, were not considered.

Table 2.2. Fiber architecture of the studied sections.

| Section | Flange layers | | | | Web layers | | | |
|----------------|---------------|---------------------------|----------|---------------------------|------------|---------------------------|----------|---------------------------|
| | mat | | roving | | mat | | roving | |
| | <i>n</i> | <i>t_i</i> (mm) | <i>n</i> | <i>t_i</i> (mm) | <i>n</i> | <i>t_i</i> (mm) | <i>n</i> | <i>t_i</i> (mm) |
| I ₁ | 3 | 0.6 – 1.2 | 2 | 2.4 - 3.5 | 4 | 0.5 – 0.8 | 2 | 2.9 - 3.4 |
| I ₂ | 2 - 3 | 0.4 – 0.8 | 1 - 2 | 1.6 – 2.4 | 3 | 0.6 – 0.9 | 2 | 1.4 – 2.4 |
| C ₁ | 4 | 0.7 – 1.2 | 3 | 1.0 – 2.0 | 4 | 0.8 – 1.6 | 3 | 1.0 – 2.0 |
| C ₂ | 3 | 0.4 – 0.7 | 2 | 1.5 – 2.5 | 3 | 0.6 – 0.8 | 2 | 1.4 – 2.0 |

2.2.2. Specimens' imperfections

To better analyze the existence of imperfections from manufacturing, which may have significant influence on the WFJ's behavior, a complementary image analysis was conducted. In a first step, the specimens were sanded, polished, and embedded in a small container with liquid epoxy resin. This process allows a better visualization of the fiber arrangement after the resin's cure. Pictures of the results, taken using a *Nikon SMZ 800* stereoscope, are shown in Figure 2.2.

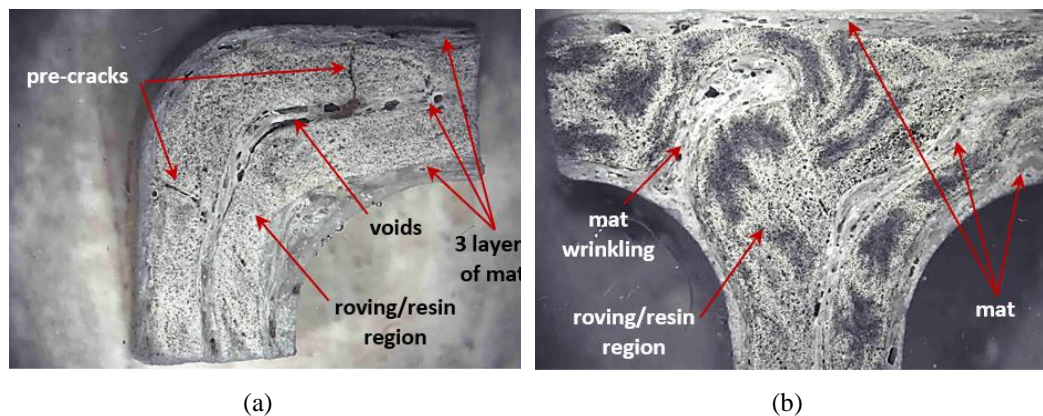


Figure 2.2. Images taken from the microscope: (a) specimen extracted from C₂; (b) specimen extracted from I₂.

It can be noticed that the fiber architecture at channels junctions is more uniform when compared to the I-sections, following the fillet curve shape.

However, regardless of the cross-section's shape, all profiles presented some sort of imperfection at the region. The main types of imperfections that directly affect the WFJs performance are: *i*) mat wrinkling due the pultrusion process; *ii*) intralaminar (matrix) pre-cracks and *iii*) incidence of void.

Although having a simpler shape, the junctions of C_1 specimens presented a little spot with mat wrinkling at the inner portion of the curve at the junctions' shape, whereas the specimens extracted from the C_2 profiles presented intralaminar pre-cracks and significant void content along the mid-thickness mat, as can be seen in Figure 2.2a. The I-sections, on the other hand, presented regions with significant mat wrinkling, as shown in Figure 2.2b. In order to complement this analysis and better evaluate the imperfection of the I-sections junctions, a high resolution micro-XCT system – *ZEISS Xradia 510 Versa* – was used to obtain a 3D image of the configuration of layers, shown in Figure 2.3. The result of the microtomography highlights the relevance of fiber wrinkling due the pultrusion process and the complexity on I-sections fiber architecture, which has a great influence on the junctions' properties, as shown below.

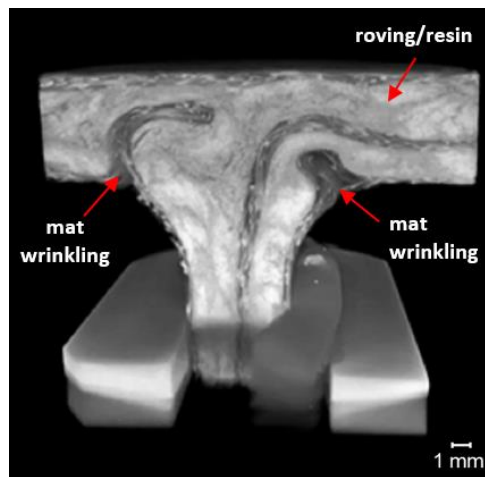


Figure 2.3. Images of specimen extracted from I_2 obtained by microtomography.

The defects described herein are quite common in commercial pultruded glass fiber-polymer profiles, used in real applications – such as offshore inspection platforms, cooling towers, deck bridges, secondary and primary structures in general –, and are often reported in literature [7,12,23,24]. If not taken into account in the design procedure, the defects could generate undesirable results in structure

behavior. This should inspire and engage the pultrusion industry to improve the production quality.

2.2.3. Test set-up and DIC technique

Figure 2.4 shows the T and L-shaped specimens extracted from I-sections and channels, respectively, obtained by cutting half of cross-section depth. The test set-up used for the characterization of WFJs rotational stiffness is shown in Figure 2.5a. The specimens were clamped to a steel angle using rigid aluminum bars and screws. The steel angle, on the other hand, was attached to a base, preventing the specimens from coming out of the load application plane. The minimum distance between the clamp tip and the specimen's web was adopted as the value of the composite thickness (t). Although this configuration might lead to a slightly rotation of the clamped flange, the chosen technique for measuring the web's rotation takes into account the concerned flange flexibility, thus, not affecting the experimental results. A laser device was used to place the specimen on the right position. The load P was applied through a roller to the specimens' free leg at a distance d_l of the junction, as shown in Figure 2.5b. All tests were conducted under displacement control at a rate of 0.6 mm/min until failure using a servo-hydraulic universal testing machine *MTS 244.41* with a load capacity of 500 kN. A load cell of 2.5 kN capacity was attached to the actuator for appropriate testing control. This configuration allows the set-up to be adapted to a wide range of cross-section types.

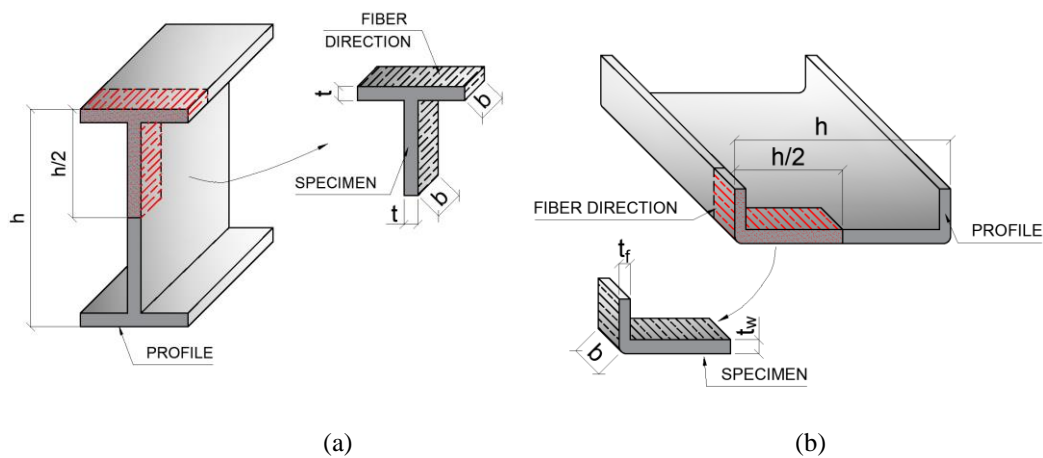


Figure 2.4. Specimens extracted from profiles: (a) from I-section profiles; (b) from channels.

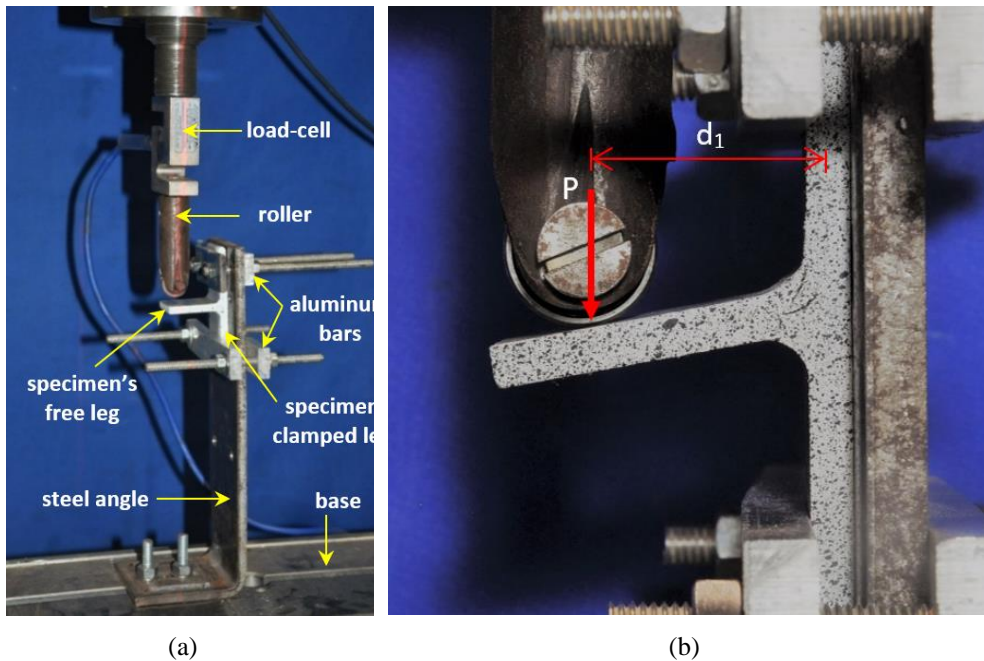


Figure 2.5. Test set-up: (a) Overview; (b) detail of the test configuration.

Regarding channels testing, four among eight specimens were positioned on the set-up in order that the applied load caused a ‘section closure’ during the test, whereas the other four were loaded in order to ‘open’ the section, as presented in Figure 2.6. This procedure was adopted since the dependency on the loading mode has been reported in literature [1], which is related to the resulting stress distribution that will be discussed further.

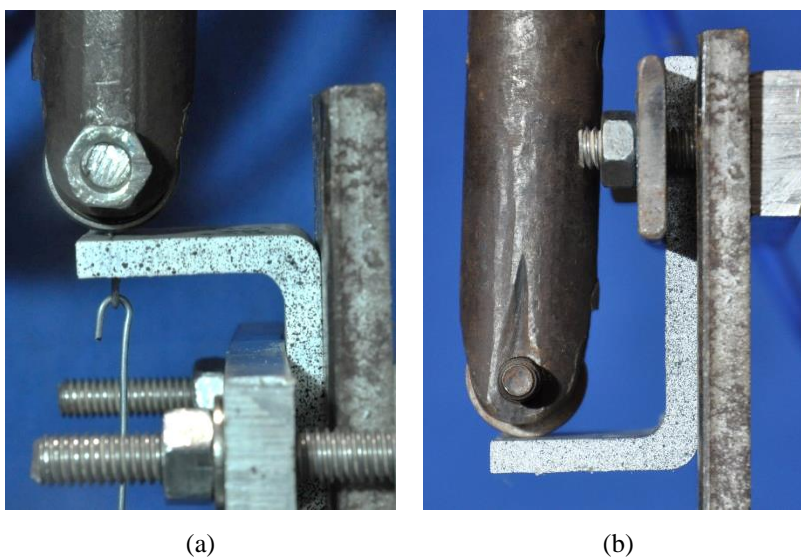


Figure 2.6. Channel section tests: (a) close-mode; (b) open-mode.

Considering the test geometry shown in Figure 2.5b, the applied moment can be computed as $M = P \times d_l$ and the rotational stiffness per unit of width k_r can be obtained as the slope of the plot M/b versus θ – where θ is the junction’s rotation and b is the specimen’s width. To solve the challenge of obtaining the free leg’s angle of rotation θ by simple and direct means, the DIC technique was used. The specimens had their cross-section painted in white to reduce possible light reflections and increase accuracy. Subsequently, a black speckle pattern was applied over the white surface, meeting the quality pattern required for the use of the technique. During the tests, photos were taken every five seconds with a *Nikon D90*, with a resolution of 4288 x 2848 pixels and subsequently, the pictures were analyzed in the free software *GOM Correlate 2020* [17]. As illustrated in Figure 2.7, the DIC allows the direct measurement of the angle of interest θ by tracking the subsets motion of a reference image (undeformed specimen) and matching it with the ones in subsequent photos, in which there is a relative rotation between the specimens’ free leg and the clamped one. The relative displacements are calculated and decomposed at the center of each subset, which are, in other words, selected portions of the dots pattern, spaced according to grid steps. In the present study, a subset size of 25 x 25 pixels and a corresponding grid step of 8 pixels were adopted. These parameters were chosen following the recommendation of a minimum of three speckles per subset [19]. The measurement error was an average of 5.9×10^{-4} radians.

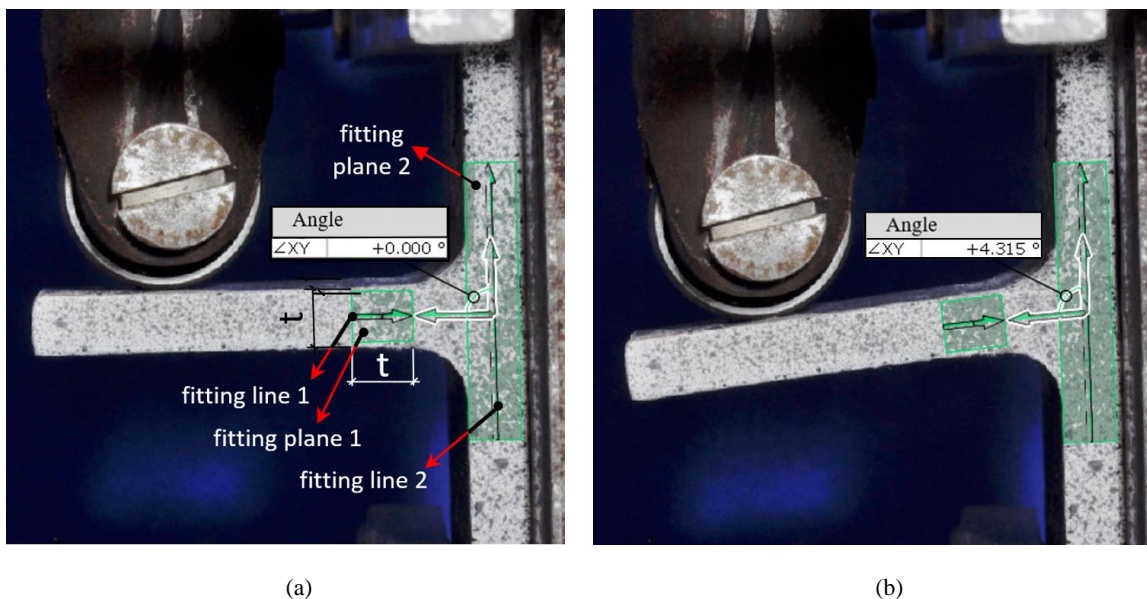


Figure 2.7. Angle of rotation measurement through software GOM: (a) undeformed shape and (b) deformed shape.

The relative rotations were measured by constructing an angle with the tool “2-Directions-Angle”, through a chain of references. The first references are two “fitting planes”, one located at the web’s specimens and the other at the flange, as shown in Figure 2.7a. The width of the “*fitting plane 1*” is equal to the specimens’ thickness – the minimum distance allowed to avoid the influence of flexure effects on the web. On the other hand, the “*plane fitting 2*” may assume any width greater than the specimens’ thickness. Fitting lines, represented by green arrows, are automatically plotted in the middle of each concerned plane, assuming as direction the rectangle’s longest side. Finally, the two directions formed by both fitting lines serve as references for the angle’s creation, represented by white with green arrows.

To validate the data obtained using *GOM* software, some specimens were instrumented with a displacement transducer, which were attached to the specimens immediately below the load application point. The displacements δ measured by the transducer were compared to those obtained through the software *GOM* through a *P versus δ* curve. For small rotations, there was a good correlation between the transducer and *GOM* measurements, with an average difference lower than 2% between the results. However, it was not possible to obtain a reliable correlation for great angles, since readings of transducer were affected by the horizontal displacements resulting from large rotations.

2.3. Results and Discussion

It is well known that there is a strong correlation between the existence of manufacturing defects and experimental results such as cracking pattern, rotational stiffness and the overall junctions’ behavior. In this first section of results, the values found from WFJs tests using DIC are reported and the aforementioned correlation between parameters is discussed.

2.3.1. Rotational stiffness

The curves of moment per unit of width (M/b) versus rotation (θ) are presented in Figure 2.8. The specimens extracted from I_2 -profiles were loaded with the mat wrinkling located both in tensioned (*a*) and compressed (*b*) region, as illustrated in Figure 2.8. The rotational spring constants per unit of width, k_r , can be

obtained through the curve slope at linear range. The average values of I-sections and channels are shown in Tables 2.3 and 2.4, respectively, with the corresponding coefficient of variation (CoV) in parentheses.

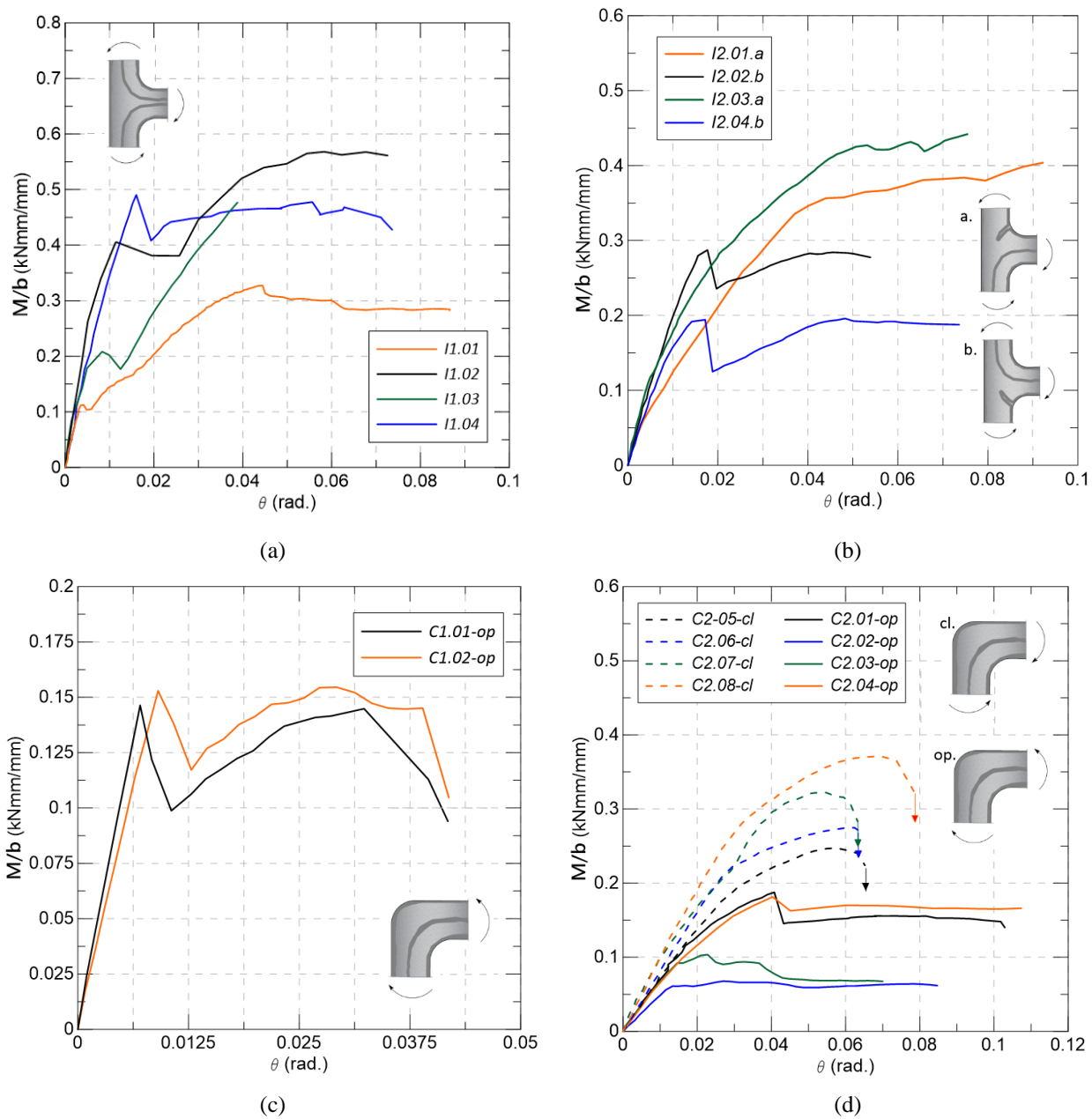


Figure 2.8. $M/b \times \theta$ curves from: (a) I₁-section; (b) I₂-section; (c) C₁-channel; (d) C₂-channel.

Table 2.3. Average rotational stiffness per unit of width k_r for I-section (CoV in parenthesis).

| <i>Specimens I₁</i> | | <i>Specimens I₂</i> | |
|--------------------------------|--------------------|--------------------------------|--------------------|
| | k_r (kN/rad) | | k_r (kN/rad) |
| I ₁ .01 | 33.5 | I ₂ .01 | 20.1 |
| I ₁ .02 | 35.1 | I ₂ .02 | 17.3 |
| I ₁ .03 | 34.3 | I ₂ .03 | 24.1 |
| I ₁ .04 | 35.3 | I ₂ .04 | 16.4 |
| Average | 34.5 (0.02) | Average | 19.5 (0.15) |

Table 2.4. Average rotational stiffness per unit of width k_r for channels (CoV in parenthesis).

| <i>Specimens C₁</i> | k_r (kN/rad) | <i>Specimen C₂</i> (open-mode) | k_r (kN/rad) | <i>Specimen C₂</i> (close-mode) | k_r (kN/rad) |
|--------------------------------|--------------------|--|--------------------|---|--------------------|
| C ₁ .01-op | 20.6 | C ₂ .01-op | 6.79 | C ₂ .07-cl | 6.64 |
| C ₁ .02-op | 16.9 | C ₂ .02-op | 4.70 | C ₂ .08-cl | 7.93 |
| | | C ₂ .03-op | 6.33 | C ₂ .09-cl | 8.54 |
| | | C ₂ .04-op | 5.92 | C ₂ .10-cl | 9.44 |
| Average | 18.9 (0.13) | Average | 5.94 (0.13) | Average | 8.14 (0.13) |

As can be seen through Tables 2.3 and 2.4, the I₁-specimens, which has a more uniform fiber architecture when compared to I₂-sections presented the lowest coefficient of variation with the highest values of rotational stiffness and greatest peak of moments, reaching 0.63 kNmm/mm. In opposition, the specimens extracted from I₂-profiles presented the largest variation in results among tested WFJs. This may be explained by their previously mentioned fiber architecture complexity, with important areas of wrinkled mat. The location of these fabrication imperfections is responsible for a significant change both in the general behavior, exhibited in Figure 2.8b, and in terms of rotational stiffness k_r , shown in Table 2.3. The specimens with the “a” configuration (wrinkling at the tensioned part), such as I₂.01 and I₂.03, developed early cracks that followed the wrinkled mat layer closer to the specimen’s tensioned face. Both presented greater load capacity when compared to those with “b” configuration (wrinkling at the compressed part). The specimen I₂.01, with wrinkling both in compressed and tensioned regions, presented the first crack at a moment per unit of width of only 0.054 kNmm/mm. The behavior concerning the “a” configuration may be related to a change in stresses trajectories due to the mat wrinkling location in the tested specimens. The wrinkle on the WFJ tensioned side redistributes the stresses to the compressed part and influences the

formation of cracks adjacent to the outermost tensioned mat layer. This leads the specimens to experience a slower stiffness degradation and achieve greater peak bending moments, behaving similarly to the channels tested in close mode. On the other hand, the specimens loaded in the “*b*” configuration presented interlaminar cracks adjacent to the junctions’ middle mat layer, leading to a faster stiffness degradation and experiencing a sharp drop at some point of the cracking development, resembling the channels tested in open-mode.

The channels presented lower values for rotational stiffness when compared to I-sections. The C_1 -specimens, with phenolic matrix and higher thickness, presented greater values for the stiffness k_r than C_2 -channels – constituted of vinyl ester resin. Regarding the maximum bending moments per unit of width, values of 0.146 and 0.154 kNmm/mm were found for specimens $C_{1.01}$ and $C_{1.02}$, being in the range of results presented by C_2 -channels tested in open mode.

Regarding the open and close-modes, the C_1 - and C_2 -specimens tested in the former configuration could sustain the load after the occurrence of the first crack. The specimens of this group presented notable differences in the overall behavior between each other, with lower peak bending moments per unit of width when compared to the specimens tested in close-mode, varying from 0.07 (for $C_{2.02-op}$) to 0.20 kNmm/mm (for $C_{2.04-op}$), which is related to the crack pattern possibilities, explained below. On the other hand, the C_2 -specimens tested in close-mode have an analogous behavior among themselves in terms of moment-rotation, presenting greater bending moments per unit of width – varying from 0.25 and 0.37 kNmm/mm – and slightly higher values for k_r than those tested in open-mode, as shown in Table 2.4. The difference in rotational stiffness of channels tested in open and close-mode configuration may be explained by the distinct response of constituent materials and layers under tension or compression stresses in both tangential and radial directions.

2.3.2. Crack pattern

Typical stresses produced in channels junctions tested in an open- and close-mode configuration are shown in Figure 2.9. The expected cracks are indicated along with tensile and compression stresses diagrams, represented by red and blue, respectively. It is worth to point out that at the position of maximum radial stress,

the tangential and radial stresses are the same, reaching the condition called as ‘isotropic point’ (I.P.) [25]. In general, the cracks observed in all tested specimens are very close to the expected pattern, *i.e.*, radial cracks form in the outer portion of junctions when the specimen is loaded in a close-mode configuration, whereas in open-mode radial and tangential cracks form at the inner part of the junction and at the interface between layers, respectively.

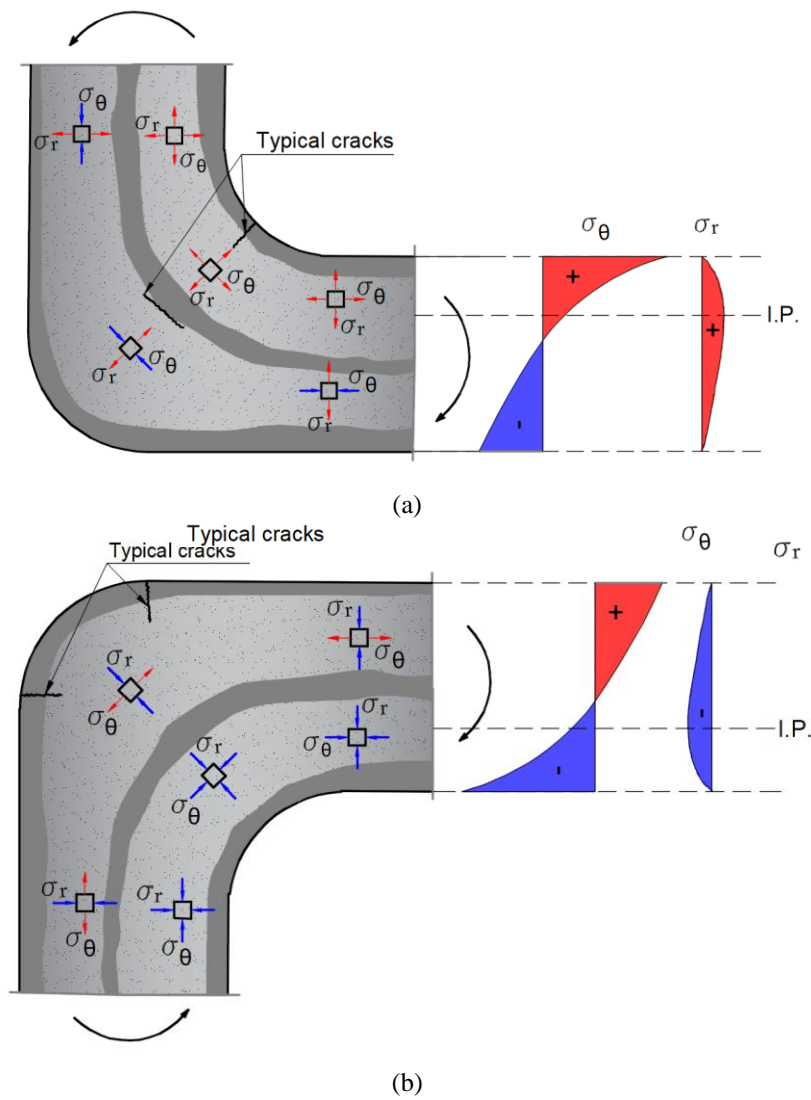


Figure 2.9. Typical cracks, radial and tangential stresses: (a) open-mode; (b) close-mode.

To support this discussion, images containing specimens’ principal strains, shown in Figure 2.10, were extracted from DIC measurements. It can be noticed that regions with larger strains correspond to the expected crack’s location presented in Figure 2.9. However, in the presence of a wrinkled mat, as can be seen

in the specimen I₂.01, the cracks tend to be formed following the interface of this weak region, changing the stresses trajectories and the WFJ's overall behavior.

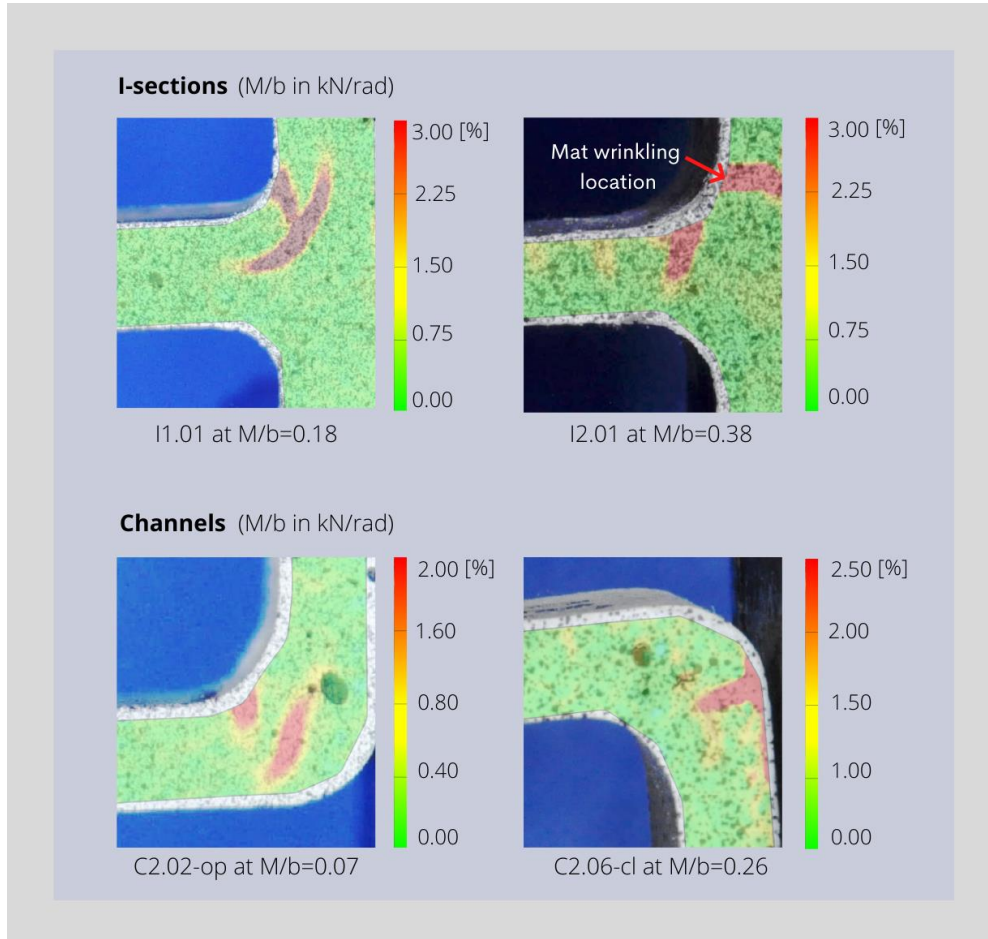


Figure 2.10. Specimens' major strain extracted from DIC measurements.

Figures 2.11 and 2.12 show pictures taken before and after the tests, using a *Nikon SMZ 800* stereoscope, for I-sections and channels, respectively. The images on the left side present the geometry of specimens and their respective defects, whereas the images on the right side present the crack patterns observed. Based on cracks' location and tensile stresses diagram, the cracks were classified in three different types: (1) *Interlaminar cracks*, which occur due to mainly radial stresses, producing interlaminar tension and separation of layers, especially in more porous zones; (2) *Cracks in wrinkled mat regions*, formed due to tangential stresses occurring in areas with mat wrinkling, which ends up leading to premature failure of the junctions; (3) *Intralaminar (matrix) cracks*, generated by tangential tensile stresses and facilitated by the fibers' change of direction due to junctions' shape,

which makes the strength to be governed by matrix and ends up failing under low tensile stresses.

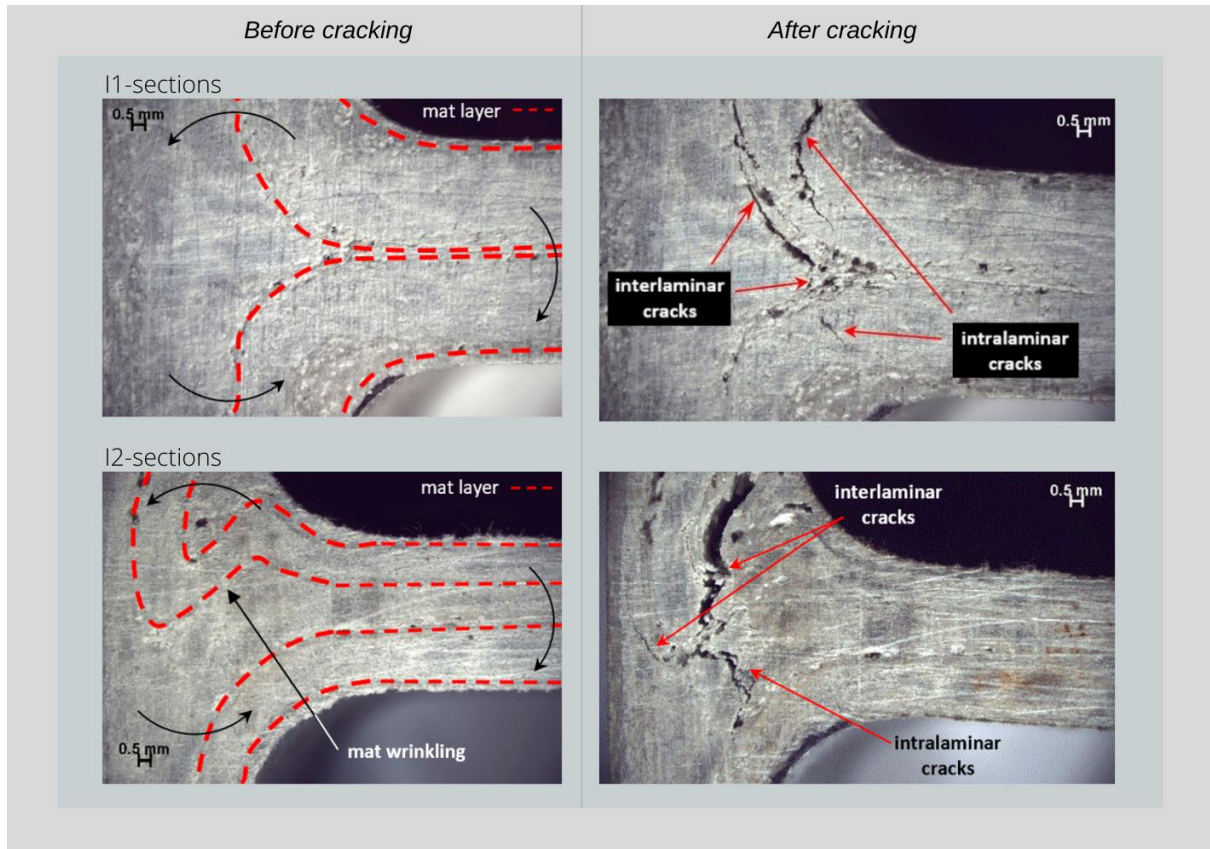


Figure 2.11. I-sections' imperfections and respective crack patterns.

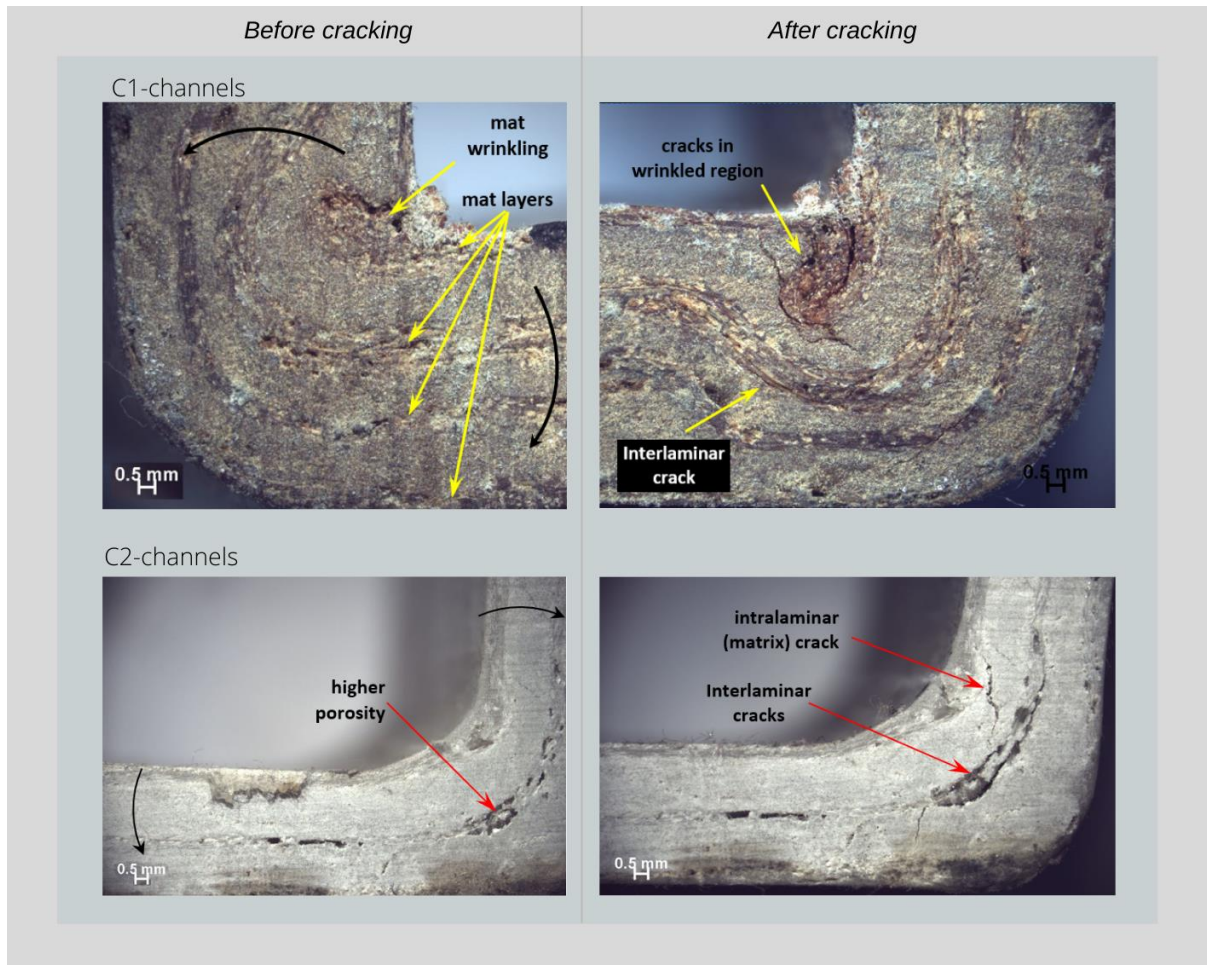


Figure 2.12. Channels' imperfections and respective crack patterns.

To complement the discussion, the cracks developed on three specimens of each cross-section were tracked with the aid of the *GOM* software and are shown in Figures 2.13 and 2.14. As can be noticed, the I-sections and C₁-channels presented a greater number of cracks and in more random positions when compared to the C₂-channels tested in open-mode. In the case of I-sections, this may be due to the complexity of stress trajectories in the T-shape specimens. Moreover, the greater number of layers and the presence of mat wrinkling, both characteristics of I- and C₁-sections, have also contribute to this observed pattern.

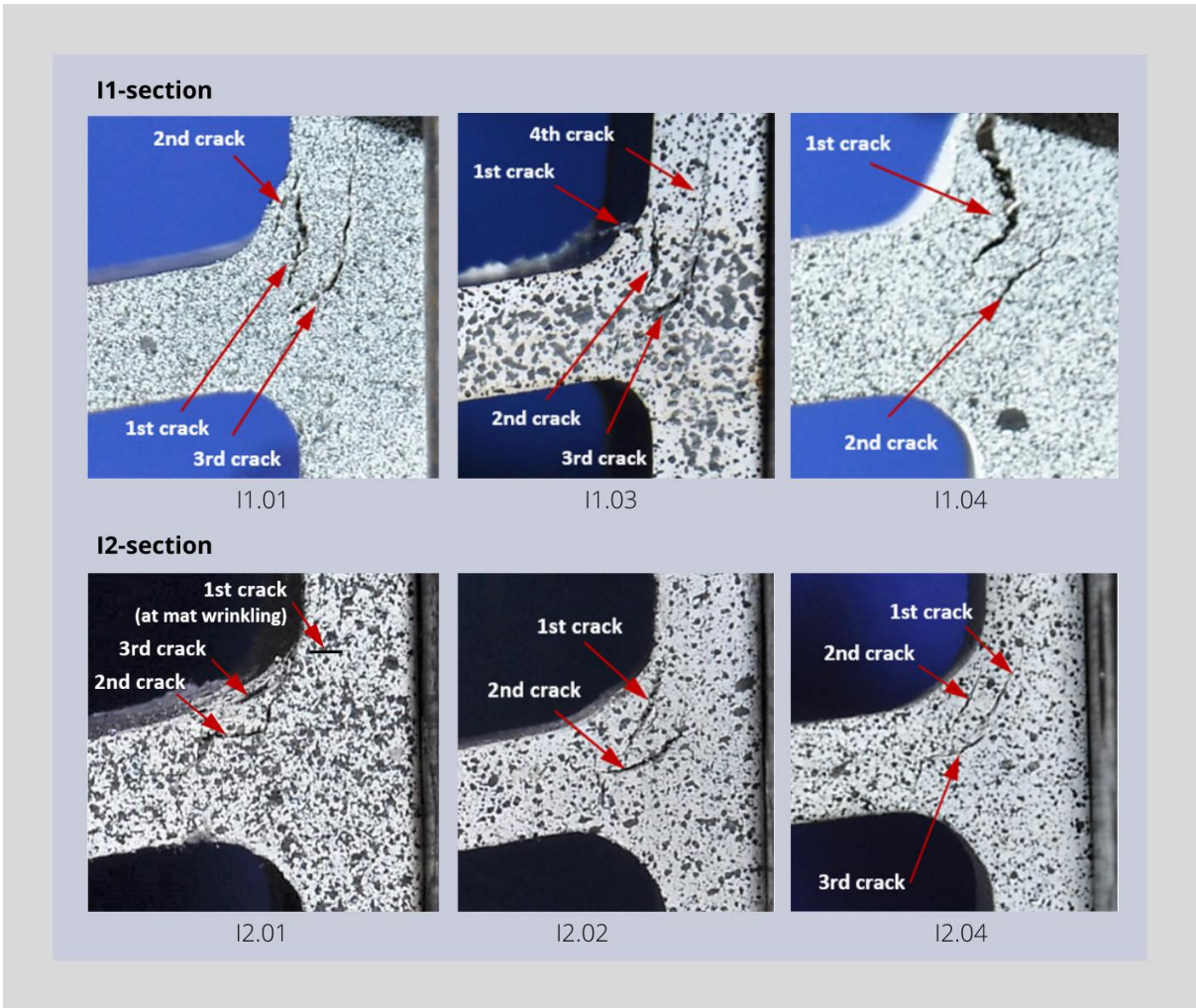


Figure 2.13. Cracks' location in specimens extracted from I-sections.

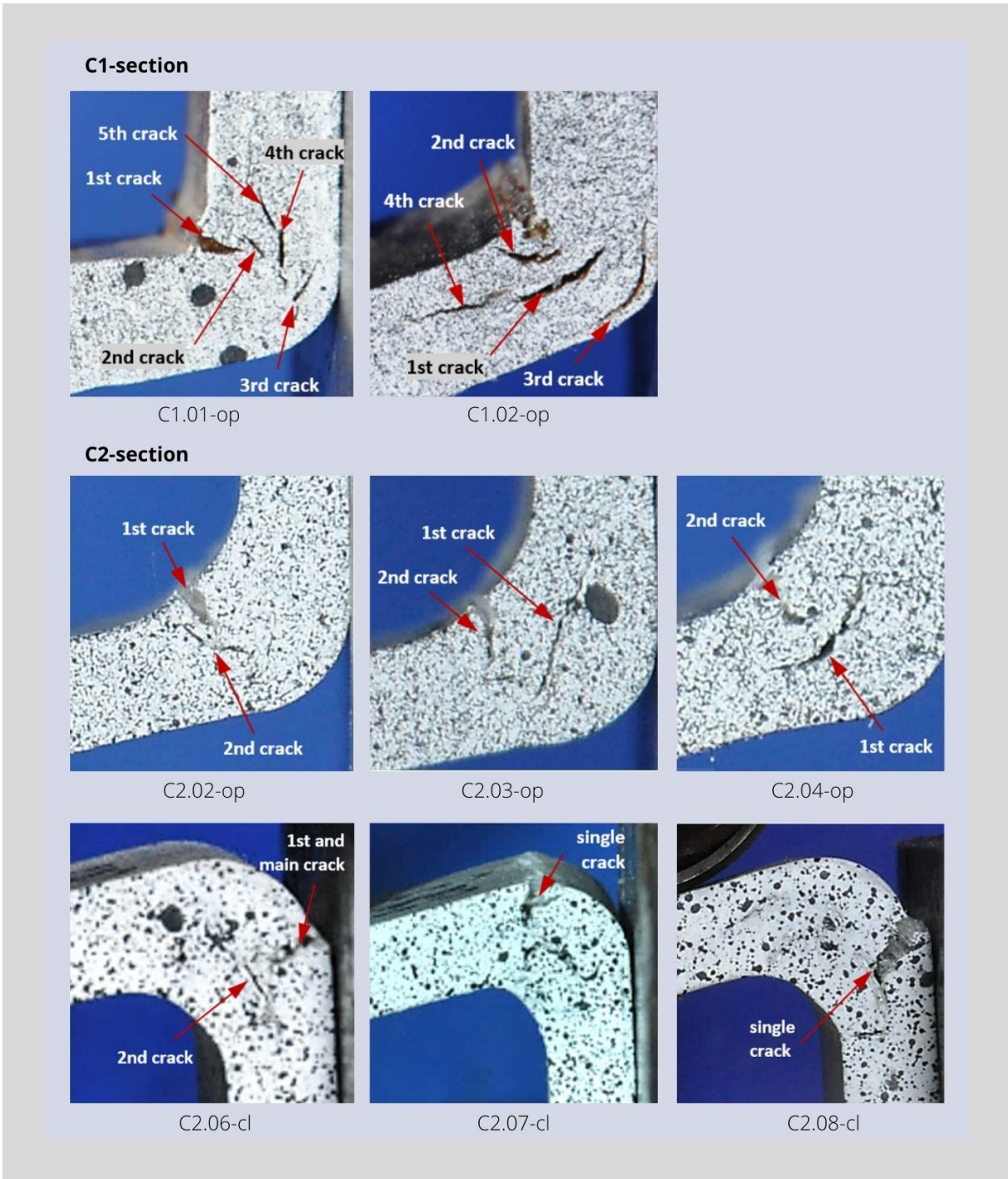


Figure 2.14. Cracks' location in specimens extracted from channels.

On the other hand, C₂-specimens tested in close-mode showed a very similar crack position between each other, as shown in Figure 2.14, presenting one dominant intralaminar crack initiated on the outer layer of the junction. This may be explained by a stress trajectory characterized by tangential tensile stresses with greatest magnitude near the outer face of the specimen, limiting the emergence of

the crack to that region. In opposition, for an open-mode configuration, tensile tangential and radial stresses develop simultaneously (see Figure 2.9) and may lead to interlaminar or intralaminar cracks in different locations, in agreement with the previously mentioned crack pattern found in C₂-channels tested in open-mode.

Finally, the cracks with greater development are often located on the adjacent regions to mats, to triangular-shaped roving core – in the case of I-sections –, and in areas with more incidence of defects such as higher porosity or mat wrinkling.

2.4. Complementary analyses

In this section, three topics are presented as suggestions to better understand the junctions' damage accumulation and rotational stiffness degradation process. Junctions' tangential and radial stresses are analyzed and calculated, and a lower bound function is proposed to express the rotational stiffness retention. Finally, an equation is proposed to estimate the WFJ's theoretical rotational stiffness, based on energy methods and original Lekhnitiskii's equations. As an example of application, the parameters determined herein may be added in numerical models where junction properties can be incorporated. Since it is known the influence of WFJs' rotational stiffness on critical buckling loads, it may allow, for instance, to obtain more reliable predictions concerning the local buckling critical behavior.

The analytical analyses described in sections 2.4.1 and 2.4.3 were not conducted for the phenolic section (C₁), due to the lack of quality of these profiles (see Table 2.1). It can be seen from Figure 2.12 that this cross-section has as a poorly defined inner radius, which hindered an accurate measurement of relevant parameters for determining junctions' strength and theoretical rotational stiffness, proposed herein.

2.4.1. Stress analysis

To better understand the damage process and obtain an order of magnitude of stresses at cracking in pultruded glass fiber-polymer WFJs, the tangential (σ_θ) and radial (σ_r) stresses at the junctions were obtained through theory of elasticity

Equations (2.1) and (2.2), reported by Kedward *et al.* [25] and originally presented by Lekhnitskii [26], as follows:

$$\sigma_r = -\frac{M}{R_o^2 b g} \left[1 - \frac{1 - c^{k+1}}{1 - c^{2k}} \left(\frac{r}{R_o} \right)^{k-1} - \frac{1 - c^{k-1}}{1 - c^{2k}} c^{k+1} \left(\frac{R_o}{r} \right)^{k+1} \right] \quad (2.1)$$

$$\sigma_\theta = -\frac{M}{R_o^2 b g} \left[1 - \frac{1 - c^{k+1}}{1 - c^{2k}} k \left(\frac{r}{R_o} \right)^{k-1} + \frac{1 - c^{k-1}}{1 - c^{2k}} k c^{k+1} \left(\frac{R_o}{r} \right)^{k+1} \right] \quad (2.2)$$

where r is the radial position in which the stresses are to be obtained; the constant c is defined as the ratio of internal and external radii, R_i and R_o , as shown in Equation (2.3); the constant k is equal to the square root of the ratio of transverse moduli in the radial (E_r) and tangential (E_θ) direction, as given by Equation (2.4); and the constant g is defined in Equation (2.5). It is important to highlight that Equations (2.1) and (2.2) are valid for pure bending problems with the outer radius equal to the inner radius plus the specimens' thickness ($R_o = R_i + t$) and will be used in the present work as a simplification.

$$c = \frac{R_i}{R_o} \quad (2.3)$$

$$k = \left(\frac{E_\theta}{E_r} \right)^{1/2} \quad (2.4)$$

$$g = \frac{1 - c^2}{2} - \frac{k}{k+1} \frac{(1 - c^{k+1})^2}{1 - c^{2k}} + \frac{k c^2}{k-1} \frac{(1 - c^{k-1})^2}{1 - c^{2k}} \quad (2.5)$$

The radial crack position that leads to the maximum stresses is presented in Equation (2.6).

$$r_{m\acute{a}x} = \left[\frac{(k+1)(1 - c^{k+1}) c (R_i R_o)^k}{(k-1)(1 - c^{k+1})} \right]^{1/(2k)} \quad (2.6)$$

Since the authors' purpose is to analyze the beginning of the damage process, the radius r , in this specific case, is the distance between the junctions' radius center and the crack onset. The radial position of the crack was measured visually from the test pictures taken every five seconds.

The tangential moduli E_{θ} were determined for each specimen with the aid of GOM software and the average value was adopted for each studied section, both for the calculation of tensile stresses and theoretical rotational stiffness. On the other hand, the radial modulus E_r was assumed to be 95% of E_{θ} , based on the average ratio of theoretical moduli resulting from a rule of mixtures approach. The values of moduli found for each section are presented in Table 2.5. The differences observed between the moduli found for close and open-mode configurations are in agreement with the experimental values of rotational stiffness and may be explained by the lack of symmetry in the layers' distribution, as previously mentioned.

Table 2.5. Tangential and radial moduli adopted.

| <i>Section</i> | <i>E_{θ} (MPa)</i> | <i>E_r (MPa)</i> |
|--------------------|--------------------------------------|-------------------------------|
| I ₁ | 6146 | 5838 |
| I ₂ | 8525 | 8098 |
| C ₂ -op | 4954 | 4706 |
| C ₂ -cl | 7217 | 6856 |

Equations (2.1) to (2.5) were used to represent the behavior of L-shape WFJs, assumed as generic curved beam sections. On the other hand, the T-shape junctions were considered as a superposition of results for two L-shapes, as illustrated in Figure 2.15. After summing the stresses, the resultant stress state was transformed into principal stresses σ_1 and σ_2 , with the respective indication of the principal plane direction (θ_p).

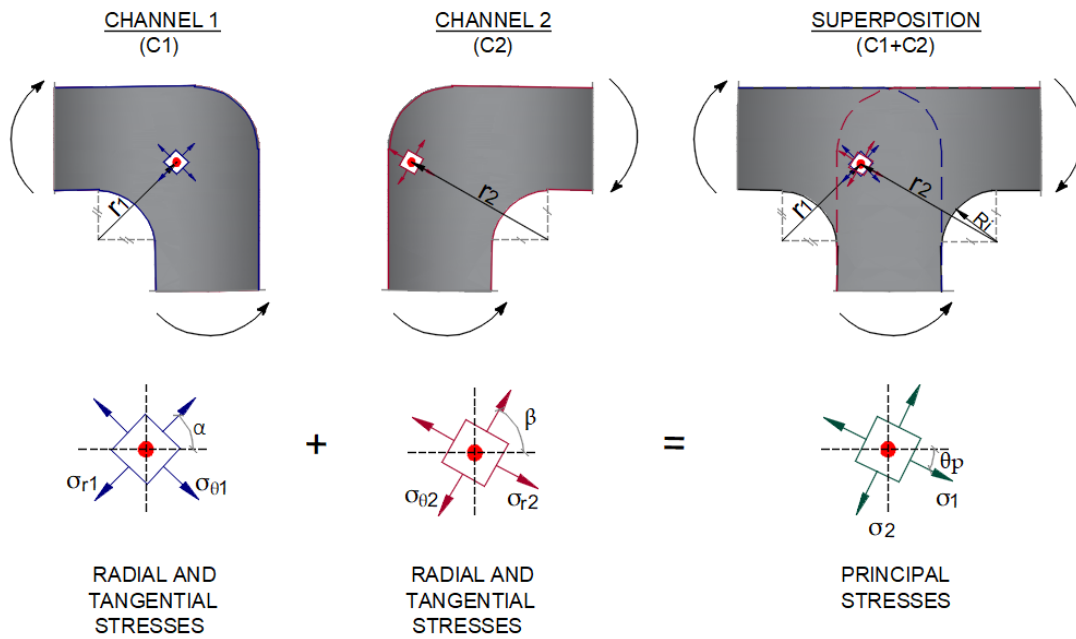


Figure 2.15. Superposition of tensile stresses in I-sections' junctions.

Tables 2.6 and 2.7 present some useful information to analyze the damage process at pultruded junctions of I-sections and channels, respectively – *i.e.*, cracking moment per unit of width (M_{crk}/b), inner radius (R_i), radial position of the first crack (r) and radial location of the maximum radial stress ($r_{m\acute{a}x}$). It is worth to point out that the junctions' external radius was assumed to be the sum of its internal radius and the specimens' thickness. Moreover, the maximum radius adopted in these calculations is limited to the external radius value. In Table 2.6, for I-sections, the principal stresses σ_1 and σ_2 , maximum shear stresses $\tau_{m\acute{a}x}$, and the principal plane orientation θ_p are indicated. Whereas for channels, in Table 2.7, the crack type, as well as radial and tangential stresses, σ_r and σ_θ , are presented. In other words, such data correspond to the stress at the point where the damage was initiated with the subsequent beginning of rotational stiffness degradation.

Table 2.6. Principal stresses at cracking for I-sections.

| <i>Specimen</i> | $M_{,crk}/b$ (kNmm/mm) | R_i (mm) | r (mm) | $r_{máx}$ (mm) | σ_1 (MPa) | σ_2 (MPa) | $\tau_{máx}$ (MPa) | θ_p (°) |
|--------------------|---------------------------|-------------------------------------|--------------------------------------|-------------------------------------|---------------------|---------------------|-----------------------|----------------|
| I ₁ .01 | 0.112 | 4.4 ⁺ / 4.6 ⁻ | 6.1 ⁺ / 13.6 ⁻ | 7.0 ⁺ / 7.3 ⁻ | 4.64 | 2.22 | 1.21 | -19.4 |
| I ₁ .02 | 0.413 | 4.3 ⁺ / 4.9 ⁻ | 4.8 ⁺ / 13.9 ⁻ | 6.8 ⁺ / 7.5 ⁻ | 20.0 | 11.75 | 4.12 | 27.9 |
| I ₁ .03 | 0.178 | 4.2 ⁺ / 4.4 ⁻ | 5.6 ⁺ / 13.8 ⁻ | 6.7 ⁺ / 7.0 ⁻ | 7.38 | 3.39 | 1.99 | -10.6 |
| I ₁ .04 | 0.344 | 4.1 ⁺ / 3.4 ⁻ | 5.1 ⁺ / 12.4 ⁻ | 6.5 ⁺ / 5.7 ⁻ | 12.8 | 11.0 | 0.92 | -19.0 |
| I ₂ .01 | 0.054 | 4.2 ⁺ / 4.3 ⁻ | 6.7 ⁺ / 9.9 ⁻ | 6.1 ⁺ / 6.3 ⁻ | 3.9 | 0.21 | 1.85 | -1.96 |
| I ₂ .02 | 0.287 | 3.1 ⁺ / 3.9 ⁻ | 4.6 ⁺ / 10.0 ⁻ | 4.9 ⁺ / 5.9 ⁻ | 28.6 | 6.33 | 11.1 | -5.18 |
| I ₂ .03 | 0.109 | 4.1 ⁺ / 4.8 ⁻ | 5.9 ⁺ / 10.9 ⁻ | 6.0 ⁺ / 6.8 ⁻ | 10.3 | 1.60 | 4.37 | -13.6 |
| I ₂ .04 | 0.147 | 4.3 ⁺ / 4.7 ⁻ | 6.3 ⁺ / 10.7 ⁻ | 6.2 ⁺ / 6.7 ⁻ | 12.7 | 2.39 | 5.13 | -11.5 |

+ values referring to the part of the I-section under tension

- values referring to the part of the I-section under compression

Table 2.7. Radial and tangential stresses at cracking for channels.

| <i>Specimen</i> | $M_{,crk}/b$ (kNmm/mm) | R_i (mm) | r (mm) | $r_{máx}$ (mm) | σ_r (MPa) | σ_θ (MPa) | <i>Crack type</i> |
|-----------------------|---------------------------|---------------|-------------|-------------------|---------------------|--------------------------|-------------------------|
| C ₂ .01-op | 0.083 | 3.39 | 7.72 | 5.18 | 1.85 | -6.80 | Tangential-interlaminar |
| C ₂ .02-op | 0.061 | 3.39 | 8.67 | 5.14 | 0.40 | -8.06 | Tangential-interlaminar |
| C ₂ .03-op | 0.084 | 3.54 | 4.17 | 5.36 | 2.54 | 13.8 | Radial-intralaminar |
| C ₂ .04-op | 0.112 | 3.34 | 7.73 | 5.10 | 2.39 | -10.2 | Tangential-interlaminar |
| C ₂ .05-cl | 0.170 | 3.76 | 9.46 | 5.57 | 0.00 | 25.2 | Radial-intralaminar |
| C ₂ .06-cl | 0.209 | 3.31 | 8.45 | 5.04 | -1.86 | 26.5 | Radial-intralaminar |
| C ₂ .07-cl | 0.145 | 3.54 | 8.27 | 5.34 | -2.31 | 15.1 | Radial-intralaminar |
| C ₂ .08-cl | 0.221 | 3.58 | 8.26 | 5.39 | -3.91 | 21.6 | Radial-intralaminar |

It can be observed a higher variability in the cracking stresses of I-sections than those of channels. The results are directly proportional to the crack moment, which is highly dependent on the distribution of layers, presence of manufacturing defects, mat wrinkling, pre-cracks and existence of voids. For I₂-sections, for instance, a variation from 0.054 to 0.287 kN mm/mm was found for the moment at cracking, resulting in principal stresses (σ_1) varying from 3.9 to 28.6 MPa. It is worth to point out that, considering a usual longitudinal tensile strength ranging between 250 and 400 MPa, the resistance of the junctions tested in open mode (see Tables 2.6 and 2.7) corresponded to less than 5% of this strength, whereas for specimens tested in close mode (see Table 2.7), this percentage increased to 11%.

Besides the bending moment, the parameters that most influence the stress values are the radial position of the first crack and the internal and external radius, which also depend on the junctions' fillet shape and on the presence of imperfections. The variation of moduli of elasticity does not have a significant influence on the obtained stresses. Although I_1 -sections present a more uniform fiber architecture without the presence of mat wrinkling, the variation observed may be an effect of the channels' superposition, since the double of parameters are used to obtain the principal stresses in this case. The channels, on the other hand, presented lower variability in results and presented compression stresses that agree with the cracks' position and stresses diagrams of this section type, as shown in Figure 2.9.

To illustrate the obtained results, Figure 2.16 presents the radial and tangential stresses of the specimen $C_{2.04}$ -op related to different cracks' radial positions, varying from 3.34 mm (R_i) to 9.14 mm (R_o) – parameter adopted as the sum of internal radius and specimens' thickness for simplification purposes. In this specimen, the maximum radial tension is expected at a radius of 5.10 mm and it is marked in the plot as the isotropic point, in which the tangential and radial stresses are both equal to 5.3 MPa. On the other hand, the crack onset occurs at a radius of 7.73 mm, indicated by the dashed blue line in the plot. At this point, a tangential crack is formed due to a radial tensile stress of 2.4 MPa and there is a compressive tangential stress of 10.2 MPa.

It can be noticed that in all specimens, the radial position of the first crack is not coincident to the radius corresponding to the maximum radial stress. This may be explained by the fact that the most susceptible regions to cracks are those with some sort of imperfection and those located at the junctions' interfaces. These spots of weakness are responsible for premature failures at weak regions with lower resistances than the maximum radial stress.

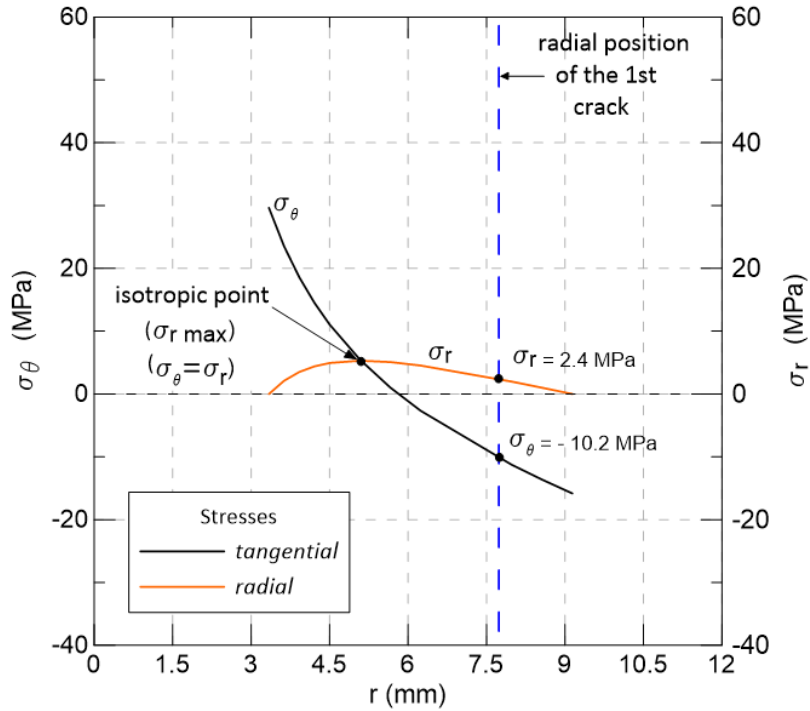


Figure 2.16. Tangential and radial stresses corresponding to radial of C_{2.04}-op.

2.4.2. Stiffness retention function

To express and predict the rotational stiffness retention behavior of pultruded WFJs, a lower bound exponential function is proposed. Curves of R_{kr} versus $\Delta\theta$ (rotation angle increments) were derived for each studied specimen from the respective experimental relation $M-\theta$ and are shown in Figures 2.17 to 2.19. The R_{kr} was calculated as the ratio between degraded and elastic rotational stiffnesses. For a given rotation θ after cracking, the degraded stiffness was calculated as the slope of the secant line connecting the origin of the $M/b \times \theta$ curve to the M/b value corresponding to the θ concerned. An idealized function R_{kr} is proposed for each studied section to express the respective experimental stiffness retention lower-bound. Equation (2.7) describes the R_{kr} curves, in which the constants A , B and C were obtained through a nonlinear regression.

$$R_{kr} = \frac{A}{(\Delta\theta + B)^C} \quad (2.7)$$

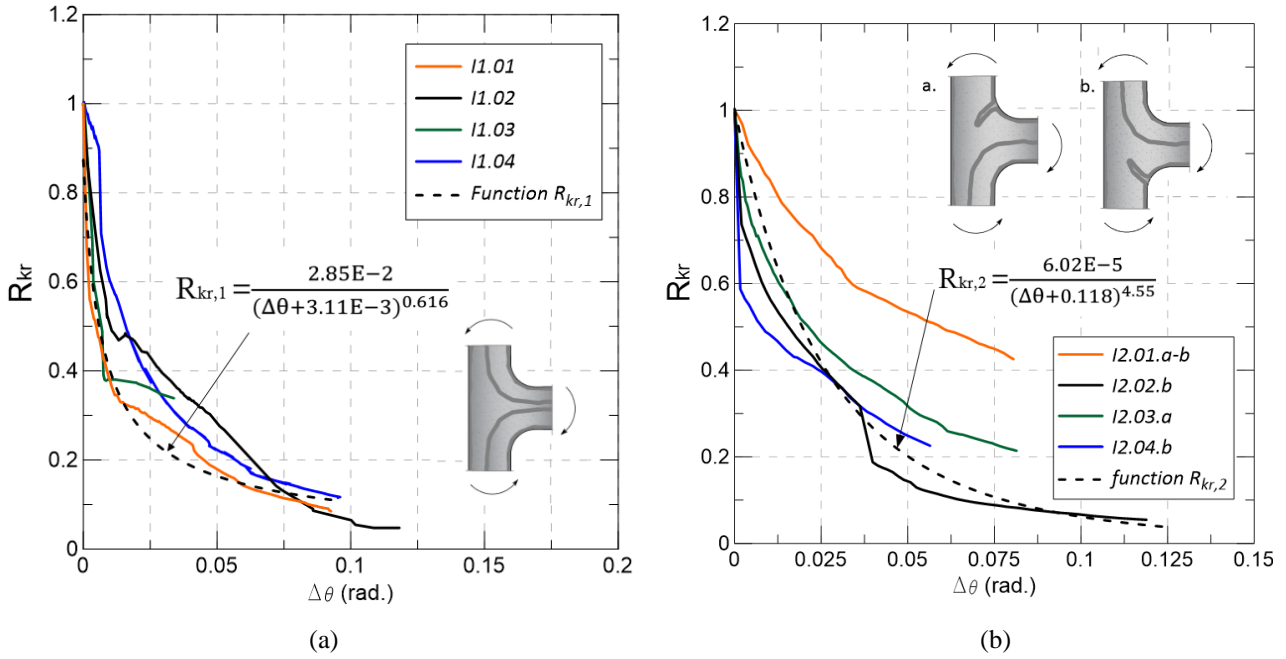


Figure 2.17. Curves of I-sections stiffness degradation: (a) I_1 -section; (b) I_2 -section.

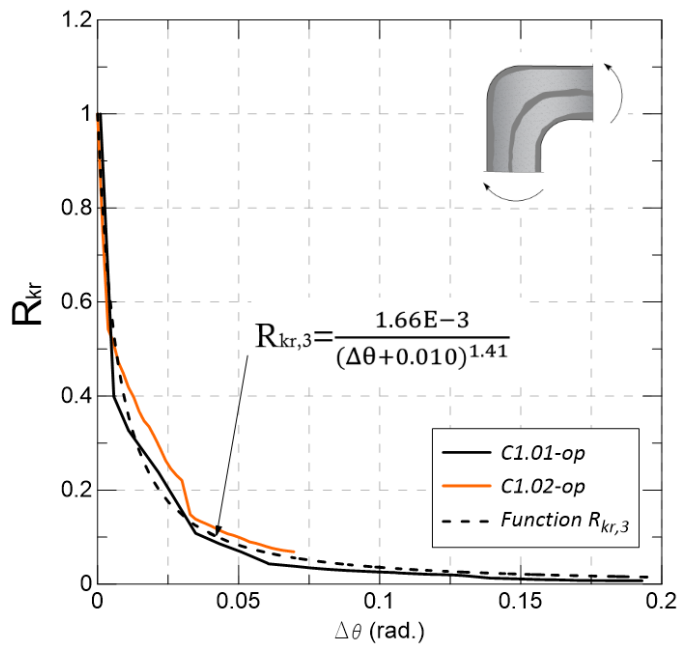


Figure 2.18. Curves of C_1 -channels stiffness degradation.

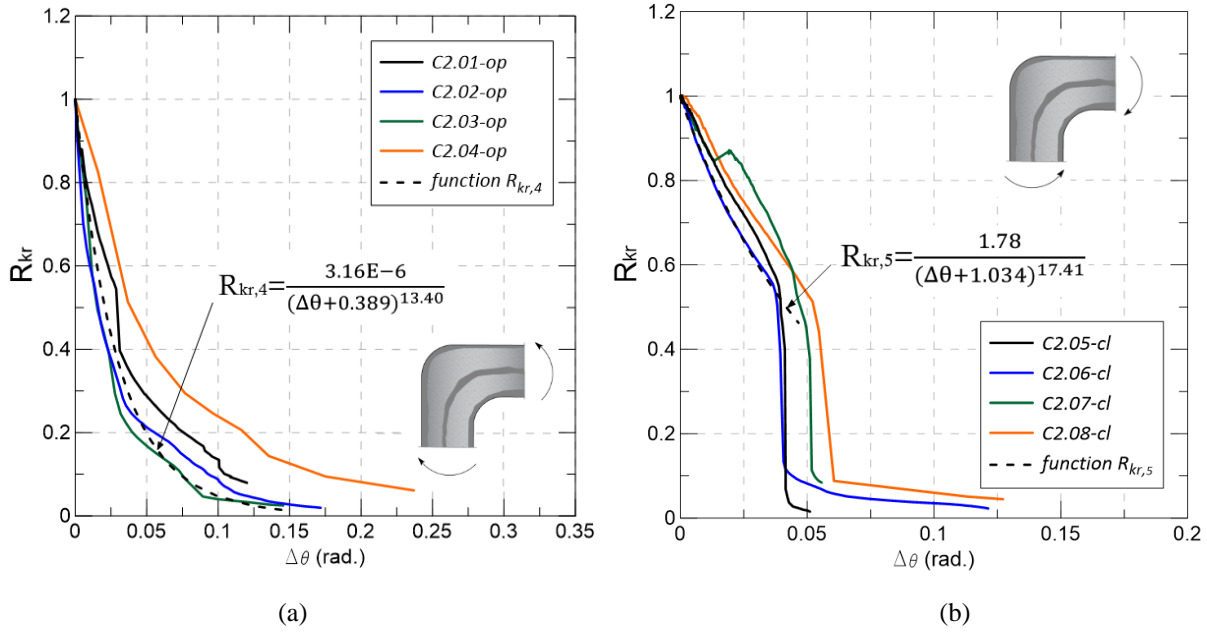


Figure 2.19. Curves of C₂-channels stiffness degradation: (a) open-mode; (b) close-mode.

All curves were derived to represent a lower-bound of experimental curves up to a loss of stiffness of 95%, except for the C₂-channels tested in close-mode. In this case, when compared to C₂-channels tested in open-mode, the specimens presented a much higher load capacity, before experiencing an abrupt drop, which occurred after 47% of the stiffness degradation for the reference experimental curve. This behavior agrees with the catastrophic failure behavior observed in *M versus θ* curves. In opposition, the channels made of vinyl-ester matrix experienced greater crack developments and the stress redistribution allowed the load to be sustained at least up to 90% of the stiffness degradation for all specimens. The exponential functions agreed well with the experimental curves, presenting more divergence, once more, in the case of I₂-sections. Among all tested sections, the lowest bound function, expressed by the following function $R_{kr,3}$, was described by the C₁-channels, which presented quality issues, with important defects in the junction's region, as previously mentioned.

$$R_{kr,3} = \frac{1.66E - 3}{(\Delta\theta + 0.010)^{1.41}}$$

To extend the proposal to a broader lower bound retention function that could serve as reference for a wider range of section geometries and test set-ups,

$R_{,kr}-\Delta\theta$ curves were extracted from moment-rotation relations reported by other authors [1,3,12]. The derived curves are shown in Figure 2.20, along with the $R_{kr,3}$ function. Mosallam *et al.* [1] tested five different sections, among H-profiles and angles tested in open-mode, whereas Xin *et al.* [12] tested three series (J1, J2 and J3) of T-shape specimens with different flange and web' thickness. Yanes-Armas and Keller [3], on the other hand, tested six series of WFJs of pultruded glass fiber-polymer bridge decks. The series nomenclatures, presented in Figure 2.20, indicate whether the specimen's web is inclined (*I*) or vertical (*V*) with respect to the flange; located far (*f*) or close (*c*) from an adhesively bonded joint; and if the tensioned junction's part was facing the obtuse (*o*) or the acute (*a*) angle side/ towards the double adhesively bonded (*d*) or single (*s*) flange.

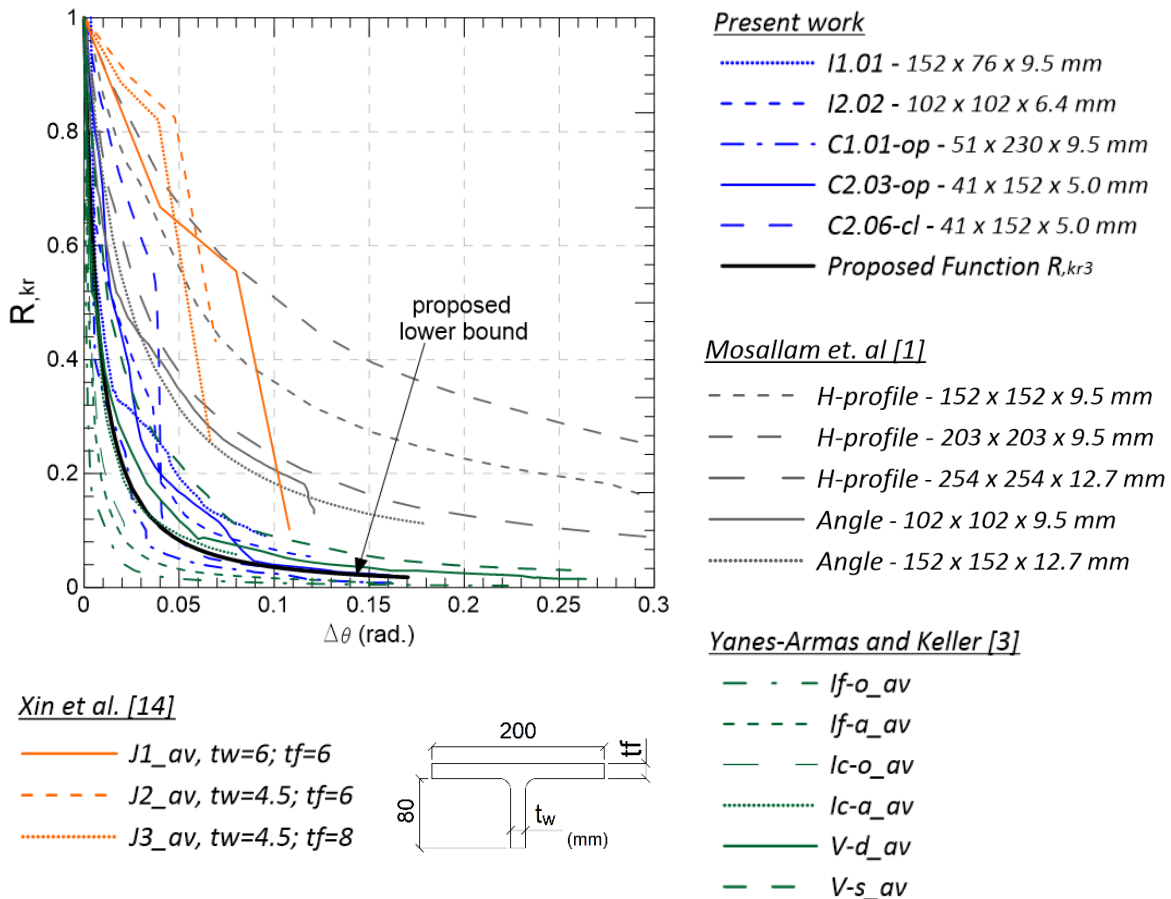


Figure 2.20. Retention curves derived from literature and proposed lower bound function.

In all, nineteen series of specimens tested through distinct set-ups, under two different load-configurations (open and close-mode) were compared. The $R_{kr,3}$

function attended well its purpose as a geometrically independent lower bound retention function in 84% of the cases. The other 16% corresponds to three series of specimens extracted from a bridge deck system (*If-o*; *If-a* and *Ic-o*), which are below the proposed lower bound limit.

2.4.3. Theoretical and experimental k_r comparison

Aiming to fill existing gaps in literature and contribute to the development of design guidelines, theoretical equations are proposed to predict the rotational stiffness per unit of width of pultruded glass fiber-polymer T- and L-shape WFJs. The formulas were derived considering the strain energy stored during rotation, described in Equation (2.8).

$$\frac{1}{2}M\theta = \frac{1}{2} \int_V \sigma \varepsilon dV \quad (2.8)$$

Considering both radial and tangential tensile stresses and generalized Hooke's law, Equation (2.8) can be rewritten as:

$$\frac{1}{2}M\theta = \frac{1}{2} \int_V \left[\frac{\sigma_\theta}{E_\theta} (\sigma_\theta - \nu\sigma_r) + \frac{\sigma_r}{E_r} (\sigma_r - \nu\sigma_\theta) \right] dV \quad (2.9)$$

In order to substitute the stresses terms σ_θ and σ_r by the formulas reported by Kedward *et al.* [25], the Equations (2.1) and (2.2) are simplified to Equations (2.10) to (2.13):

$$\sigma_r = -\frac{M}{R_o^2 bg} f_r(r) \quad (2.10)$$

Where

$$f_r(r) = \left[1 - \frac{1 - c^{k+1}}{1 - c^{2k}} \left(\frac{r}{R_o} \right)^{k-1} - \frac{1 - c^{k-1}}{1 - c^{2k}} c^{k+1} \left(\frac{R_o}{r} \right)^{k+1} \right] \quad (2.11)$$

And

$$\sigma_\theta = -\frac{M}{R_o^2 bg} f_\theta(r) \quad (2.12)$$

Where

$$f_\theta(r) = \left[1 - \frac{1 - c^{k+1}}{1 - c^{2k}} k \left(\frac{r}{R_o} \right)^{k-1} + \frac{1 - c^{k-1}}{1 - c^{2k}} k c^{k+1} \left(\frac{R_o}{r} \right)^{k+1} \right] \quad (2.13)$$

Considering an L-shape junction with volume delimited by quarters of circles with radii r_o and r_i , and replacing Equations (2.1) and (2.2) in Equation (2.9):

$$M\theta = \int_{R_i}^{R_o} \left[\frac{\frac{M}{R_o^2 b g} f_\theta(r)}{E_\theta} \left(\frac{M}{R_o^2 b g} f_\theta(r) - \nu \frac{M}{R_o^2 b g} f_r(r) \right) + \frac{\frac{M}{R_o^2 b g} f_r(r)}{E_r} \left(\frac{M}{R_o^2 b g} f_r(r) - \nu \frac{M}{R_o^2 b g} f_\theta(r) \right) \right] b \frac{\pi}{2} r dr \quad (2.14)$$

Finally, the proposed theoretical rotational stiffness for a L-shape junctions is $k_{th,L} = M/\theta$ is given as:

$$k_{th,L} = \frac{2R_o^4 g^2}{\pi} \frac{1}{\int_{R_i}^{R_o} \left[\frac{f_\theta(r)}{E_\theta} (f_\theta(r) - \nu f_r(r)) + \frac{f_r(r)}{E_r} (f_r(r) - \nu f_\theta(r)) \right] r dr} \quad (2.15)$$

A similar methodology can be used to develop equations for T-shape junctions. The main difference with respect to L-shape is that a T-shape specimen can be assumed as the sum of two L-shapes, but with a superposition of area in half of each L-shape. In terms of material volume, a T-shape junction has approximately 3/2 of the material volume of an L-shape, leading to a rotational stiffness also 3/2 of that expressed in Equation (2.16). It is important to point out that although C- and I-sections have been adopted in the present study, the analytical expressions proposed could be extended to any type of section with square junctions, including rectangular and square hollow sections. However, further studies are required to confirm this hypothesis.

$$k_{th,T} = \frac{3R_o^4 g^2}{\pi} \frac{1}{\int_{R_i}^{R_o} \left[\frac{f_\theta(r)}{E_\theta} (f_\theta(r) - \nu f_r(r)) + \frac{f_r(r)}{E_r} (f_r(r) - \nu f_\theta(r)) \right] r dr} \quad (2.16)$$

The analytical (k_{th}) and experimental (k_r) values of rotational stiffness for each specimen were compared and the results are presented in Figure 2.21 and

Table 2.8. The analytical values obtained through Equations (2.15) and (2.16) agreed well with experimental results. A maximum difference between the results of 24% was found for I-sections, against a minimum ratio k_{th}/k_r of 1%. For C₂-channels, constituted of vinyl ester matrix, this same ratio varied from 3% to 38%. These greater differences may be related with the orthotropic ratio E_r/E_θ , since this parameter have a significant influence on the theoretical rotational stiffness value.

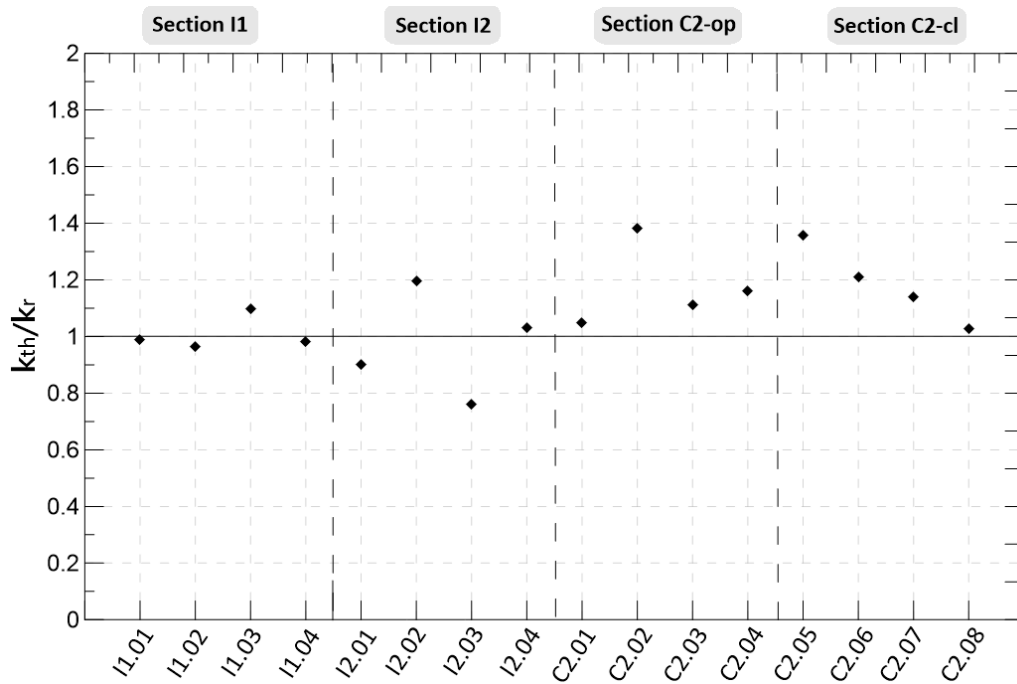


Figure 2.21. Comparison between theoretical and experimental rotational stiffness.

Table 2.8. Comparison between experimental and predict results.

| <i>Specimen</i> | k_{th} (kN/rad) | k_r (kN/rad) | k_{th}/k_r |
|-----------------------|-------------------|--------------------|--------------|
| I ₁ .01 | 33.1 | 33.5 | 0.99 |
| I ₁ .02 | 33.9 | 35.1 | 0.97 |
| I ₁ .03 | 37.7 | 34.3 | 1.10 |
| I ₁ .04 | 34.4 | 35.3 | 0.98 |
| I ₂ .01 | 18.1 | 20.1 | 0.90 |
| I ₂ .02 | 20.7 | 17.3 | 1.20 |
| I ₂ .03 | 18.1 | 24.1 | 0.76 |
| I ₂ .04 | 17.0 | 16.4 | 1.03 |
| C ₂ .01-op | 7.11 | 6.79 | 1.05 |
| C ₂ .02-op | 6.50 | 4.70 | 1.38 |
| C ₂ .03-op | 7.03 | 6.33 | 1.11 |
| C ₂ .04-op | 6.87 | 5.92 | 1.16 |
| C ₂ .05-cl | 9.02 | 6.64 | 1.36 |
| C ₂ .06-cl | 9.59 | 7.93 | 1.21 |
| C ₂ .07-cl | 9.72 | 8.54 | 1.14 |
| C ₂ .08-cl | 9.70 | 9.43 | 1.03 |
| | | Average | 1.08 |
| | | Standard deviation | 0.16 |

Considering that analytical results proposed in Equations (2.15) and (2.16) in general overpredicted the experimental data, a knockdown factor was determined in order to have only 5% of the theoretical rotational stiffness k_r greater than the experimental one. Assuming a normal distribution for the ratio of k_{th}/k_r described by a mean of 1.08 and a standard deviation of 0.16 (Table 2.8), a knockdown factor of 0.745 can be anticipated.

The theoretical parameter k_r was also compared with the experimental rotational stiffness reported by Xin et al [12], obtained from good quality specimens of J1 series (see [12]). The proposed formulation agreed fairly well with such experimental results, presenting differences varying from 19 to 31%. Although manufacturing imperfections, incidence of voids and particularities of fiber architecture are not incorporated in the formulation, in general, the proposed theoretical equations may be, nevertheless, a suitable option to determine the WFJs rotational stiffness parameters.

2.5. Conclusions

This work brings the suggestion of a simple method to characterize the rotational stiffness of WFJs of pultruded glass fiber-polymers. The DIC technique was used, allowing to obtain the necessary free leg's rotation angle in a direct manner, without the need of additional equations or special testing apparatus, besides avoiding issues related, for instance, with the appropriate distance between testing clamps and junctions' face. The analyses conducted in this work aim to contribute to the understanding of the junctions' rotational stiffness degradation process and bring important discussions about the WFJs behavior, such as the influence of imperfections, expected crack patterns and stresses. The parameters determined herein may be used to obtain more reliable responses regarding the composites' local buckling behavior, that have proven to be influenced by the semi-rigid web-flange junctions. The following conclusions can be drawn:

- The I_1 -sections presented the highest rotational stiffness values and load capacity. The specimens that showed most variability in results were those extracted from I_2 -sections, which presented important mat wrinkling areas in the junction region, that proved to have a significant influence in the rotational stiffness parameter. It was observed that mat wrinkling located at the tensioned junctions' side may change the stresses trajectories, having influence on the rate of properties degradation. At this configuration, I_2 -sections behaved similarly to channels tested in close mode, attesting the change in the overall composite's response.
- A notable difference in terms of overall behavior was noticed for C_2 -channels tested in open- and close-mode. In the former, the cracks experienced greater developments, allowing the load to be sustained at least up to 90% of the stiffness degradation. On the other hand, C_2 -specimens tested in close-mode presented higher load capacity, before experiencing a catastrophic failure after less than 55% of their stiffness

degradation.

- From theory of elasticity equations reported originally by Lekhnitsky [26], tangential and radial stresses at the occurrence of the first crack were calculated for channels, whereas principal stresses were calculated for the specimens extracted from I-sections. The I-sections, especially I₂-specimens, presented the most variability in results once more. This occurred since the parameters that most influence the equations – such as the crack moment, internal and external radii and radial position of the crack – are dependent on the presence of imperfections. It was observed that, in all cases, the cracks did not occur at the radial position of maximum radial stress, which may be explained by the fact that regions of interface and with some sort of defects represent a point of weakness, leading to premature cracks in the composites.
- Normalized curves describing the rotational stiffness degradation behavior were presented for each studied specimen. A lower bound function was proposed to express the WFJs rotational stiffness retention and it was proven to be applied for a wide range of profiles, set-ups and load-mode configurations. In general, the idealized curves fitted well with the experimental results, presenting greater gaps for I₂-sections. All specimens presented a smooth decay of stiffness, except for the channels tested in close-mode as aforementioned and for the I₂-sections with mat wrinkling in the tensioned region, which experienced quick drops of stiffness.
- Based on the strain energy stored during rotation, equations were proposed to predict the theoretical rotational stiffness per unit of width for any type of section with L-and T-shape junctions. The analytical and experimental results of I-sections specimens agreed fairly well, reaching a maximum difference of 20%. For channels, differences of 38% were observed between theoretical and experimental results. These high differences may have relation with the adopted orthotropic

ratio E_r/E_θ , adopted in this work as 95% based on the rule of mixtures approach. The incidence of voids and the presence of imperfections may also have contributed to the found results. Due to the high variability often presented by pultruded profiles, the proposed equations may be considered a suitable option to predict pultruded WFJs' rotational stiffness.

2.6. References

- [1] MOSALLAM, A. S. et al. Structural evaluation of axial and rotational flexibility and strength of web-flange junctions of open-web pultruded composites. **Composites Part B: Engineering**, v. 66, p. 311–327, 2014.
- [2] MOSALLAM, B. A. S.; MEMBER, A.; BANK, L. C. Short-term behavior of pultruded fiber-reinforced plastic frame. v. 118, n. 7, p. 1937–1954, 1992.
- [3] YANES-ARMAS, S.; CASTRO, J. DE; KELLER, T. Rotational stiffness of web-flange junctions of pultruded GFRP decks. **Engineering Structures**, v. 140, p. 373–389, 2017.
- [4] TURVEY, G. J.; ZHANG, Y. A computational and experimental analysis of the buckling, postbuckling and initial failure of pultruded GRP columns. **Computers and Structures**, v. 84, n. 22–23, p. 1527–1537, 2006.
- [5] ASCIONE, L. et al. Local buckling behavior of FRP thin-walled beams: A mechanical model. **Composite Structures**, v. 98, p. 111–120, 2013.
- [6] CINTRA, G. G.; CARDOSO, D. C. T.; VIEIRA, J. D. Parameters affecting local buckling response of pultruded GFRP I-columns: Experimental and numerical investigation. **Composite Structures**, v. 222, n. January, p. 110897, 2019.
- [7] LIU, T.; HARRIES, K. A. Flange local buckling of pultruded GFRP box beams. **Composite Structures**, v. 189, n. January, p. 463–472, 2018.
- [8] KOLLÁR, L. P. Local buckling of fiber reinforced plastic composite structural members with open and closed cross sections. **Journal of Structural Engineering**, v. 129, n. 11, p. 1503–1513, 2003.
- [9] TURVEY, G. J.; ZHANG, Y. Shear Failure Strength Of Web-Flange Junctions In Pultruded GRP Profiles. **Advanced Polymer Composites for Structural**

- Applications in Construction: ACIC 2004**, v. 36, p. 553–560, 2004.
- [10] TURVEY, G. J.; ZHANG, Y. Tearing failure of web-flange junctions in pultruded GRP profiles. **Composites Part A: Applied Science and Manufacturing**, v. 36, n. 2 SPEC. ISS., p. 309–317, 2005.
- [11] ASCIONE, F.; MANCUSI, G. The influence of the web-flange junction stiffness on the mechanical behaviour of thin-walled pultruded beams. **Composites Part B: Engineering**, v. 55, p. 599–606, 2013.
- [12] XIN, H. et al. Impact of hygrothermal aging on rotational behavior of web-flange junctions of structural pultruded composite members for bridge applications. **Composites Part B: Engineering**, v. 110, n. February, p. 279–297, 2017.
- [13] FEO, L.; MOSALLAM, A. S.; PENNA, R. Mechanical behavior of web-flange junctions of thin-walled pultruded I-profiles: An experimental and numerical evaluation. **Composites Part B: Engineering**, v. 48, p. 18–39, 2013.
- [14] LAWRENCE C. BANK AND JIANSHEN YIN. Failure of web-flange junction in postbuckled pultruded I-beams. **Journal of Composites for Construction**, v. 3, n. 4, p. 177–184, 1999.
- [15] BANK, L. C., NADIPELLI, M., GENTRY, T. R., & YIN, J. S. **Local buckling of pultruded FRP beams: Theory and experiment**. Structures Congress XII. ASCE. **Anais...**1994
- [16] TURVEY, G. J.; ZHANG, Y. Characterisation of the rotational stiffness and strength of web-flange junctions of pultruded GRP WF-sections via web bending tests. **Composites Part A: Applied Science and Manufacturing**, v. 37, n. 2, p. 152–164, 2006.
- [17] GOM CORRELATE. **Evaluation Software for 3D Testing**. Disponível em: <<https://www.gom.com/3d-software/gom-correlate.html>>. Acesso em: 20 dec. 2020.
- [18] LEKHNITSKII, S. G. Anisotropic plates No. FTD-HT-23-608-67. **Foreign Technology Div Wright-Patterson Afb Oh**, 1968.
- [19] SUTTON, MICHAEL A., JEAN JOSE ORTEU, AND H. S. **Image correlation for shape, motion and deformation measurements: basic concepts, theory and applications**. [s.l.] Springer Science & Business Media, 2009.
- [20] SAUSE, M. G. R. Digital image correlation. **Springer Series in Materials Science**, v. 242, n. 12, p. 57–129, 2016.

- [21] **ISO (International Organization for Standardization). ISO 1172: Textile-glass reinforced plastics – Prepregs, moulding compounds and laminates – Determination of the textile-glass and mineral-filler content – Calcination methods.** . Geneva, Switzerland: [s.n.].
- [22] **CINTRA, G. G. Local Buckling Behavior of Pultruded Glass-Fiber Reinforced Polymer (pGFRP) I-Section Columns.** 2017. 2017.
- [23] **YANES-ARMAS, S.; CASTRO, J. DE; KELLER, T.** Energy dissipation and recovery in web-flange junctions of pultruded GFRP decks. **Composite Structures**, v. 148, p. 168–180, 2016.
- [24] **POULTON, M.; SEBASTIAN, W.** Taxonomy of fibre mat misalignments in pultruded GFRP bridge decks. **Composites Part A: Applied Science and Manufacturing**, v. 142, n. December 2020, p. 106239, 2021.
- [25] **KEDWARD, K. T.; WILSON, R. S.; MCLEAN, S. K.** Flexure of simply curved composite shapes. **Composites**, v. 20, n. 6, p. 527–536, 1989.
- [26] **LEKHNITSKIY, S. G.** Anisotropic Plates. **Gordon and Breach Science**, p. 477, 1969.

3. Mode I and Mode II Fracture Behavior in Pultruded Glass Fiber-Polymer Bridge Decks – Experimental Investigation

3.1. Introduction

The structural applications of pultruded glass fiber-polymer bridge decks have experienced an expansion in the last few decades, being designed mostly to carry pedestrian, cyclists and light weight vehicles [1]. Their corrosion resistance provides longer life cycles and significant reduction of maintenance costs when compared to traditional materials. Moreover, the material presents high compressive and tensile strength parallel to fibers, whereas their lightweight allows a fast and easy installation. In replacement applications over reinforced concrete, the dead load reduction also increases the live load capacity [2].

The pultruded glass fiber-polymer bridge decks are constructed by bonding units of composite materials with adhesive joints [1]. The decks are supported by longitudinal bridge girders, generally having the rovings aligned transversely to the traffic direction [3]. However, such composites usually present weak interlaminar strengths, resulting commonly in delamination in the junction region, transversely to the pultrusion direction, as shown in Figure 3.1. The effect of this kind of damage influences the composite behavior, reducing its ultimate load and global stiffness [4]. Further, delamination may also affect serviceability if occurring at early loading stages.

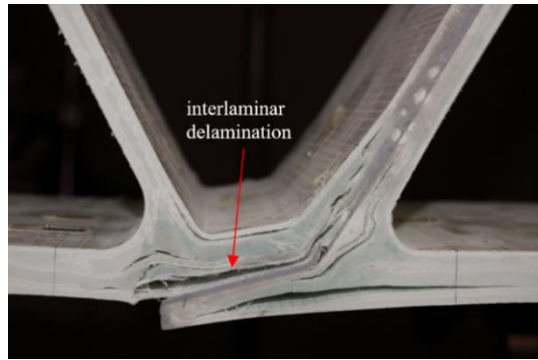


Figure 3.1. Delamination on a bridge deck system (adapted from [2]).

In this context, it is important to introduce basic concepts of Fracture Mechanics, as the strain energy released rate (SERR), which is defined by Irwin as the energy available (G) for crack extension, measured per increment of crack extension and per unit of thickness [5]. In Linear Elastic Fracture Mechanics (LEFM), the central assumption is that all the fracture process is reduced to the single point of the crack tip [6]. The stresses in the vicinity of this crack tip may be divided into three modes (see Figure 3.2) related to the crack surface displacements [5]. Mode I, dominant in many practical cases [5], is characterized by an opening that occurs perpendicular to the crack plane, whereas Mode II corresponds to shear loading, in which the crack surfaces slide relative to each other in the plane. On the other hand, Mode III causes out-of-plane shear displacements. The SERR can be, thus, divided into the three aforementioned components according to the separate mechanisms observed in the fracture process [7]. The crack growth will occur when the SERR is larger than the energy required for crack extension, called critical SERR (G_c), and which is a measure of fracture toughness [8,9]. The latter is also called, in some works [10], of steady state toughness, which corresponds to the plateau of the R-curve (SERR vs. crack length curve). Throughout this work, only in-plane modes will be addressed. The SERR related to crack initiation will be named as G_{tip} and the critical SERR required for crack propagation as G_{tot}

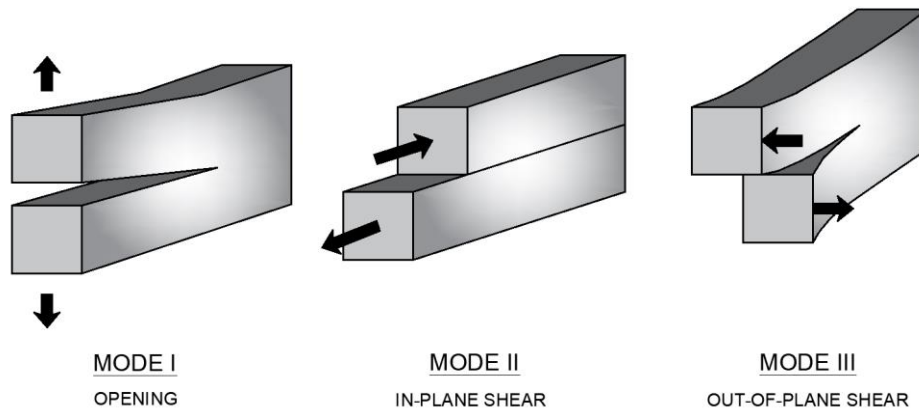


Figure 3.2. Mode I and Mode II of loading.

Due to the relevance to understand the fracture behavior and obtain the delamination toughness, different experimental methods have been standardized for this purpose, among which one may cite the Double Cantilever Beam (DCB) and the End-Loaded-Split (ELS). Such methods are extensively documented in literature to assess the fracture toughness under pure Mode I and Mode II of loading. To the best of the author's knowledge, with exception of the studies addressing the delamination in adhesively bonded joints, no experimental investigations about the interlaminar fracture of pultruded fiber-polymers have been carried out previously. The few experimental investigations about the fracture behavior of pultruded fiber-polymer materials that can be found in the literature are focused on intralaminar and translaminar fracture. Almeida-Fernandes *et al.* [11,12] recently reported experimental investigations on the transverse fracture behavior of pultruded glass fiber-polymer composites based on compact compression (CC), compact tension (CT) and wide compact tension (WCT) tests, in which the failure occurred in the roving direction. The authors also conducted numerical simulations to assess the fracture toughness related to the web-crippling tests [13]. El-Hajjar and Haj-Ali [14,15] conducted experimental and numerical analyses to assess the Mode I stress-intensity factor of thick glass fiber-polymer materials for transverse (90°) and longitudinal (0°) directions using the single-edge-notch tension ESE(T) specimen. Liu *et al.* [16] also investigated the Mode I fracture property of pultruded fiber-polymers along the fiber direction through three-point flexural tests on single edge notched (SEN) specimens.

Regarding the testing techniques, there is currently no standard or guideline concerning the determination of fracture toughness for pultruded elements. Double-cantilever beam (DCB) and end-loaded split (ELS) are well-established methods and have been used for a wide variety of materials, but their applicability to pultruded fiber-polymers is unknown. One of the main challenges of the application of DCB and ELS tests in pultruded composites is related to the initial starter crack (or initial separation). The standards for polymer matrix composites recommend inserting a thin film made of, for instance, polyimide, at the midplane of the laminate, to introduce an initiation site for delamination. Nevertheless, pultruded glass fiber-polymer elements are manufactured through an automatic continuous process in factories, precluding the aforementioned technique. In this context, Burda *et al.* [17] performed DCB tests in pultruded glass fiber reinforced epoxy rods, evaluating four different methods for the introduction of the initial separation. The authors observed that the different methods provided different values of initiation and propagation from each other, pointing out that a pre-crack made with a diamond wire saw combined with a knife blade tapping resulted in reproducible low initiation values. Specimens at least 250-mm long with pre-cracks limited to 35 mm were recommended to characterize the full R-curve behavior, which describes the SERR plotted against the delamination crack growth. No plateau was observed in the R-curves. Besides this research, very few other DCB and ELS experiments in pultruded fiber-polymers are reported in the literature, mostly focused on the behavior of adhesively bonded joints [18–21]. Among these works, it is worth citing Ye Zhang *et al.* [19] and Shahverdi *et al.* [18], who observed part of the fracture occurring in the pultruded material. The authors conducted DCB and ELS tests to calculate the critical strain energy release rate (SERR) based on the existing standards.

The authors conducted DCB and ELS tests to calculate the critical SERR based on the existing standards. In the former, a fiber-tear failure at the mat layer was observed, whereas the latter investigated the G_c parameters for three different crack paths: *i.* failure between the adhesive and the mat layer, *ii.* between two mat layers and *iii.* between roving and mat layers. Lower values of SERR were found for the first crack path, both in terms of crack initiation and propagation.

Tables 3.1 and 3.2 present detailed information of the previous works focused on pultruded profiles and the reported G_c parameters for Modes I and II. It can be noticed a great variability between the found values. Furthermore, the limited number of studies available, especially related to the interlaminar fracture and to Mode II, added to the complexity in obtaining fracture parameters and the well-known high variability observed in general properties in this type of material are aggravating factors that increase the need of reliable guidelines for the accurate determination of fracture characteristics for this material. Moreover, the lack of fracture parameters data for pultruded glass fiber-polymers in literature is a relevant obstacle for appropriate numerical damage simulations, which often cause researchers to adopt properties without an experimental basis [22].

Table 3.1. Average SERR in J/m² reported in literature for Mode I.

| Authors | Matrix | Crack path | Experimental G_I | | Numerical G_I | |
|---|-----------------------|---|--------------------|---------------|-----------------|-------------|
| | | | Initiation | Propagation | Initiation | Propagation |
| Ye Zhang <i>et al.</i> [19] | Isophthalic polyester | fiber-tear failure at the mat layer (interlaminar) | 196 - 702 | 1,506 – 1,674 | 316.1 | 1982.7 |
| Shahverdi <i>et al.</i> [18] | Isophthalic polyester | between the adhesive and the mat layer (interlaminar) | 151 | 536 | NR | |
| | | between two mat layers (interlaminar) | 360 | 1,102 | | |
| | | between roving and mat layers (interlaminar) | 456 | 851 | | |
| Almeida-Fernandes <i>et al.</i> [12] | NR | in the roving layer direction (longitudinal intralaminar) | 6,600 – 27,000 | | - | |
| Hajjar and Haj-Ali [14] | Polyester | transversely to the roving direction (translaminar) | 15,000 – 18,500* | | NR | |
| | | along the roving direction (longitudinal intralaminar) | 8,600 – 8,900* | | NR | |

| | | | | | |
|-----------------|----|---|-------|-------|---|
| Liu et al. [16] | NR | along the roving direction between the fibers and the matrix (intralaminar) | 4,680 | 7,711 | - |
|-----------------|----|---|-------|-------|---|

*Estimated based on the reported stress-intensity factor

NR – Non-reported.

Table 3.2. Average SERR in J/m² values reported in literature for Mode II.

| Authors | Matrix | Crack path | Experimental GII | | Numerical GII | |
|-----------------------|-----------------------|---|------------------|-------------------|---------------|-------------|
| | | | Initiation | Propagation | Initiation | Propagation |
| Ye Zhang et al. [19] | Isophthalic polyester | fiber-tear failure at the mat layer (interlaminar) | 904.2 – 1,337.1 | 1,722.4 – 2,292.8 | 1,199.6 | 2,177.9 |
| Shahverdi et al. [18] | Isophthalic polyester | between the adhesive and the mat layer (interlaminar) | 1,156 | 1,736 | NR | |
| | | between two mat layers (interlaminar) | - | 2,670 | | |
| | | between roving and mat layers (interlaminar) | - | - | | |

NR – Non-reported.

This scarcity of fracture mechanics data hampers the investigations on the failure behavior of these composites, being a relevant obstacle for appropriate numerical damage simulations. It is often required to conduct an extensive experimental investigation to obtain the concerned composite's fracture parameters. In this scenario, the present work aims to complement this scarcity, providing interlaminar fracture mechanic data obtained from classical and standardized tests, such as DCB and ELS. Experimental procedures for both Mode I and Mode II were conducted. The starter crack (or initial separation) required to perform the experimental procedures was introduced via a water jet machine. In all, nine different methods were applied to obtain the fracture toughness G_{Ic} and G_{IIc} . The results are discussed and compared with the values reported by previous authors. In the next chapters, the found parameters are compared with numerical models and applied in a multi-crack finite element method (FEM) analysis of pultruded glass fiber-polymer web-flange junctions.

3.2. Theoretical background

3.2.1. SERR in Mode I

Based on the energy balance approach in the LEFM field, Equation (3.1) expresses the Irwin-Kies formula, which serves as the basis of measurement of the fracture energy [23], used in this work as a synonym for fracture toughness or critical SERR.

$$G = \frac{P^2}{2b} \frac{dC}{da} \quad (3.1)$$

Where P is the applied load, b is the specimen's width, a is the delamination or crack length measured from the loading line and C is the compliance known as the ratio of δ/P , in which δ is the applied displacement.

It should be noticed that the SERR is not dependent on the loading system, allowing the formulation to be valid for fixed grip, constant load or any other arbitrary loading condition [5]. Standard methods for the G calculation were derived from this relation, presenting differences basically in the determination of the derivate of dC/da [19].

The standard *ASTM D5528-01* [24] presents three different methods in order to quantify the strain energy released rate (SERR) for Mode I: *i. Modified Beam Theory (MBT)*, *ii. Compliance Calibration (CC)* and *iii. Modified Compliance Calibration (MCC)* methods. The formulae used for each method are expressed in Equations from (3.2) to (3.4).

$$MBT_{ASTM} \text{ method} \quad G_I = \frac{3P\delta}{2b(a + |\Delta|)} \quad (3.2)$$

$$CC_{ASTM} \text{ method} \quad G_I = \frac{nP\delta}{2ba} \quad (3.3)$$

$$MCC_{ASTM} \text{ method} \quad G_I = \frac{3P^2C^{2/3}}{2A_1bh} \quad (3.4)$$

where δ is the displacement correspondent to the applied load P and h is the specimen thickness. The parameter Δ expressed in Equation (3.2) is an attempt to correct a possible overestimation of G_I due to rotations that may occur at the

delamination front [25]. It is obtained experimentally by the plot of $C^{1/3}$ vs. the delamination length a , as shown in Figure 3.3. On the other hand, the parameter n of Equation (3.3) represents the slope of the logarithmic functions of the compliance ($\log C$) and the delamination length ($\log a$) plotted against each other ($\log C$ vs. $\log a$). Finally, in Equation (3.4), the parameter A_I indicates the slope of the curve (a/h) vs. ($C^{1/3}$).

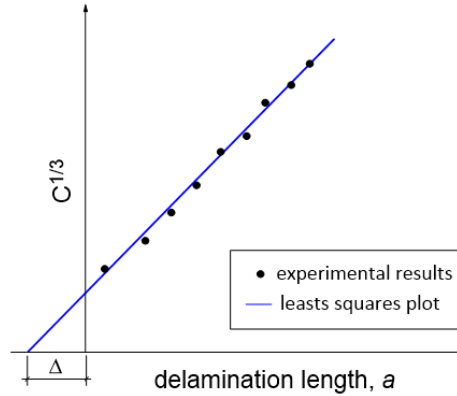


Figure 3.3. Determination of parameter Δ according to MBT method.

The standardized MBT_{ASTM} method derives from the elementary beam theory, with the addition of the correction parameter Δ . However, for a crack occurring out of the specimen midplane, this formulation might be inaccurate. To consider the asymmetry generated in this scenario, Mollón *et al.* [26] presented a formulation to determine G_I based on an equivalent stiffness EI_{eq} , as follows:

$$MBT-EI_{eq} \text{ method} \quad G_I = \frac{3P^2(a + |\Delta|)^2}{2b(EI_{eq})} \quad (3.5)$$

where $(1/EI_{eq})^{1/3}$ is the slope of the plot $C^{1/3}$ vs. a .

Regarding the CC method, an alternative function, expressed in Equation (3.6), is adopted in some works [27,28] to describe the compliance of compact tension (CT) specimens. The critical SERR in Mode I can be obtained by Equation (3.7) and is dependent on the optically measured crack length. Hereafter, the method in which the presented expressions are used will be designated as CC-f method.

$$CC-f \text{ method} \quad C = (\alpha a + \beta)^\chi \quad (3.6)$$

$$G_I = \frac{P^2}{2b} \alpha \chi (\alpha a + \beta)^{\chi-1} \quad (3.7)$$

The parameters α , β and χ are the constants calculated to best fit the experimental data.

Likewise, the standardized MCC_{ASTM} method also requires the visual crack length determination in DCB tests. However, to eliminate this optical measurement dependency, an effective crack length a_{eff} - see Equation (3.8) – can be determined as a function of the measured compliance presented in Equation (3.6). The critical SERR G_{Ic} can also be expressed according to Equation (3.7). This procedure is adopted in many works [12,28–30] and is considered by some authors as the most appropriate data reduction scheme for determining the critical SERR [28]. However, it requires additional experiments and increase the complexity in obtaining the compliance vs delamination length curves by numerical simulations [28].

$$MCC-a_{eff} \text{ method} \quad a_{eff} = \frac{C^{1/\chi} - \beta}{\alpha} \quad (3.8)$$

More conservative G_c values have been found for $MCC-a_{eff}$ method when compared to CC-f and another popular approach known as J-integral, which accounts for nonlinearities within the fracture process zone (FPZ) at the crack tip [29,30]. On the other hand, some authors have observed that although the $MCC-a_{eff}$ method is able to provide a good response for the cohesive behavior, being well correlated with the J-integral, the former is slightly less accurate than the latter. In P vs. δ curves obtained from FEM analyses, the $MCC-a_{eff}$ has underestimated the peak load in 6.9% and overpredicted the critical SERR for propagation by 2% [30]. In this context, Almeida-Fernandes [12] stated that the method significantly underestimated the critical SERR when compared to other methods, such as J-Integral and CC-f. This fact was attributed to the influence of fiber pull-out in loading/unloading cycles, as well as to the thickness (maximum of 9.9 mm) of specimens. However, the $MCC-a_{eff}$ method has the advantage of being simpler since it is based on LEFM conditions. In this work, in an attempt to maintain the

simplicity and accuracy for obtaining the SERR parameters of pultruded glass fiber-polymer specimens, six methods based on LEFM are assessed and discussed, among which three are standardized (MBT_{ASTM} , CC_{ASTM} and MCC_{ASTM}) and the other three incorporate modifications proposed by the aforementioned authors ($MBT-EI_{eq}$, $CC-f$ and $MCC-a_{eff}$).

3.2.2. SERR in Mode II

For Mode II, the standard *ISO 15114* [31] proposes other three methods for the assessment of the fracture energy, which are also used in this research to analyze the data provided by ELS tests: *i. Experimental compliance method (ECM)*, *ii. Simple beam theory (SBT)* and *iii. Corrected beam theory using effective crack length (CBTE)*. The equations 3.9, 3.11 and 3.13 are used to obtain the parameter G_{II} , whereas the formulations 3.10, 3.12 and 3.14 expresses the compliance solution for each method, respectively.

$$EMC \text{ method} \quad G_{II} = \frac{3P^2 a^2 m}{2b} \quad (3.9)$$

$$C = C_0 + ma^3 \quad (3.10)$$

where C_0 and m are constants that represent the linear regression of the compliance function related to the crack length a .

$$SBT \text{ method} \quad G_{II} = \frac{9P^2 a^2}{4b^2 t_s^3 E_1} \quad (3.11)$$

$$C = \frac{3a^3 + L_f^3}{2bt_s^3 E_1} \quad (3.12)$$

where t_s is the half of the specimen's thickness, L_f is the testing free length and E_1 is the specimen's flexural modulus.

$$CBTE \text{ method} \quad G_{II} = \frac{9P^2 a_e^2}{4b^2 t_s^3 E_1} \quad (3.13)$$

$$C = \frac{3(a_e)^3 + (L_f + \Delta_{clamp})^3}{2bt_s^3 E_1} \quad (3.14)$$

$$a_e = \left[\frac{1}{3} \{ 2bCt_s^3 E_1 - (L_f + \Delta_{clamp})^3 \} \right]^{1/3} \quad (3.15)$$

where a_e is the effective (calculated) crack length and Δ_{clamp} is the clamp correction obtained in the clamp calibration tests, which are conducted by clamping one side of the ELS specimen with different free lengths and applying a maximum load of 150 N to elastically deform the specimen. The loads and displacements are recorded, allowing the plot of the curve $C^{1/3}$ vs. each tested free length L_f . The Δ_{clamp} can be obtained by Equation (3.16).

$$C^{1/3} = (\alpha L_f + \alpha |\Delta_{clamp}|) \quad (3.16)$$

where α is the slope of the curve $C^{1/3}$ vs. L_f expressed in Equation (3.17).

$$\alpha = \left(\frac{1}{2bt_s^3 E_1} \right)^{\frac{1}{3}} \quad (3.17)$$

The flexural modulus E_I can also be deduced from the slope of the clamp calibration data and can be written as follows:

$$E_1 = \frac{1}{2b (t_s \alpha)^3} \quad (3.18)$$

The SBT formulation is obtained based on a shear-corrected beam analysis and some researchers have shown that the approach may underestimate the SERR values [19]. On the other hand, the EMC method, which can be considered as equivalent to MCC for Mode II, presented similar results provided by finite element models [19]. The CBTE method assumes the beam theory, although considering an effective crack length that eliminates the dependency of the measured delamination length, which is often difficult to quantify. Some authors observed that this method might lead to less accurate values for crack initiation due to geometrical characteristics and generated asymmetries in the fracture process [19].

3.3. Experimental Program

3.3.1. Materials

In all, five DCB and five ELS tests were performed in specimens extracted from a *DuraSpan* bridge deck system [32], manufactured by Martin Marietta Composites Inc. (Raleigh, United States). Throughout this work, the specimens were named as DCB.01 to DCB.05 and ELS.01 to ELS.05. The cross-section geometry of the deck's unit module is presented in Figure 3.4. The given pultruded structure is constituted of E-glass fibers embedded in an isophthalic polyester matrix. All experiments described hereafter were conducted in the *Composite Construction Laboratory* (CCLab) at the *École Polytechnique Fédérale de Lausanne* (EPFL). The experiments were conducted under ambient laboratory conditions (approx. 22°C and 50% RH).

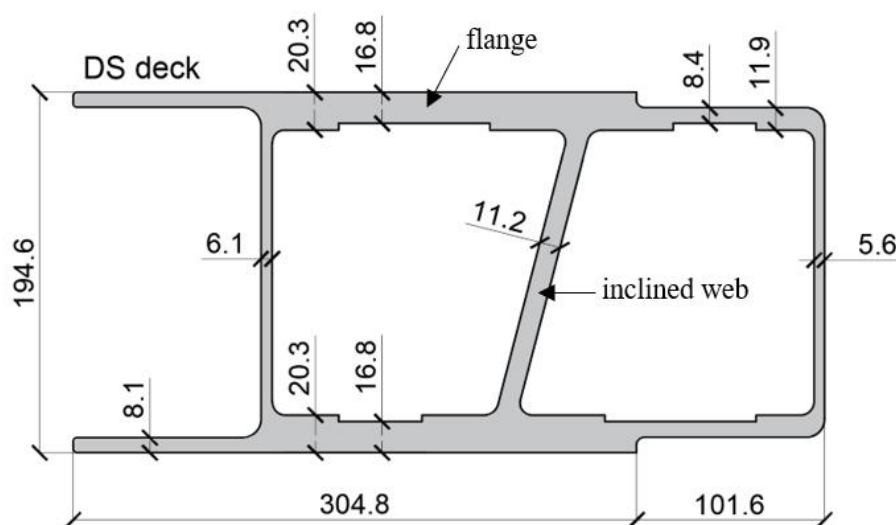


Figure 3.4. Unit section of DS deck (dimensions in mm).

Burn-off tests were conducted in specimens extracted from the *DS* bridge deck at the *Laboratory for Processing of Advanced Composites* (LPAC) in the *École Polytechnique Fédérale de Lausanne* (EPFL), following the recommendations of *ISO 1172:1996* [33] and the methodology presented in [34]. The composite's fiber architecture is composed of rovings (*r*), triaxial fabrics (*f*) oriented in -45° , 90° , and 45° , and non-structural mats, as shown in Figure 3.5. The found average fiber volume ratios are presented in Table 3.3, with their respective standard deviation

and coefficient of variation (CoV) indicated in parentheses. It was found an average roving volume content of 22% at the flange and 13.5% at the web. On the other hand, the triaxial fabrics constitute 30.4% and 34.5% of the flange and web volumes, respectively. The non-structural mats were considered as part of the triaxial fabrics both in the fiber content estimate and in the numerical model, presented in the next Chapter.

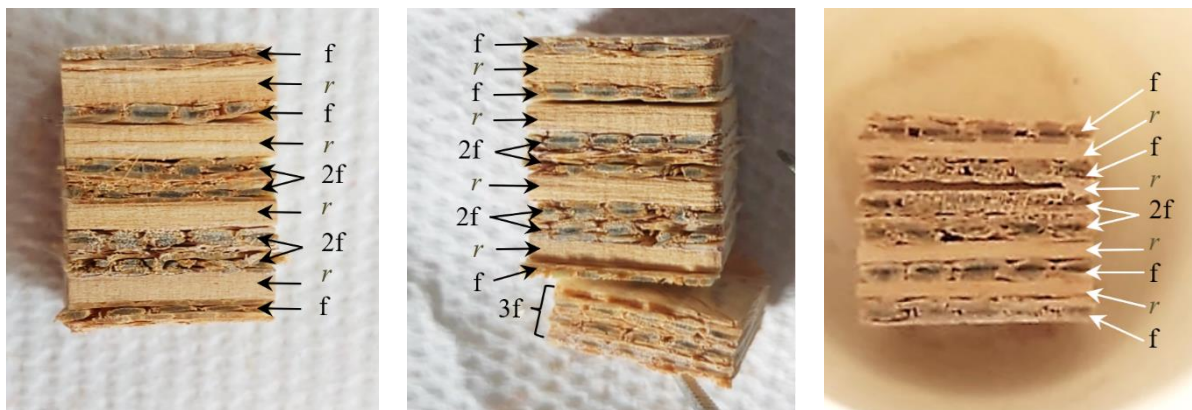


Figure 3.5. Fiber architecture: (a) flange (t=16.8 mm); (b) flange (t=20.3 mm); (c) web.

Table 3.3. Fiber volume ratio.

| | $V_{f,total}$ (%) | V_{roving} (%) | V_{fabric} (%) |
|--------------------------------|----------------------------|----------------------------|----------------------------|
| web | 48 ± 1.12 (0.023) | 13.5 ± 1.02 (0.076) | 34.5 ± 1.24 (0.036) |
| flange (t = 16.8 mm) | 52.3 ± 0.72 (0.014) | 23.6 ± 1.82 (0.077) | 28.8 ± 2.36 (0.082) |
| flange (t = 20.3 mm) | 52.5 ± 1.68 (0.032) | 19.7 ± 1.20 (0.061) | 32.8 ± 0.49 (0.015) |
| flange | 52.4 ± 1.21 (0.023) | 22.0 ± 2.46 (0.112) | 30.4 ± 2.70 (0.089) |
| flange + roving | 50.8 ± 2.44 (0.048) | 18.8 ± 4.6 (0.244) | 31.9 ± 3.01 (0.094) |

3.3.2. DCB tests

In order to determine Mode I SERR, double cantilever beam (DCB) experiments were conducted in five specimens of 250-mm length, which were

extracted from *DS* decks flanges, as shown in Figure 3.6. The specimens were cut having the length perpendicular to the roving direction and its fiber architecture was composed of four roving layers, interspersed with seven layers of triaxial fabrics. The existing standards for DCB tests recommend the specimens to have a constant thickness, however, the flanges of the used bridge deck system were originally manufactured with a thickness variation along the cross-section, as shown in Figure 3.4. Therefore, a water jet cutting machine was used to remove the spare parts from the flanges, resulting in a variation of thickness of less than 0.14 mm. The average width of the specimens was 23 ± 0.90 mm against an average thickness of 15.5 ± 0.44 mm. The water jet cutting machine was also used to introduce an initial separation in the specimens midplane of 60 mm of length and having 1 mm of thickness. The used test fixture is presented in Figure 3.7. The initial delamination length a_0 adopted is measured from the load application line.

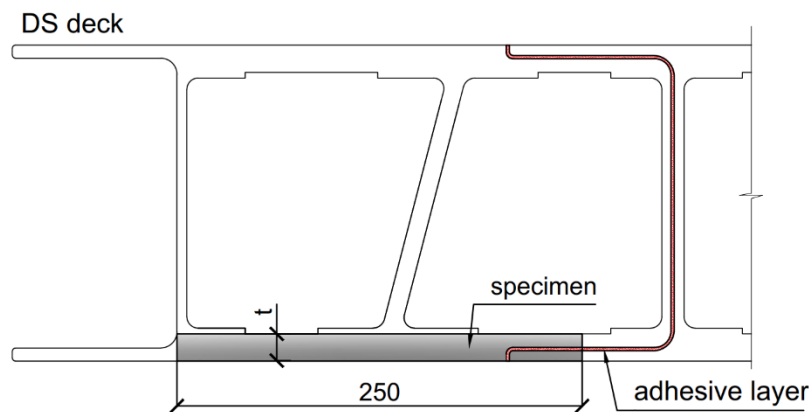


Figure 3.6. Specimens extracted from the *DS* bridge deck system.

Several preliminary tests were carried out to evaluate a suitable way to attach the specimen to the pair of aluminum plates linked to the piano-hinged loading blocks shown in Figure 3.7. The *Sikadur-32* adhesive presented good results for this purpose, and it was used in all tests presented hereafter. The experiments were conducted under displacement control on a servo-hydraulic universal testing machine *Walter + Bai* with a load capacity of 40 kN. Based on existing standards for DCB [24], the displacements were applied at a rate of 1mm/min until reaching a delamination crack growth (*hereafter called pre-crack length*) of less than 5 mm and subsequently unloaded at a rate of 25 mm/min.

Thereafter, the specimens were reloaded at the same constant crosshead speed of 1mm/min. To eliminate the influence of the adhesive region, a minimum distance of 25 mm was kept between the considered final crack length and the beginning of the adhesive layer, which illustrated in Figure 3.7a.

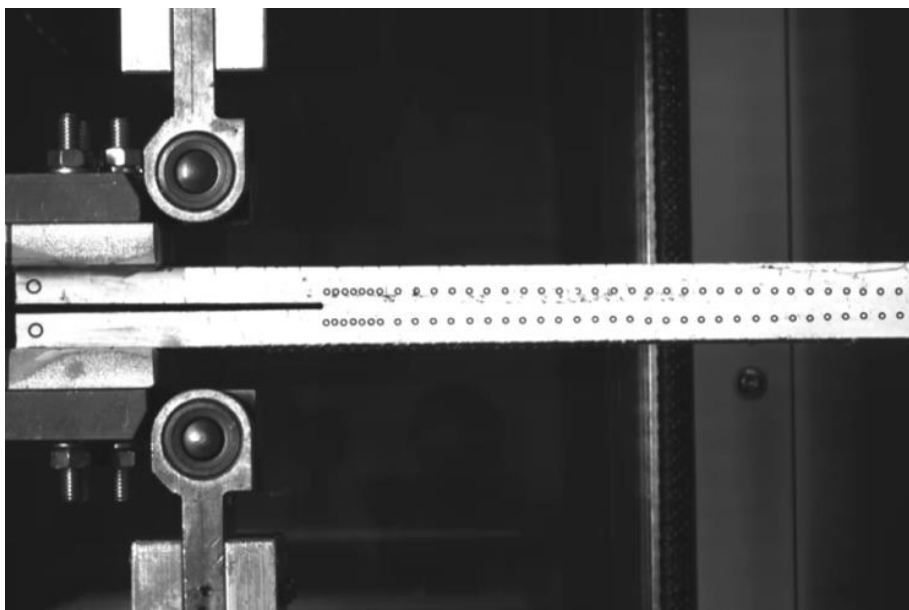
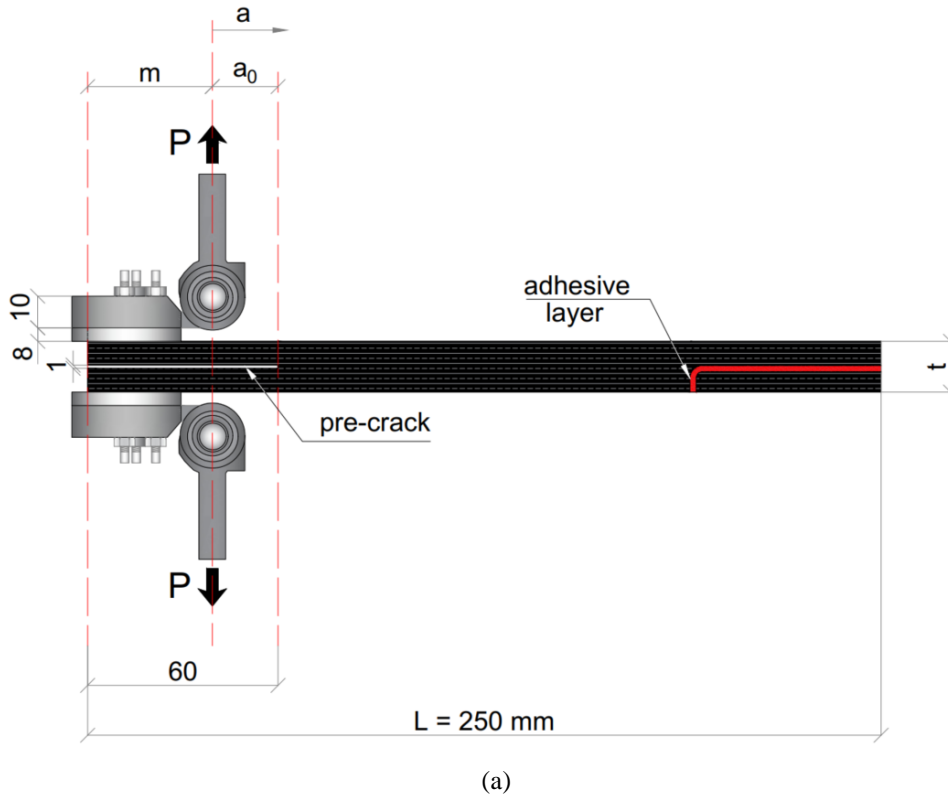


Figure 3.7. DCB test fixture: (a) scheme (dimensions in mm); (b) picture taken with video-extensometer technique.

To accurately capture the development of the crack propagation, the video-extensometer technique was used. Photos were taken every three seconds using a *Progressive Scan IT CCD* and an *XCG-5005E* camera with a resolution of 2448 x 2048 pixels and an acquisition frequency of 1 Hz. The specimens' face was polished and painted in white to improve the visualization of the crack growth. Subsequently, several pairs of circular targets were drawn ahead the initial separation, spaced approximately every 1.7-mm over at least the first 10 centimeters and every 3.4-mm over the rest of the length, as shown in Figure 3.7b. For each registered picture, the corresponding load and displacement increments were recorded, whereas the respective CODs were measured at the first pair of black targets ahead the initial separation.

The SERR for Mode I was obtained from MBT_{ASTM} , $MBT-EI_{eq}$, CC_{ASTM} , $CC-f$, MCC_{ASTM} and $MCC-a_{eff}$ and the results are discussed further ahead.

3.3.3. ELS tests

End-loaded-split (ELS) tests were conducted to evaluate the Mode II SERR. The same procedure used for DCB specimens cutting was adopted and an initial separation with 100 mm of length and 1 mm of thickness was introduced in its midplane by means of a water jet cutting machine. Five specimens of 310-mm length, average width of 25.3 ± 0.03 -mm, and average thickness of 16.0 ± 0.03 -mm were extracted from *DS* flanges, as shown in Figure 3.8, and tested. The maximum thickness variation along the specimen length was lower than 0.34 mm.

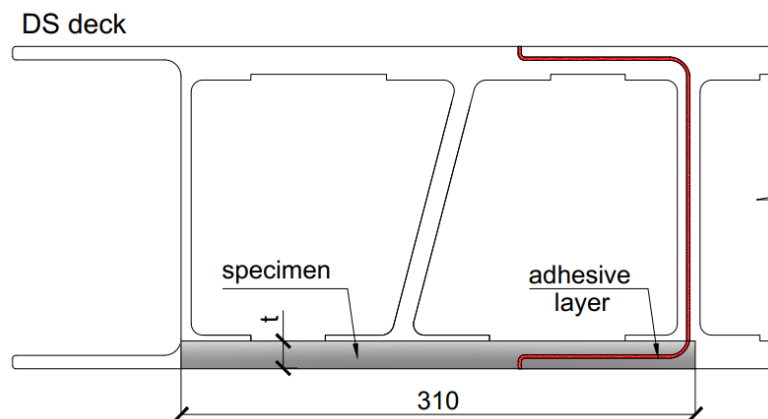


Figure 3.8. ELS specimens extracted from the *DS* deck.

The experiments were conducted under displacement control on a table machine *Walter + Bai* with a load capacity of 50 kN. The setup test is shown in Figure 3.9. An aluminum angle having 3 mm of thickness was bonded to the specimen with *Sikadur 32* to prevent the specimen from slipping out of the loading line. Following recommendations of existing standards [31], after a calibration of the test fixture, a pre-cracking procedure was performed. The specimens were clamped with a free length, L_f , set as 113.5 mm and loaded at a displacement rate of 1mm/min until reaching a pre-crack of less than 5 mm. Subsequently, the specimens were unloaded at a rate of 25 mm/min. After this pre-cracking procedure, the specimens were clamped with a new free length, L_f , of 180 mm, as shown in Figure 3.9, and reloaded at the same constant crosshead speed of 1mm/min until, until the final crack delamination was reached. To guarantee the clamping, the specimen was positioned and simply supported by the fixture presented in Figure 3.10a, and fixed with screws at the top, as shown in Figure 3.10b. As performed for DCB, a minimum distance of 25 mm was kept between the considered final crack length and the beginning of the adhesive layer to eliminate the influence of the latter.

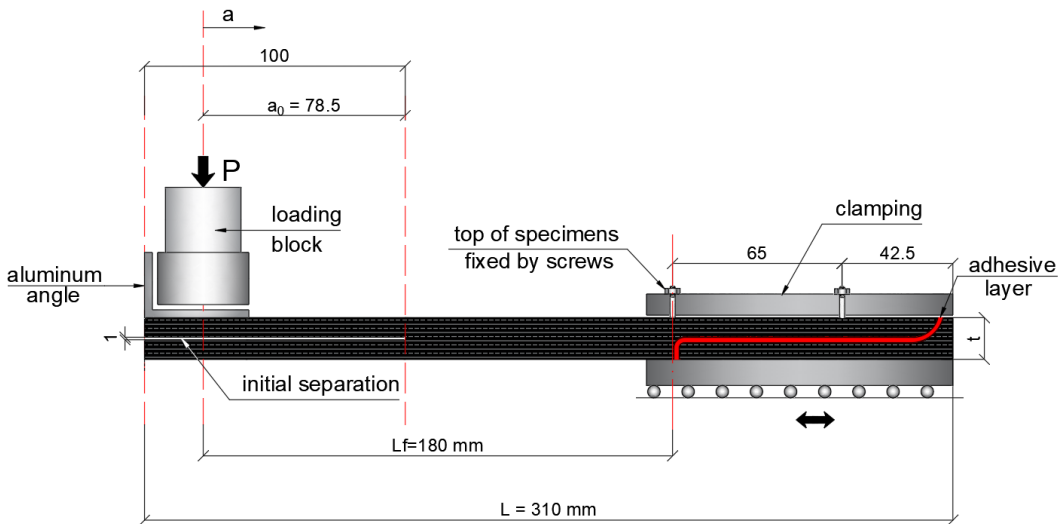


Figure 3.9. ELS test fixture scheme.

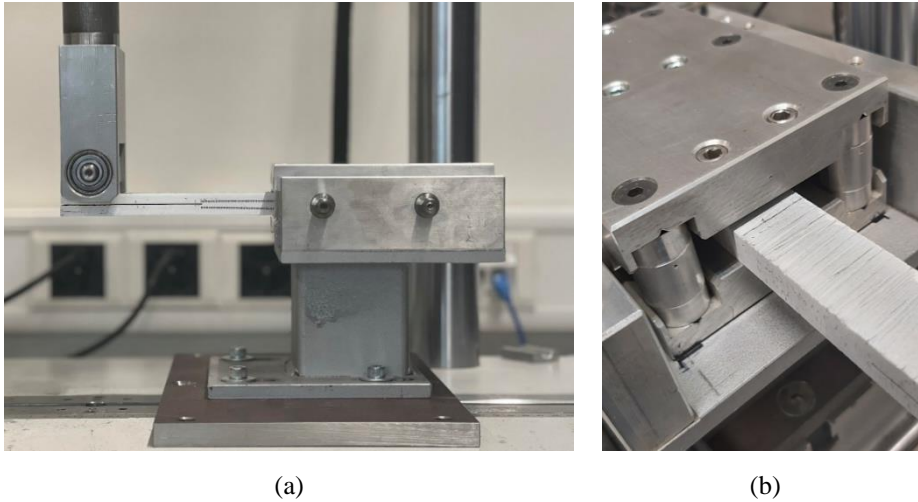


Figure 3.10. ELS test fixture: (a) front view; (b) clamping.

The video-extensometer was also used to capture the Mode II crack propagation. However, in ELS tests, the pair of black dots were spaced every 1.7 mm along the overall specimen length, due to greater difficulty in following the crack development. The pictures were registered every three seconds and the corresponding load and displacement increments were recorded. Figure 3.11 shows a detailed view of the pair of circular targets drawn on the ELS specimens faces. As can be noticed, the specimen ELS.05 presented some voids near its midplane, where the crack is supposed to develop. Similar initial defects were observed on the specimens ELS.03 and ELS.04. This is relevant in this case, since it constitutes an additional challenge for the accurate reading of crack length data at these regions.

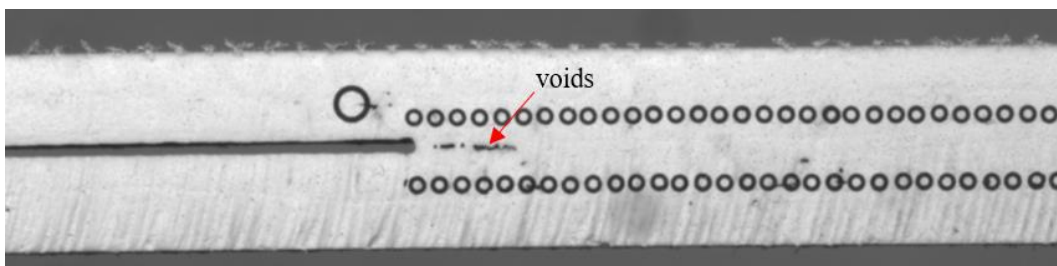


Figure 3.11. Detail of pair of black dots on the ELS.05 specimen.

3.4. DCB experimental results

3.4.1. Failure modes

All DCB specimens experienced interlaminar failure between the two adjacent multiply fabrics layers at its midplane, as presented in Figure 3.12. The values of the pre-crack length introduced by the pre-loading varied from 1.70 to 3.57 mm. The crack propagation typically followed the fiber architecture configuration, as shown in Figure 3.13, *i.e.*, the crack remained between the same fabric layers until reaching in average approximately 108 mm of total crack length and 11.1 mm of crack opening displacement (COD). Audible noises were heard followed by an abrupt crack deviation at the final stages of the DCB.02 and DCB.04 tests due to the imminent encounter with the existent adhesive layer shown in Figure 3.7.

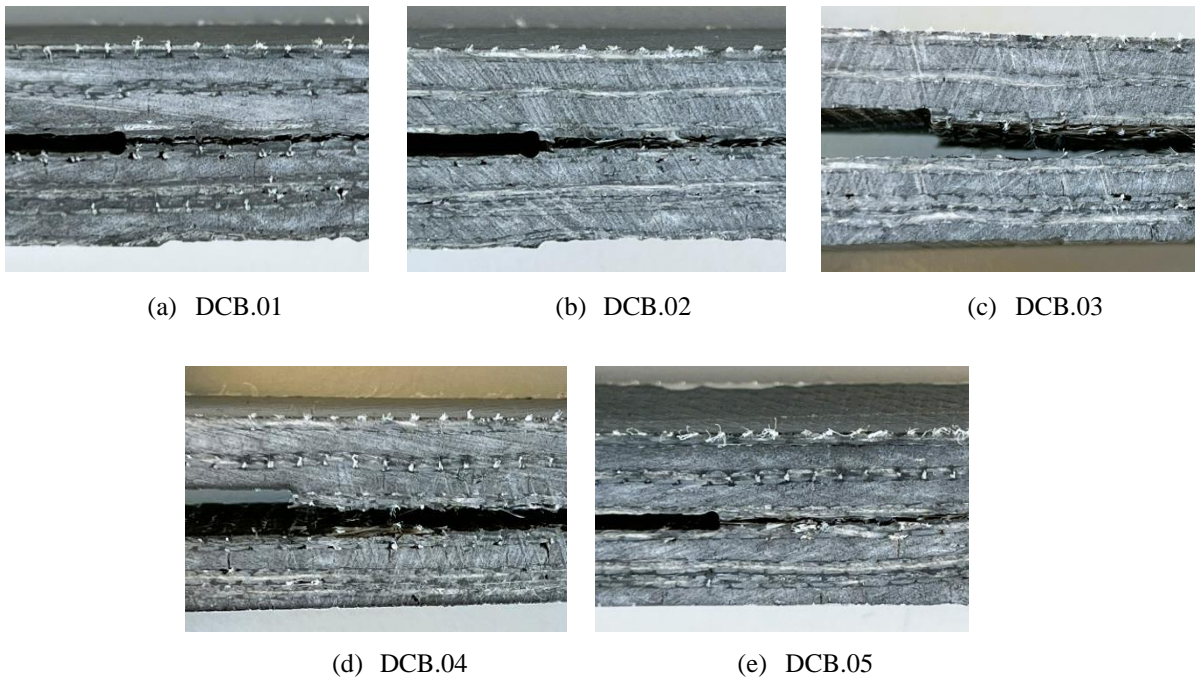


Figure 3.12. Failure mode of DCB specimens: (a) DCB.01; (b) DCB.02; (c) DCB.03; (d) DCB.04; (e) DCB.05.

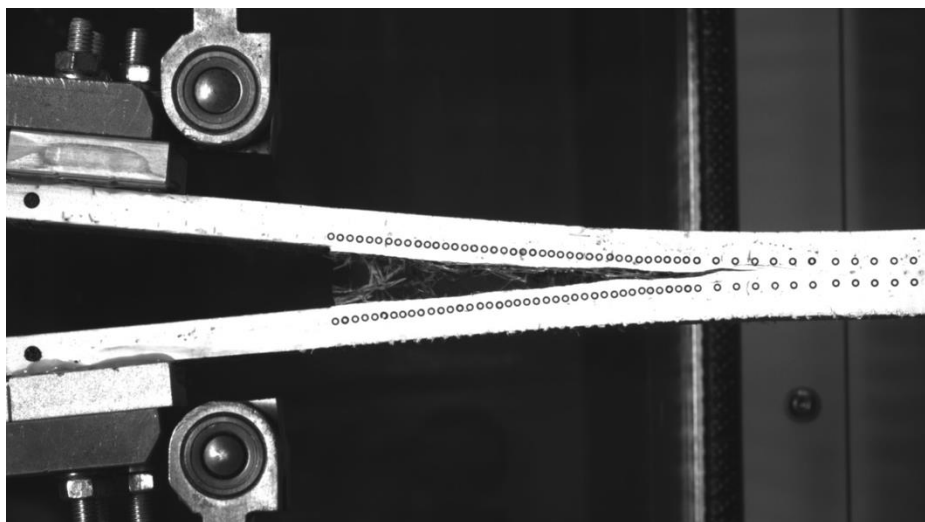


Figure 3.13. Delamination growth between fabric layers at the midplane DCB.01 specimen.

The presence of fiber bridging, shown in Figure 3.14, was observed in all specimens, to lesser or greater degree. The specimen DCB.06 was, clearly, the one that least presented the development of such mechanism, whereas in DCB.01, it was possible to visually notice a large fiber amount crossing the crack along the crack length.

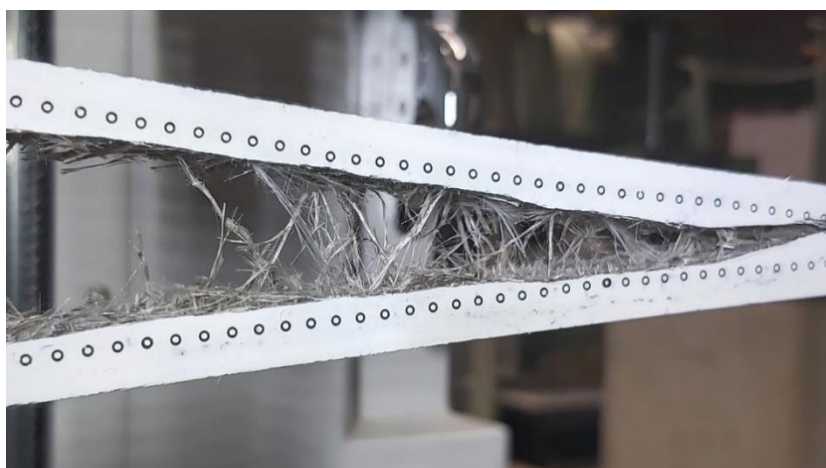


Figure 3.14. Fiber bridging observed in DCB.05.

3.4.2. Asymmetry assessment

Since the cracks propagated through the layers path, an asymmetry is generated at some points of the specimen, as can be seen in Figure 3.13. A maximum eccentricity of 1.30 mm between the crack line and the symmetry axis was registered for the specimen DCB.01. Therefore, this asymmetry effect was assessed following the procedure reported by Zhang *et al.* [19]. The relative through-thickness displacements related to Mode I were compared with the shear displacements related to Mode II. The former is represented by the vertical distance between the points P_1 and P_2 of Figure 3.15, whereas the latter is defined by the horizontal one. Figure 3.16 shows, through a typical graph having the respective relative displacements plotted against the crack length, that the Mode I is the dominant fracture mode for the specimen, with an increase up to 28 mm in the vertical distance between the points. On the other hand, the horizontal relative displacement achieves its maximum value for DCB.04 with 0.7 mm, showing that the Mode II can be neglected.

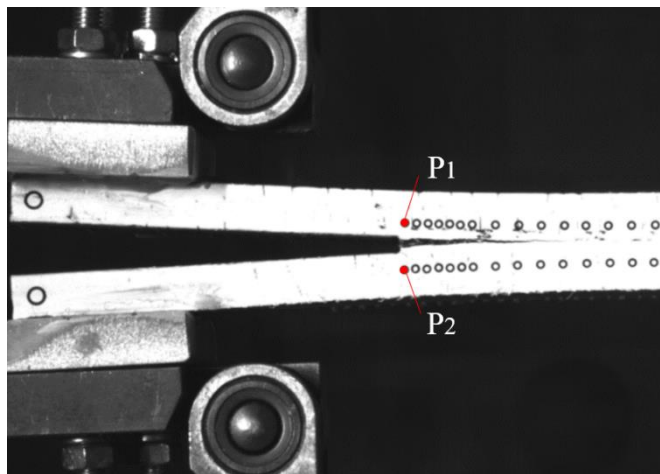


Figure 3.15. Points definition for the assessment of the asymmetry effect.

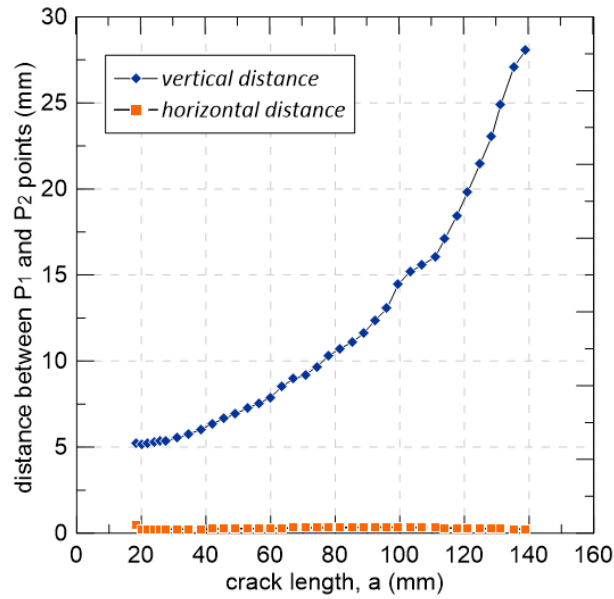


Figure 3.16. Fracture modes assessment for DCB.01.

3.4.3. Load-displacement and compliance responses

The load P vs. displacement δ curves of all five specimens are presented in Figure 3.17a and the compliance δ/P vs. the measured crack length, a , curve is plotted in Figure 3.17b. It can be observed that all specimens have shown a very similar behavior in terms of both curves. With exception of DCB.01, all specimens have reached close peak loads, ranging between 0.367 and 0.385 kN. The DCB.01 presented an unreliable increase in the maximum load ($P_{max} = 0.408$ kN) compared to the other specimens, which may be explained by a possible small initial torque applied on the piano-hinges blocks screws used in the test fixture, leading to a load relief at the first seconds of testing. The difference noticed in the compliance curve of DCB.01, when compared to the other specimens, may be due to the same reason. All specimens presented similar compliance behavior, with a nonlinear increase of δ/P as the crack propagated, revealing a dominance of softening mechanisms over the stiffening generated by the presence of fiber bridging.

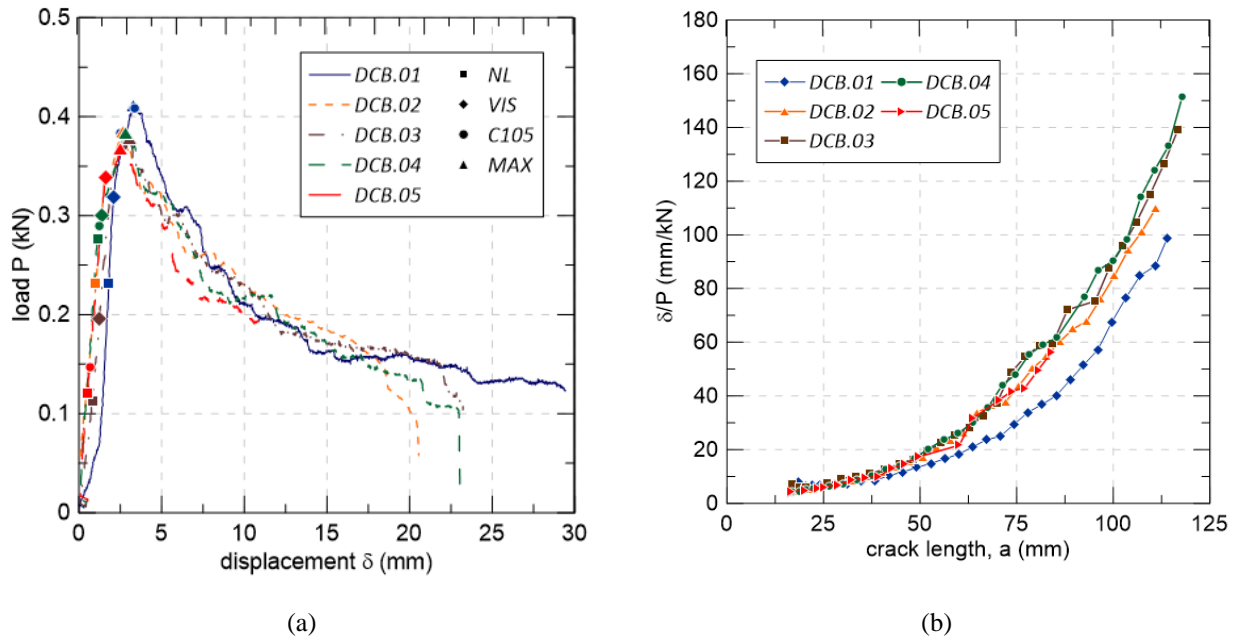


Figure 3.17. Curves obtained experimentally: a) load vs. displacement curves with fracture SERR initiation points; b) compliance vs. crack length curves.

3.4.4. Crack initiation points

The standards define the concept of different crack initiations points (*NL*, *VIS* and *C105*) to be identify in the experimental curves. The *NL* represents the onset of nonlinearity, or in other words, the value for crack initiation (G_{tip}) where a deviation from linearity in the load-displacement curve occurred. On the other hand, *VIS* represents the point in which the delamination growth is visually observed, whereas *C105* is that at which the compliance increased by 5%. The *MAX* point corresponds to the maximum load achieved.

The crack initiation points identified in the DCB experiments are indicated in Figure 3.17a and detailed in Table 3.4. It can be observed that, as expected, the *NL* is the lower bounder for SERR initiation, preceding the *VIS* and *C105* points. The *C105* points occurred before the peak loads points (*MAX*) in all specimens, with exception of DCB.01, where both points were coincident. The *NL* point varied from less than 2% (DCB.02) to 42% (DCB.03) of the value corresponding to the visualization of the crack.

Table 3.4. Values of the load P in kN at the crack initiation points.

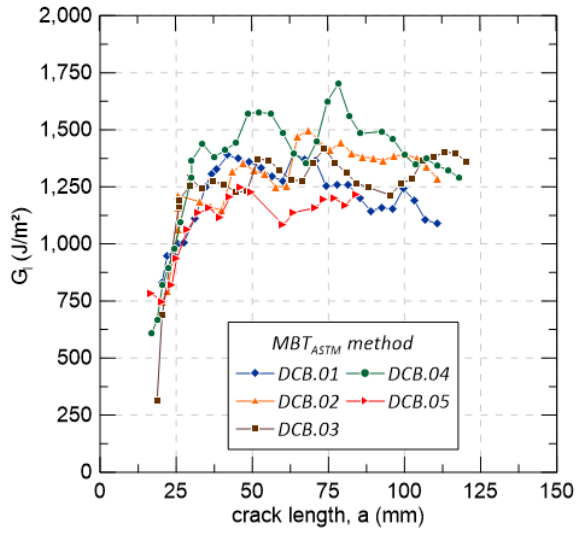
| <i>Load at (kN)</i> | <i>DCB.01</i> | <i>DCB.02</i> | <i>DCB.03</i> | <i>DCB.04</i> | <i>DCB.05</i> |
|---------------------|---------------|---------------|---------------|---------------|---------------|
| <i>NL</i> | 0.232 | 0.334 | 0.113 | 0.284 | 0.335 |
| <i>VIS</i> | 0.319 | 0.338 | 0.196 | 0.300 | 0.338 |
| <i>C105</i> | 0.408 | 0.341 | 0.370 | 0.290 | 0.336 |
| <i>MAX</i> | 0.408 | 0.385 | 0.378 | 0.384 | 0.367 |

3.4.5. R-curves and SERR values for Mode I

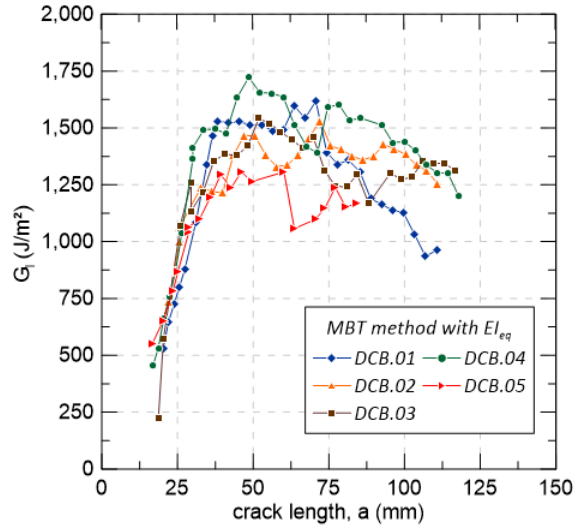
The derived R-curves for the six data reduction methods are shown in Figures 3.18 to 3.20. The obtained fitting constants for all methods are listed in Table 3.5. A comparison between the six methods applied in DCB.02 experiment can be seen through Figure 3.21. The initiation values $G_{I,tip}$ were attributed to *VIS* points and are indicated in Table 3.6, along with the correspondent initial pre-crack length introduced in each specimen. Additionally, Table 3.7 shows the critical SERR for crack propagation, obtained as the average of SERR values at the R-curve plateau.

Table 3.5. Fitting constants for data reduction methods.

| <i>Method</i> | <i>DCB.01</i> | <i>DCB.02</i> | <i>DCB.03</i> | <i>DCB.04</i> | <i>DCB.05</i> |
|---|---|---|---|---|---|
| <i>MBT_{ASTM}</i> <i>MBT-EI_{eq}</i> | $\Delta = 34.5$ | $\Delta = 27.2$ | $\Delta = 27.8$ | $\Delta = 22.8$ | $\Delta = 27.7$ |
| <i>CC_{ASTM}</i> | n = 1.62 | n = 1.88 | n = 1.83 | n = 1.97 | n = 1.78 |
| <i>CC-f</i> <i>MCC-a_{eff}</i> | $\alpha = 0.0010$ $\beta = 0.797$ $\chi = 26.3$ | $\alpha = 0.0035$ $\beta = 0.133$ $\chi = 3.40$ | $\alpha = 0.0035$ $\beta = 0.184$ $\chi = 3.85$ | $\alpha = 0.0037$ $\beta = 0.170$ $\chi = 3.83$ | $\alpha = 0.0035$ $\beta = 0.265$ $\chi = 4.90$ |
| <i>MCC_{ASTM}</i> | $A_1 = 2.09$ | $A_1 = 1.90$ | $A_1 = 1.86$ | $A_1 = 1.80$ | $A_1 = 1.82$ |

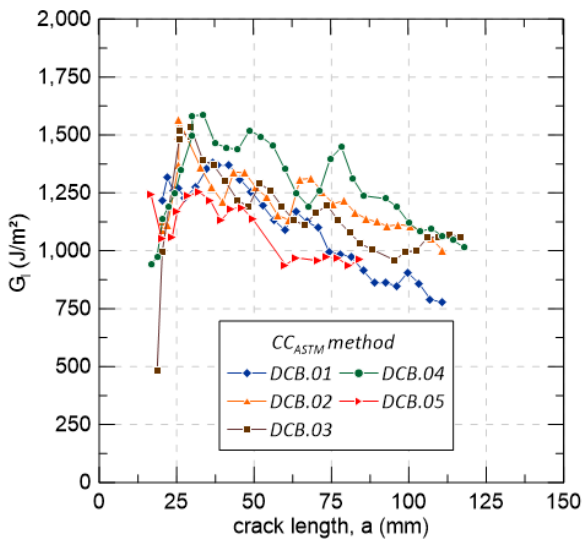


(a)

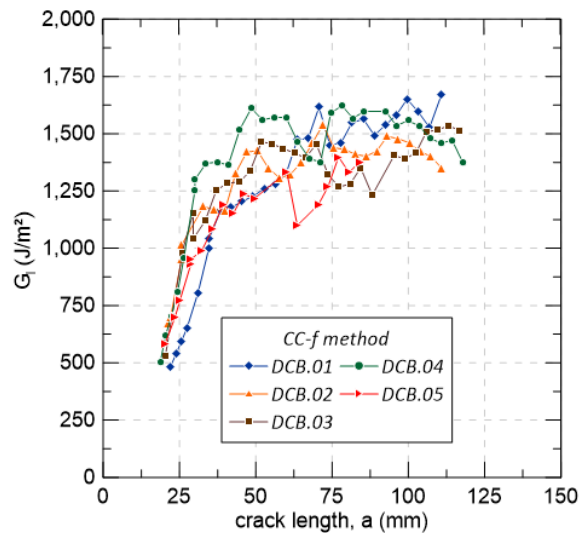


(b)

Figure 3.18. R-curves derived from MBT methods: (a) MBT_{ASTM} ; (b) $MBT-EI_{eq}$



(a)



(b)

Figure 3.19. R-curves derived from CC methods: (a) CC_{ASTM} ; (b) $CC-f$ [27]

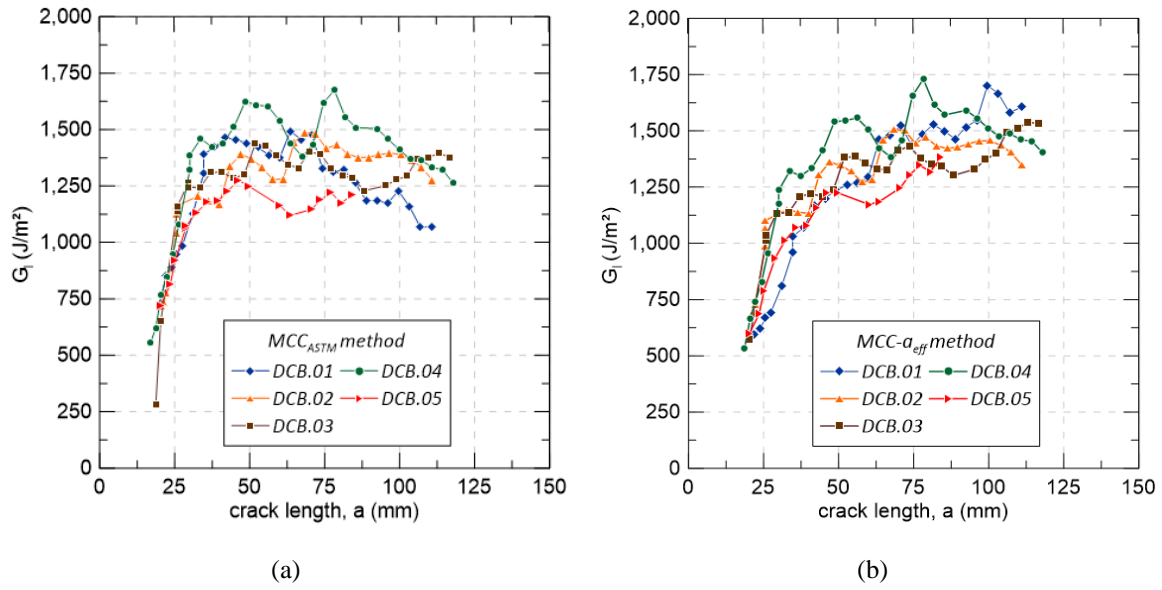


Figure 3.20. R-curves derived from MCC methods: (a) MCC_{ASTM}; (b) MCC- a_{eff}

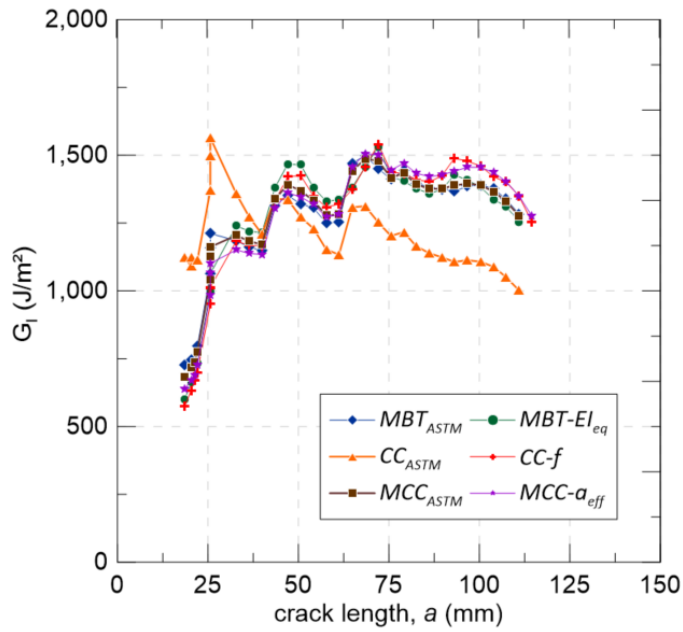


Figure 3.21. Comparison between MBT, CC and MCC method (DCB.02)

Table 3.6. Initiation values for SERR from different methods.

| <i>Specimens</i> | <i>a_l</i> (mm) | <i>SERR for crack initiation G_{l,tip} (J/m²)</i> | | | | | |
|---------------------------|------------------------------|--|----------------------------|--------------------------|----------------------|---------------------------|----------------------------|
| | | MBT_{ASTM} | MBT-EI_{eq} | CC_{ASTM} | CC-f | MCC_{ASTM} | MCC-a_{eff} |
| <i>DCB.01</i> | 3.52 | 832 | 532 | 1,217 | 399 | 732 | 510 |
| <i>DCB.02</i> | 3.57 | 745 | 663 | 1,091 | 633 | 717 | 671 |
| <i>DCB.03</i> | 1.83 | 315 | 223 | 481 | 207 | 283 | 250 |
| <i>DCB.04</i> | 1.88 | 667 | 532 | 975 | 501 | 620 | 535 |
| <i>DCB.05</i> | 1.70 | 747 | 651 | 1,051 | 582 | 719 | 598 |
| <i>average ± sd (cov)</i> | | 661 ± 181 (0.273) | 520 ± 159 (0.306) | 963 ± 254 (0.263) | 465 ± 151 (0.325) | 615 ± 171 (0.278) | 513 ± 143 (0.279) |

Table 3.7. Propagation SERR values from different methods.

| <i>Specimens</i> | <i>Critical SERR for crack propagation G_{l,tot} (J/m²)</i> | | | | | |
|---------------------------|--|----------------------------|--------------------------|----------------------|---------------------------|----------------------------|
| | MBT_{ASTM} | MBT-EI_{eq} | CC_{ASTM} | CC-f | MCC_{ASTM} | MCC-a_{eff} |
| <i>DCB.01</i> | 1,265 | 1,352 | 1,070 | 1,406 | 1,321 | 1,390 |
| <i>DCB.02</i> | 1,336 | 1,355 | 1,211 | 1,365 | 1,344 | 1,359 |
| <i>DCB.03</i> | 1,297 | 1,319 | 1,195 | 1,339 | 1,313 | 1,315 |
| <i>DCB.04</i> | 1,445 | 1,483 | 1,311 | 1,465 | 1,462 | 1,448 |
| <i>DCB.05</i> | 1,158 | 1,178 | 1,086 | 1,184 | 1,174 | 1,173 |
| <i>average ± sd (cov)</i> | 1,300 ± 93 (0.07) | 1,337 ± 97 (0.07) | 1,175 ± 88 (0.08) | 1,352 ± 94 (0.07) | 1,323 ± 92 (0.07) | 1,337 ± 93 (0.07) |

With exception of the CC_{ASTM}, in all methods it is possible to identify a typical curve for specimens experiencing delamination growth with the presence of fiber bridging, in which the energy release rate increase is noticeable up to a maximum level, reaching the steady-state SERR value, characterized by a well-defined plateau that corresponds to the full development of fiber bridging mechanism. As can be seen, five methods (MBT_{ASTM}, MCC_{ASTM}, MBT-EI_{eq}, CC-f and MCC-a_{eff}) presented very similar R-curves. On the other hand, for CC_{ASTM} method, it can be observed by Figure 3.21 a clear downward tendency in SERR values for the specimen DCB.02 at the plateau region. This behavior was observed for all specimens when using the given method. The DCB.01 specimen, for instance, presented a SERR value for crack propagation ($G_{l,tot}$) lower than the one for initiation ($G_{l,tip}$). Although this fact was only observed for the CC_{ASTM} method, it is important to remind that this might be due to the previously mentioned initial

load relief during the experiment. This observed downward tendency might be due to the absence of the parameter Δ , which is present in the MBT_{ASTM} and $MBT-EI_{eq}$ equations – see Equations (3.2) and (3.5) – in order to account for rotations at the delamination front. To illustrate this statement, Figure 3.22 presents the R-curves of DCB.02 specimen for both CC_{ASTM} and MBT_{ASTM} methods, with and without the addition of the parameter Δ . It can be observed in Figure 3.22 that the addition of the parameter Δ has significant influence in the steady state propagation curve shape, correcting the downward tendency in SERR values. However, the inclusion of the parameter in the CC_{ASTM} formulation led to $G_{I,tot}$ values up to 38% lower than all the other data reduction methods, also being 30% lower than the value obtained from the original CC_{ASTM} equation.

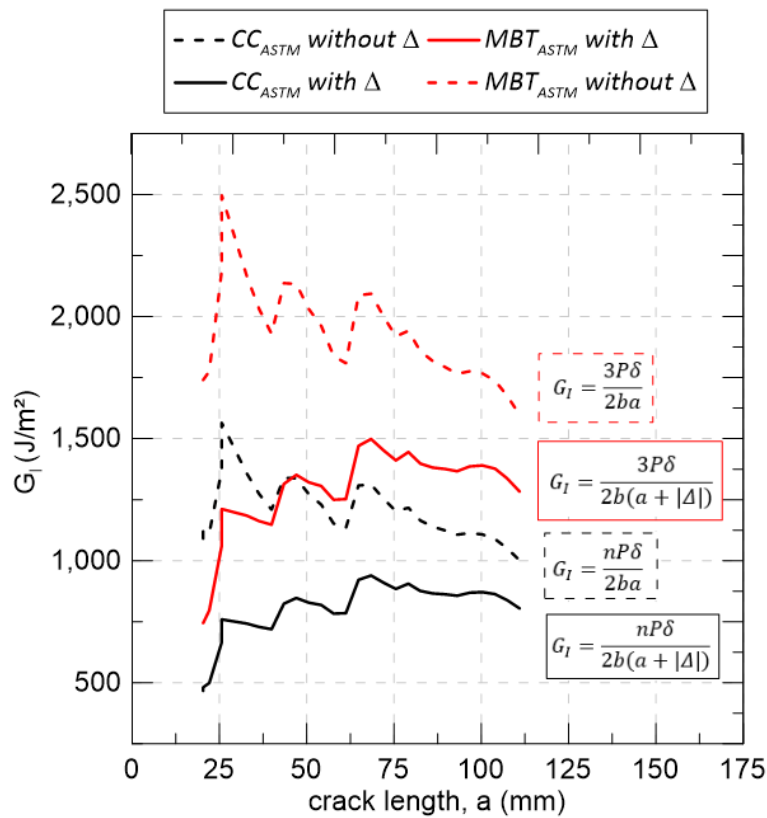


Figure 3.22. R-curves of DCB.02 for CC_{ASTM} and MBT_{ASTM} methods with and without the addition of the parameter Δ .

With respect to the initiation values for all the six methods investigated, it is worth to point out that it was observed a higher scattering when compared to values reported in literature for composite materials produced *in loco*, with a

standardized introduction of an initial delamination length [35]. This may be due to the initial separation method, which introduces delamination with different sharpness for each specimen and preclude the possible damage control around the crack tip. Furthermore, pultruded profiles are known as materials with high incidence of defects, as discussed in Chapter 2, which may significantly affect the crack initiation. In this scenario, it can be highlighted the difference between the SERR initiation values for the DCB.03 and the other specimens. This is explained by the fact that the specimen DCB.03 experienced the crack initiation at very early stages of loading when compared to other specimens, possibly due to small voids located at the crack initiation region.

As previously mentioned, the CC_{ASTM} method resulted on the highest average SERR for crack initiation, representing more than twice the values found by CC-f method. Apart of CC_{ASTM} , the average initiation values of $G_{I,tip}$ obtained for the other five methods presented a maximum difference of 29.6%. On the other hand, the average SERR for crack propagation obtained through the same five methods presented a difference up to 3.8%. In this context, the SERR for crack initiation represented from 34.4 % to 50.8% of the $G_{I,tot}$ for crack propagation. In opposition, for CC_{ASTM} , a ratio of 82% was obtained for initiation and propagation values. The given method has proven to be the most conservative for determining the propagation values for $G_{I,tot}$, with results up to 12% lower than the ones obtained by other methods.

No significant differences were found for propagation SERR obtained through the MBT_{ASTM} and $MBT-EI_{eq}$. Thus, it can be concluded that, the MTB formulation provided in the ASTM standard is suitable enough to determine the critical SERR in experiments where the crack growth led to a slight level of asymmetry in the specimens. However, for crack initiation, the $MBT-EI_{eq}$ method led to SERR values 14.8% lower when compared to the MBT_{ASTM} . Similar conclusions can be drawn regarding the MCC methods using optically measured (MCC_{ASTM}) and effective crack length ($MCC-a_{eff}$). For the steady state SERR propagation, differences up to 1% were observed, whereas for crack initiation values, the $MCC-a_{eff}$ method led to results 16.5% lower than former, presenting very similar values to the ones found by $MBT-EI_{eq}$ method. This divergence is expected due to the difficulty in determining the crack initiation by visual means.

3.4.6. Fiber bridging length

The starting point of the plateau in R-curves, which indicates that the fiber bridging mechanism is fully developed, was used to estimate the bridging length of the composites. The results are shown in Table 3.8, along with their correspondent crack opening displacements (COD). The average value of the opening crack for a fully developed fiber bridging was 0.49 mm and this information is relevant to determine the cohesive law used in FEM models in the next chapter. The DCB.01 presented the largest values of fiber bridging lengths and its behavior might be compared to a large-scale bridging, since the specimen's thickness is close to 16 mm. In opposition, DCB.02 and DCB.03 presented approximately only 7 mm and 9 mm of fiber bridging length, respectively.

Table 3.8. Fiber bridging length and correspondent COD.

| <i>Specimens</i> | <i>Fiber bridging length (mm)</i> | <i>COD (mm)</i> |
|---------------------|-----------------------------------|-----------------|
| <i>DCB.01</i> | 16.2 | 0.42 |
| <i>DCB.02</i> | 7.08 | 0.35 |
| <i>DCB.03</i> | 8.99 | 0.41 |
| <i>DCB.04</i> | 13.2 | 0.62 |
| <i>DCB.05</i> | 12.1 | 0.68 |
| <i>average ± sd</i> | 11.5 ± 3.18 | 0.49 ± 0.12 |
| <i>(cov)</i> | (0.276) | (0.261) |

3.4.7. Comparison with previous works

The SERR results found in this work are of the same order of magnitude as the values for interlaminar failure reported by Ye Zhang *et al.* [19] and Shahverdi *et al.* [18], as shown in Table 3.1. For the crack path adjacent to the mat layer, Ye Zhang *et al.* [19] found SERR for crack initiation and propagation varying, respectively, from 196 to 702 J/m² and from 1,506 to 1,674 J/m². Whereas Shahverdi *et al.* [18] found initiation and propagation values of 360 and 1,102 J/m², respectively. In this work, considering only the five methods that presented more similar results (MBT_{ASTM}, MCC_{ASTM}, MBT-EI_{eq}, CC-f and MCC-a_{eff}), energy release rates ranging from 465 to 661 J/m² were found for crack initiation, whereas for crack propagation, SERR varying from 1,300 to 1,352 J/m² were calculated.

3.5. ELS experimental results

3.5.1. Failure modes

Differently from DCB tests, the interlaminar failure in ELS specimens occurred in different locations: The ELS.01 and ELS.05 presented the delamination between two adjacent fabric layers, whereas the ELS.02 to ELS.04 experienced a crack growth at the interface between fabric and roving layers, as shown in Figure 3.23. The grooves observed on the specimens' lateral sides were generated by the cutting process with the water jet machine and it was not possible to remove them via manual polishing.

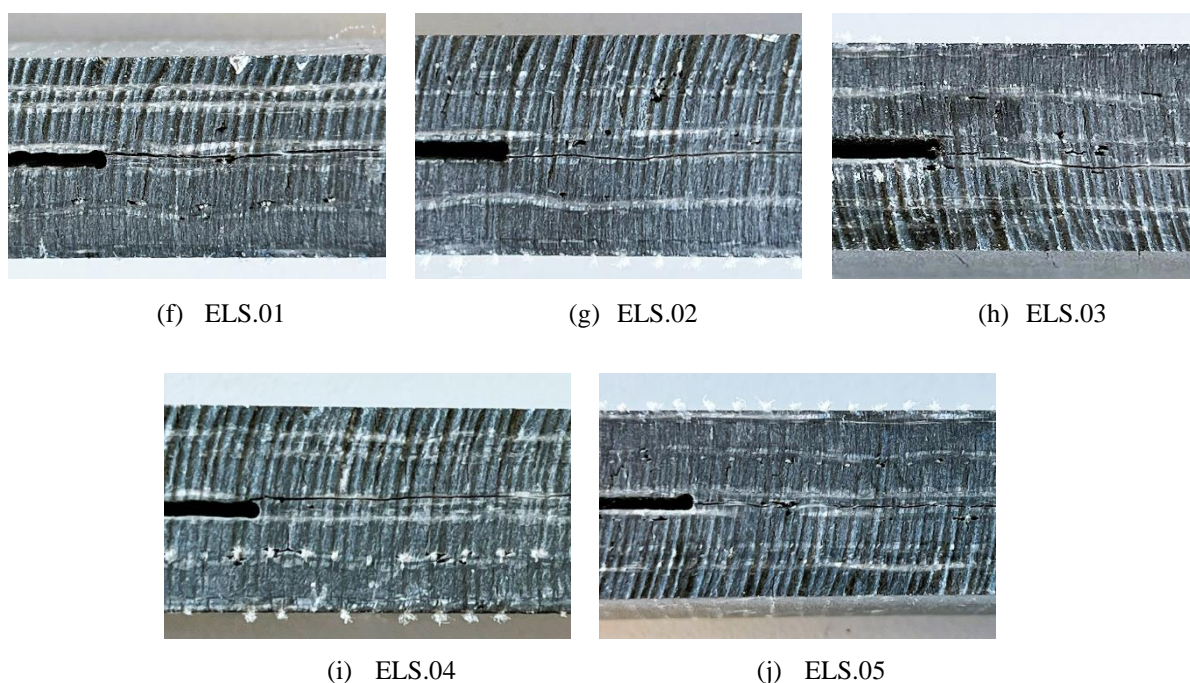


Figure 3.23. Failure mode of ELS specimens: (a) ELS.01; (b) ELS.02; (c) ELS.03; (d) ELS.04; (e) ELS.05.

The crack propagation in Mode II occurred following the interface between layers until reaching an average total crack length of 136 mm. Figure 3.24 shows the typical failure mode presented in all tests. In general, the asymmetry generated in ELS specimens was greater than those observed in DCB tests. For instance, in the specimen ELS.01, it was observed a minimum eccentricity between the crack and the section's centroid of 0.65 mm along all the specimen's length and a

maximum eccentricity of 2 mm. All other specimens presented an eccentricity lower than 1.30 mm.

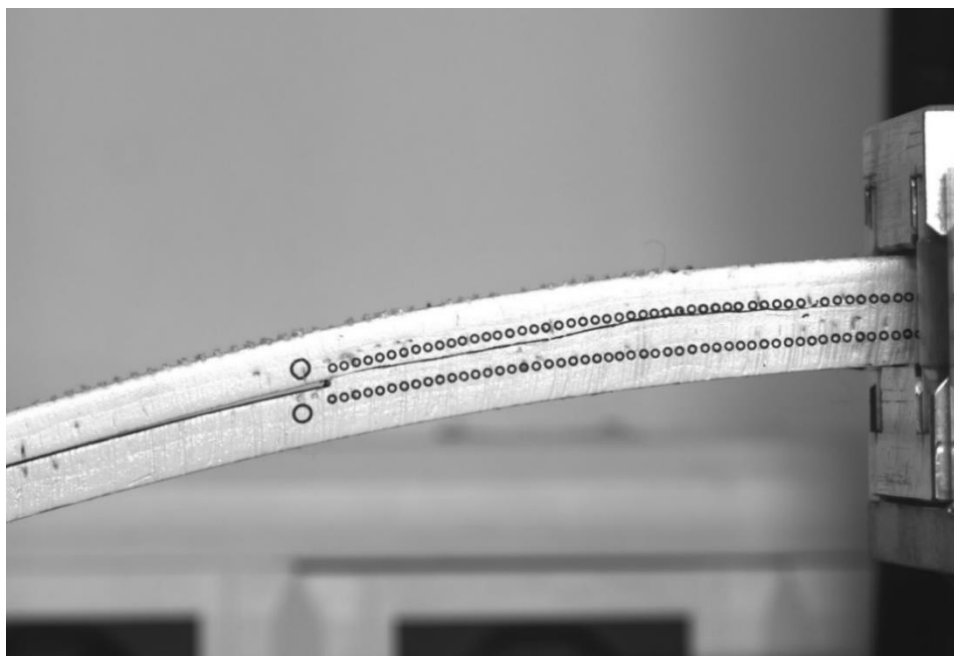


Figure 3.24. Maximum deflection of ELS.01 ($P_{max} = 467.6$ N).

3.5.2. Asymmetry assessment

In order to verify the effect of this asymmetry in the fracture mode, the difference between the distances d_2 and d_1 , indicated in Figure 3.25, should be analyzed, as conducted in [36]. In opening mode, d_1 and d_2 present disproportionate increases between each other along the crack propagation, whereas for pure Mode II, the difference $d_2 - d_1$ should remain constant. Based on this, the Mode I was considered negligible in the ELS tests conducted in this work, as can be observed in Figure 3.25.

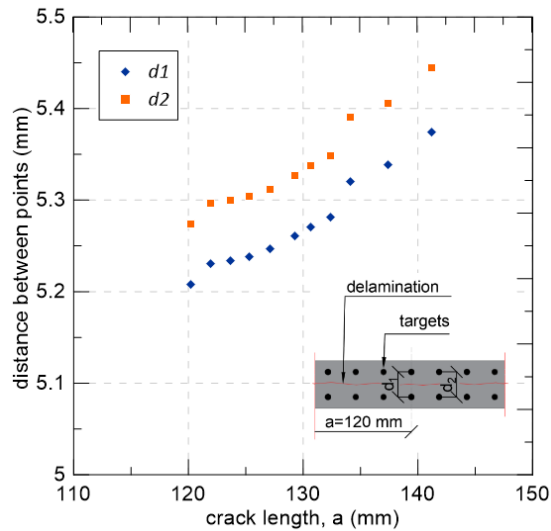


Figure 3.25. Fracture modes assessment for ELS.01: distance between $d1$ and $d2$ vs. crack length.

3.5.3. Load-displacement and compliance responses

In general, all specimens experienced a fast delamination growth after crack initiation, with abrupt and high increases in crack length, among which some can be identified in P vs. δ curves (see Figure 3.26) through sudden drops of the load. All specimens presented similar initial stiffness, with maximum loads varying from 550.3 N (ELS.04) to 603.02 N (ELS.02). The ELS.02 presented the greatest peak load, above the average of the other four specimens, and the latest crack initiation. This might have been caused by a pre-crack misidentification, even with the aid of the video-extensometer, occurred during the pre-cracking procedure. All specimens presented a similar compliance curve, shown in Figure 3.26b, with an increase of δ/P as the crack propagates.

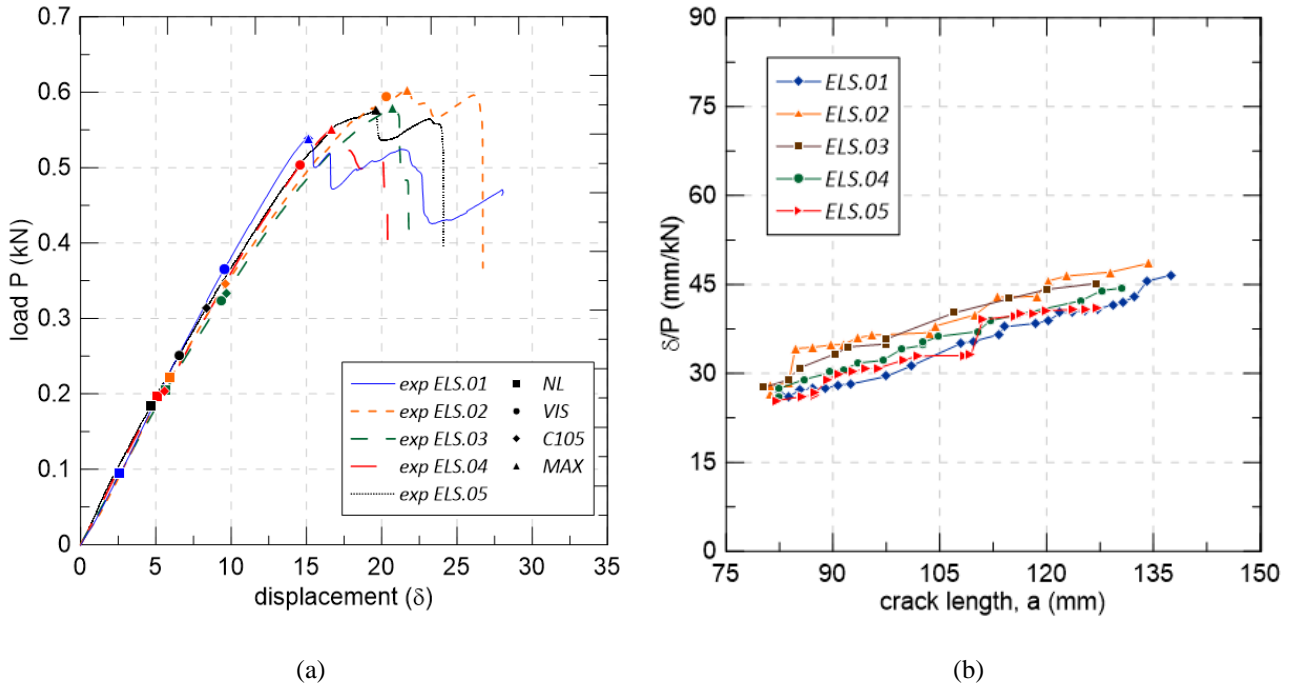


Figure 3.26. (a) load vs displacement curves of ELS specimens with fracture SERR initiation points; (b) compliance vs. crack length curves.

3.5.4. Crack initiation points

The *NL*, *VIS* and *C105* and *MAX* points are indicated in Figure 3.26a and detailed in Table 3.9. According to recommendations of the standard ISO 15114, the crack initiation point is defined as the lowest value between the *C105* point – which as previously mentioned indicates a 5% of increase in the initial compliance – and the maximum load point (*MAX*).

Table 3.9. Values of the load P at the crack initiation points.

| <i>Load at (kN)</i> | <i>ELS.01</i> | <i>ELS.02</i> | <i>ELS.03</i> | <i>ELS.04</i> | <i>ELS.05</i> |
|---------------------|---------------|---------------|---------------|---------------|---------------|
| <i>NL</i> | 0.094 | 0.222 | 0.204 | 0.196 | 0.183 |
| <i>VIS</i> | 0.366 | 0.594 | 0.323 | 0.503 | 0.250 |
| <i>C105</i> | 0.539 | 0.345 | 0.334 | 0.204 | 0.314 |
| <i>MAX</i> | 0.539 | 0.603 | 0.578 | 0.550 | 0.570 |

It can be noticed that the crack initiation point was significantly higher for the specimen ELS.01, when compared to the others. In this case, the increase of 5%

in initial compliance was reached after the peak load, and therefore the *C105* point is equal to the *MAX* one. This occurred since the ELS.01 was the only specimen to experience a slightly softening in the compliance curve between the loss of linearity and the visualization of the crack, as shown in Figure 3.27, suggesting a prevalence of stiffening mechanisms during this short period of time, which delayed the crack initiation and the consequent increase in compliance. The transition point (TP) indicates the minimum of the compliance curve and represents a change in the fracture process at the load $P=238$ N, where the crack propagation starts to play a dominant role over the driving forces acting at the crack tip.

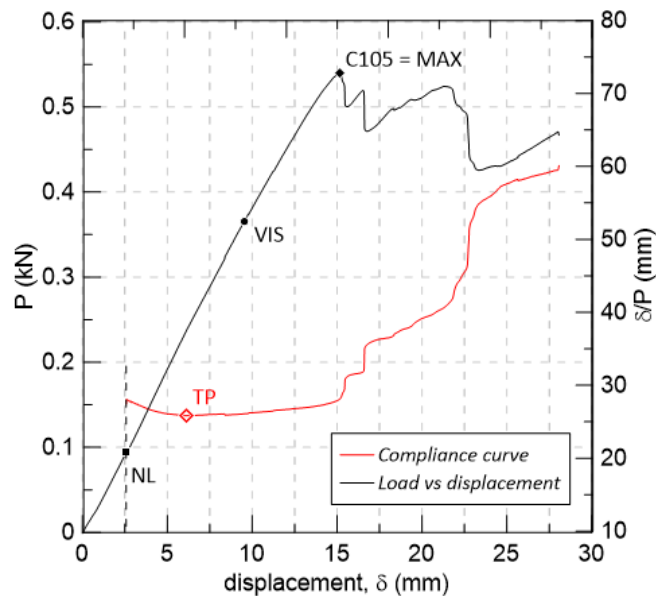


Figure 3.27. Decrease in compliance in the ELS.01 specimen.

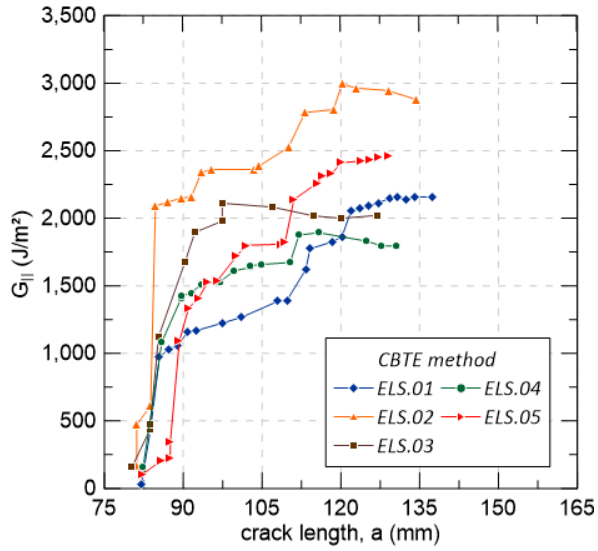
3.5.5. R-curves and SERR values for Mode II

The SERR values for Mode II were obtained from EMC, SBT and CBTE methods with the application of formulae described in Section 3.2.2. The flexural modulus EI and the parameter Δ_{clamp} – both used to determine the fracture toughness through SBT and CBTE methods –, were obtained by the calibration tests, being equal to 22.2 GPa and 57, respectively. The generated R-curves for each method are shown in Figure 3.28. Tables 3.10 and 3.11 presents the $G_{II,tip}$ and $G_{II,tot}$ values in detail, along with the pre-crack lengths achieved in each test. It is possible to observe that, with exception of ELS.03 and ELS.04, all specimens experienced an

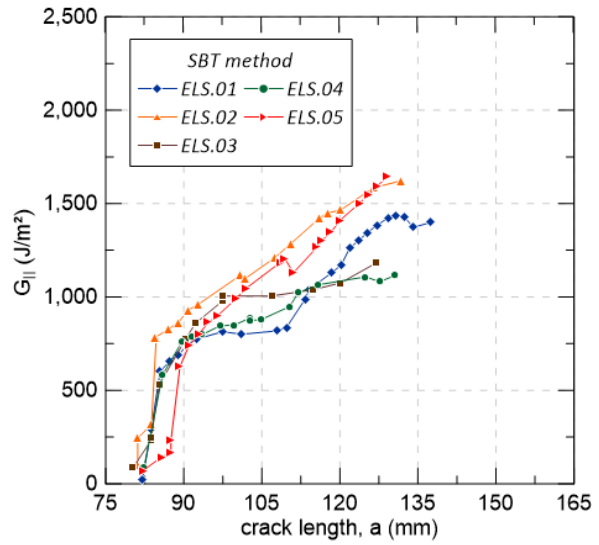
increase of $G_{II,tot}$ until the end, without a well-defined plateau. This indicates a possible fiber bridging not yet fully developed, which is difficult to confirm visually during the test due the mode of loading.

This increase in SERR and the lack of a plateau is even more evident for SBT and EMC methods. The latter reached, in general, intermediary average SERR values for both crack initiation and propagation, presenting results very close to the ones provided by CBTE method, with differences lower than 1% and 8% for crack propagation and initiation, respectively. In opposition, the SBT has proven to be the most conservative method, as shown in Figure 3.28, with differences up to 45% when compared to the other methods, both for crack initiation and propagation. This result agrees well with literature that highlights the deficiency of the concerned method. The high values found for $G_{II,tip}$ of ELS.01 specimen, in all methods, was caused by the misidentification in the respective crack initiation previously explained, which generated a great coefficient of variation (CoV) between the results.

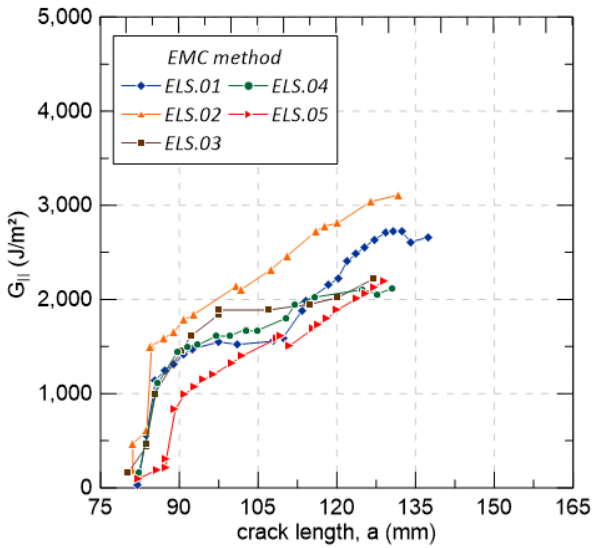
It can also be observed a certain similarity between the SERR obtained for different crack paths. For instance, differences of 26.5% and 12.5% were found between the initiation and propagation SERR values, respectively, of the ELS.01 specimen, which experienced the delamination between roving and fabric layers, and the specimen ELS.05, which experienced the crack between two fabric layers.



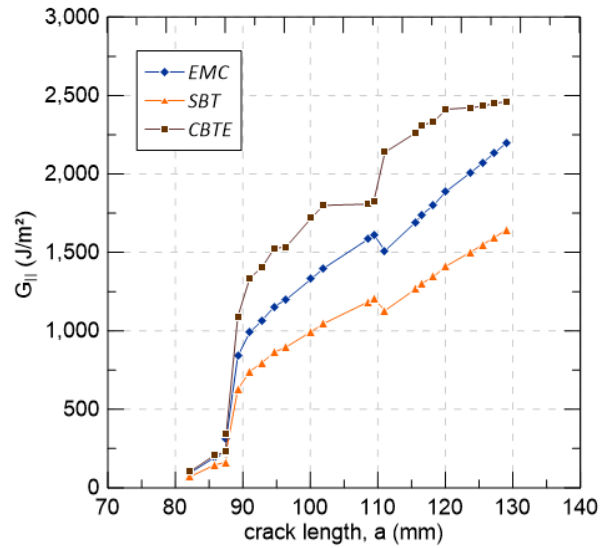
(a)



(b)



(c)



(d)

Figure 3.28 - R-curve obtained from different methods: (a) CBTE method; (b) SBT method; (c) EMC method; (d) comparison between the three methods (ELS.05).

Table 3.10. Initiation values for SERR from different methods.

| Specimens | a_1 (mm) | SERR for crack initiation $G_{II,tip}$ (J/m ²) | | |
|------------------|------------|--|-----------|-----------|
| | | CBTE | SBT | EMC |
| ELS.01 | 3.53 | 1,158 | 748 | 1,423 |
| ELS.02 | 2.64 | 474.2 | 244 | 467 |
| ELS.03 | 1.71 | 470.9 | 247 | 464 |
| ELS.04 | 3.85 | 155.7 | 88.3 | 168 |
| ELS.05 | 3.64 | 346.2 | 234 | 313 |
| average ± | | 522 ± 340 | 312 ± 226 | 568 ± 442 |
| sd (cov) | | (0.652) | (0.723) | (0.778) |

Table 3.11. Propagation SERR values from different methods.

| Specimens | Critical SERR for crack propagation $G_{II,tot}$ (J/m ²) | | |
|---------------------|---|-------------|-------------|
| | CBTE | SBT | EMC |
| ELS.01 | 2,121 | 1,373 | 2,638 |
| ELS.02 | 2,417 | 1,107 | 2,023 |
| ELS.03 | 2,016 | 1,020 | 2,014 |
| ELS.04 | 1,690 | 0,961 | 1,779 |
| ELS.05 | 2,305 | 1,395 | 1,866 |
| average ± sd | 2,124 ± 291 | 1,177 ± 184 | 2,104 ± 307 |
| (cov) | (0.137) | (0.156) | (0.146) |

3.5.6. Comparison with previous works

The results obtained in this work were compared with the ones reported in Zhang *et al.* [19] and Shahverdi *et al.* [18]. The former found G_{II} values varying from 904 to 1,337 J/m² and from 1,772 to 2,293 J/m² for crack initiation and propagation, respectively. On the other hand, Shahverdi *et al.* [18] reported SERR of 1,156 and 2,670 J/m² for crack initiation and propagation between the epoxy adhesive and the mat layer. Differences for $G_{II,tot}$ values equal to 7.7% and 20.8% were found between this work and the previous authors' research. In opposition, a great difference was found between the results reported in literature and the ones calculates in this work by SBT method. The SBT is referred in literature as a method that underestimate the SERR values, however, this effect was apparently

accentuated in the ELS tests conducted in this research, resulting in values 46% lower than those reported in previous works. Differences up to 68% were also observed for SERR required for crack initiation, when comparing to the previous researches. This high variability might be expected due to the high incidence of defects in pultruded materials.

Zhang *et al.* [19] observed that CBTE might lead to less accurate results for crack initiation and stated that the values provided by the ECM method agreed well with FEM analyses. In the present research, the CBTE presented very similar results when compared to ECM method, with 8% of difference between $G_{II,tip}$ values obtained by each method.

3.6. Comparison between G_I and G_{II}

Previous works have stated that, regardless the material or method of calculation, the critical fracture energy for Mode II is always higher than the one related to Mode I [19,25]. Nevertheless, in this research, average lower values of $G_{II,tot}$ were found through SBT approach when compared to almost all the methods used to calculate the critical SERR for Mode I, with differences up to 11.9%. On the other hand, CBTE and EMC methods, which presented very similar outcomes, resulted in greater $G_{II,tot}$ values than those obtained for Mode I, in agreement with the literature, with a ratio of $G_{II,tot}/G_{I,tot}$ ranging from 1.57 to 1.63. In literature, this ratio is approximately 1.2 for crack propagation and varies from 2 to 3 for crack initiation [37]. However, in this work, disregarding the results provided by CC_{ASTM} and SBT methods, which presented discrepant results when compared to the other methods, the ratio found for crack initiation ranged from 0.78 to 1.12.

3.7. Conclusions

This work aims to bring clarity about the application of standardized methods for the determination of Mode I and Mode II interlaminar fracture parameters in pultruded specimens where it is not applicable to insert a thin pre-

crack during fabrication. Experimental and numerical investigations are conducted on DCB and ELS specimens having the initial separation of 1-mm of thickness introduced via a water jet machine. The video-extensometer technique was used to conduct an accurate crack length measurement, especially in Mode II.

The following conclusions can be drawn:

- The DCB specimens presented R-curves with an increase of SERR before reaching a plateau, indicating the presence of fiber bridging, which was also observed in the experiments. On the other hand, ELS specimens did not present a clear and well-defined plateau, experiencing, in general, a SERR increase until the final crack length was reached.
- Among the six methods (three standardized and three non-standardized) assessed to determine G_{Ic} , the CC_{ASTM} was the only one that presented a non-typical R-curve behavior with a clear downward tendency in the plateau region. This response could possibly be caused by the absence of the parameter Δ in the formulation. However, the inclusion of the parameter in the CC_{ASTM} formulation led to SERR values for crack propagation ($G_{I,tot}$) up to 38% lower than all the other data reduction methods.
- The other five methods (MBT_{ASTM} , MCC_{ASTM} , $MBT-EI_{eq}$, $CC-f$ and $MCC-a_{eff}$) used for Mode I presented very similar results in terms of SERR for crack propagation, with differences lower than 3.8% between each other. The results showed that for the specimens analyzed in this work, *i.e.*, in which the crack growth led to a slight level of asymmetry, it would not be necessary to consider improved methods (for instance, $MBT-EI_{eq}$ or $MCC-a_{eff}$) than the ones recommended by the ASTM standard, especially for the crack propagation SERR evaluation.
- For Mode II, the SBT method presented G_{IIC} results below the expected, being even lower than the values found for Mode I. On the other hand, CBTE and EMC methods provided very similar SERR values, both for crack initiation and propagation, with differences lower than 8% and 1%, respectively, between each other.

- For both Modes, a higher scattering was observed for crack initiation SERR values. This might be associated to the pre-crack method and the well-known high incidence of defects in pultruded profiles, precluding a damage control around the crack tip, which may have influence at the crack initiation.
- The ratio of G_{IIc}/G_{Ic} ranged between 1.57 and 1.63 for crack propagation and varied from 0.78 to 1.12 for crack initiation. The latter is different from the average presented in literature, since in this work both Modes presented similar SERR for crack initiation.

All these results will be compared with numerical models in the next Chapter.

3.8. References

- [1] HOLLAWAY, L. C. A review of the present and future utilisation of FRP composites in the civil infrastructure with reference to their important in-service properties. **Construction and Building Materials**, v. 24, n. 12, p. 2419–2445, 2010.
- [2] YANES-ARMAS, S.; CASTRO, J. DE; KELLER, T. System transverse in-plane shear stiffness of pultruded GFRP bridge decks. **Engineering Structures**, v. 107, p. 34–46, 2016.
- [3] LEE, J. et al. Experimental characterization of a pultruded GFRP bridge deck for light-weight vehicles. **Composite Structures**, v. 80, n. 1, p. 141–151, 2007.
- [4] TURON, A. et al. Accurate simulation of delamination growth under mixed-mode loading using cohesive elements : Definition of interlaminar strengths and elastic stiffness. **Composite Structures**, v. 92, n. 8, p. 1857–1864, 2010.
- [5] M. JANSSEN, J. ZUIDEMA, AND R. J. H. W. **Fracture Mechanics**. 2nd. ed. [s.l.] Delft University Press, 2002.
- [6] BAZANT, Z. P.; CEDOLIN, L.; HUTCHINSON, J. W. **Stability of Structures: Elastic, Inelastic, Fracture, and Damage Theories**. [s.l.: s.n.]. v. 60
- [7] ORIFICI, A.C., THOMSON, R.S., DEGENHARDT, R., BISAGNI, C., BAYANDOR, J. Development of a finite-element analysis methodology for the propagation of delaminations in composite structures. **Mechanics of Composite**

Materials, v. 43, n. 1, p. 9–28, 2007.

[8] T.L.ANDERSON. **Fracture Mechanics. Fundamentals and Applications**.

[s.l.] CRC Press, 2005.

[9] TURON, A. et al. A damage model for the simulation of delamination in advanced composites under variable-mode loading. **Mechanics of Materials**, v. 38, n. 11, p. 1072–1089, 2006.

[10] HEIDARI-RARANI, M.; SHOKRIEH, M. M.; CAMANHO, P. P. Finite element modeling of mode I delamination growth in laminated DCB specimens with R-curve effects. **Composites Part B: Engineering**, v. 45, n. 1, p. 897–903, 2013.

[11] ALMEIDA-FERNANDES, L. et al. Compressive transverse fracture behaviour of pultruded GFRP materials: Experimental study and numerical calibration. **Composite Structures**, v. 247, n. February, 2020.

[12] ALMEIDA-FERNANDES, L.; CORREIA, J. R.; SILVESTRE, N. Transverse Fracture Behavior of Pultruded GFRP Materials in Tension: Effect of Fiber Layup. **Journal of Composites for Construction**, v. 24, n. 4, p. 1–17, 2020.

[13] ALMEIDA-FERNANDES, L.; SILVESTRE, N.; CORREIA, J. R. Fracture toughness-based models for web-crippling of pultruded GFRP profiles. **Composites Part B: Engineering**, v. 230, n. September 2020, 2022.

[14] EL-HAJJAR, R.; HAJ-ALI, R. Mode-I fracture toughness testing of thick section FRP composites using the ESE(T) specimen. **Engineering Fracture Mechanics**, v. 72, n. 4, p. 631–643, 2005.

[15] HAJ-ALI, R.; EL-HAJJAR, R. Crack propagation analysis of mode-I fracture in pultruded composites using micromechanical constitutive models. **Mechanics of Materials**, v. 35, n. 9, p. 885–902, 2003.

[16] LIU, W.; FENG, P.; HUANG, J. Bilinear softening model and double K fracture criterion for quasi-brittle fracture of pultruded FRP composites. **Composite Structures**, v. 160, p. 1119–1125, 2017.

[17] BURDA, I.; BRUNNER, A. J.; BARBEZAT, M. Mode I fracture testing of pultruded glass fiber reinforced epoxy rods: Test development and influence of precracking method and manufacturing. **Engineering Fracture Mechanics**, v. 149, p. 287–297, 2015.

[18] SHAHVERDI, M.; VASSILOPOULOS, A. P.; KELLER, T. Mixed-mode

- quasi-static failure criteria for adhesively-bonded pultruded GFRP joints. **Composites Part A: Applied Science and Manufacturing**, v. 59, p. 45–56, 2014.
- [19] ZHANG, Y.; VASSILOPOULOS, A. P.; KELLER, T. Mode I and II fracture behavior of adhesively-bonded pultruded composite joints. **Engineering Fracture Mechanics**, v. 77, n. 1, p. 128–143, 2010.
- [20] SHAHVERDI, M.; VASSILOPOULOS, A. P.; KELLER, T. A phenomenological analysis of Mode I fracture of adhesively-bonded pultruded GFRP joints. **Engineering Fracture Mechanics**, v. 78, n. 10, p. 2161–2173, 2011.
- [21] SHAHVERDI, M.; VASSILOPOULOS, A. P.; KELLER, T. Modeling effects of asymmetry and fiber bridging on Mode I fracture behavior of bonded pultruded composite joints. **Engineering Fracture Mechanics**, v. 99, p. 335–348, 2013.
- [22] ALMEIDA-FERNANDES, L. et al. Fracture toughness-based models for damage simulation of pultruded GFRP materials. **Composites Part B: Engineering**, v. 186, n. November 2019, 2020.
- [23] BAZANT, Z. P., & CEDOLIN, L. **Stability of structures: elastic, inelastic, fracture and damage theories**. Sigapore: World Scientific, 2010.
- [24] RAHEEM, Z. **Standard Test Method for Mode I Interlaminar Fracture Toughness of Unidirectional Fiber-Reinforced Polymer Matrix Composites 1**. **Standard Test Method for Mode I Interlaminar Fracture Toughness of Unidirectional Fiber-Reinforced Polymer Matrix Composites 1**. [s.l: s.n.].
- [25] HASHEMI S, KINLOCH AJ, W. J. The analysis of interlaminar fracture in uniaxial fibre-polymer composites. **Proceedings of the Royal Society of London. A. Mathematical and Physical Sciences**, v. 427, n. 1872, p. 173–199, 1990.
- [26] MOLLÓN, V. et al. Mixed mode fracture toughness: An empirical formulation for GI/GII determination in asymmetric DCB specimens. **Engineering Structures**, v. 32, n. 11, p. 3699–3703, 2010.
- [27] DÁVILA, C. G.; ROSE, C. A.; CAMANHO, P. P. A procedure for superposing linear cohesive laws to represent multiple damage mechanisms in the fracture of composites. **International Journal of Fracture**, v. 158, n. 2, p. 211–223, 2009.
- [28] LAFFAN, M. J. et al. Measurement of the in situ ply fracture toughness associated with mode I fibre tensile failure in FRP. Part I: Data reduction. **Composites Science and Technology**, v. 70, n. 4, p. 606–613, 2010.

- [29] ALMEIDA-FERNANDES, L.; SILVESTRE, N.; CORREIA, J. R. Characterization of transverse fracture properties of pultruded GFRP material in tension. **Composites Part B: Engineering**, v. 175, n. April, 2019.
- [30] BERGAN, A. et al. **A Mode I cohesive law characterization procedure for through-the-thickness crack propagation in composite laminates** **Composites Part B: Engineering**, 2016.
- [31] **ISO 15114-2014 Fibre-reinforced plastic composites - Determination of the mode II fracture resistance for unidirectionally reinforced materials.pdf.** , [s.d.].
- [32] DARPA. **Final Technical Report. Advanced composites for bridge infrastructure renewal – Phase II, Task 16 – Modular composite bridge.** [s.l: s.n.].
- [33] **ISO (International Organization for Standardization). ISO 1172: Textile-glass reinforced plastics – Prepregs, moulding compounds and laminates – Determination of the textile-glass and mineral-filler content – Calcination methods.** . Geneva, Switzerland: [s.n.].
- [34] CINTRA, G. G. **Local Buckling Behavior of Pultruded Glass-Fiber Reinforced Polymer (pGFRP) I-Section Columns.** 2017. 2017.
- [35] CAMESELLE-MOLARES, A. et al. Numerical simulation of two-dimensional in-plane crack propagation in FRP laminates. **Composite Structures**, v. 200, n. April, p. 396–407, 2018.
- [36] ZHANG, Y.; VASSILOPOULOS, A. P.; KELLER, T. Stiffness degradation and fatigue life prediction of adhesively-bonded joints for fiber-reinforced polymer composites. **International Journal of Fatigue**, v. 30, n. 10–11, p. 1813–1820, 2008.
- [37] TURVEY, G. J.; ZHANG, Y. Tearing failure of web-flange junctions in pultruded GRP profiles. **Composites Part A: Applied Science and Manufacturing**, v. 36, n. 2 SPEC. ISS., p. 309–317, 2005.

4. Mode I and Mode II Fracture Behavior in Pultruded Glass Fiber-Polymers Bridge Decks – Numerical Investigation

4.1. Introduction

In order to obtain the fracture toughness parameter, several numerical approaches have been used to decrease the time-consuming experiments and to simulate the progressive damage behavior in composites. For interlaminar failure in quasi-static analysis, virtual crack closure technique (VCCT) and the cohesive zone modelling (CZM) are usual approaches and both methods require the fracture toughness G_c as input for the assessed mode loading [1]. The former is one of the most popular methods employed to calculate the fracture components at the crack tip [2]. It requires the presence of an initial crack to be applicable and is used typically for brittle crack growth [3]. The method has bases in Linear Elastic Fracture Mechanics (LEFM) and assumes that the energy required for crack propagation is equal to the one needed to close two separated crack surfaces [4]. Although being an effective method, the VCCT requires complex moving mesh techniques for crack propagation [5,6]. In parallel, the CZM also has been extensively used in order to model fracture process zones (FPZ) in quasi-brittle materials. The method overcomes some obstacles presented by VCCT, especially when it is required to take into account the nonlinear zone ahead of the crack tip [3]. Moreover, it can predict efficiently both the composite progressive failure, fiber bridging in particular, and crack initiation [4]. Nevertheless, it is important to point out that the use of cohesive elements for simulating progressive delamination requires refined meshes and, very commonly, may present convergence issues [6].

The CZM simulates the damage according to cohesive laws and the determination of its respective parameters still constitutes a challenge for an accurate numerical analysis, especially when it comes to Mode II. The high variability inherent to pultruded glass fiber-polymer properties, added to the R-

curve dependence of specimens' geometry in particular cases, increase the complexity in performing reliable simulations [7–9]. To accomplish this task, fitting procedures are often used to calibrate the fracture parameters based on the experimental curves. Two-part cohesive laws (for instance, bilinear or linear-exponential) are commonly adopted in literature. However, to account for fiber bridging mechanisms, some authors [10–12] have proven the efficiency of the use of a three-part cohesive law (bilinear-exponential), describing a non-linear behavior for tractions generated due to fiber bridging. Regardless of the material, several works mention the influence of the cohesive laws shape on the progressive failure behavior [4,13–15]. Furthermore, this influence tends to increase with the relative size of the fracture process zone compared to the specimens' dimensions [16].

Despite the several studies addressing CZM for fiber-polymer materials, very few studies are focused on the interlaminar fracture behavior characterization of pultruded fiber-polymers. Almeida-Fernandes *et al.* [17] recently implemented a numerical model by using fitting procedures to simulate Compact Tension (CT) and Wide Compact Tension (WCT) experiments. The authors used the Hashin criterion to stipulate the intralaminar damage initiation and two types of cohesive laws (bilinear and linear-exponential) to describe the damage evolution of pultruded glass fiber-polymer specimens. Despite its good agreement with experimental results, the numerical methodology adopted is considered valid for simplified cases as the one studied. The authors found a better convergence in terms of average ultimate loads by using the bilinear cohesive law, whereas the exponential softening law presented the best fit for the crack growth, indicating the need for further research. In another study, Almeida-Fernandes *et al.* [18] used a bilinear cohesive law to obtain numerically the transverse intralaminar compressive fracture toughness of pultruded glass fiber-polymer Compact Compression (CC) specimens. Shahverdi *et al.* [2] also fitted the experimental Double Cantilever Beam (DCB) and End-Loaded-Split (ELS) data to developed mixed-mode failure criteria for adhesively-bonded pultruded glass fiber-polymer joints. The authors applied the VCCT to calculate the interlaminar fracture components at the crack tip and employed an exponential cohesive law to quantify the effects of the fiber bridging. Ye Zhang *et al.* [19] also simulated DCB and ELS experiments via 3D finite element models. On the other hand, Liu *et al.* [20] adopted a bilinear model and a

double fracture toughness K criterion (used to obtain the fracture parameters of wood). In this case, K means the stress intensity factor and the word “double” refers to two stages of crack development: initial cracking and failure. The double K , correspond, thus, to the initial cracking fracture toughness and the failure fracture toughness. The criterion was used to analyze the intralaminar Mode I crack propagation along the fiber direction of pultruded fiber-polymer specimens. In this study, the fiber bridging mechanism was found to be 40% of the total fracture energy.

In order to use CZM technique, it is required to estimate fracture mechanic parameters, which may be an exhausting procedure depending on the adopt cohesive law shape and, consequently, the number of variables. Therefore, it is important to expand the available database for these composites in order to facilitate the evolution of future investigations. Furthermore, in order to avoid time-consuming in the fitting procedures, it is very useful to understand how each specific parameter of the cohesive three-part traction separation law (interfacial strength, maximum fiber bridge traction, SERR due to crack initiation and propagation) influence on the composite’s behavior and the respective load *vs.* displacement curves.

In this scenario, this work aims to study the interlaminar fracture in pultruded glass fiber-polymer composite, evaluating the use of cohesive laws with different shapes to numerically simulate DCB and ELS tests described in the previous Chapter. The onset delamination and progressive failure of the specimens were predicted through 2D non-linear finite element models, where CZM is used. Three different shapes for traction-separation laws (bilinear, trilinear and bilinear-exponential) were implemented via a VUMAT subroutine in Abaqus 2021 [21]. The results were discussed to determine the one that best expresses the experimental data presented in the previous chapter. Further, a second objective of this research is to assess how different parameters of a three-part cohesive law affect pultruded glass fiber-polymers progressive failure and their load *vs.* displacement curves, facilitating future fitting procedures in numerical analyses. A parametric study is conducted to evaluate the influence of four different parameters of cohesive laws in the presence of fiber bridging, namely the interlaminar strength σ_c ; the fiber

bridging traction σ_{max} ; the energy required for crack initiation G_{tip} ; and the energy dissipated due to fiber bridging G_{br} .

4.2. CZM - theoretical background

4.2.1. Traction separation laws

The cohesive zone model (CZM) is a very powerful tool to predict the onset and progressive failure of composite materials. The cohesive element behavior is defined by a traction-separation law that correlates the surface tractions, σ , with the crack opening displacements (COD), along the FPZ of an interfacial crack. A typical example of a two-part traction separation law used in quasi-brittle materials is given in Figure 4.1. The crack initiates when the stress at the crack tip reaches the interface through-thickness strength (σ_c), corresponding to a COD δ_c . As the COD increases, the cohesive tractions decrease, until vanishing when the final COD δ_f is reached. The area under the cohesive law corresponds to the fracture toughness G_c . In other words, the cohesive zone model is, thus, characterized by the bulk material properties, the *damage initiation condition*, and the *crack evolution function* – which describes the crack tractions behavior, σ , between the interval from the COD of crack initiation δ_c to the final opening displacement δ_f .

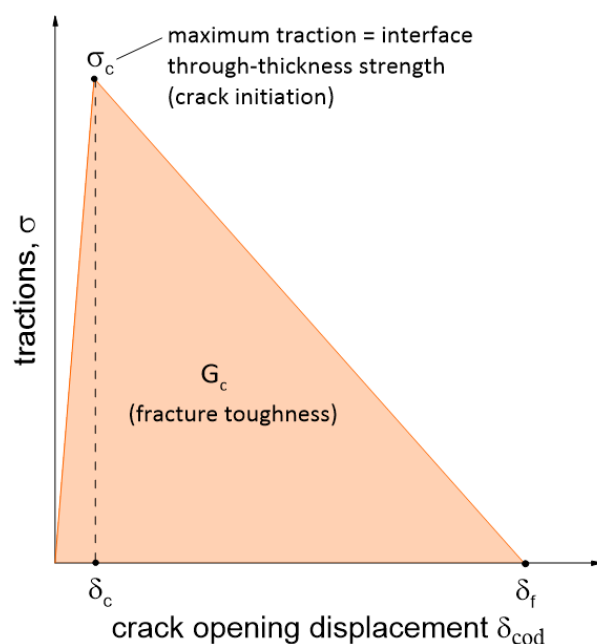


Figure 4.1. Typical traction separation law with linear softening.

As previously mentioned, a wide variety of studies have shown that the traction-separation law shape is determinant when simulating progressive damage for different materials. Different shapes, such as triangular, trapezoidal, and cubic forms, among others have been proposed in literature. One of the most adopted cohesive laws for composite materials is the bilinear one illustrated in Figure 4.1, due to its effectiveness and simplicity. However, in the existence of stiffening mechanisms such as fiber bridging, research available in literature [11,12,22] has shown that the energy dissipated may be divided in two main processes, as presented by the three-part cohesive law in Figure 4.2: 1. *the energy required to initiate the damage growth at the crack tip, G_{tip}* , illustrated in orange; and 2. *energy dissipated due to fiber bridging, G_{br}* , represented in green. The total and critical SERR (G_c), in this case, corresponds to the total area under the cohesive law curve ($G_{tot} = G_{tip} + G_{br}$). In this cohesive law shape, two parameters are added: the maximum bridging tractions $\sigma_{m\acute{a}x}$ and the corresponding COD δ_I .

It is worth pointing out that fiber bridging is one of the most effective toughening mechanisms that increases the energy dissipated level during the fracture process of the material. It can be classified as an extrinsic mechanism for occurring behind the crack tip. On the other hand, there are intrinsic damage mechanisms, such as microcracking or microvoid formation, that act ahead the crack tip. In other words, "*fracture is the result of a mutual competition of intrinsic (damage) mechanisms ahead of the crack tip that promote cracking and extrinsic (shielding) mechanisms mainly behind the tip to impede it*" [23]. The former is inherent to the material, differently from the latter, which are dependent on the crack size, specimen's geometry and fiber architecture [7,23].

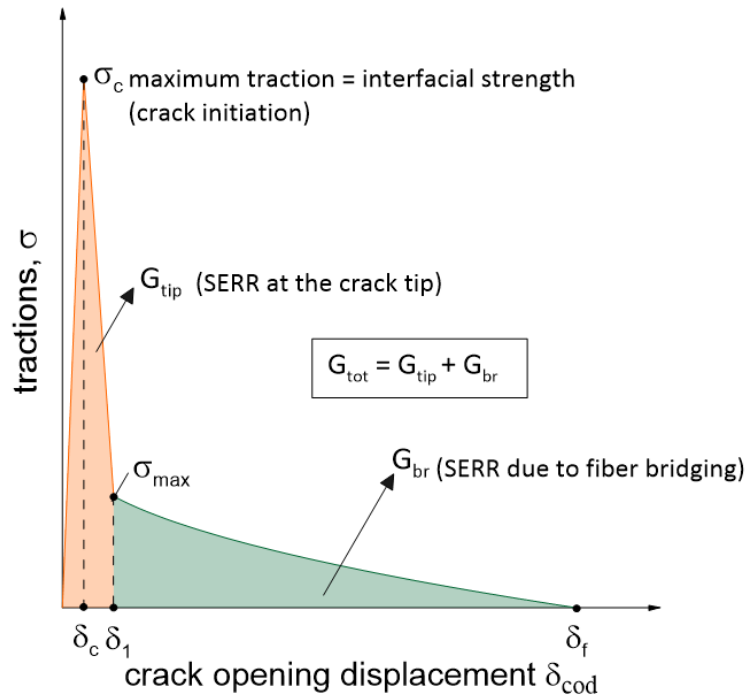


Figure 4.2. Traction separation law that accounts for fiber bridging mechanism.

To illustrate the cohesive law behavior in Mode I, Figure 4.3 shows the tractions over the fracture process zone (FPZ) in a specimen with fiber bridging. It is shown that the tractions are maximum at the crack tip, tending to decrease until zero as the maximum crack opening displacement, δ_f , is achieved. The indicated cracked region starts where the fiber breakage occurs, generating a stress-free region, whereas the non-damaged material corresponds to an elastic region. On the other hand, the indicated damage region accounts with two damage processes – the first (DP1), ahead the crack tip, is associated to damage and microfractures of the matrix [24]. It is related to the orange area of the cohesive law in Figure 4.2. Meanwhile, the second damage process (DP2) is related to the green area of Figure 4.2, corresponding to the energy dissipated due to fiber bridging mechanisms (G_{br}) behind the crack tip.

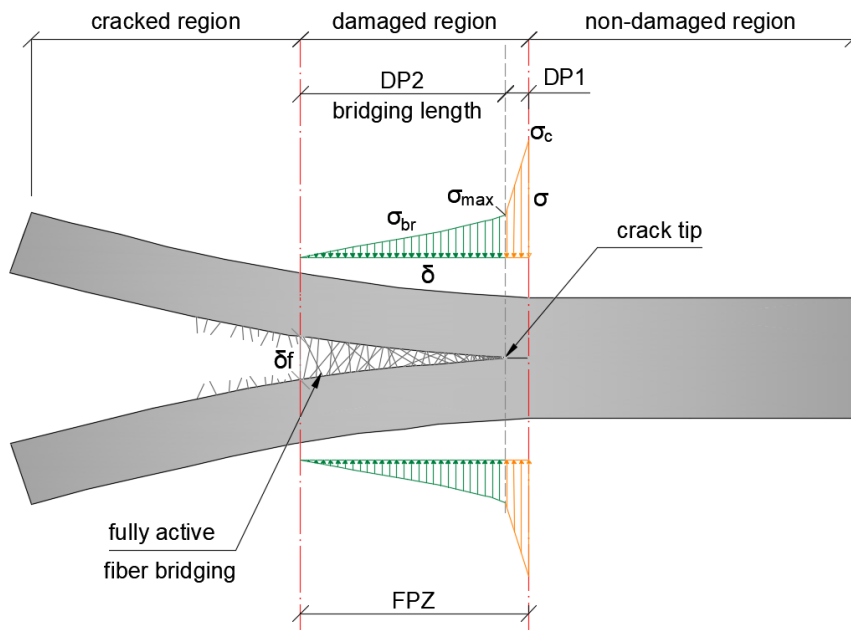


Figure 4.3. Fracture process zone of Mode I delamination with fiber bridging (adapted from [22]).

4.2.2. R-curve responses and CZM length

Some parameters used in cohesive laws may be estimated from the experimental R-curves. Figure 4.4 illustrates a typical R-curve response for specimens with fiber bridging, representing the SERR related to the crack length, a . It is important to point out that the definition of crack tip is different in the fracture mechanics context and the CZM. The former is the one used in this work and considers the crack tip as the point where bridging and fracture process initiate. The plateau enables the determination of the steady state toughness G_{tot} and its starting point indicates that the fiber bridging mechanism is fully developed [22]. Thus, it is possible to estimate the fiber bridging length through the experiments, as shown in Figure 4.4. In this context, when the fiber bridging length is comparable to some of the specimens' dimensions, the R-curve becomes dependent on the specimen's size and geometries [10], resulting in the so-called large-scale bridging (LSB) effect.

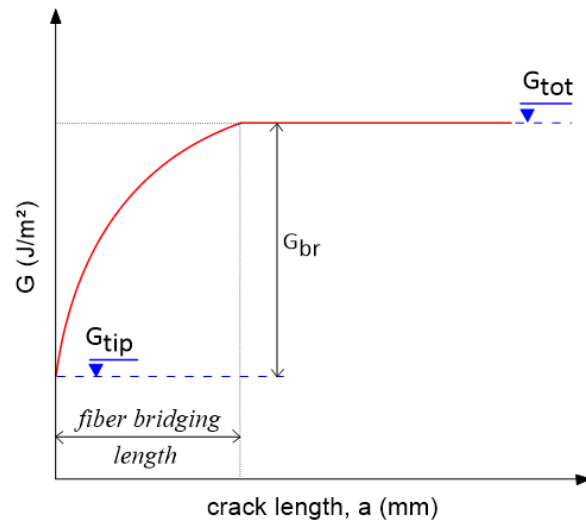


Figure 4.4. Typical shape of R-curve for DCB tests.

As previously mentioned, a fine discretization is needed in finite element method (FEM) models to guarantee accuracy in tractions distributions ahead of the crack-tip, with the recommendation of at least 3 to 5 cohesive elements in the cohesive zone length [25,26]. The CZM length for a bilinear traction separation law, *i.e.*, for a failure mode without fiber bridging, can be determined as expressed by the Equation (4.1), reported by Turon *et al.* [6].

$$l_{czm} = M \frac{E_{22} G_{tot}}{\sigma_c^2} \quad (4.1)$$

Where G_{tot} is the critical energy release rate (or fracture toughness) E_{22} is the transverse young modulus of the material; σ_c is the normal cohesive (interfacial) strength and M is a parameter that depends on the cohesive zone theory adopted. The Hilleborg's [27] and Rice's [28] models are the most commonly used, in which M is assumed to be equal to 1 [6]. The l_{czm} is inversely related to the material's brittleness, *i.e.*, the more brittle, the lower the material's cohesive zone length [3]. On the other hand, J. Chen [29] used the critical crack length a_m , expressed in Equation (4.2), to capture the crack below its critical value and determine the mesh refinement at the CZM for a bilinear traction separation law. The author used from 2 to 3 cohesive elements to discretize the crack length.

$$a_m = \frac{E_{22} G_{tot}}{\psi^2 \sigma_c^2 \pi} \quad (4.2)$$

Where ψ is a crack shape parameter adopted as 1.12. In this work, the Equation (4.2) was used.

4.3. Numerical Investigation

4.3.1. Traction separation laws

Three different traction separation laws were applied for the simulation of both DCB and ELS experiments to evaluate which one best simulates the fracture process of pultruded glass fiber-polymer specimens. A user material subroutine (VUMAT) was implemented in Abaqus/Explicit based on the theory presented by Gonzalez *et al.* [30]. Besides the classical bilinear cohesive law extensively used in literature, two other laws were used to take into account the effects of the fiber bridging stiffening mechanism: 1. *bilinear-exponential law* and 2. *trilinear law*. Figure 4.5 illustrates the cohesive laws shape assessed in this work.

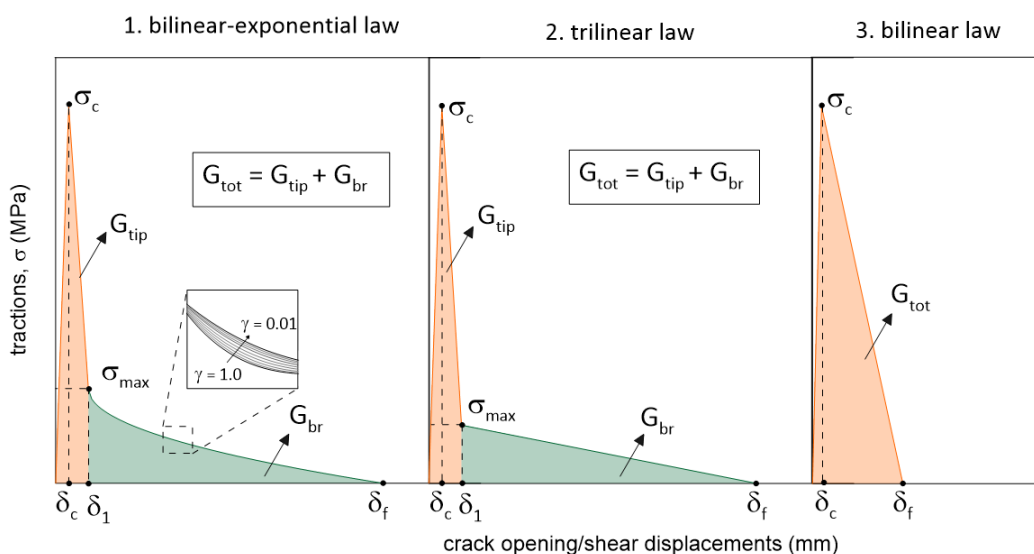


Figure 4.5. Cohesive laws' shape assessed: a) bilinear-exponential law; b) trilinear law; c) bilinear law.

The different traction separation laws implemented via VUMAT are expressed in Table 4.1. As can be seen, the main difference between the three-part cohesive laws is that, in the bilinear-exponential one, the fiber bridging tractions σ_{br} are represented by a non-linear behavior [12,22], in which the parameter γ varies from 0.01 to 1.0 depending on the curvature of the exponential softening. On the

other hand, the bridging tractions σ_{br} of the trilinear law are governed by a linear function.

Table 4.1. Traction separation laws implemented via VUMAT.

| <i>Cohesive law</i> | <i>Traction separation law</i> | <i>COD interval</i> |
|-----------------------------|---|--|
| <i>bilinear-exponential</i> | $\sigma(\delta) = \left(\frac{\sigma_c - \sigma_{max}}{\delta_c - \delta_1} \right) (\delta_{cod} - \delta_c) + \sigma_c$ | $\delta_c \leq \delta_{cod} \leq \delta_1$ |
| | $\sigma_{br}(\delta) = e^{-\gamma \sqrt{\delta_{cod} - \delta_1}} \sigma_{max} \left(1 - \sqrt{\frac{\delta_{cod} - \delta_1}{\delta_f - \delta_1}} \right)$ | $\delta_1 \leq \delta_{cod} \leq \delta_f$ |
| <i>trilinear</i> | $\sigma(\delta) = \left(\frac{\sigma_c - \sigma_{max}}{\delta_c - \delta_1} \right) (\delta_{cod} - \delta_c) + \sigma_c$ | $\delta_c \leq \delta_{cod} \leq \delta_1$ |
| | $\sigma_{br}(\delta) = \frac{\sigma_{max}}{\delta_1 - \delta_f} (\delta_{cod} - \delta_f)$ | $\delta_1 \leq \delta_{cod} \leq \delta_f$ |
| <i>bilinear</i> | $\sigma(\delta) = -\frac{\sigma_c}{\delta_f} \delta_{cod} + \sigma_c$ | $\delta_c \leq \delta_{cod} \leq \delta_1$ |

In all cases, the tractions response σ obeys to the Equation (4.3) [22].

$$\sigma(\delta_{cod}) = (1 - D(\delta))K_0\delta_{cod} \quad (4.3)$$

Where $D(\delta_{cod})$ is the damage variable, K_0 is the initial cohesive stiffness assumed as 100.000 N/mm³ [31] and δ_{cod} is the crack opening displacement (COD) in the Mode I. Analogously, for Mode II, the shear displacements were considered. Thus, the damage variable defined in the VUMAT subroutine for the bilinear-exponential and the trilinear law is presented in Equation (4.4), whereas the damage for the bilinear law is defined in Equation (4.5).

$$D(\delta_{cod}) = \begin{cases} 0 & \text{for } 0 \leq \delta_{cod} \leq \delta_c \\ 1 - \frac{\sigma(\delta_{cod})}{K_0\delta_{cod}} & \text{for } \delta_c < \delta_{cod} \leq \delta_1 \\ 1 - \frac{\sigma_{br}(\delta_{cod})}{K_0\delta_{cod}} & \text{for } \delta_1 < \delta_{cod} \leq \delta_f \end{cases} \quad (4.4)$$

$$D(\delta_{cod}) = \begin{cases} 0 & \text{for } 0 \leq \delta_{cod} \leq \delta_c \\ 1 - \frac{\sigma(\delta_{cod})}{K_0 \delta_{cod}} & \text{for } \delta_c < \delta_{cod} \leq \delta_f \end{cases} \quad (4.5)$$

4.3.2. Fitting procedure

In order to estimate the parameters to be adopted for the cohesive laws, a fitting procedure based on the experimental load vs. displacement curves was conducted. A first attempt of using the average experimental results obtained in Chapter 3 was made. However, the results for the Compliance Calibration (CC_{ASTM}) and the Simple Beam Theory (SBT) methods, obtained according to *ASTM D5528-01* and *ISO 15114*, were not considered, due to the great differences observed when compared to the other methods. These preliminary analyses resulted in the traction separation laws shown in Figures 4.6 and 4.7, which were defined according to the following methodology:

For bilinear-exponential and trilinear laws:

- For both Modes I and II, the maximum traction σ_c was adopted as 30% of the tensile strength of the polymeric matrix σ_t , which in this case is an isophthalic polyester resin ($\sigma_t = 65$ MPa [32]). This hypothesis was based on successful recommendations in literature applied to other fiber-polymer materials [5,24].
- The final opening displacement δ_f for both bilinear and bilinear-exponential laws was estimated through the experimental R-curves for the correspondent average crack length (a) where the fiber bridging mechanism was fully developed.
- The parameters G_{tip} and G_{tot} were adopted as the average experimental SERR for crack initiation and propagation, respectively (without considering the CC_{ASTM} method).
- The parameter σ_{max} was obtained through the compatibility of the areas corresponding to the energy related to fiber bridging (G_{br}) and to the damage initiated at the crack tip (G_{tip}).

For bilinear laws:

- The maximum traction σ_c was also adopted as 30% of the tensile strength of the polymeric matrix.
- the parameter G_{tip} was determined according to the average experimental SERR for crack initiation, without considering the CC_{ASTM} and SBT methods.
- The parameter δ_f was obtained through the compatibility of the areas corresponding to the energy related to the damage initiated at the crack tip (G_{tip}).

In other words, these preliminary analyses were based only on the experimental results and on the fracture toughness area compatibility. Therefore, the fracture parameters presented in Figures 4.6 and 4.7 were determined without an additional fitting procedure. The results for these analyses are described in Section 4.4.

In a second analysis, the fracture parameters were slightly adjusted to best fit the experimental *vs.* displacement curves, aiming to analyze which data reduction method provided the closest results to the numerical model. For the bilinear-exponential and the trilinear laws, the σ_c and δ_f were the same used in the preliminary analysis, whereas the parameters σ_{max} , G_{tot} and G_{tip} were obtained through an iterative process. On the other hand, for the bilinear law, both G_{tip} and δ_f were varied in order to achieve the best results. This fitting procedure was also based on the parametric study presented in the Section 4.7, which provides information about the influence of each parameter in the load *vs.* displacement behavior. The traction separation laws that best represented the experimental cracks cohesive behavior for both Modes I and II are discussed in Sections 4.5 and 4.6.

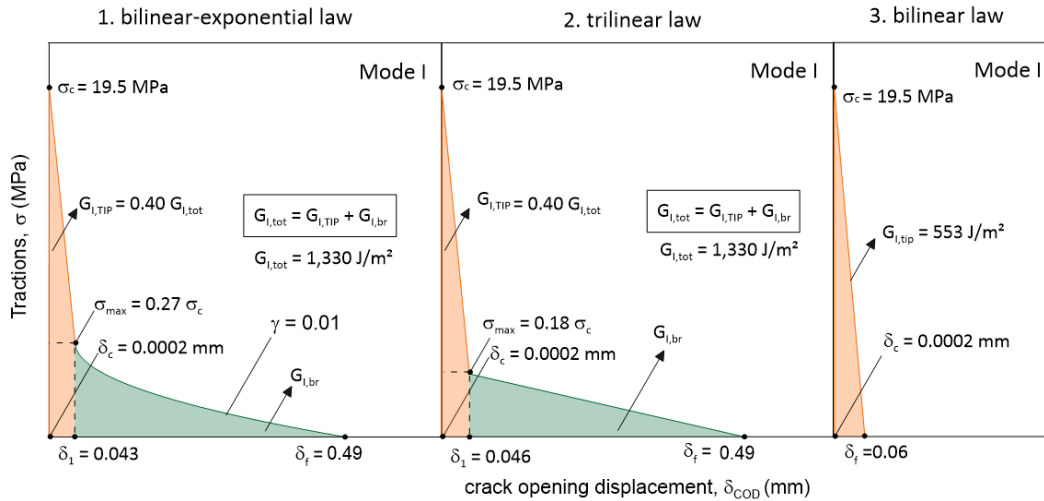


Figure 4.6. Preliminary cohesive laws used for the DCB model.

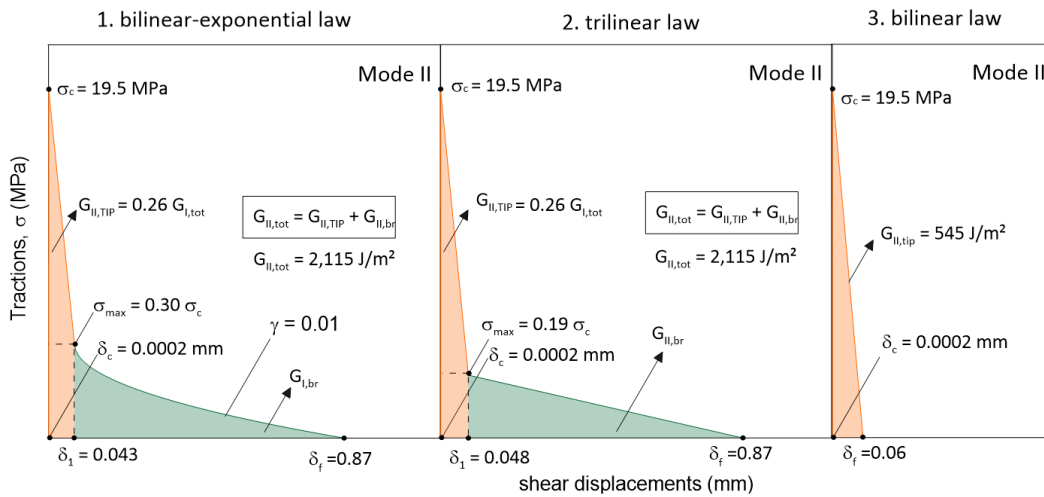


Figure 4.7. Preliminary cohesive laws used for the ELS model.

4.3.3. DCB model

The DCB experiments were simulated in a two dimensional plane-strain finite element model in Abaqus/Explicit 2021 v.6.21-6 [21], which was used in this case for comparison purposes with Chapter 5. The interspersed roving and triaxial multi-ply fabrics specimen's layers were modeled. A scheme of the adopted layer's distribution and the mesh refinement are presented in Figure 4.8. Two different materials were considered to constitute the composite, according to its respective fiber volume ratio: *i. Triaxial fabrics + resin* (in grey); *ii. Roving + resin* (in red). The layers' thicknesses were estimated based on the specimens' visual observation and burn-off tests. As can be seen in Figure 4.8, the composite layup is not

symmetric. The specimen having 16 mm of thickness was modeled with seven layers of triaxial fabric with 1 mm of thickness each, while four layers of roving + resin were considered (three with 2.5 mm and one with 1.5 mm of thickness). The elastic adopted properties, indicated in Table 4.2, were obtained by using the rule of mixtures and verified with the aid of the software *ESAComp* [32]. For the roving layers, the shear moduli G_{13} and G_{23} were considered equal to the G_{12} , for sake of simplicity.

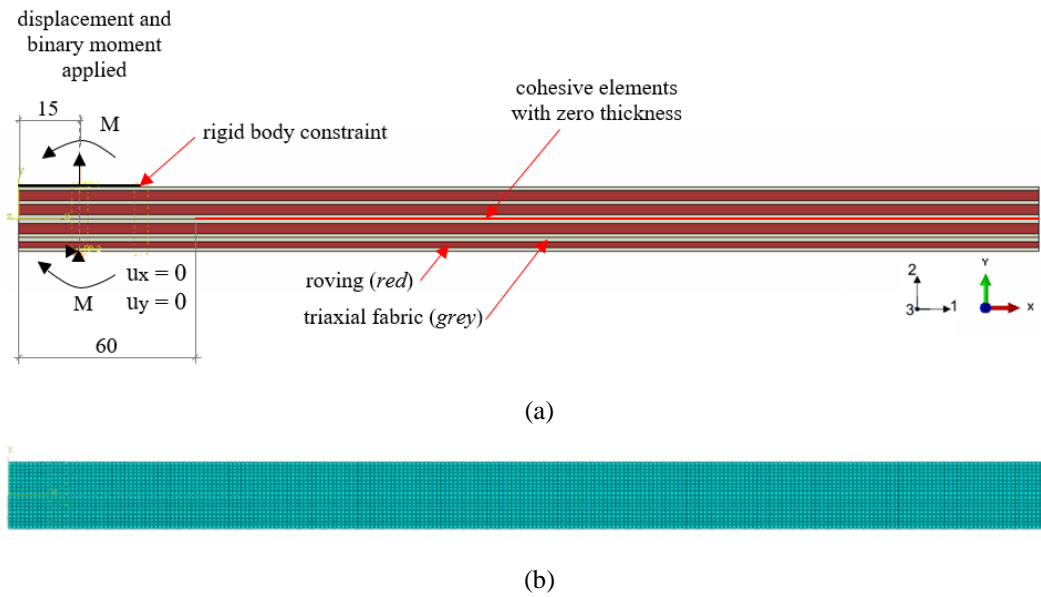


Figure 4.8. Scheme of DCB experiments modelling: (a) distribution of layers and adopted boundary conditions; (b) adopted mesh of 1 mm.

Table 4.2. Elastic properties adopted for the DCB model.

| Layers | | E_{11} (MPa) | E_{22} (MPa) | E_{33} (MPa) | ν_{12} | ν_{13} | ν_{23} | G_{12} (MPa) | G_{13} (MPa) | G_{23} (MPa) |
|--------|------------------------------|-------------------|-------------------|-------------------|------------|------------|------------|-------------------|-------------------|-------------------|
| Flange | transverse to roving + resin | 5,460 | 5,460 | 31,000 | 0.30 | 0.05 | 0.05 | 2,100 | 2,100 | 2,100 |
| | tri-fabric + resin | 26,510 | 5,460 | 12,340 | 0.27 | 0.27 | 0.35 | 3,720 | 6,960 | 3,680 |

To model the experimental test configuration, a displacement of 25 mm is applied on the top of the composite, at 15 mm from its edge, as shown in Figure 4.8. A rigid body constraint was used between the specimen and the applied displacement to simulate the effects of the used aluminum plates. A binary moment that takes into account the eccentricity of 30 mm between the piano-hinges loading

blocks and the actual displacement application is also considered. At this same load application line, the bottom part of the flange is restrained in horizontal (x) and vertical (y) directions in order to simulate the boundary conditions provided by the universal machine of testing. The displacements obtained through the model were computed at 15 mm from the specimens' edge, which corresponds to the load transfer point in the experiments.

Four-node bilinear quadrilateral elements (CPE4R) were used in a structured and uniform fine mesh, as shown in Figure 4.8b. At the specimen middle plane, an initial separation having 60 mm long was introduced from its left edge, between the two adjacent fabric layers (in grey). At this middle plane extension, a layer with four-node two-dimensional cohesive elements (COH2D4) having zero thickness was modeled in order to simulate the fracture process zone. The cohesive zone length was calculated through the Equation (4.2) and a value of approximately 5 mm was found. Therefore, a mesh of 1 mm was adopted to account with 5 elements in the cohesive zone. The model comprised 5,020 nodes and 4,690 elements.

4.3.4. ELS model

Analogous to the DCB model, the multilayered specimen tested in ELS experiments was simulated in a 2D plane-strain model, as presented in Figure 4.9. The adhesive layer was not modeled since no significant changes in the results were identified in complementary models where the given layer was considered. Since the ELS and DCB specimens were extracted from the same *DS* deck, the elastic properties adopted in the models are the same and are described in the previously mentioned Table 4.2. A displacement boundary condition of 25 mm was applied at 21.5 mm from the edge via a rigid body constraint to simulate the load distribution provided by the loading blocks on the aluminum plates attached to the specimens in experiments. Both the top and bottom of the flange were restrained in the vertical (y) direction at the points and regions indicated in Figure 4.9a, in an attempt to simulate the pair of screws at the top and the continuous clamped region at the bottom. The same mesh of 1 mm, used in the DCB model, was adopted for this simulation. A “contact pair” (tool of Abaqus) with frictionless tangential behavior was defined to model properly the existing interaction between the two separated

surfaces during the analysis. The displacements obtained through the FEM model were computed at 21.5 mm from the specimens' edge to ensure compatibility with experimental tests.

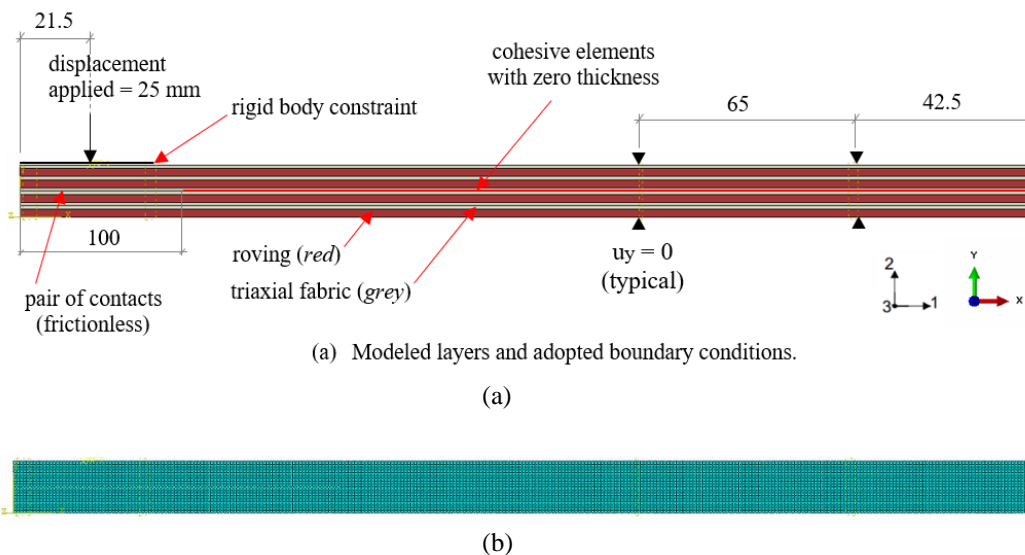


Figure 4.9. Scheme of ELS experiments modelling: (a) layers' distribution and adopted boundary conditions; (b) Adopted mesh of 1 mm.

As in DCB models, four-node bilinear quadrilateral (CPE4R) and cohesive elements (COH2D4) having zero thickness were also used to describe the bulk material and the fracture process zone, respectively. In this case, an initial separation having 100 mm long was introduced from the specimens' left edge at its middle plane. The model comprised 6,220 nodes and 5,790 elements.

4.4. Results of preliminary numerical analyses

As previously mentioned in Section 4.3.2, preliminary analyses were conducted in order to determine suitable fracture parameters for the traction separation laws to be used in numerical models. In these analyses, the parameters were obtained based only on the experimental results and on the fracture toughness area compatibility, *i.e.*, no fitting procedure was applied. The load vs. displacement curves obtained through the three different cohesive laws (see Figures 4.6 and 4.7), both for DCB and ELS models are presented in Figure 4.10.

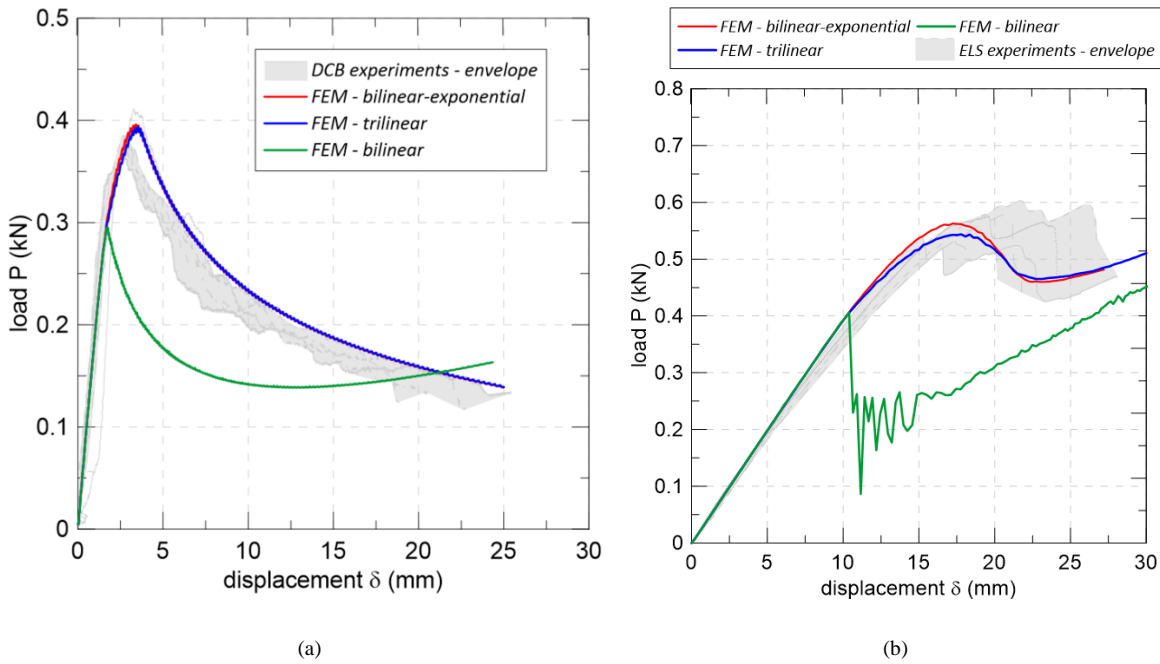


Figure 4.10. Load vs. displacement curves: (a) DCB models; (b) ELS models.

As can be seen, for DCB and ELS models, the bilinear law led to very inaccurate results, both in terms of peak load and in the post-peak curve region. On the other hand, good results were found for trilinear and bilinear-exponential laws, especially for Mode II. In general, the trilinear laws generated curves slightly closer to the obtained experimentally. For the Mode I, the numerical model slightly overestimated the peak loads obtained experimentally, disregarding the specimen DCB.01. It is important to point out that this overestimation is not related to the initial load relief occurred in DCB.01 experiment, since this specimen provided very similar SERR results when comparing to the other specimens, especially for crack propagation.

For this reason, the trilinear and bilinear-exponential laws of Mode I were slightly adjusted, as shown in the next section, to better fit the experimental P vs. δ curve of the other four specimens. In parallel, an attempt to adjust the parameters of the bilinear laws was also made, due to the numerical inaccurate results observed in Figure 4.10 and to the scattered values for crack initiation obtained experimentally when considering all the data reduction methods evaluated.

4.5. Results and discussion for DCB models

4.5.1. Adopted cohesive laws

After the fitting procedure previously mentioned, the traction separation laws that resulted in the best fit with experimental P vs. δ curves are shown in Figure 4.11. In the bilinear-exponential law, the best fit was found for a $G_{I,tip}$ adopted as 42% of the $G_{I,tot}$, with a parameter γ equal to 0.01. On the other hand, for the trilinear law, a lower value of $G_{I,tip}$ was required, being equal to 29% of the $G_{I,tot}$. In parallel, a good fit was observed for σ_{max} assumed as 25% and 20% of σ_c for the bilinear-exponential and trilinear laws, respectively. Different values of δ_f were tested for the bilinear law in order to consider the same interfacial strength of 19.5 MPa adopted for the other cohesive laws. Therefore, the value of 0.13 mm indicated in Figure 4.11 is the one that best fits the experimental results. The found fracture toughness $G_{I,tot}$ was 1,250 J/m² for both the trilinear and bilinear-exponential laws, whereas a value of 998 J/m² was obtained for the bilinear law.

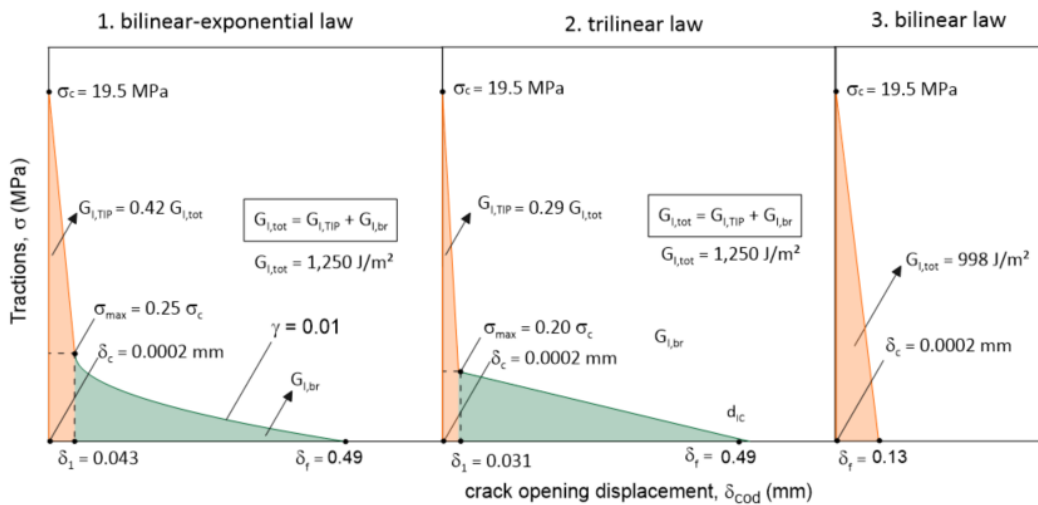


Figure 4.11. Cohesive laws used for the simulation of DCB experiments: (a) bilinear-exponential law; (b) trilinear law; (c) bilinear law.

4.5.2. General behavior

The Mode II was considered negligible in the DCB FEM model, with the relative shear displacements representing less than 1% of the opening ones. Figure 4.12 presents the comparison between the experimental results (represented through a grey envelope) and the load vs. displacement curves obtained numerically for

different cohesive laws. Although exponential softening laws have been indicated in literature [12,33] as the best option to simulate fracture mechanisms with fiber bridging, both fitted trilinear and bilinear-exponential cohesive laws agreed well with the experiments, presenting a maximum difference of only 3% between the peak loads obtained numerically and experimentally for specimens DCB.02 to DCB.05. On the other hand, differences up to 18.4% were observed between the experimental and numerical peak loads when considering the bilinear law, confirming that this type of law is not appropriated to take into account the effects of the bridging mechanism. However, the fitted bilinear law was able to properly simulate the P vs. δ post-peak curve softening.

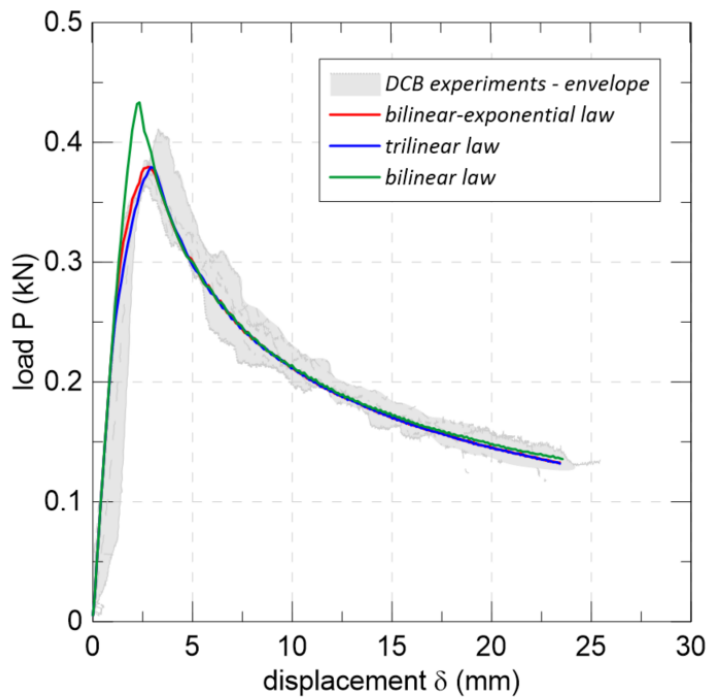


Figure 4.12. Comparison between the use of different traction-separation laws.

Figure 4.13 shows the typical deformed shaped of DCB specimens obtained for the three FEM models, with the cohesive elements indicated in red.

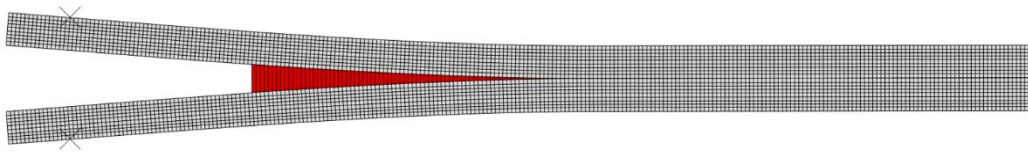


Figure 4.13. Deformed shape of DCB specimens.

Although the fitted bilinear law has overestimated the peak load in P vs. δ curves, it presented good agreement in terms of compliance and propagated crack length, as shown in Figures 4.14 and 4.15a. In parallel, the bilinear-exponential and the trilinear laws also simulated well the composite compliance and crack lengths, with very similar responses between each other. It was observed that the difference in the laws' shape has no significant influence in the opening displacement values, as can be seen in Figure 4.15b. Nevertheless, it can be observed that the experimental CODs were not very well simulated by the DCB model, which underestimated in average up to 27% the values obtained experimentally.

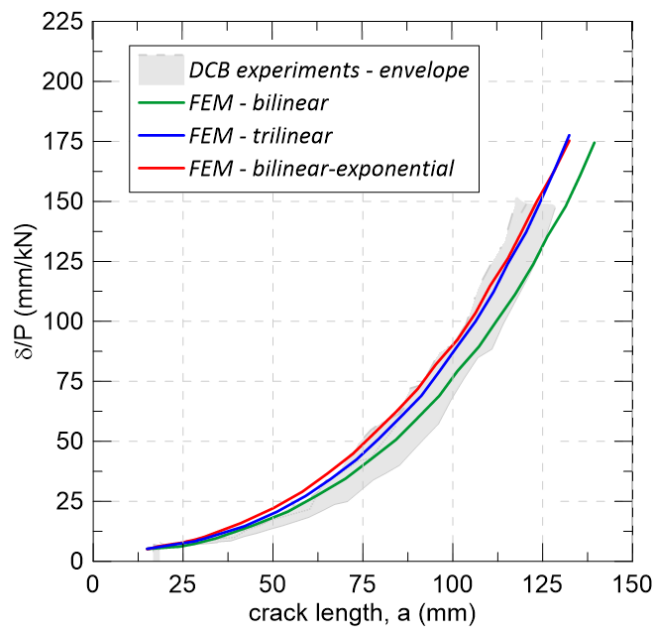


Figure 4.14. Comparison between the DCB experimental and numerical compliance curves.

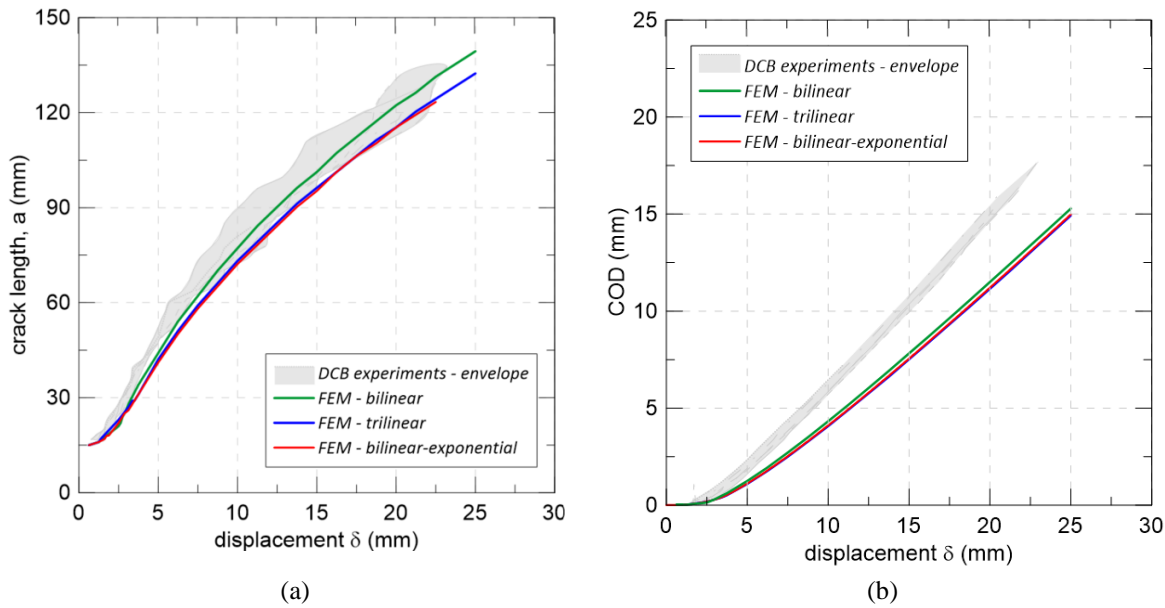


Figure 4.15. Comparison between numerical and experimental curves: (a) crack length vs. displacement; (b) crack opening displacement (COD) vs. displacement (δ).

4.5.3. R-curve and SERR values

The SERR values found in the FEM model for both crack initiation ($G_{I,tip}$) and propagation ($G_{I,tot}$) are shown in Table 4.3, along with the experimental values found through six different methods described in Chapter 3. Among the given methods, three are included in the recommendations of *ASTM D5528-01* [34]: MBT_{ASTM} (*Modified Beam Theory*), CC_{ASTM} (*Compliance Calibration*) and MCC_{ASTM} (*Modified Compliance Calibration*). On the other hand, the formulation of the other three is reported in literature: $MBT-EI_{eq}$ (*Modified Beam Theory* calculated from an equivalent stiffness [35]), $CC-f$ (*Compliance Calibration* based on an alternative function [36,37]) and, finally, $MCC-a_{eff}$ (*Modified Compliance Calibration* with an effective crack length a_{eff} , which eliminates the optical measurement dependency of the delamination length).

In the numerical model, the $G_{I,tip}$ values were obtained for the corresponding COD of δ_I [22] – see Figure 4.11 – for the trilinear and bilinear-exponential laws. The latter presented, in general, results closer to the experimental values, especially when compared to $CC-f$ method, where a difference of only 3% was observed between the SERR results for crack initiation. On the other hand, the CC_{ASTM} method presented $G_{I,tip}$ values twice as high as those obtained through the FEM model. In opposition, the $MCC-a_{eff}$ and $MBT-EI_{eq}$ presented $G_{I,tip}$ results that agreed

well with the numerical values obtained with the bilinear-exponential cohesive law, with differences of 12.2 % and 13.5%, respectively. Finally, the trilinear law led to $G_{I,tip}$ values 37% lower than those obtained through the bilinear-exponential cohesive law.

A value of 1,250 J/m² for crack propagation ($G_{I,tot}$) was obtained for both bilinear-exponential and trilinear laws after fitting the experimental P vs. δ curves. Based on this, the CC-f method presented the highest difference (8.1%) from the $G_{I,tot}$ obtained through FEM models. In opposition, the $G_{I,tot}$ obtained through MBT_{ASTM} method presented the lowest difference (4%) from the numerical $G_{I,tot}$ value. The bilinear law, on the other hand, underestimated in 20% the SERR values when compared to the other cohesive laws.

Table 4.3. SERR values obtained experimentally and in FEM models.

| <i>Experimental methods</i> | EXPERIMENTAL RESULTS: | |
|---------------------------------|--|---|
| | <i>Average G_I (J/m²)</i> | |
| | For crack initiation <i>($G_{I,tip}$)</i> | For crack propagation <i>($G_{I,tot}$)</i> |
| <i>MBT_{ASTM}</i> | 661 ± 181 | 1,300 ± 93 |
| <i>MBT-EI_{eq}</i> | 520 ± 159 | 1,337 ± 97 |
| <i>CC_{ASTM}</i> | 963 ± 254 | 1,175 ± 88 |
| <i>CC-f</i> | 465 ± 151 | 1,352 ± 94 |
| <i>MCC_{ASTM}</i> | 615 ± 171 | 1,323 ± 92 |
| <i>MCC-a_{eff}</i> | 513 ± 143 | 1,337 ± 93 |
| <i>Cohesive Laws</i> | NUMERICAL RESULTS: | |
| | <i>$G_{I,tot}$ (J/m²)</i> | |
| | For crack initiation <i>($G_{I,tip}$)</i> | For crack propagation <i>($G_{I,tot}$)</i> |
| <i>Bilinear-exponential</i> | 450 | 1,250 |
| <i>trilinear</i> | 285 | 1,250 |
| <i>bilinear</i> | - | 998 |

Figures 4.16 to 4.18 present a comparison between the R-curves obtained numerically and experimentally (grey envelope) for the six reduction methods. As can be noticed, both trilinear and bilinear-exponential laws agreed better with the

composite's behavior observed experimentally. In opposition, the bilinear cohesive law underestimated the experimental steady state values of the SERR (defined by the plateau). Among all the six methods, it can be observed that the MBT_{ASTM} and the MCC_{ASTM} resulted in a better agreement with numerical simulations. On the other hand, CC_{ASTM} , $CC-f$ and $MCC-a_{eff}$ presented greater differences than other methods when compared to those obtained through the FEM model.

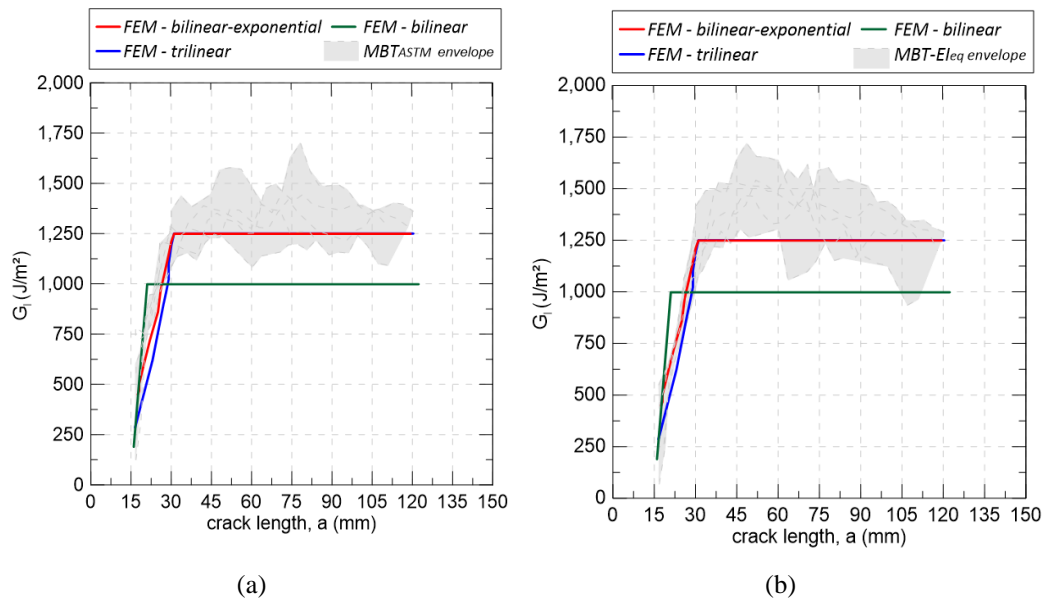


Figure 4.16. Comparison between R-curves obtained numerically and from MBT's methods: a) MBT_{ASTM} method; b) $MBT-EI_{eq}$ method.

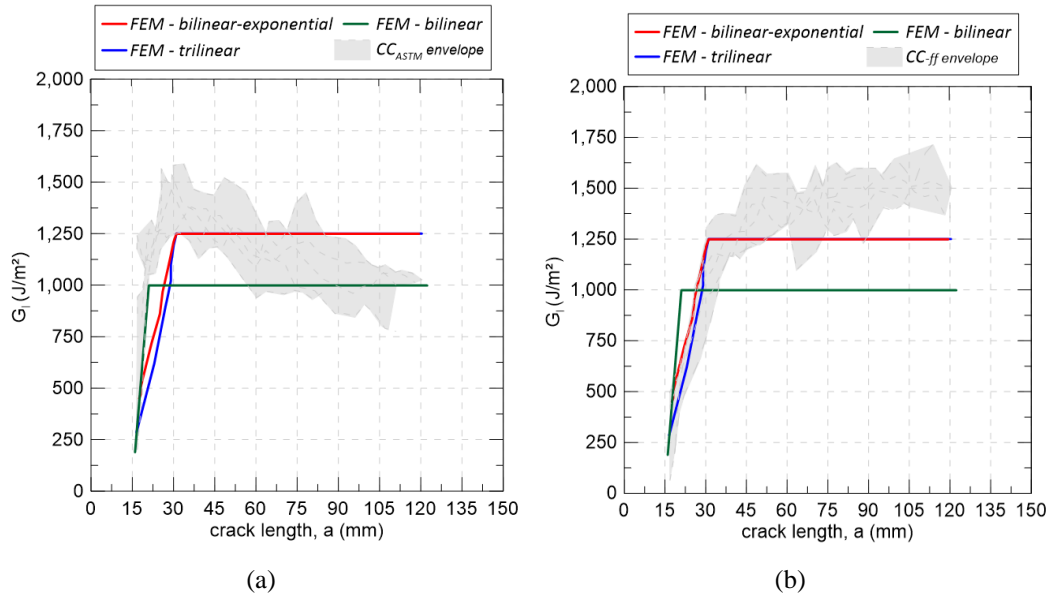


Figure 4.17. Comparison between R-curves obtained numerically and from CC methods: a) CC_{ASTM} method; b) $CC-f$ method.

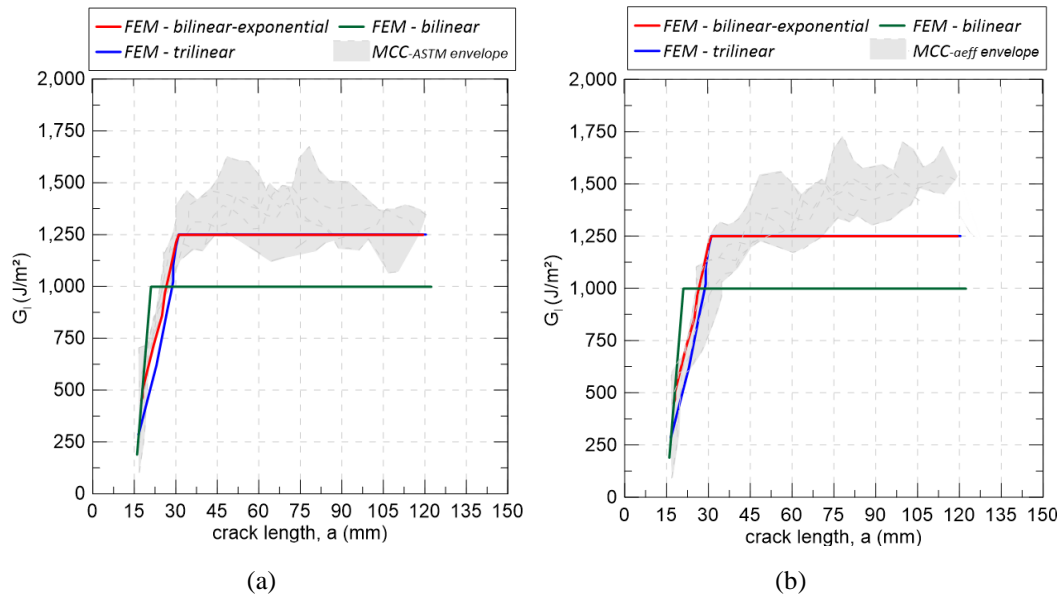


Figure 4.18. Comparison between R-curves obtained numerically and from MCCs methods: a) MCC_{ASTM} method; b) $\text{MCC-}a_{\text{eff}}$ method.

4.6. Results and discussion for ELS models

4.6.1. Adopted cohesive laws

The task of obtaining the parameters for the traction separation laws in Mode II is not an easy one, especially due to the lack of references in literature. In this work, for the trilinear and bilinear-exponential laws, the parameters found experimentally were used due to the good convergence of numerical and experimental P vs. δ curves. However, as previously mentioned, the bilinear law was adjusted due to the high scattering observed for the experimental SERR for crack initiation.

The traction separation laws adopted for Mode II are shown in Figure 4.19. Both for the bilinear-exponential and the trilinear laws, the $G_{II,tip}$ was adopted as 26% of the total fracture energy $G_{II,tot}$, which was found to be equal to 2,115 J/m^2 in all cases. The parameter σ_{max} was adopted as 30% and 19% of the interfacial strength σ_c for the bilinear-exponential and trilinear laws, respectively. For the exponential softening function, the parameter γ was adopted as 0.01. As performed in DCB simulations, several combinations were tested for the bilinear cohesive law, and the value of 0.22 mm was adopted as δ_f . For the other laws, the value of 0.87

mm was used, based on the experimental results, although it is not possible to estimate accurately this value, since the fiber bridging was not fully developed in Mode II R-curves, as it will be seen further ahead.

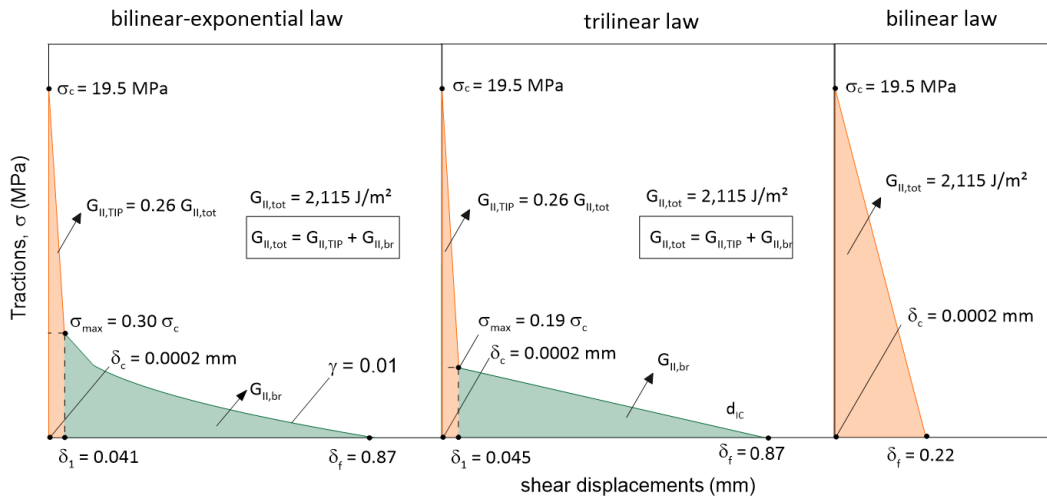


Figure 4.19. Cohesive laws used for the simulation of ELS experiments: (a) bilinear-exponential law; (b) trilinear law; (c) bilinear law.

4.6.2. General behavior

The typical deformed shape observed in FEM models is illustrated in Figure 4.20.

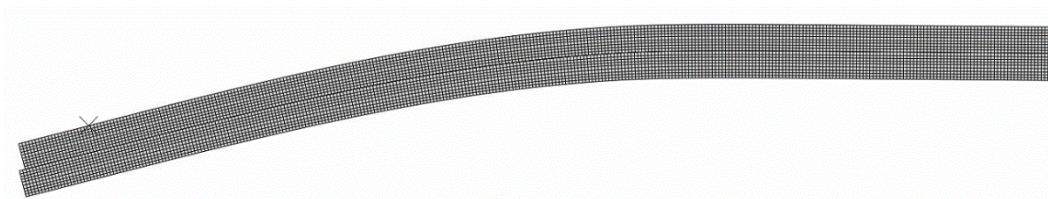


Figure 4.20. Typical deformed shape of ELS specimens.

The numerical and experimental (grey envelope) P vs. δ curves are shown in Figure 4.21. It can be noticed that the use of the average experimental SERR values obtained through the CBTE and EMC methods enabled to numerically simulate very well the composites curves load vs. displacement. In general, the numerical models slightly overestimated the specimen's stiffness. This small difference may be influenced by the adopted shear properties of rovings in the model, since the shear moduli G_{13} and G_{23} were considered equal to the G_{12} , for sake of simplicity. Despite of that, the FEM results for trilinear and bilinear-

exponential laws agreed well with experiments. The bilinear cohesive law, on the other hand, led to a very inaccurate response, overestimating the peak load in 33%, before presenting a sharp drop in the load. This brittle behavior can be observed through an abrupt increase in its respective compliance curve, presented in Figure 4.22, from the point where the crack length reaches approximately 97 mm. It is also well described in the graphs shown in Figure 4.23, which present the variation in crack length and shear displacements according to the vertical displacement applied (δ) on the specimen. In the given graphs, it can be seen an abrupt increase both in crack length – with a variation from 97 to 167 mm – and in shear displacement, which varied from 0.17 to 0.91 mm.

With respect to the other cohesive laws, both bilinear-exponential and trilinear laws were not able to simulate very well the composite's compliance, although a better convergence has been observed for the former. On the other hand, a good agreement was obtained for the three-part laws with respect to the shear displacement *vs.* vertical displacement (δ) curves. Both laws presented very similar results for the propagated crack length and shear displacements. However, the models were not able to represent very accurately the variation of the crack length according to the applied displacement, as shown in Figure 4.23a. The experimentally measured crack lengths were lower than those obtained through the FEM models. This might be related to the especial difficulty in identifying and tracking the crack initiation and propagation in Mode II, even with the aid of the video extensometer. Moreover, it is important to point out that, as previously mentioned, there are issues related to the experiments, such as the presence of defects, voids asymmetry caused by the fiber architecture, that are hard to control and thus, to be simulated in the model. As these parameters may have led to the scattering in the experimental tests, they may have contributed to the inaccuracy of the model, since it was not possible to take them into account.

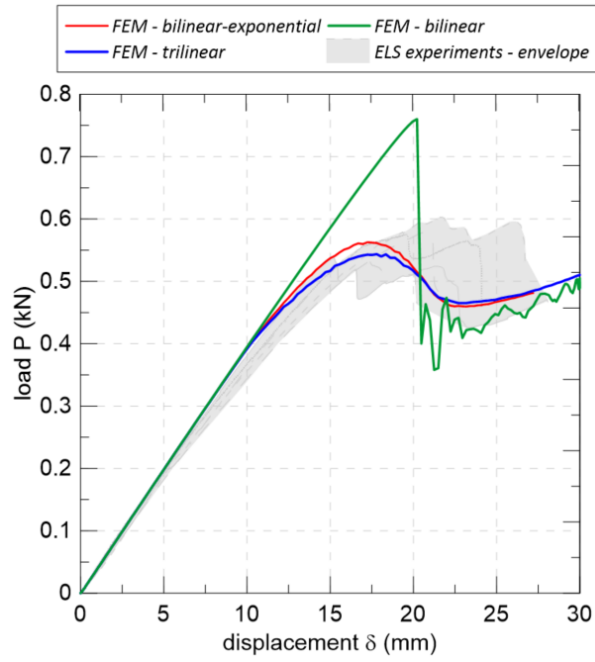


Figure 4.21. Comparison between ELS numerical and experimental results: load vs. displacement curves.

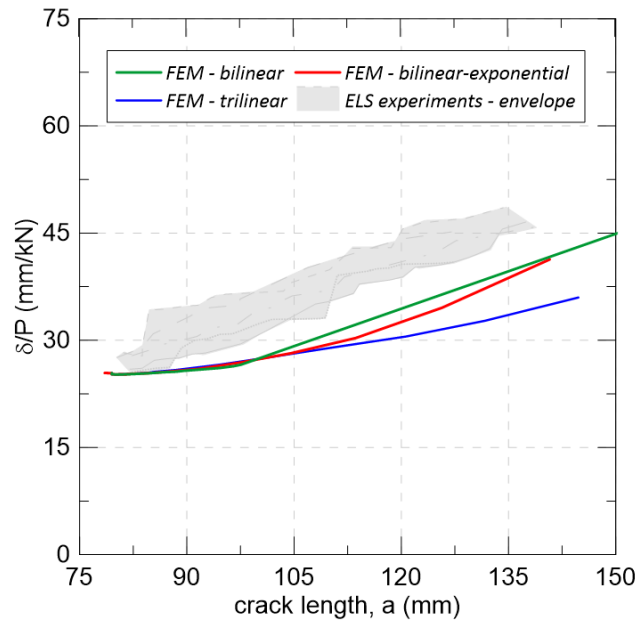


Figure 4.22. Comparison between the ELS experimental and numerical compliance curves.

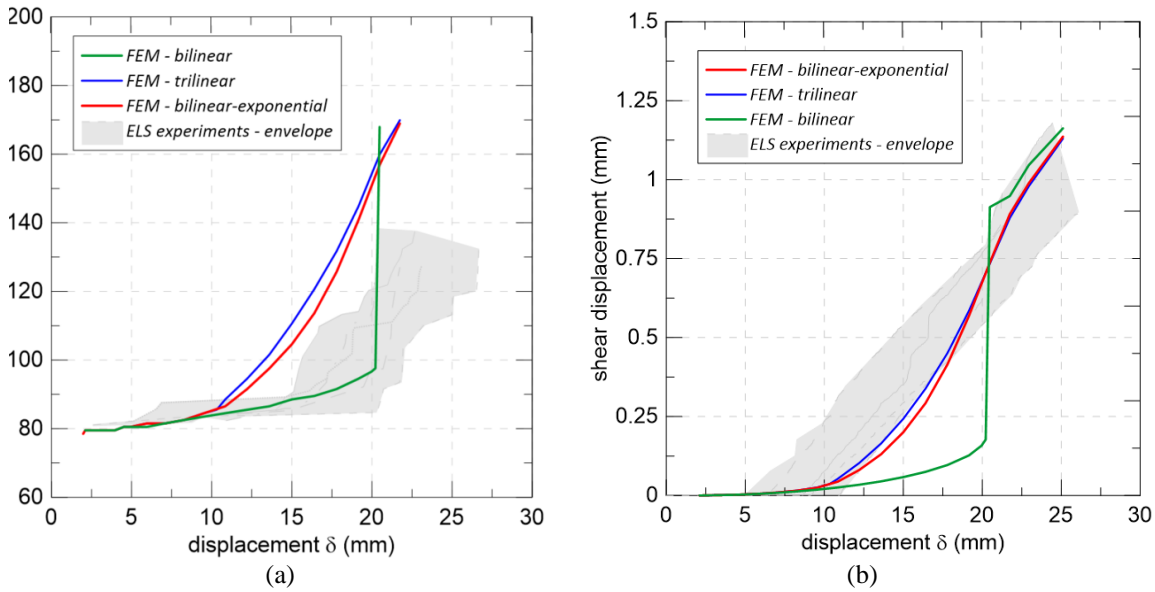


Figure 4.23. Comparison between numerical and experimental curves: (a) crack length vs. displacement; (b) shear displacement vs. displacement (δ).

4.6.3. R-curves and SERR values

The FEM parameters related to the crack initiation ($G_{II,tip}$) and crack propagation ($G_{II,tot}$) are shown in Table 4.4. The former was obtained for the corresponding shear displacement δ_I , according to references in literature [22] – see Figure 4.11 – for the trilinear and bilinear-exponential laws. On the other hand, the latter, as previously mentioned, was obtained based on the average results of CBTE and EMC methods for bilinear-exponential and trilinear laws, whereas a fitting procedure was conducted to determine the fracture properties for the bilinear law.

The trilinear law led to closer results to CBTE and EMC methods for the $G_{II,tip}$ parameter, with a maximum difference of 22.5%. On the other hand, the $G_{II,tip}$ obtained when using the bilinear-exponential law presented a maximum difference of 26.9% from the same methods. Regarding the SERR for crack propagation, since the parameters adopted in the numerical models were based on the average results of CBTE and EMC methods and both presented very similar outcomes, a difference lower than 1% was observed between the $G_{II,tot}$ obtained through each method individually and the FEM models. In opposition, the SBT method resulted in an average $G_{II,tot}$ 44% lower than the one obtained numerically.

Table 4.4. Values of G_{IIc} obtained experimentally and in FEM models.

| <i>Experimental methods</i> | EXPERIMENTAL RESULTS: | |
|-----------------------------|---|--|
| | <i>Average G_{II} (J/m²)</i> | |
| | For crack initiation <i>($G_{II,tip}$)</i> | For crack propagation <i>($G_{II,tot}$)</i> |
| <i>CBTE</i> | 522 ± 340 | 2,124 ± 291 |
| <i>SBT</i> | 312 ± 226 | 1,177 ± 184 |
| <i>EMC</i> | 568 ± 442 | 2,104 ± 307 |
| <i>Cohesive Laws</i> | NUMERICAL RESULTS: | |
| | <i>$G_{II,tot}$ (J/m²)</i> | |
| | For crack initiation <i>($G_{II,tip}$)</i> | For crack propagation <i>($G_{II,tot}$)</i> |
| <i>Bilinear-exponential</i> | 415 | 2,115 |
| <i>trilinear</i> | 440 | 2,115 |
| <i>bilinear</i> | - | 2,115 |

The R-curves for both numerical models and experiments are presented in Figure 4.24. It can be observed that the obtained numerical curves indicate an important presence of fiber bridging, which is not fully developed. The three-part cohesive laws resulted in a slower SERR increase when compared to the experimental R-curves obtained from EMC and CBTE methods. The fact that the experimentally measured crack lengths are lower than the ones obtained numerically contributes to this result. It is also interesting to notice that the second branch slope of the numerical curves for both bilinear-exponential and trilinear laws are similar to the ones obtained experimentally – especially for the CBTE method –, indicating that, apparently, the parameter G_{tip} should be higher. However, many attempts to fit greater values of G_{tip} into the model were made, without success.

Although the given numerical results have apparently shown a good agreement with the R-curves generated by SBT method, it is important to remember that this method underestimated the G_{tot} obtained through FEM models. Likewise, the classical bilinear law presented a significant fast increase in the SERR before reaching 100 mm of crack length. However, this response represents an unreliable good agreement with the experiments, since this behavior is related to incorrect values of load and an abrupt drop in the P vs. δ curve, as shown in Figure 4.21.

Thus, further investigations are necessary to evaluate this issue, since none of the three methods (SBT, EMC and CBTE) could accurately express the SERR related to the crack propagation in Mode II obtained through the FEM model.

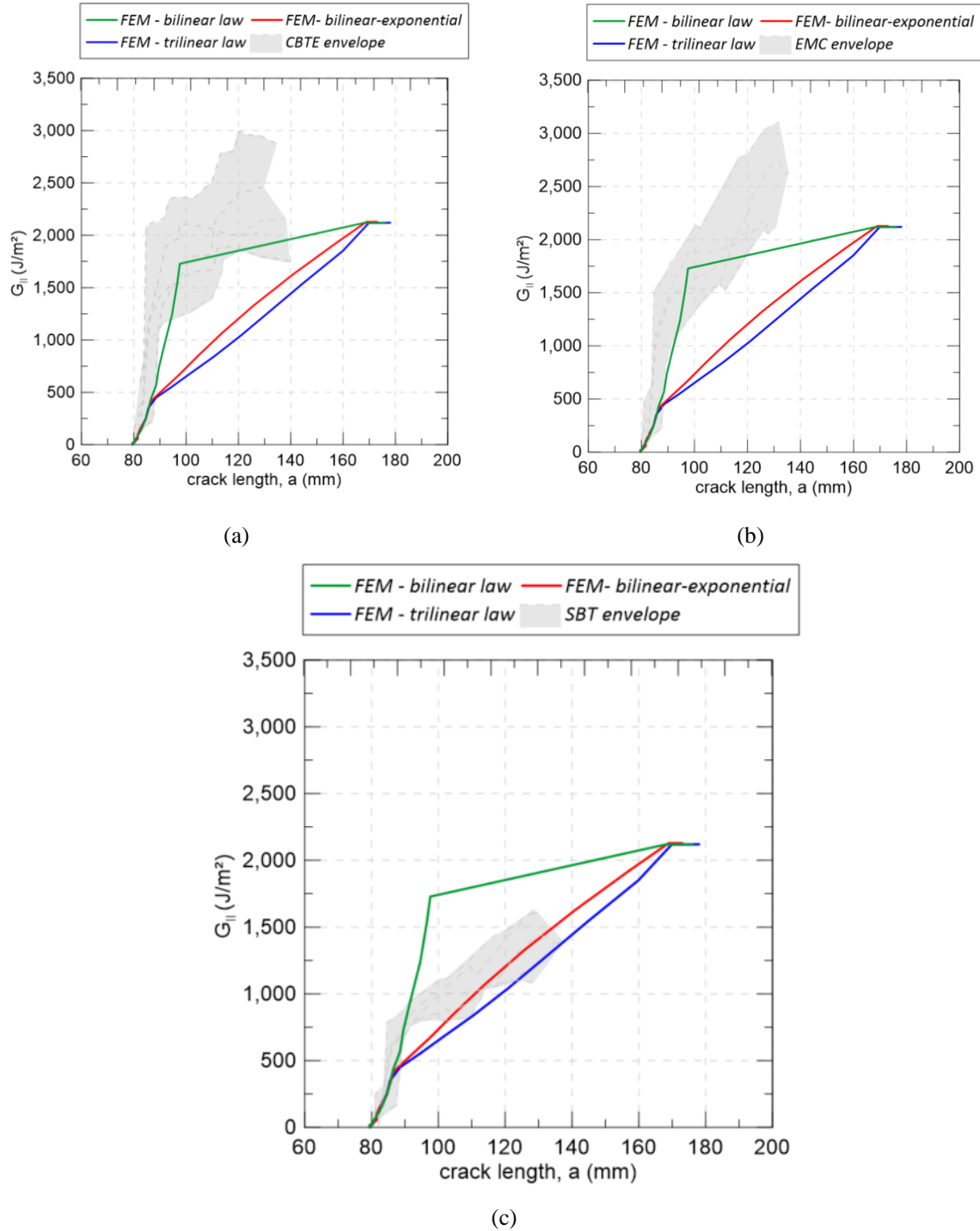


Figure 4.24. Comparison of R-curves from ELS numerical models and experimental tests: (a) CBTE method; (b) EMC method; (c) SBT method.

4.7. Parametric study of the cohesive law

A parametric study was performed in order to understand how each parameter of a three-part cohesive law influences in the progressive failure of DCB and ELS specimens. Two different cohesive law shapes (trilinear and bilinear-exponential laws) were evaluated. The main parameters σ_c , σ_{max} , G_{tip} and G_{tot} were varied and the responses in terms of load vs. displacements were discussed. The corresponding opening and shear displacements δ_c , δ_l and δ_f were modified when necessary to assure the compatibility with the area correspondent to the fracture energy under the cohesive law.

4.7.1. Effect of the interfacial strength (σ_c)

Values of 5, 10 and 15 MPa were adopted for the interfacial strength σ_c to assess the differences generated in the load vs. displacements behavior. The other adopted parameters used in both bilinear-exponential laws in DCB and ELS analyses are listed in Table 4.5. The results are shown in Figure 4.25. In general, the parameter σ_c influences the peak load and the point where occurs the loss of linearity, which is independent on the adopted cohesive law shape for both DCB and ELS tests. In the former, for instance, both bilinear-exponential and trilinear laws led to a nonlinear behavior beginning at approximately 0.072 kN for $\sigma_c = 5$ MPa and at 0.173 kN for $\sigma_c = 15$ MPa.

Table 4.5. Adopted parameters for cohesive laws to assess the σ_c influence.

| σ_c (MPa) | σ_{max} (MPa) | G_{tip} (J/m ²) | G_{tot} (J/m ²) | γ |
|------------------|----------------------|-------------------------------|-------------------------------|----------|
| 5 | 0.2 σ_c | 0.25 G_{tot} | 1,250 | 0.01 |
| 10 | | | | |
| 15 | | | | |

In DCB tests, the σ_c value and the laws shape change the curve behavior mainly until the maximum load is reached, without any significant differences observed at the post-peak region. It can be noticed that increases in the σ_c parameter led to an augmentation in maximum loads, although this behavior tended to become less significant for higher values of σ_c . For instance, the σ_c variation from 5 to 10

MPa is followed by an increase in 15% in the peak load considering the trilinear law, against only 7% of increase when σ_c varies from 10 to 15 MPa. For the bilinear-exponential law, these variations were equivalent to 17% and 8%, respectively. Lower peak loads were typically observed for bilinear-exponential laws, with an average difference of 7.8% from the maximum loads resulted from trilinear laws.

On the other hand, for ELS tests, the change in the curves' behavior due to the cohesive laws shape and to σ_c increase could be noticed until the final applied displacement. Greater final loads were observed for lower values of the interfacial strength σ_c . Moreover, as can be noticed, the influence of the laws shape in the overall curve behavior tended to become more significant for greater values of σ_c . As observed in DCB models, increases of 30% and 16% were registered in the peak loads for σ_c variations from 5 to 10 MPa and from 10 to 15 MPa, respectively, when considering a trilinear law. Meanwhile, for the same variations of σ_c , the bilinear-exponential law led to increases of 19% and 15% in the peak loads, respectively.

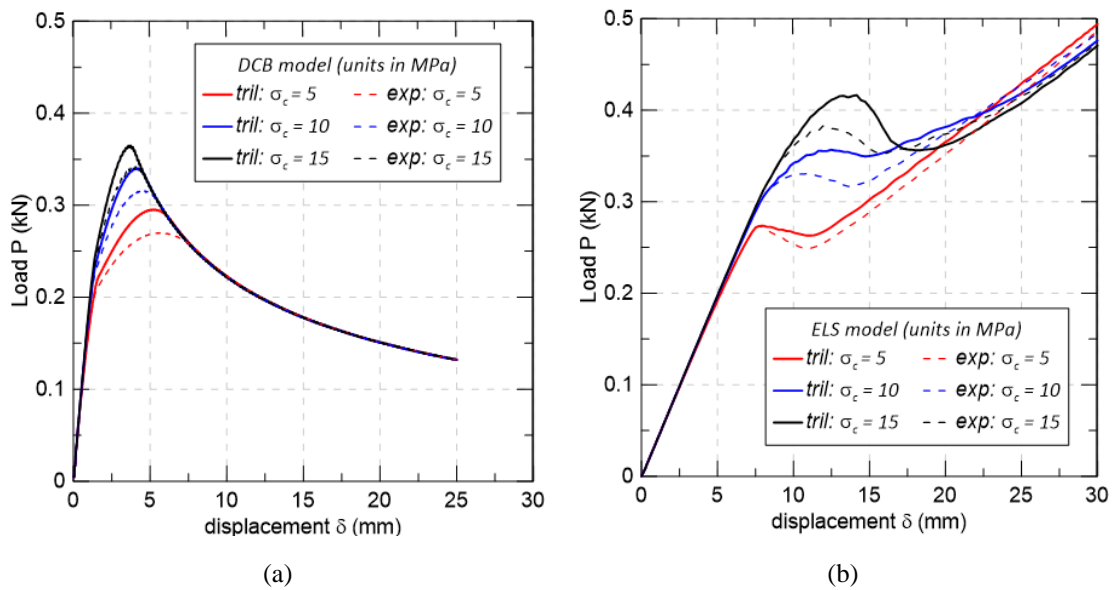


Figure 4.25. Influence of σ_c parameter: (a) in DCB tests; (b) in ELS tests.

4.7.2. Effect of the maximum fiber bridge traction (σ_{max})

Values for σ_{max} of 1, 2.5 and 4 MPa were tested, and the corresponding load vs. displacements curves are shown in Figure 4.26. The other adopted parameters used in both bilinear-exponential laws in DCB and ELS analyses are listed in Table 4.6. It can be observed that the influence of the parameter σ_{max} is very similar to that observed for σ_c . However, in this case, the loss of linearity point is the same for all curves and is not dependent on the parameter σ_{max} . For both DCB and ELS models, higher values of σ_{max} resulted in greater values of peak loads, especially for trilinear laws. In DCB models, no significant differences could be observed in the P vs. δ curve softening, in opposition to what occurred in ELS analyses. A σ_{max} variation from 1 to 2.5 MPa led to increases of 17% and 25% in the peak loads for DCB and ELS models, respectively, when adopting the trilinear law, whereas augmentations of 7% and 14% were observed for the same tests when varying the parameter from 2.5 to 4 MPa. For the bilinear-exponential law, increases of 32% were registered in the peak loads for both DCB and ELS models for a σ_{max} variation from 1 to 4 MPa.

Table 4.6. Adopted parameters for cohesive laws to assess the σ_{max} influence.

| σ_{max} (MPa) | σ_c (MPa) | G_{tip} (J/m ²) | G_{tot} (J/m ²) | γ |
|----------------------|------------------|-------------------------------|-------------------------------|----------|
| 1 | 19.5 | 0.25 G_{tot} | 1,250 | 0.01 |
| 2.5 | | | | |
| 4 | | | | |

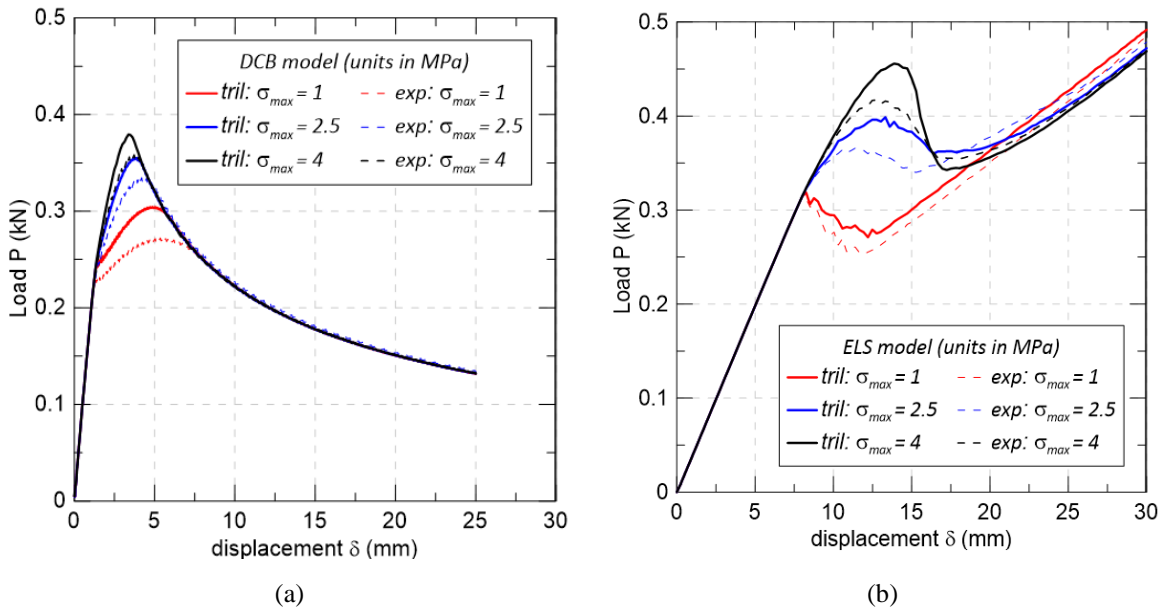


Figure 4.26. Influence of σ_{max} parameter: (a) in DCB tests; (b) in ELS tests.

4.7.3. Effect of the SERR due to crack initiation (G_{tip})

Although the parameter G_{tip} is the one that led to the smallest differences in the load vs. displacements curves, it is important to point that its significant influence in R-curves was observed in the experimental data fitting procedure. Values for G_{tip} equal to 20%, 40% and 60% of the total fracture energy G_{tot} were tested and the respective P vs. δ curves are shown in Figure 4.27. The other adopted parameters used in both bilinear-exponential laws in DCB and ELS analyses are listed in Table 4.7. In this parametric study, the G_{tot} was considered as 1,250 J/m² for both DCB and ELS tests. It was noticed that reductions of G_{tip} led to an earlier loss of linearity, also with a decrease in peak loads. In DCB models, increases of approximately 4% were observed in the peak load due the G_{tip} variation from both 20% to 40% and from 40% to 60% of G_{tot} , independent of the cohesive law used. The non-linearity starts approximately at the same point for both traction separation laws, occurring at P = 0.198 kN when $G_{tip} = 0,2 G_{tot}$ and at P = 0.287 kN for $G_{tip} = 0,6 G_{tot}$. Differences lower than 5% were observed between the peak loads of the trilinear and the respective bilinear-exponential laws. On the other hand, in ELS models, increases of 12% and 7% were observed in the peak loads when G_{tip} varied from 20% to 60% of G_{tot} , considering a trilinear and bilinear-exponential laws, respectively.

Table 4.7. Adopted parameters for cohesive laws to assess the G_{tip} influence.

| G_{tip} (J/m ²) | σ_c (MPa) | σ_{max} (MPa) | G_{tot} (J/m ²) | γ |
|-------------------------------|------------------|----------------------|-------------------------------|----------|
| 0.2 G_{tot} | 19.5 | 0.2 σ_c | 1,250 | 0.01 |
| 0.4 G_{tot} | | | | |
| 0.6 G_{tot} | | | | |

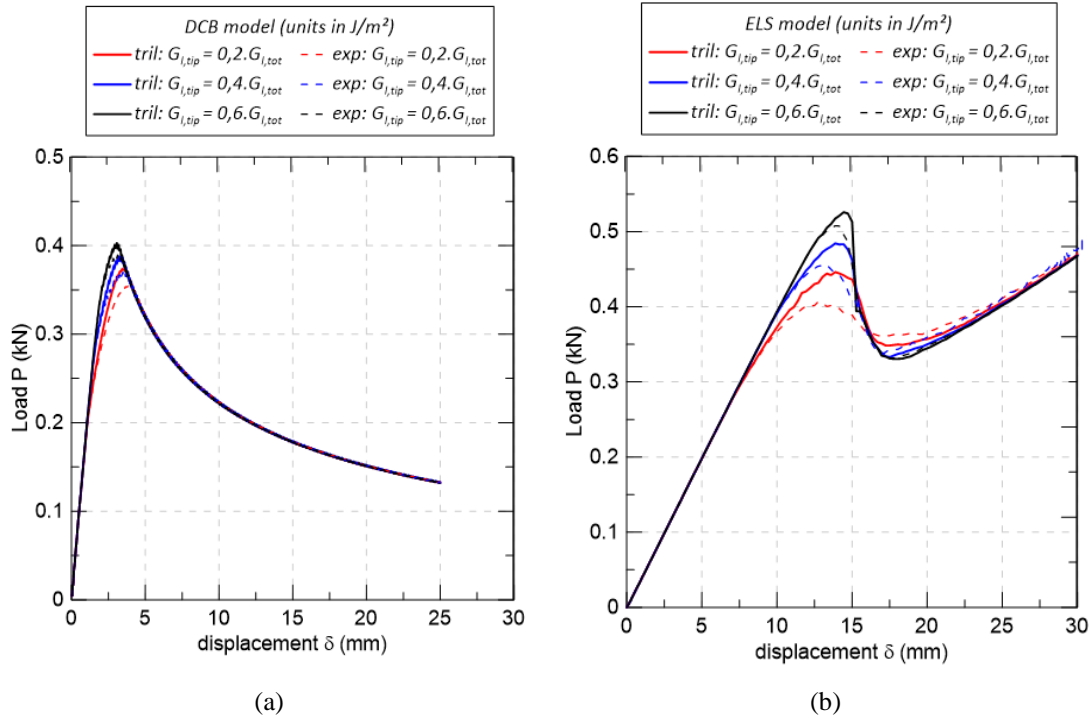


Figure 4.27. Influence of σ_{max} parameter: (a) in DCB tests; (b) in ELS tests.

4.7.4. Effect of the SERR due to fiber bridging (G_{tot})

The parameter G_{tot} presented the greatest influence on the P vs. δ curves, significantly changing the composites overall behavior both in DCB and ELS models, as can be seen in the Figure 4.28. The other adopted parameters used in both bilinear-exponential laws in DCB and ELS analyses are listed in Table 4.8. As observed for other parameters, the influence of the cohesive law shape increased as the G_{tot} value augmented as well. However, in this case, greater G_{tot} led to higher load values along all the curve P vs. δ . In DCB models, the peak loads when considering trilinear laws with G_{tot} equal to 3,000 J/m² were 59% higher than the results provided by models where G_{tot} equal to 1,000 J/m² was adopted. On the other hand, for the bilinear-exponential laws, this proportion corresponded to 30%.

For the ELS models, it can be noticed that the total fracture energy was directly related with the post-peak behavior. In other words, higher G_{tot} values apparently simulated composites with a more pseudo-ductile behavior. The peak loads presented increases of 29% and 27% when varying the total fracture energy from 1,000 to 3,000 J/m², considering the trilinear and bilinear-exponential laws, respectively.

Table 4.8. Adopted parameters for cohesive laws to assess the G_{tot} influence.

| G_{tot} (J/m ²) | σ_c (MPa) | σ_{max} (MPa) | G_{tip} (J/m ²) | γ |
|-------------------------------|------------------|----------------------|-------------------------------|----------|
| 1,000 | 19.5 | $0.2 \sigma_c$ | $0.2 G_{tot}$ | 0.01 |
| 2,000 | | | | |
| 3,000 | | | | |

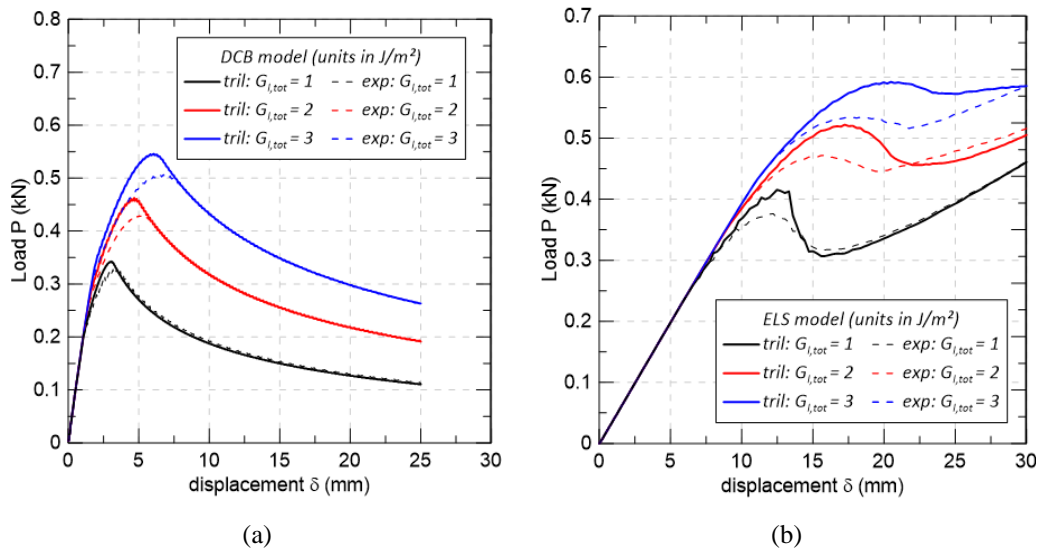


Figure 4.28. Influence of σ_{max} parameter: (a) in DCB tests; (b) in ELS tests.

4.7.5. Effect of the parameter γ

The parameter γ related to the curvature of the exponential function influences the overall behavior of P vs. δ curves from the loss of linearity point. The other adopted parameters used in both bilinear-exponential laws in DCB and ELS analyses are listed in Table 4.9. In the DCB model, when varying γ from 0.01 to 1.0, a decrease of 13% was observed for the maximum load, along with a shift downwards of all the post-peak curve regions. On the other hand, for the ELS model, this variation led to a decrease of 10% in the peak load. In this case, it can

be noticed that the curves with $\gamma = 0.01$ and $\gamma = 1.0$ tended to get closer in the post-peak region.

Table 4.9. Adopted parameters for cohesive laws to assess the γ influence.

| γ | σ_c (MPa) | σ_{max} (MPa) | G_{tip} (J/m ²) | G_{tot} (J/m ²) |
|----------|------------------|----------------------|-------------------------------|-------------------------------|
| 0.01 | 19.5 | $0.2 \sigma_c$ | $0.25 G_{tot}$ | 1,250 |
| 1 | | | | |

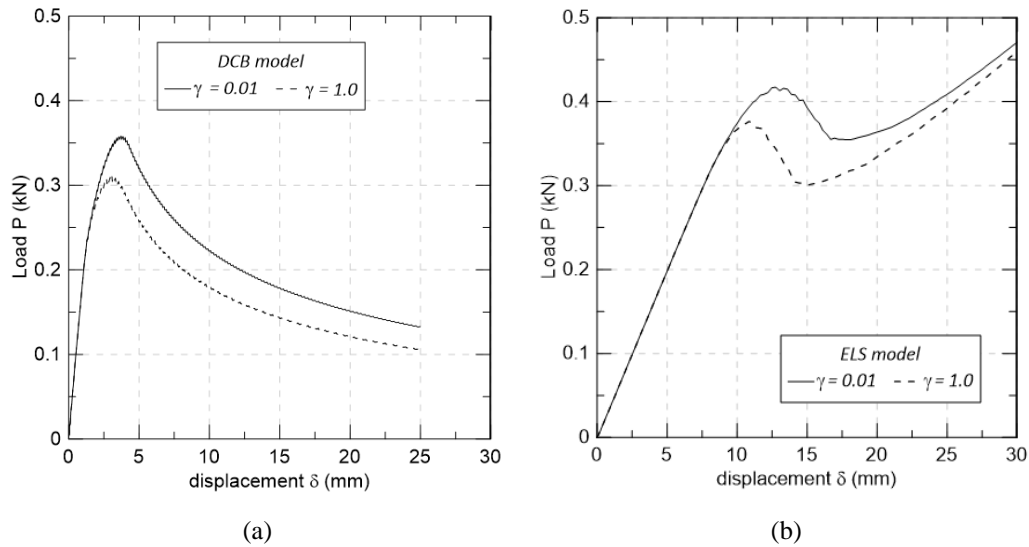


Figure 4.29. Influence of the parameter γ : (a) in DCB tests; (b) in ELS tests.

4.8. Conclusions

In this work, CZM was used to numerically simulate the DCB and ELS experimental tests. Three different cohesive laws (with bilinear, bilinear-exponential and trilinear shapes) were tested to investigate the appropriate shape and parameters to be used in pultruded glass fiber-polymers with fiber bridging. A parametric study was conducted to give some elucidation for fitting procedures with three-part cohesive laws. The numerical results and values for SERR were compared with those obtained experimentally presented in Chapter 3.

The following conclusions can be highlighted:

- Regarding the fitted trilinear and bilinear-exponential laws, both provided good results in terms of the load *vs.* displacement curves for Modes I and II, especially in terms of peak load. However, the latter presented SERR values closer to the ones obtained experimentally, both for crack initiation and propagation. The classical fitted bilinear law generally overestimated the peak load in both fracture modes, proving once more that it is not suitable for expressing the behavior of specimens with fiber bridging. Nevertheless, it is important to point out that it led to good agreements in terms of compliance, COD and crack length predictions, also simulating well, for Mode I, the post-peak region in *P vs. δ* curves.
- For mode I, the MBT_{ASTM} presented the closest results to the numerical model for the SERR for crack propagation ($G_{I,tot}$), with a difference of 4%, whereas CC-f presented the furthest results, with a difference of 8.1%. On the other hand, for the SERR for crack initiation ($G_{I,tip}$), the CC-f presented the closest results to the numerical model, when considering the bilinear-exponential law. In terms of R-curve, the MBT_{ASTM} and the MCC_{ASTM} resulted in a very good agreement with numerical simulations.
- For Mode II, the use of the average experimental SERR values, both for crack initiation and propagation obtained through the CBTE and EMC methods enabled to numerically simulate very well the composites load *vs.* displacement curves. On the other hand, the SERR for both crack initiation and propagation obtained through the SBT method resulted in differences up to 44% from the numerical model. Furthermore, none of the data reduction methods used to predict the experimental SERR could accurately express the compliance response, R-curve behavior and crack lengths obtained by FEM models.
- For both Modes, the use of 30% of the matrix tensile strength to represent the interfacial strength σ_c along with the δ_f obtained through experimental tests resulted in a good fit of experimental *P vs. δ* curves.
- The parametric study has shown how each parameter of the three-part cohesive law has a different influence depending on the type of test. Higher values of σ_c , σ_{max} and G_{tip} mainly result in greater peak loads, whereas the parameter G_{tot} might lead to a general shift of the curve. The bilinear-

exponential law tends to result in lower values of corresponding loads, and this effect becomes more significant as the parameter γ value increases.

4.9. References

- [1] BEAUMONT, P. W., ZWEBEN, C. H., GDUTOS, E., TALREJA, R., POURSAARTIP, A., CLYNE, T. W., ... & SOUTIS, C. (EDS. . **Comprehensive composite materials II (vol. 6)**. Amsterdam, The Netherlands: Elsevier, 2018.
- [2] SHAHVERDI, M.; VASSILOPOULOS, A. P.; KELLER, T. Mixed-mode quasi-static failure criteria for adhesively-bonded pultruded GFRP joints. **Composites Part A: Applied Science and Manufacturing**, v. 59, p. 45–56, 2014.
- [3] ELICES, M. et al. The cohesive zone model: Advantages, limitations and challenges. **Engineering Fracture Mechanics**, v. 69, n. 2, p. 137–163, 2001.
- [4] LIU, P. F. et al. Finite element analysis of the influence of cohesive law parameters on the multiple delamination behaviors of composites under compression. **Composite Structures**, v. 131, p. 975–986, 2015.
- [5] HEIDARI-RARANI, M.; SHOKRIEH, M. M.; CAMANHO, P. P. Finite element modeling of mode I delamination growth in laminated DCB specimens with R-curve effects. **Composites Part B: Engineering**, v. 45, n. 1, p. 897–903, 2013.
- [6] TURON, A., DAVILA, C. G., CAMANHO, P. P., & COSTA, J. An engineering solution for mesh size effects in the simulation of delamination using cohesive zone models. **Engineering fracture mechanics**, v. 74, n. 10, p. 1665–1682, 2007.
- [7] GUTKIN, R. et al. Modelling the R-curve effect and its specimen-dependence. **International Journal of Solids and Structures**, v. 48, n. 11–12, p. 1767–1777, 2011.
- [8] SUO, Z.; BAO, G.; FAN, B. **Delamination R-curve phenomena due to damage** *Journal of the Mechanics and Physics of Solids*, 1992.
- [9] GHADIRDOKHT, A.; HEIDARI-RARANI, M. Delamination R-curve behavior of curved composite laminates. **Composites Part B: Engineering**, v. 175, n. June, p. 107139, 2019.
- [10] SØRENSEN, B. F.; JACOBSEN, T. K. Large-scale bridging in composites:

- R-curves and bridging laws. **Composites Part A: Applied Science and Manufacturing**, v. 29, n. 11, p. 1443–1451, 1998.
- [11] TAMUZS, V.; TARASOV, S.; VILKS, U. Progressive delamination and fiber bridging modeling in double cantilever beam composite specimens. **Engineering Fracture Mechanics**, v. 68, n. 5, p. 513–525, 2001.
- [12] SORENSEN, L. et al. Bridging tractions in mode I delamination: Measurements and simulations. **Composites Science and Technology**, v. 68, n. 12, p. 2350–2358, 2008.
- [13] VOLOKH, K. Y. Comparison between cohesive zone models. **Communications in Numerical Methods in Engineering**, v. 20, n. 11, p. 845–856, 2004.
- [14] CHANDRA, N. et al. Some issues in the application of cohesive zone models for metal-ceramic interfaces. **International Journal of Solids and Structures**, v. 39, n. 10, p. 2827–2855, 2002.
- [15] ALFANO, G. On the influence of the shape of the interface law on the application of cohesive-zone models. **Composites Science and Technology**, v. 66, n. 6, p. 723–730, 2006.
- [16] SONG, S. H.; PAULINO, G. H.; BUTTLAR, W. G. Influence of the cohesive zone model shape parameter on asphalt concrete fracture behavior. **AIP Conference Proceedings**, v. 973, n. 2008, p. 730–735, 2008.
- [17] ALMEIDA-FERNANDES, L.; SILVESTRE, N.; CORREIA, J. R. Fracture toughness-based models for web-crippling of pultruded GFRP profiles. **Composites Part B: Engineering**, v. 230, n. September 2020, 2022.
- [18] ALMEIDA-FERNANDES, L. et al. Compressive transverse fracture behaviour of pultruded GFRP materials: Experimental study and numerical calibration. **Composite Structures**, v. 247, n. February, 2020.
- [19] ZHANG, Y.; VASSILOPOULOS, A. P.; KELLER, T. Mode I and II fracture behavior of adhesively-bonded pultruded composite joints. **Engineering Fracture Mechanics**, v. 77, n. 1, p. 128–143, 2010.
- [20] LIU, W.; FENG, P.; HUANG, J. Bilinear softening model and double K fracture criterion for quasi-brittle fracture of pultruded FRP composites. **Composite Structures**, v. 160, p. 1119–1125, 2017.
- [21] DASSAULT SYSTÈMES. **Abaqus**. Disponível em:

<<https://www.3ds.com/support/hardware-and-software/simulia-system-information/abaqus-2021/>>. Acesso em: 19 jul. 2022.

[22] CAMESELLE-MOLARES, A. et al. Numerical simulation of two-dimensional in-plane crack propagation in FRP laminates. **Composite Structures**, v. 200, n. April, p. 396–407, 2018.

[23] LAUNEY, M. E.; RITCHIE, R. O. On the fracture toughness of advanced materials. **Advanced Materials**, v. 21, n. 20, p. 2103–2110, 2009.

[24] CAMESELLE-MOLARES, A.; VASSILOPOULOS, A. P.; KELLER, T. Experimental investigation of two-dimensional delamination in GFRP laminates. **Engineering Fracture Mechanics**, 2018.

[25] SONG, K.; DAVILA, C.; ROSE, C. Guidelines and parameter selection for the simulation of progressive delamination. **2008 ABAQUS User's Conference**, p. 1–15, 2008.

[26] SOTO, A. et al. Cohesive zone length of orthotropic materials undergoing delamination. **Engineering Fracture Mechanics**, v. 159, p. 174–188, 2016.

[27] HILLERBORG, A.; MODEER, M.; PETERSSON, P. E. Analysis of crack formation and crack growth in concrete by means of fracture mechanics and finite elements. **American Concrete Institute, ACI Special Publication**, v. SP-249, p. 225–237, 2008.

[28] RICE, J. R. The mechanics of earthquake rupture. **Physics of the Earth's Interior**, n. January 1980, p. 555–649, 1980.

[29] CHEN, J. Simulation of multi-directional crack growth in braided composite T-piece specimens using cohesive models. **Fatigue and Fracture of Engineering Materials and Structures**, v. 34, n. 2, p. 123–130, 2011.

[30] GONZÁLEZ, E. V. et al. Simulation of delamination by means of cohesive elements using an explicit finite element code. **Computers, Materials and Continua**, v. 9, n. 1, p. 51–92, 2009.

[31] ERSOY, N. et al. A comparative numerical study aiming to reduce computation cost for mode-I delamination simulations. **ECCM 2018 - 18th European Conference on Composite Materials**, n. June, p. abntabnt, 2020.

[32] BANK, L. C. **Composites for construction: structural design with FRP materials**. [s.l: s.n.].

[33] SHAHVERDI, M.; VASSILOPOULOS, A. P.; KELLER, T. Modeling effects

of asymmetry and fiber bridging on Mode I fracture behavior of bonded pultruded composite joints. **Engineering Fracture Mechanics**, v. 99, p. 335–348, 2013.

[34] RAHEEM, Z. **Standard Test Method for Mode I Interlaminar Fracture Toughness of Unidirectional Fiber-Reinforced Polymer Matrix Composites 1** **Standard Test Method for Mode I Interlaminar Fracture Toughness of Unidirectional Fiber-Reinforced Polymer Matrix Composites 1**. [s.l: s.n.].

[35] MOLLÓN, V. et al. Mixed mode fracture toughness: An empirical formulation for GI/GII determination in asymmetric DCB specimens. **Engineering Structures**, v. 32, n. 11, p. 3699–3703, 2010.

[36] DÁVILA, C. G.; ROSE, C. A.; CAMANHO, P. P. A procedure for superposing linear cohesive laws to represent multiple damage mechanisms in the fracture of composites. **International Journal of Fracture**, v. 158, n. 2, p. 211–223, 2009.

[37] LAFFAN, M. J. et al. Measurement of the in situ ply fracture toughness associated with mode I fibre tensile failure in FRP. Part I: Data reduction. **Composites Science and Technology**, v. 70, n. 4, p. 606–613, 2010.

5. Novel Multi-crack Damage Approach for Pultruded Fiber-Polymer Web-flange Junctions

5.1. Introduction

Over the last four decades, pultruded glass-fiber polymers have been earning their place in the structural field. The lightness and high strength, combined with the tolerance to de-icing salts and easy installation made these composites to find large applications, among which one may cite pedestrian bridges, *off-shore* structures, buildings rehabilitation and bridge decks [1]. However, there remain topics not fully understood, especially concerning their failure mechanisms and multi-crack behavior. Most of the available numerical models intending to evaluate the composites crack behavior are focused on the fracture assessment due to a single crack, in contrast to the actual failure behavior of multilayered composites. Very few works in literature are focused on the multi-crack behavior of fiber-polymer elements. Chen [2] investigated the multi-directional and single crack propagation in a T-piece from a braided composite, by using a bilinear constitutive law. The author succeeded by using cohesive models to simulate the fracture behavior and predict failure loads of a specimen under pull-out end condition. Moreover, both power law and Benzeggagh-Kenane equation [3] were tested to simulate damage evolution and no significant differences were observed in load-displacement curves when comparing the use of both laws. Chen and Fox [4] investigated the general multi-delamination of the same T-piece specimen under mixed mode loading conditions (bending and pulling force). Liu *et al.* [5] studied the effects of cohesive law parameters on the post buckling and multiple delamination of laminates under compression. The authors used the Cohesive Zone Model (CZM), implementing both bilinear and exponential laws and concluding that the cohesive shapes have not large effect on the load responses, although improved results were observed for

exponential laws. Moreover, it was observed that zero-thickness cohesive elements led to more computational efficiency and numerical convergence.

To the best of the author's knowledge, no previous research has addressed to the multiple and parallel crack behavior of pultruded elements. However, the progressive failure of this type of material is often related to several small imperfections and interface issues, which may often result in multiple layered delamination. In this context, a multi-failure damage approach to interlaminar fracture – especially focused on weak regions with more incidence of defects such as the junctions – is valuable for pultruded fiber-polymer composites structural design. Furthermore, the progressive failure achieved by multiple cracks may also help the composite to experience a pseudo-ductile behavior. In other words, in brittle materials, strategies are needed to obtain an inelastic non-linear behavior, which may be achieved through the energy dissipated from damage mechanisms [6]. Several studies in literature are focused on the investigation of different means to provide pseudo-ductility to this type of material [7], although it has not been intentionally exploited in existing design codes [8].

In parallel, it is well known that delamination and failure process are often related to the web-flange junctions (WFJs), both in bridge decks [9,10] and in pultruded profiles [11–16]. As discussed in Chapter 2, the particular fiber architecture at junctions, with more incidence of defects, mat wrinkling and presence of resin-rich zones [17,18] is responsible for the fast properties degradation that occurs through a progressive damage accumulation. Due to the WFJs' important role in composite's general behavior and failure, experimental works focused on characterizing its stiffness and strength are available in literature [19–25]. Added to this, some authors have dedicated significant efforts to develop numerical analyses able to predict the WFJs rotational stiffness, understanding how the boundary conditions of WFJs experiments affect the junctions characterization, while evaluating the influence of the junctions' semi-rigidity on the buckling loads and overall composites' behavior [18,26–28]. Nevertheless, in this context, only few numerical models addressing the crack propagation assessment in WFJs have been reported in literature. Fascetti *et al.* [29] developed a nonlinear lattice model using Tsai-Hill failure criterion to simulate pull-out tests and evaluate the crack propagation path, strength and stiffness in WFJs of pultruded glass fiber-polymer

I-beams. Although not considering the particularities of the different layers composing the junction, the authors' model was able to correctly predict the crack path observed experimentally, without the need to be superimposed by the user. Bank and Yin [16] proposed a numerical node-separation procedure to simulate the progressive failure in the post-buckling regime of I-beams due to local web-flange separation. According to the authors, the composite's failure mode, usually initiated at the junctions, can be modified by improvements in fiber architecture, with, for instance, the addition of biaxial fabrics at junction's region, which would enhance the transverse tensile strength. Recently, Yan *et al.* [30] simulated the Mode I delamination in 3D woven composite T-joints subjected to quasi-static tensile pull-off loading. The authors used a voxel based cohesive zone model and stated that although more accurate tractions separation laws have been proposed in literature, a bilinear constitutive law was adopted due to commercial availability. The quadratic stress criterion and the mixed mode power law were selected for damage initiation and evolution, respectively.

In view of all that, the main objective of this chapter is to present the development of a methodology that allows to assess the contribution of each crack to the overall behavior of WFJs with multiple cracks. The novel approach is applied to experiments conducted on WFJs extracted from bridge decks [21] that led to the progressive growth of three relevant curved and parallel main cracks. A numerical investigation is also carried out to compare results of simulations considering fracture properties estimated from the novel methodology with those obtained from specific tests on flat parts (see Chapters 3 and 4). Besides promoting the understanding on the progressive multiple delamination growth at the composite's weakest region, the multi-crack analysis could help to reduce time-consuming experiments and improve the existing design codes. Additionally, WFJs experiments were conducted on a second type of bridge deck composed by a different number of layers and distinct sequence of roving and fabric layers, with the purpose to address a discussion on the influence and benefits of multiple interspersed layers on the composite's behavior.

5.2. Experimental program

5.2.1. DS decks tests

Yanes-Armas *et al.* [21] conducted web-cantilever bending tests on WFJs of the *DuraSpan* (DS) bridge deck system. The load was applied at 65 mm from the junction under displacement control at a rate of 0.01 mm/s. For the validation of the numerical model presented in this chapter, the experimental results regarding the *If-o* series reported in [21] will be used. The two first characters “*I*” and “*f*” indicate that the specimens were extracted from the deck part with an inclined web and having the respective web-flange junction located farther to the adhesively bonded joints, as illustrated in Figure 5.1a. The additional character “*o*” indicates that the load was applied in order to produce tensile stresses on the obtuse angle side of the junction, as shown in Figure 5.1b. The decks were constituted of rovings, triaxial multi-ply fabrics (oriented in -45° , 90° and 45°) and non-structural mats embedded in isophthalic polyester resin. The fiber architecture in the tensioned part of the tested WFJs is formed by three layers of triaxial fabrics, interspersed with three layers of rovings.

The dimensions of the specimens extracted from DS decks, with 50-mm of width, are indicated in Figure 5.1a, along with the test fixture used in [21]. In all, three specimens from *If-o* series (named hereafter as *If-o₁*, *If-o₂* and *If-o₃*) were tested and their junction’s rotational stiffness were found to be significantly high, reaching “infinite” values (see [21]). A resin pocket located near the roving core and some inequality in triaxial fabric distribution across the web thickness was observed at all specimens, as detailed in [7].

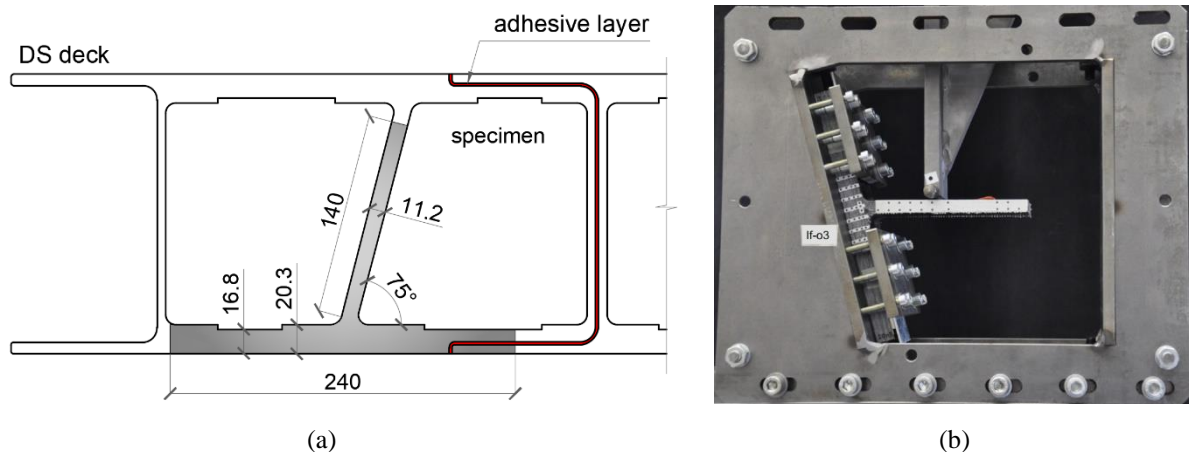


Figure 5.1. WFJs experiments in DS decks: (a) specimens’ dimensions; (b) test fixture [7].

Burn-off tests conducted at the *Laboratory for Processing of Advanced Composites (LPAC)* in the *École Polytechnique Fédérale de Lausanne (EPFL)* showed that the flange's glass fiber volume ratio is equal to 52.4%, among which the roving and triaxial fabric volumes correspond to 22% and 30.4%, respectively. On the other hand, the web is composed by 48% of glass fiber volume content, among which 13.5% are roving and 34.5% are triaxial fabrics. The non-structural mats were considered as part of the triaxial fabrics both in the fiber content estimated and in the numerical model. To evaluate the triangular core material constituent, a small piece of the junction was subjected to an additional burn-off test. Although the triangular core is usually reported in literature as a resin-rich zone [17], it was observed that, in *DS* decks, this region is filled with roving, as shown in Figure 5.2.

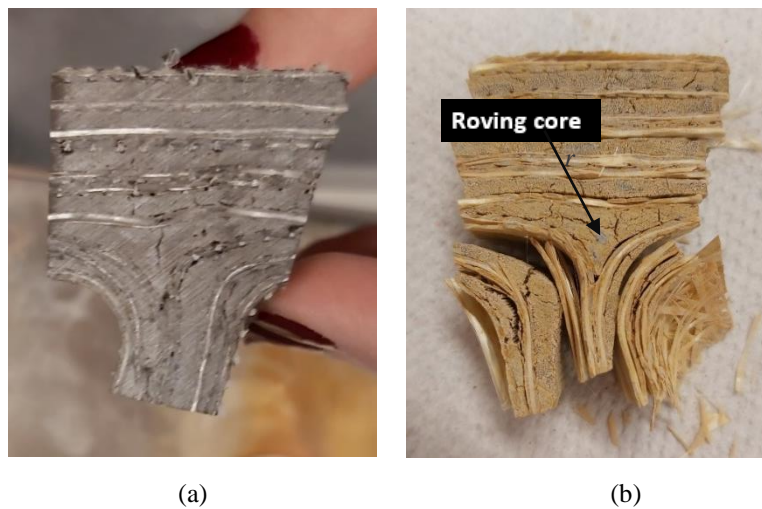


Figure 5.2. Assessment of the triangular core constituent: (a) junction before burn-off; (b) junction after burn-off.

The load vs. displacement curves obtained from *DS* decks experiments are presented in Figure 5.3a and were carefully reported and analyzed in [21]. As can be observed, all specimens presented a similar initial stiffness. While the *If-01* and *If-02* presented similar peak load values, equal to 0.95 kN and 0.99 kN, respectively, the *If-03* specimen reached the highest maximum load among the three experiments, equal to 1.28 kN. All specimens were able to bear similar values of load (between 0.65 and 0.8 kN) after the observed sharp drops, still experiencing displacement increasing and cracks development. This behavior was achieved by the occurrence

of multiple cracks, located at the different layers of the composite. The through-thickness tensile stresses have governed the WFJs failure in the upper curved layers of the junction [7]. In order to numerically simulate the given multi-crack behavior, the respective crack lengths were measured in this work, as will be discussed in the next topic. However, it is important to point out that after several preliminary studies, it was observed that the crack analysis should be focused on the experimental data corresponding to a maximum displacement applied of 4 mm, since after this stage several minor cracks would play a relevant role in the composite's failure process, hampering the accuracy of the investigation. Therefore, the load vs. displacement curves assessed in this research are presented in Figure 5.3b.

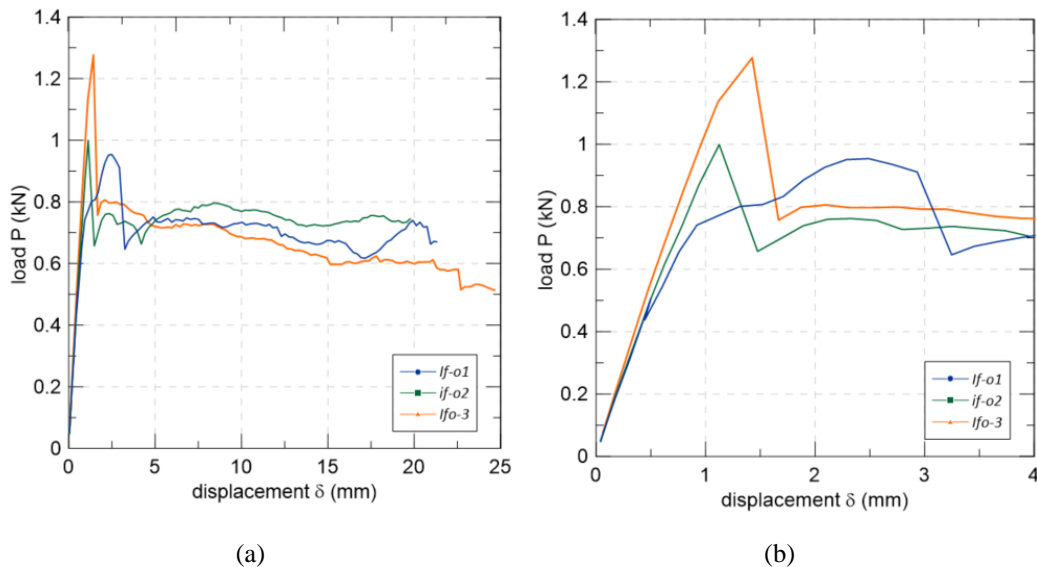


Figure 5.3. Load vs. displacement curves: (a) until the final displacement applied; (b) until a displacement applied of 4 mm.

5.2.2. Cracks measurement methodology

The specimens $If-o1$, $If-o2$ and $If-o3$ presented similar crack patterns, as shown in Figure 5.4, with the propagation of multiple cracks, among which three have shown greater development when compared to the others, both in terms of length and crack opening. In other words, although minor cracks have occurred, three main and parallel cracks, described hereafter as a_1 (first crack visually identified), a_2 (second crack visually identified) and a_3 (third crack visually

identified), were assumed to govern the failure process during all experiments in all specimens. In order to easily identify their location, each main crack will be designated as *inner crack* (subscript -i), *middle crack* (subscript -m) or *outer crack* (subscript -o), according to Figure 5.5. The crack pattern used as reference to this work, *i.e.*, obtained for a displacement applied of 4 mm, is presented in Figure 5.6, where the nomenclature adopted to identify the major cracks (a_1 , a_2 and a_3) and the minor ones (a_x and a_y) is illustrated.

Minor cracks, having initial crack length lower than 3 mm and without any further development during testing were neglected in order to simplify the cracks assessment. It is important to point out that, in all specimens, it was observed that the longer cracks were formed by the progressive union of several smaller cracks, increasing the difficulty in classifying properly the main cracks lengths. Minor parallel cracks presenting a significant length were considered as being part of the main cracks, aiming not to preclude the accuracy of the numerical analysis. For instance, for the specimen *If-o3*, the crack indicated with a yellow arrow in Figure 5.6c was considered as a part of the main crack a_{1-m} , due to its significant length.

Furthermore, some cracks experienced layers jump, as, for instance, the crack a_{2-o} in *If-o1* specimen. However, in an attempt to simplify and enable the analysis and numerical model, it was assumed that all the three cracks occurred between roving and fabric layers.

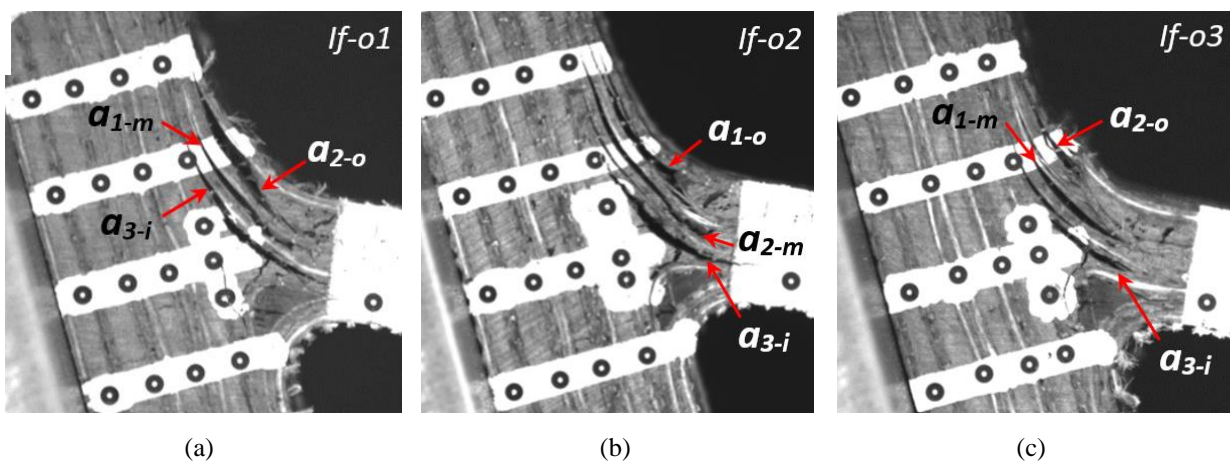


Figure 5.4. Crack pattern with three main cracks: (a) *If-o1* at $\delta = 11.4$ mm; (b) *If-o2* at $\delta = 11.1$ mm; (c) *If-o3* at $\delta = 11.0$ mm.

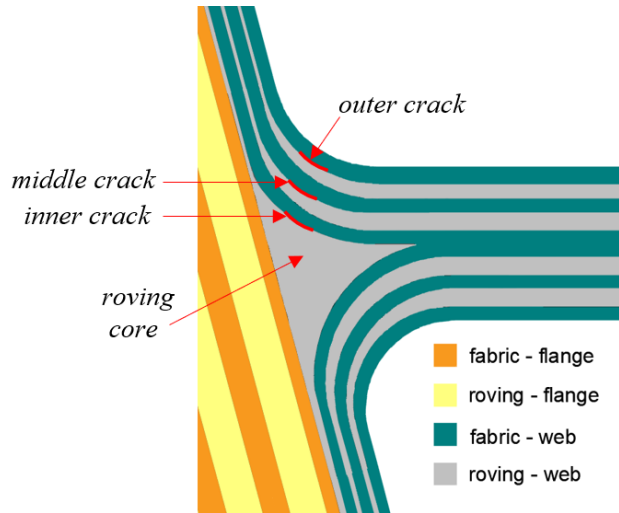


Figure 5.5. Main cracks definition

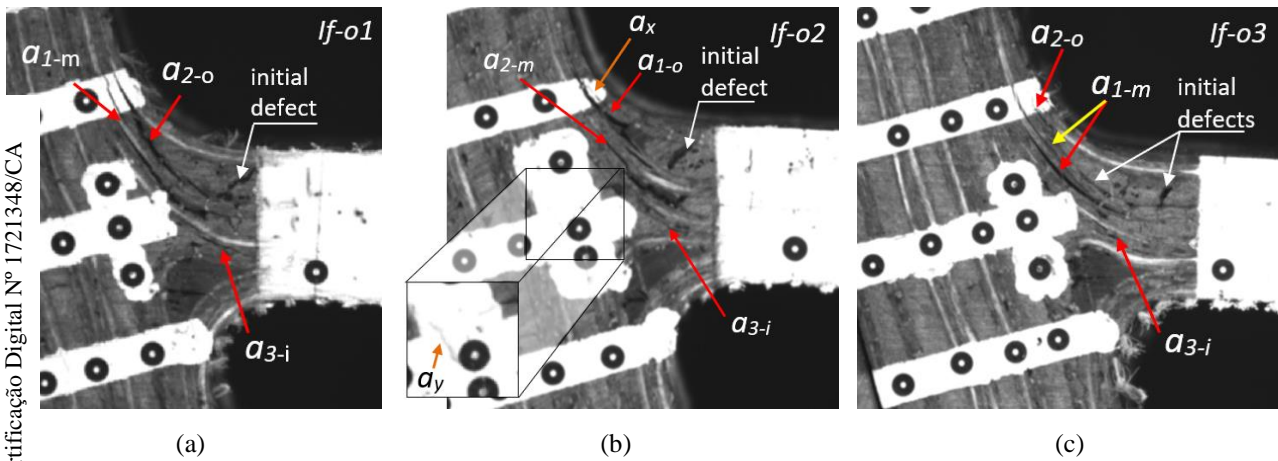


Figure 5.6. Major and minor cracks nomenclature: (a) *If-o1* specimen at $P = 0.71$ kN; $\delta = 4.0$ mm; (b) *If-o2* specimen at $P = 0.66$ kN; $\delta = 4.2$ mm; (c) *If-o3* specimen at $P = 0.76$ kN; $\delta = 4.1$ m.

The crack lengths were measured visually through high-quality photos taken every 2 seconds during the test, with a *Sony XCG-5005E* progressive scan. The cracks were mapped in the pictures taken at approximately each 21 seconds with the aid of the software *AutoCAD 2020* [31]. Although the visual technique allows some uncertainties, it has been broadly used in fracture mechanics approaches, with satisfactory results reported in literature, *e.g.* [32–35].

5.2.3. Novel approach to multi-crack assessment

The main assumption of the proposed approach consists in assuming for all the three cracks a_1 , a_2 and a_3 the same function correlating the compliance with the

crack length, also considering that the cracks occur in the same material, *i.e.*, in the interface between rovings and triaxial fabrics. Taken this into account, it was assumed a *total crack length*, a_t , given by the sum of a_1 , a_2 and a_3 . In order to quantify their dominance over the smaller cracks and understand better the failure process, the sum of the minor crack lengths (a_x and a_y in the case of *If-o2*) is also considered, resulting in the total crack length named as a_s hereafter. It is important to highlight that, according to literature [36], unidirectional curved laminates, with similar shape to WFJs, present a large Mode I dominance, which simplifies the analysis. Considering the Compliance Calibration (CC) Method, the strain energy release rate (SERR) for a single crack with length a is defined by Equation (5.1).

$$G = \frac{P^2}{2b} \frac{\partial C}{\partial a} \quad (5.1)$$

Where P is the applied load, b is the specimen's width and $\partial C/\partial a$ is the variation of the compliance (C) related to the propagation of the aforementioned crack of length a . The compliance function can be expressed according to Equation (5.2) – reported by Laffan *et al.* [37] and originally presented by Dávila *et al.* [38] –, in which the parameters α , β and χ are constants determined from regression of the compliance vs. the crack length curve. In this work, the coefficient χ was assumed equal to 2.0 for sake of simplicity, based on previous works [38].

$$C = (\alpha a + \beta)^\chi \quad (5.2)$$

Considering now a number N of cracks that develop on the same material, the Equations (5.3) and (5.4) express the compliance and SERR of a composite with multiple cracks, respectively. In these equations, a_i represents the length of the i_{th} crack, with i varying from 1 to N . Based on the fundamental assumption described in the beginning of this section, α and β are considered the same for all the cracks. Moreover, these equations consider that each crack contributes independently to the compliance.

$$C(a_1, a_2, \dots, a_N) = \sum_{i=1}^N (\alpha a_i + \beta)^\chi \quad (5.3)$$

$$G(a_1, a_2, \dots, a_N) = \frac{P^2}{2b} \sum_{i=1}^N \frac{\partial C}{\partial a_i} \quad (5.4)$$

In order to express the compliance and the fracture toughness as a function of the total crack length a_t (sum of the cracks), a coefficient k_i equal to $\frac{a_i}{a_t}$ is introduced, resulting in Equations (5.5) and (5.6).

$$C(a_1, a_2, \dots, a_N) = \sum_{i=1}^N (\alpha k_i a_t + \beta)^\lambda \quad (5.5)$$

$$G(a_1, a_2, \dots, a_N) = \frac{P^2}{2b} a_t \chi k_i \sum_{i=1}^N (\alpha k_i a_t + \beta)^{\lambda-1} \quad (5.6)$$

From this approach, it is possible to have a general and better comprehension of the fracture process generated by the multiple cracks. This approach enables the assessment of the compliance vs. total crack length a_t and the strain energy release rate (SERR) vs. total crack length a_t (R-curve), in which it is possible to separate the SERR related to each crack, as long as the crack lengths are measured separately during the experiment.

5.2.4. AS decks tests

In order to complement the experimental program and investigate the benefits of the existence of multiple layers, exploratory analogous WFJs tests were also performed in *ASSET* (AS) bridge decks for a qualitative comparison. These composites were manufactured by the Fiberline Composites A/S (Middelfart, Denmark) and are constituted by one thick unidirectional roving layer between four fabric layers and non-structural mats, as shown in Figure 5.7, *i.e.*, having less than half the number of layers of *DS* decks. Burn-off tests were conducted at the *Laboratory for Processing of Advanced Composites* (LPAC) in the *École Polytechnique Fédérale de Lausanne* (EPFL) following the recommendations of *ISO 1172:1996* [39] and the methodology presented in [40], showing that the AS decks present a higher glass fiber volume ratio than *DS* decks. In the former, the total glass fiber content constitutes 61.3% and 48.2% of the flange and web volumes, respectively. It was not possible to separately measure the fiber volume

content of roving, mats, and structural fabrics. As observed for *DS* decks, the triangular core material of *AS* decks is also constituted of roving.

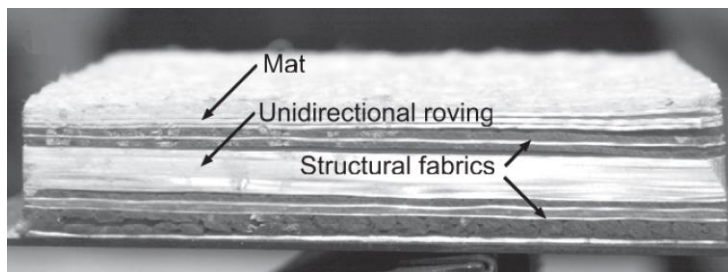


Figure 5.7. Fiber architecture of *AS* decks [41].

Five specimens having 49.7 ± 2 mm of width were tested on a table machine *Walter + Bai* with a load capacity of 50 kN. The specimens' dimensions are illustrated in Figure 5.8. The same set-up from *DS* tests was used, although with adaptations to consider the *AS* decks' different angle (60°) between the web and flange. The specimens' flange was clamped on only one junction's side by means of a steel plate having 10-mm of thickness and a set of 8-mm-diameter bolts, spaced of 28 mm, as shown in Figure 5.9. The tests were conducted under a displacement rate of 0.01 mm/s, with exception of the fourth specimen (*AS.04*), which was loaded at a rate of 0.005 mm/s. The load was applied in order to tension the junction on the acute angle side, with exception of the fifth specimen (*AS.05*). Different lever-arms were used in each test in order to track a possible change in the brittle behavior observed in load *vs.* displacement. The conditions of each specimen test are summarized in Table 5.1.

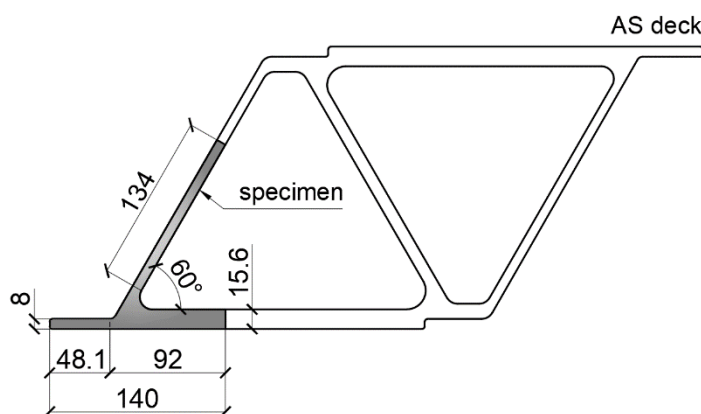


Figure 5.8. WJJs specimens' dimensions extracted from *AS* decks.

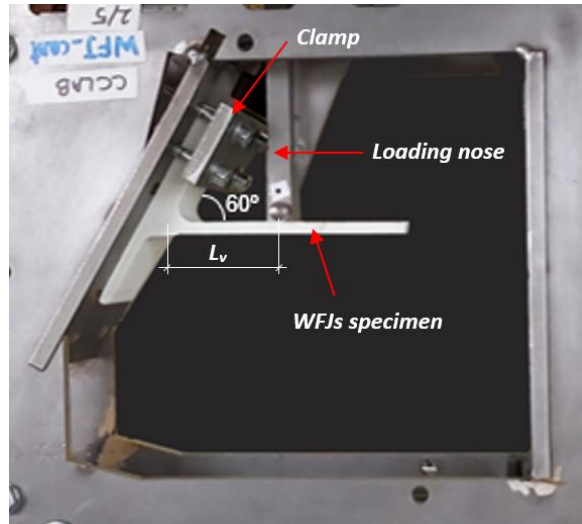


Figure 5.9. Used test fixture.

Table 5.1. AS tests information.

| <i>Specimen</i> | <i>Displacement rate (mm/s)</i> | <i>Lever arm (Lv) (mm)</i> | <i>Tensioned angle</i> |
|-----------------|---------------------------------|----------------------------|------------------------|
| AS.01 | 0.01 | 77 | acute |
| AS.02 | 0.01 | 82 | acute |
| AS.03 | 0.01 | 98 | acute |
| AS.04 | 0.005 | 99 | acute |
| AS.05 | 0.01 | 81 | obtuse |

5.3. Numerical investigation

5.3.1. Properties and boundary conditions

The concerned multi-layered pultruded junction was simulated in a two dimensional plane-strain finite element model, using Abaqus/Explicit 2021 v.6.21-6 [42], which was chosen for presenting better results in terms of convergency when compared to Abaqus/Standard. *DS* decks present several interspersed layers of roving and triaxial multi-ply fabrics, as previously shown in Figure 3.5, containing 9 layers in web and at least 11 layers in the flange. A scheme of the model with the layers distribution is presented in Figure 5.10, where four different materials were considered to constitute the junction specimen, according to its respective fiber volume ratio: 1. Triaxial fabrics and resin present in flange (orange); 2. Roving and resin present in flange (yellow); 3. Triaxial fabrics and resin present in web

(green); 4. Roving and resin present in web (grey). The layers individual modelling aims to lead to more accurate results, in view of the complex fiber architecture of this type of composite at the junctions. The triangular core was modeled with the properties of the *roving and resin* existing in the flange, according to the results of burn-off tests. The material properties used in the model were the same used in previous chapters. They were calculated based on the rule of mixtures and are presented in Table 5.2. It is important to point out that the properties on the roving direction are indicated by axis 3, while the axis 2 corresponds to the through thickness properties and the axis 1 corresponds to the other transverse direction, as shown in Figure 5.11. In the curved part of the junction, the axes follow the edge with an arc shape.

To simulate the experiment configuration, the flange was restricted on both sides, in the vertical (x) and horizontal (y) direction, corresponding to the experimental clamped regions, as shown in Figure 5.10. The remaining part of the flange outside edge was also restricted in the x axis. A displacement of 4 mm was applied at 91 mm of the web's end. The model account with 22,715 nodes and 6,039 elements.

Table 5.2. Materials properties used in the numerical model.

| <i>Layers</i> | E₁₁ (MPa) | E₂₂ (MPa) | E₃₃ (MPa) | v₁₂ | v₁₃ | v₂₃ | G₁₂ (MPa) | G₁₃ (MPa) | G₂₃ (MPa) | |
|---------------|-------------------------------------|--------------------------------|--------------------------------|-----------------------|-----------------------|-----------------------|--------------------------------|--------------------------------|--------------------------------|-------|
| Flange | transverse to roving + resin | 5,460 | 5,460 | 31,000 | 0.30 | 0.05 | 0.05 | 2,100 | 2,100 | 2,100 |
| | tri-fabric + resin | 26,510 | 5,460 | 12,340 | 0.27 | 0.27 | 0.35 | 3,720 | 6,960 | 3,680 |
| Web | transverse to roving + resin | 4,670 | 4,670 | 23,400 | 0.30 | 0.06 | 0.06 | 1,800 | 1,800 | 1,800 |
| | tri-fabric + resin | 24,580 | 5,460 | 10,640 | 0.16 | 0.36 | 0.16 | 3,110 | 6,120 | 3,150 |

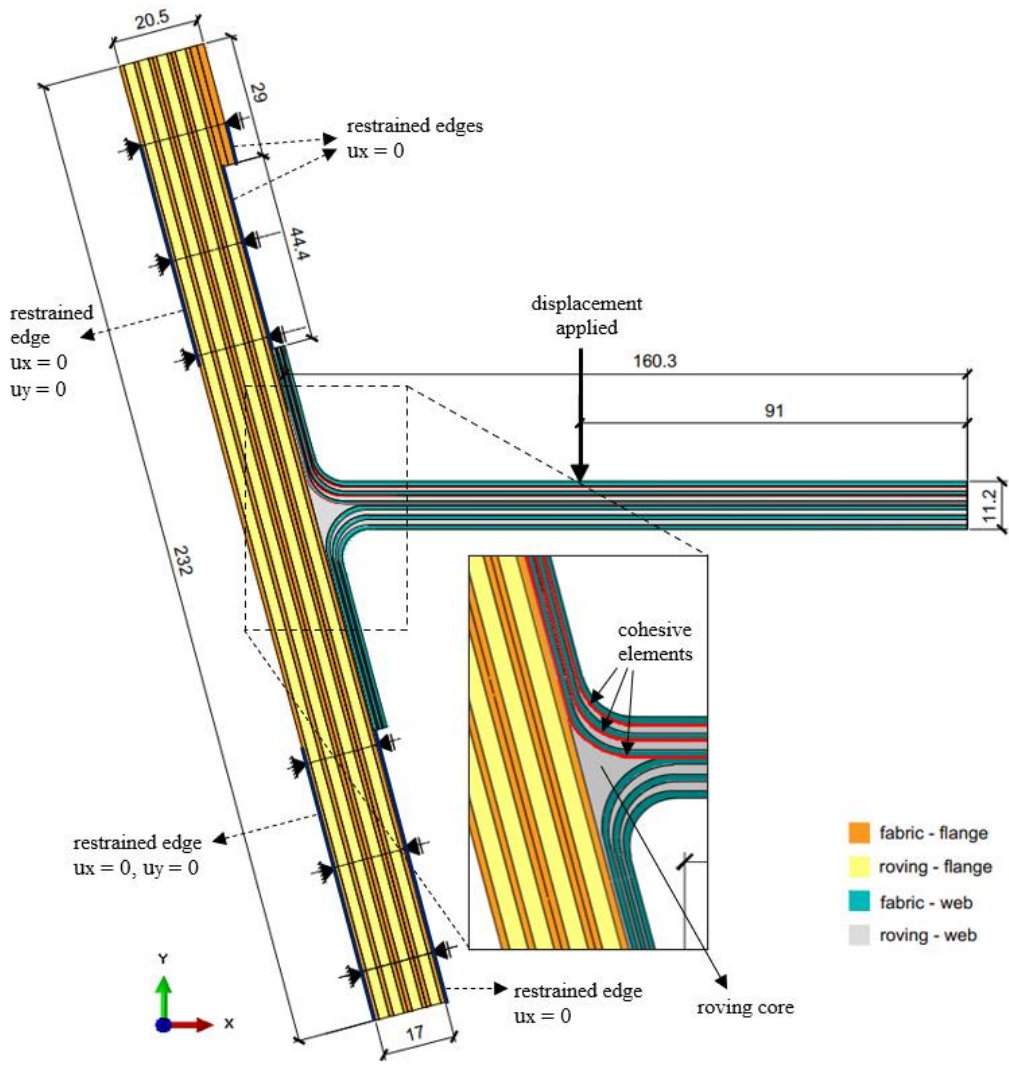


Figure 5.10. Scheme of the WFJs model.

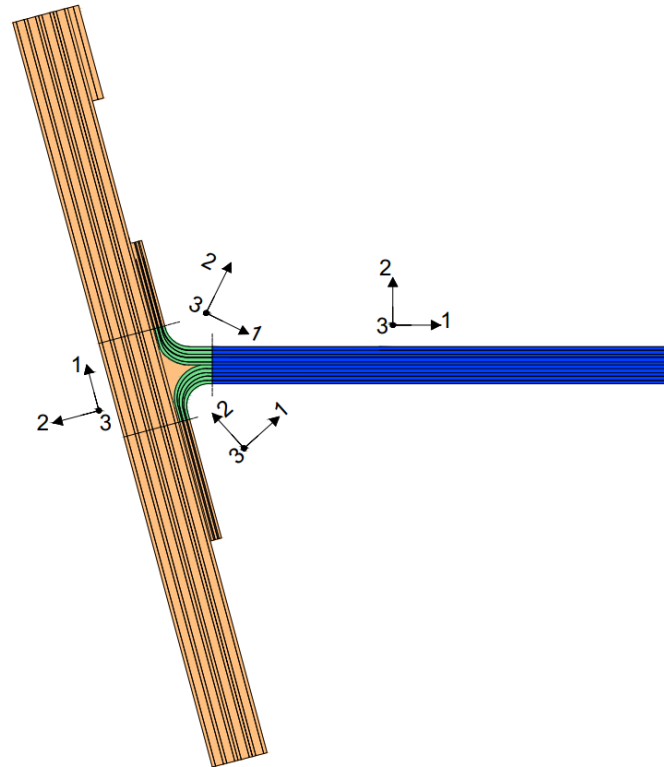


Figure 5.11. Local axis corresponding to the adopted properties (see Table 5.2).

5.3.2. Mesh elements and size

Four-node bilinear quadrilateral elements (CPE4R) were used in a non-structured mesh on the most part of the junction's flange, while three-node linear triangles (CPE3) elements were used as transition elements, also being applied in the deltoid region and adjacent to the cohesive element's layers. Four-node two-dimensional cohesive element elements (COH2D4) having zero thickness were applied in order to discretize the fracture process zone of each one of the three curved and parallel cracks. As previously mentioned, the cracks were assumed to follow interlaminar paths, occurring between the roving and fabric layers located in the tensioned part of the junction, according to experimental observations, as shown in Figures 5.6a, b and c. After a mesh convergence study, elements' sizes varying from 0.25 mm (near the cracked region and in the roving core) to 1 mm (in the uncracked regions and at the edges) were adopted according to the equation for the critical crack length [2] – see Equation (4.2) presented in Chapter 4.

5.3.3. Traction separation laws

Traction separation laws with both bilinear-exponential and bilinear shapes (see Figure 5.12) were used, based on the results of the proposed multi-crack approach, as described in the Section 5.4.2. For comparison purposes, the traction separation laws used in the Chapter 4 were also tested.

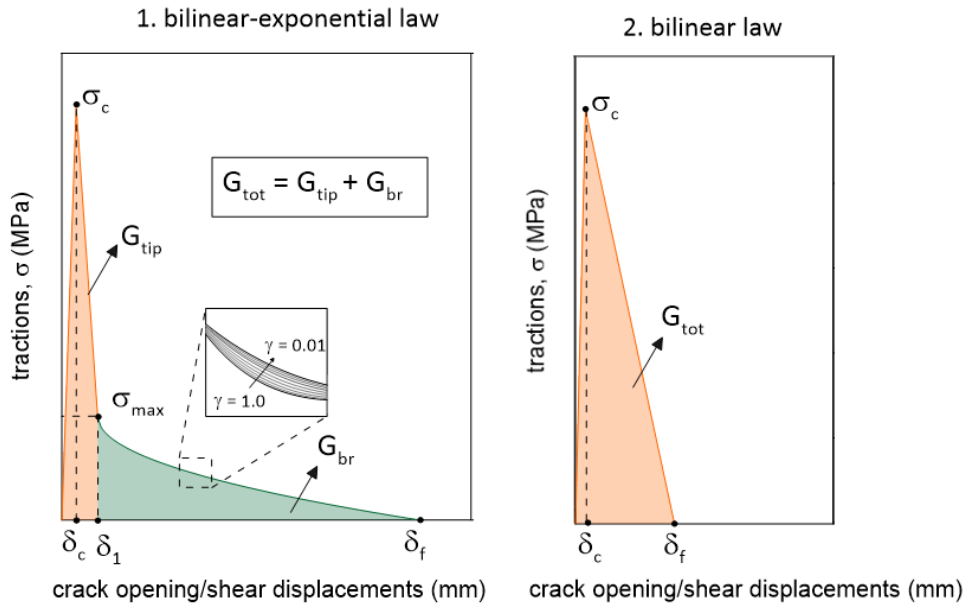


Figure 5.12. Traction separations laws shape adopted.

The bilinear-exponential law shapes were implemented via a VUMAT subroutine in Abaqus/Explicit based on the theory presented by Gonzalez *et al.* [43]. The fiber bridge tractions were represented by a non-linear behavior following formulations available in literature [44,45] (see Table 4.1 in Chapter 4) and the parameter γ related to the curvature of the exponential softening was adopted as 0.01 in all numerical tests. The damage evolution under mixed-mode loading was computed by the Benzeggagh-Kenane (BK) fracture criterion [3], presented in Equation (5.7), and the damage onset was defined according to Equation (5.8) [43]:

$$G_c = G_{Ic} + (G_{IIc} - G_{Ic}) \left(\frac{G_{II}}{G_I + G_{II}} \right)^\eta \quad (5.7)$$

$$\delta_c = \delta_{c,I} + (\delta_{c,II} - \delta_{c,I}) \left(\frac{G_{II}}{G_I + G_{II}} \right)^\eta \quad (5.8)$$

where G_{Ic} and G_{IIc} are the fracture toughnesses in Mode I and II, respectively, whereas G_I and G_{II} are the energy release rates in Mode I and Mode II, respectively. The η is a material parameter, adopted in this work as 2.0 [2]. The parameter δ_c corresponds to the COD related to the crack initiation and the subscripts I and II refer to the Modes I and II, respectively.

Two additional correlations were proposed, according to Equations (5.9) and (5.10).

$$G_{tip} = G_{tip,I} + (G_{tip,II} - G_{tip,I}) \left(\frac{G_{II}}{G_I + G_{II}} \right)^\eta \quad (5.9)$$

$$\delta_1 = \delta_{1,I} + (\delta_{1,II} - \delta_{1,I}) \left(\frac{G_{II}}{G_I + G_{II}} \right)^\eta \quad (5.10)$$

where δ_I is the COD corresponding to the maximum fiber bridge traction and G_{tip} is the SERR due to crack initiation.

On the other hand, the bilinear law was applied via the tools available in ABAQUS default. The quadratic damage initiation criterion was used to describe the damage initiation, whereas the damage evolution under mixed-mode loading was also computed by the Benzeggagh-Kenane (BK) fracture criterion [3], using the η parameter as 2.0 [2].

5.3.4. Adopted fracture parameters

The attempt to fit the accurate fracture parameters in the numerical model to simulate the multiple delamination of junction's specimens is a big challenge. Due to the high dependency of R-curves on specimens' geometry, it is very difficult to obtain experimental basis for this type of procedure. At the same time, the difficulty in simulating the WFJs specimens, which has a particular fiber architecture, with high incidence of defects, voids and mat wrinkling is also an issue. Added to this, the multi-crack behavior involves complex mechanisms, requiring assumptions and simplifications to enable the analysis. The numerical model presented herein was based on an attempt to control and minimize most of parameters that could have led to an inaccurate composite's response. Several

preliminary numerical tests were conducted based on the results reported in Chapters 2, 3 and 4, as well as on the R-curves obtained from the novel approach proposed for the multi-crack assessment. The methodology of two main models will be presented hereafter.

5.3.4.1. Model 1 – based on the DCB and ELS parameters

A first attempt of using the same bilinear-exponential cohesive laws adopted in the previous Chapters, for DCB and ELS models, was made. The interfacial strength was adopted as 19.5 MPa (30% of the matrix tensile strength) and the other fracture parameters, both for Mode I and II, are shown in Figure 5.13.

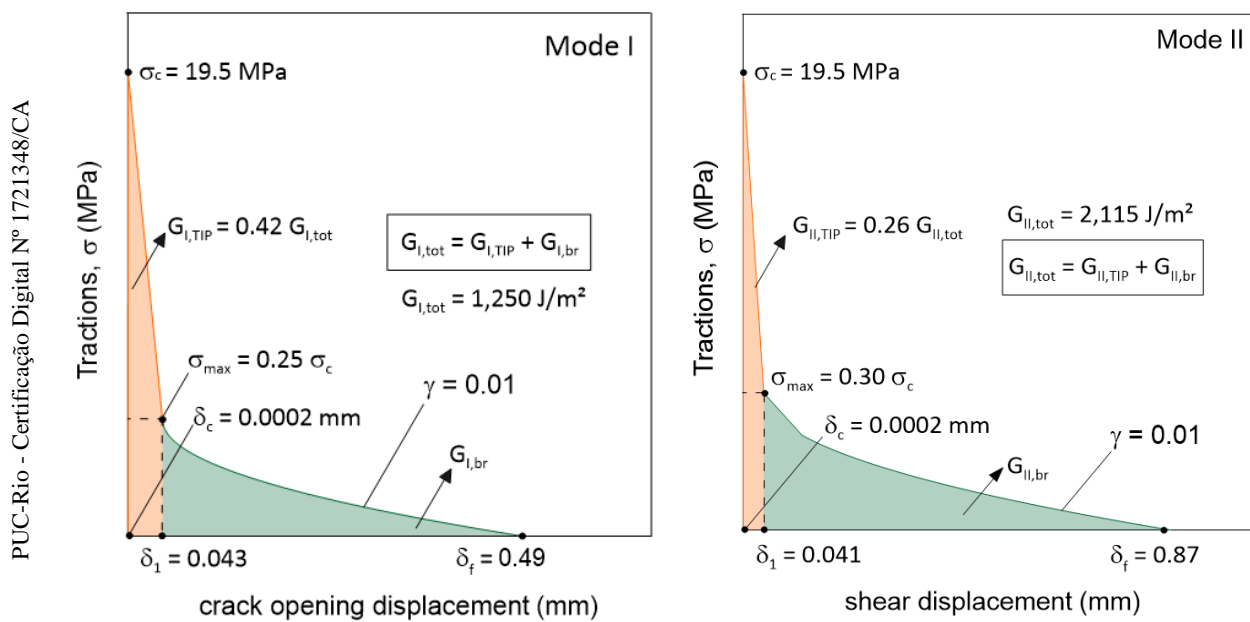


Figure 5.13. Traction separation laws used in the Model 1.

5.3.4.2. Model 2 - based on the proposed novel approach

The SERR for crack initiation and propagation was based on the *If-02* specimen results derived from the novel approach for the multi-crack assessment, reported further ahead in the Section 5.4.2. Different traction-separation law shapes were assumed for the middle and the inner/outer cracks, as shown in Figure 5.14.

The same values were used for Mode I and II. The details that motivated the chosen parameters are given in Section 5.4.3.

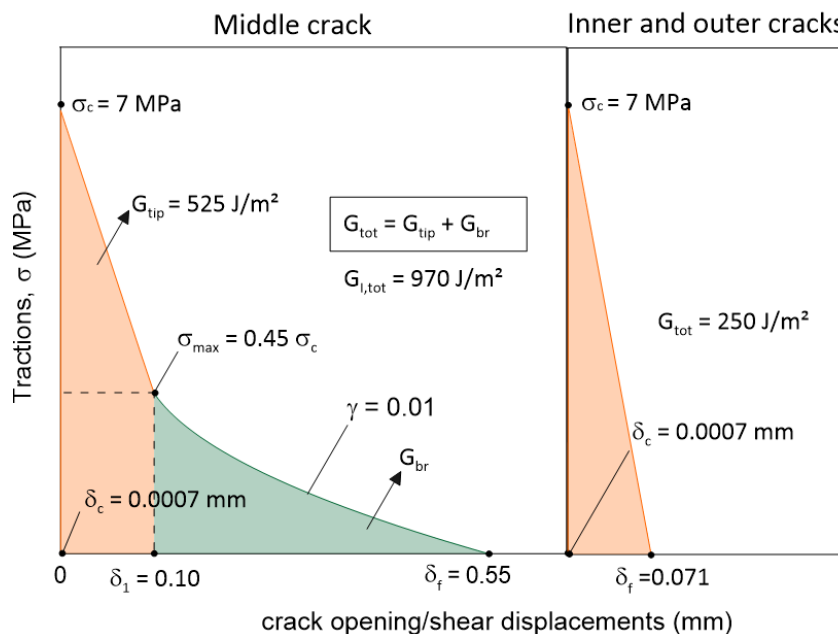


Figure 5.14. Traction separation laws used in Model 2.

5.4. Results and discussion

5.4.1. Cracks assessment and measurement

In this work, the visual measurement of the crack initiation has agreed well with the loss of linearity observed in the experiments, as can be noticed in Figures 5.15a to 5.17a, where the load and the crack length development with the applied displacement δ can be observed for specimens *If-01*, *If-02* and *If-03*, respectively. To complement the analysis, Figures 5.15b to 5.17b present the load vs. the crack lengths curves. It is worth mentioning that, among the three specimens, the *If-02* was the one that presented a more controlled failure process, in which the main cracks followed a well-defined interlaminar path since its initiation.

For the specimen *If-01*, the middle crack *a1-m* occurred at a displacement applied equal to 0.92 mm, being the one with the greater final crack length (14 mm). The outer crack *a2-o* and the inner crack *a3-i* initiated approximately at an applied displacement of 2.93 mm. The given specimen started presenting a non-linearity at

approximately 0.75 kN due to the gradual arising of a_{1-m} crack. A peak load of 0.96 kN was observed for this specimen, followed by a sudden drop due to the abrupt emergence of the a_{2-o} crack - with an initial length equal to 10 mm – and the a_{3-i} crack. On the other hand, the specimens $If-o_2$ and $If-o_3$ presented a linear behavior until a sudden drop caused by initiation of multiple cracks, having a peak load of 1.05 kN and 1.25 kN, respectively. In the $If-o_2$ experiment, the outer a_{1-o} and the middle a_{2-m} cracks formed at the same time, corresponding to a displacement applied of 1.13 mm. On the other hand, the inner a_{3-i} crack occurred at 3.25 mm of applied displacement. In this case, the outer crack a_{1-o} presented the greater development, with a final crack length of 12.8 mm. In the specimen $If-o_3$, the middle crack a_{1-m} occurred at a displacement of 1.1 mm and reached a final crack length of almost 19.8 mm. On the other hand, the outer crack a_{2-o} occurred at a displacement of 3.2 mm, presenting the smaller development in crack length during all experiment. The inner crack a_{3-i} occurred for a δ equal to 3.9mm.

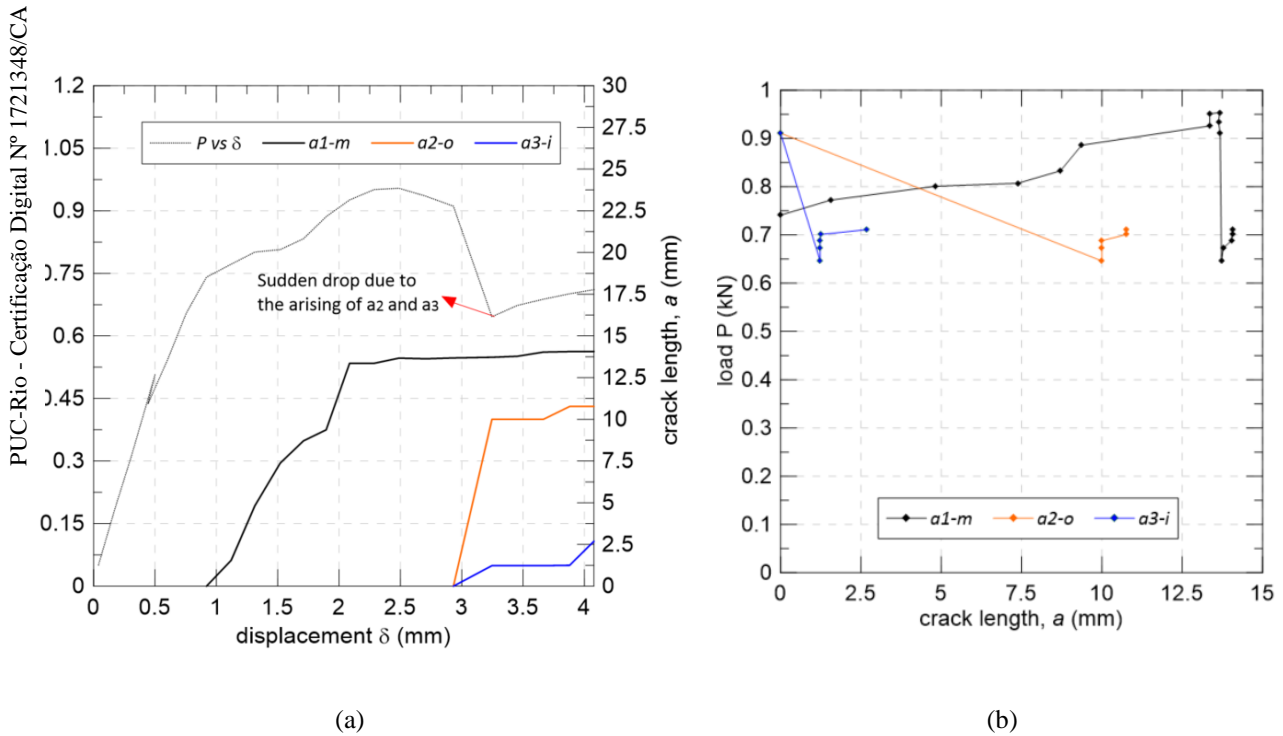


Figure 5.15. $Ifo-1$ experimental curves: (a) load and crack lengths vs. displacement; (b) load vs. individual crack lengths.

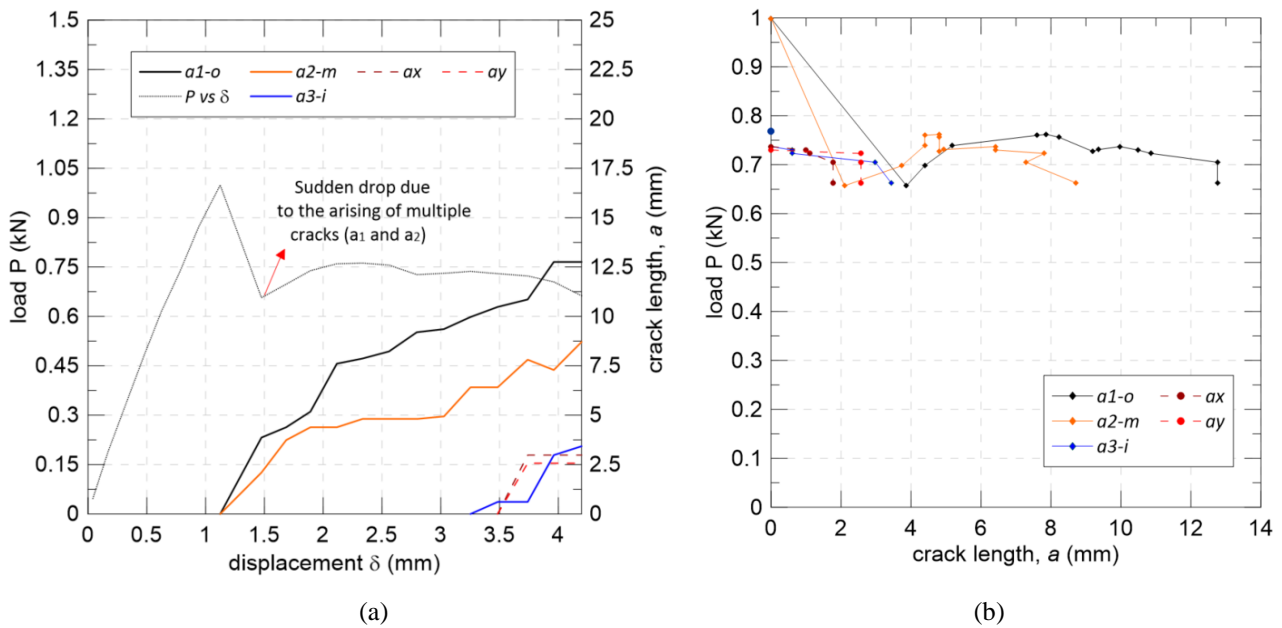


Figure 5.16. *If-o₂* experimental curves: (a) load and crack lengths vs. displacement; (b) load P vs. individual crack lengths.

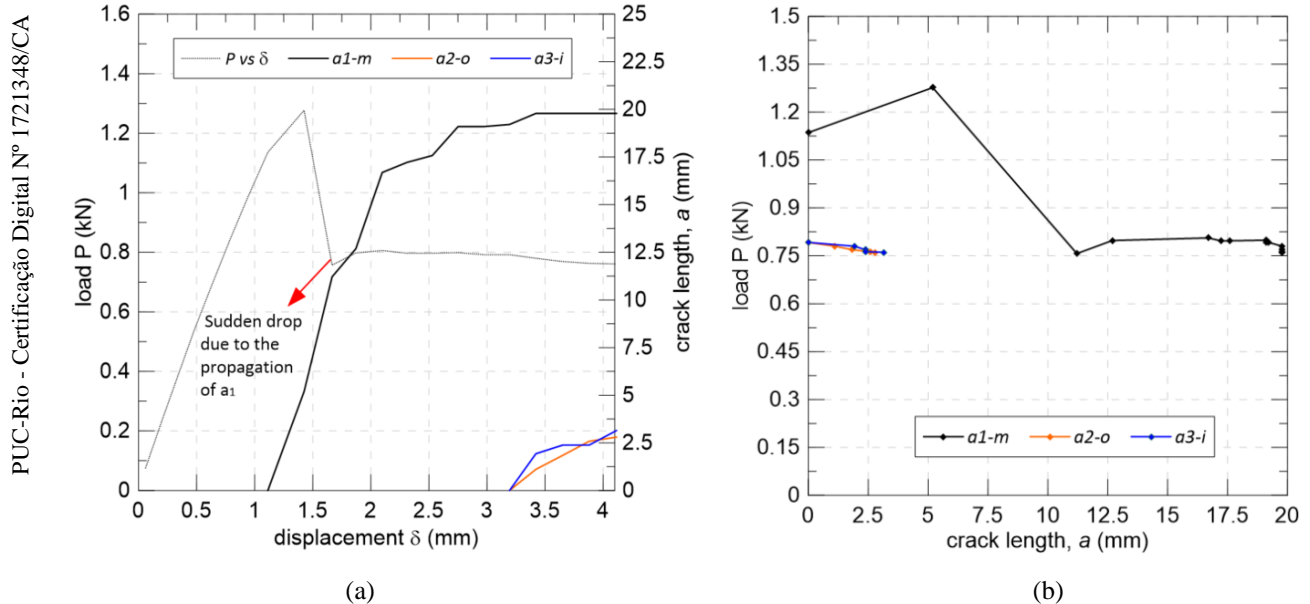


Figure 5.17. *Ifo-3* experimental curves: (a) load and crack lengths vs. displacement; (b) load P vs. individual crack lengths.

5.4.2. Novel multi-crack approach

5.4.2.1. Sum of crack lengths assessment

Figures 5.18a to 5.20a present the evolution of the sum of the crack lengths (major cracks a_t and minor cracks a_s) related to the applied displacement δ , while

the variation of the load (P) according to the growth of a_t and a_s is shown in Figure 5.18 5.18b to 5.20b. For $If-o_1$, $If-o_2$ and $If-o_3$ specimens, the sum of the main crack lengths reached 27.5 mm, 24.9 mm and 25.8, respectively. It can be also seen that for the specific case of $If-o_2$, the minor cracks represented only 5% of the total sum of the crack lengths. Likewise, for the other two specimens, the major cracks corresponded to 100% of the sum of the total crack lengths.

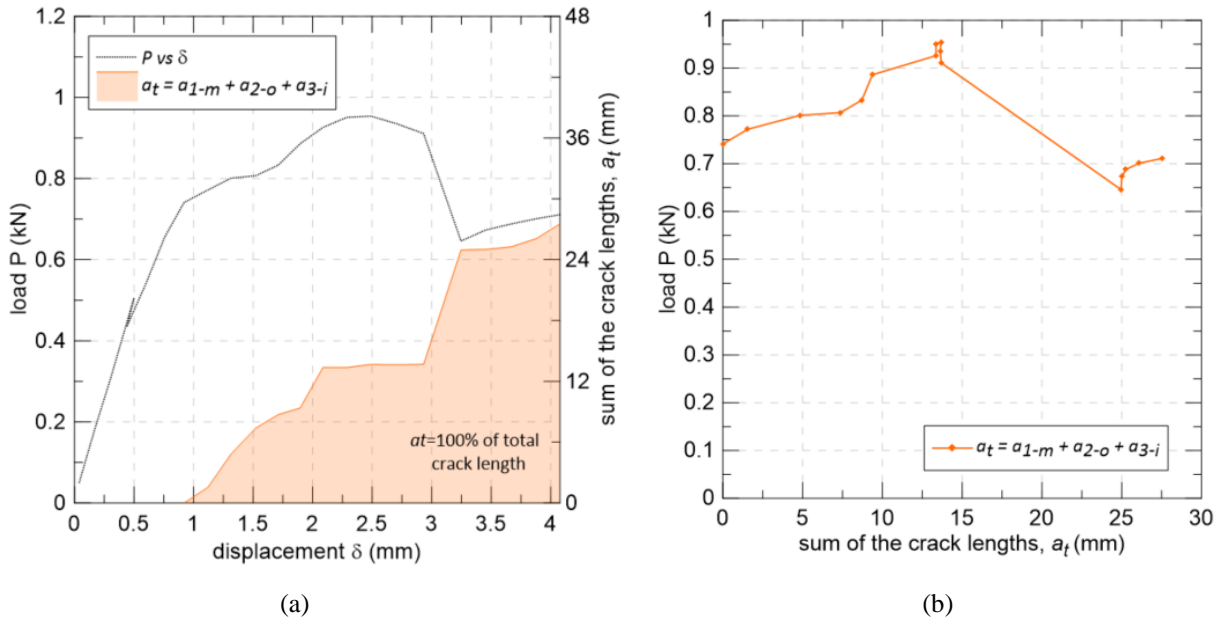


Figure 5.18. Proposed multi-crack approach for $If-o_1$: (a) P vs. δ and total crack length a_t vs. displacement applied δ ; (b) load P vs. total crack length a_t .

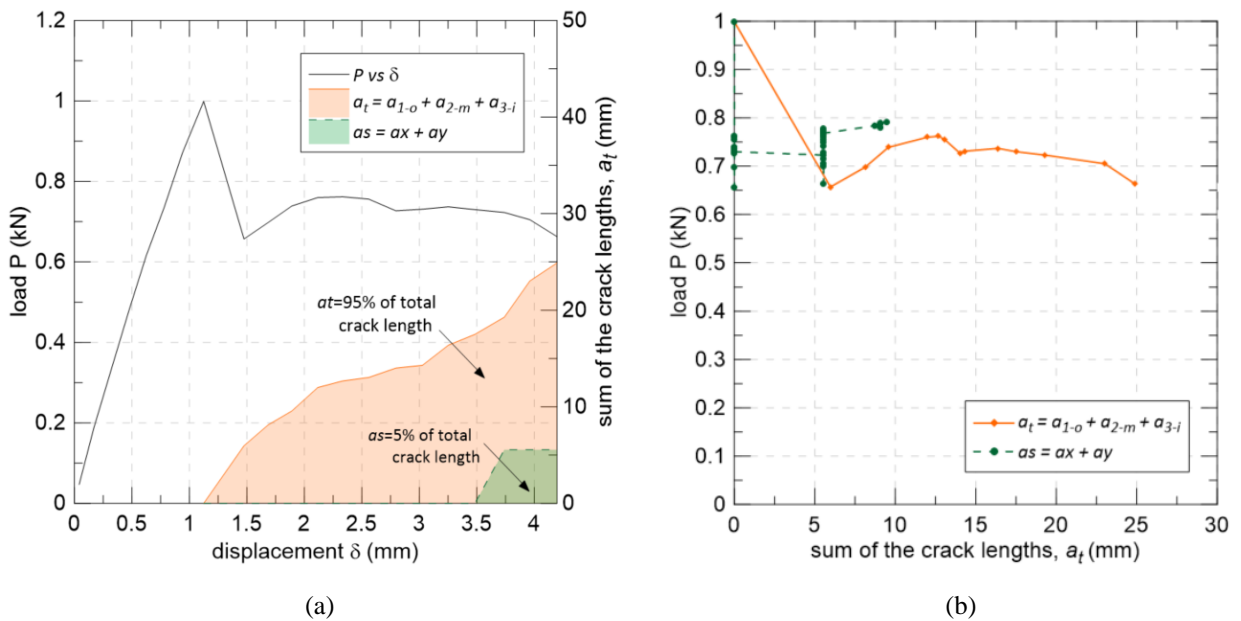


Figure 5.19. Proposed multi-crack approach for $If-o_2$: (a) P vs. δ and total crack length a_t vs. displacement applied δ ; (b) load P vs. total crack length a_t .

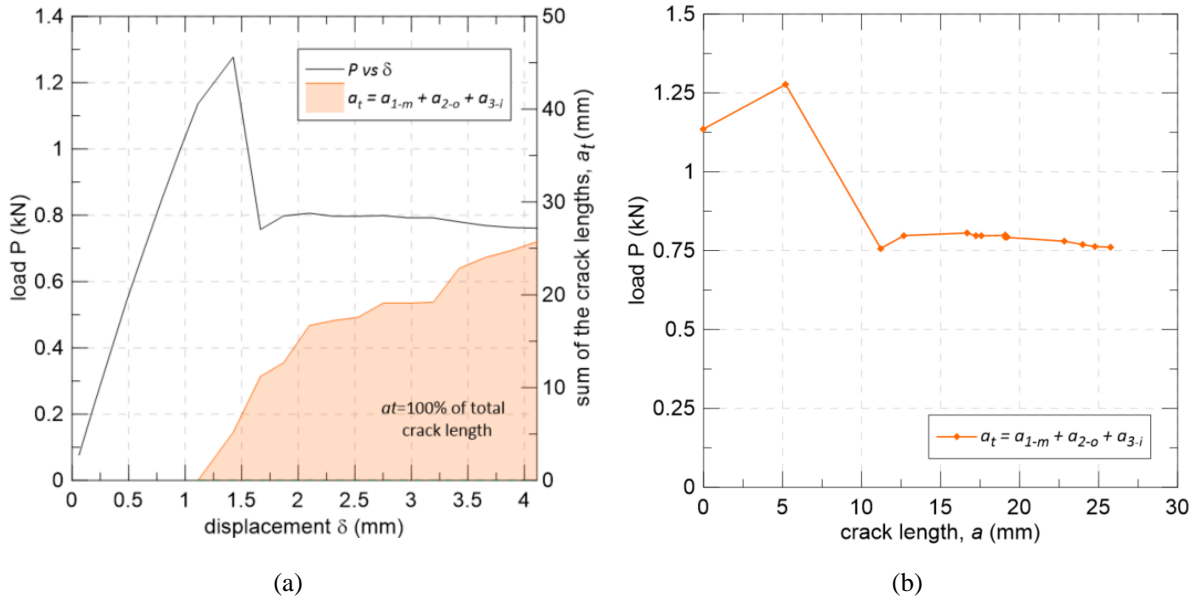


Figure 5.20. Proposed multi-crack approach for *If-o3*: (a) P vs. δ and total crack length a_t vs. displacement applied δ ; (b) load P vs. total crack length a_t .

5.4.2.2. Compliance curves

Figures 5.21a to c show the *If-o1*, *If-o2* and *If-o3* experimental curves for compliance (δ/P) vs. total crack length (a_t), along with the curve fitted through the compliance function reported by Laffan *et al.* [37] (see Section 5.2.3). The adopted parameters α , β and χ are indicated in the graphs. Additionally, Figure 5.21d presents a comparison between the experimental compliance curves found for the three specimens, also considering the sum of the main crack lengths. It can be seen that the adopted compliance function fitted well the experimental curves, although an inaccuracy in the fitting can be noticed for the specimens *If-o1* and *If-o3* before the sum of the crack lengths achieve 5 mm. All three specimens presented very similar compliance curves, with a continuous ascending, indicating the dominance of softening mechanisms, such as the crack propagation, during the failure process.

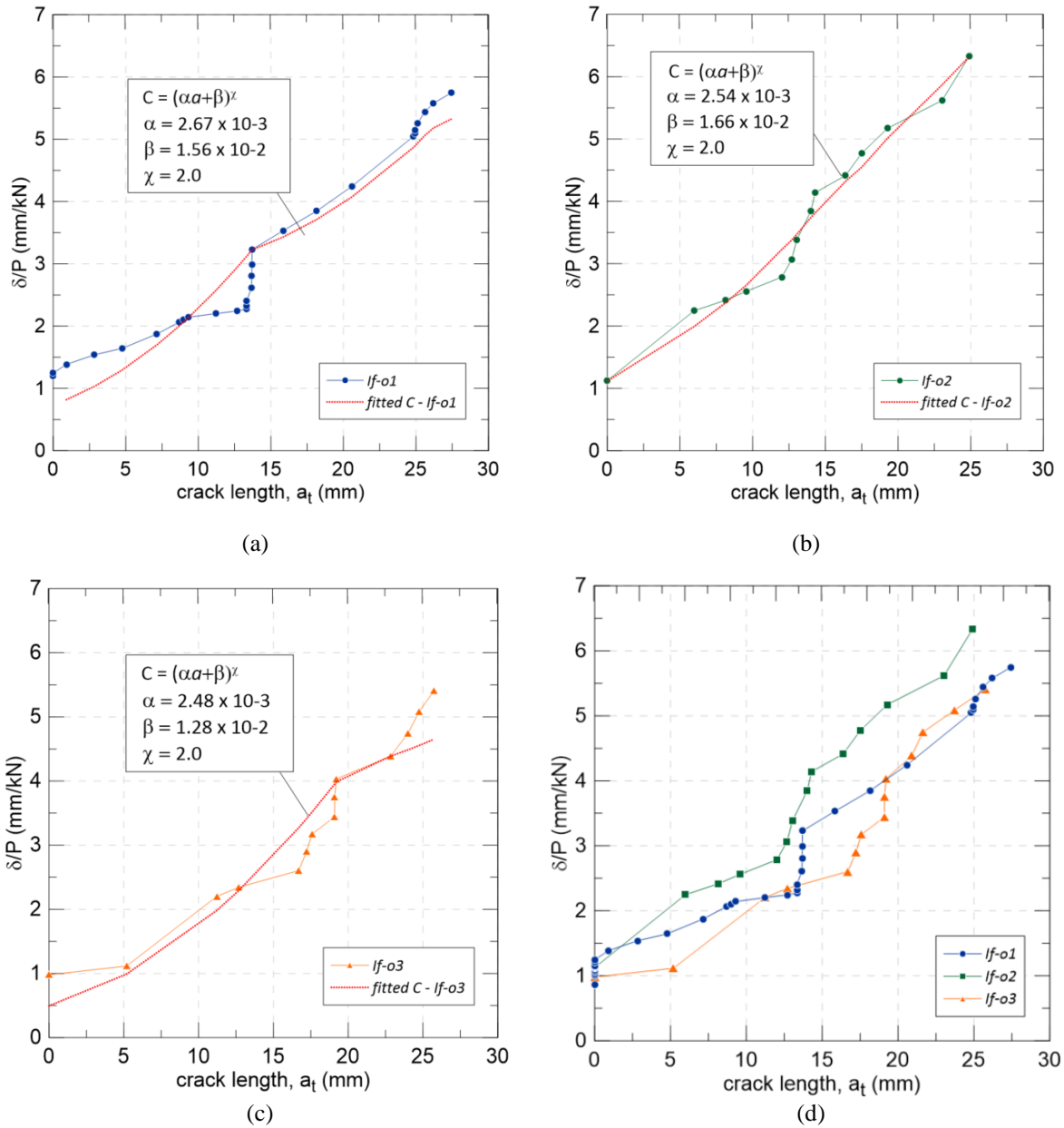


Figure 5.21. Compliance calibration for calculation of critical SERR: (a) specimen *If-o1*; (b) specimen *If-o2*; (c) specimen *If-o3* and (d) comparison between the three specimens.

5.4.2.3. R-curve of *If-o1* specimen

The R-curves for the *If-o1* specimen are shown in Figure 5.22. Through this novel approach, it is possible to separate the portion of SERR related to each crack: the blue curve refers to the crack propagation of the middle crack a_{1-m} , whereas the green one is the SERR related to the sum of the cracks $a_{1-m} + a_{2-o}$; finally, the orange curve represents the SERR for the three cracks $a_{1-m} + a_{2-o} + a_{3-i}$.

As can be seen, the given R-curve shape is different from the typical R-curves extracted from classical fracture mechanics tests related to a single crack. The ascending branch, indicated by the regions from I to III, may be related to the presence of fiber bridging in the middle crack a_{1-m} . Meanwhile, the regions II and III are characterized by the occurrence of parallel small cracks that posteriorly becomes part of the middle crack a_{1-m} . On the other hand, the descending curve branch, initiated after the region III, is related to the simultaneous and abrupt occurrence of the cracks a_{2-o} and a_{3-i} , which are responsible for the visually identified partial closure of the first crack a_{1-m} . Therefore, this progressive descending branch might be related to the loss of the fiber bridging in the middle crack a_{1-m} due to its closure. It shows that the formation of delayed cracks may modify significantly the contribution of a previously formed crack. Finally, the SERR increase at the region V is related to the ascending in the P vs. δ curve after the sharp drop caused by the occurrence of the cracks a_{2-o} and a_{3-i} . The novel approach also enabled the determination of the SERR for crack initiation (G_{tip}) of the middle crack a_{1-m} , which is approximately equal to 630 J/m². Although the fitted compliance function presented similar slope when compared to the compliance experimental curve before the a_{2-o} and a_{3-i} cracks initiation, greater slopes were observed for the former.

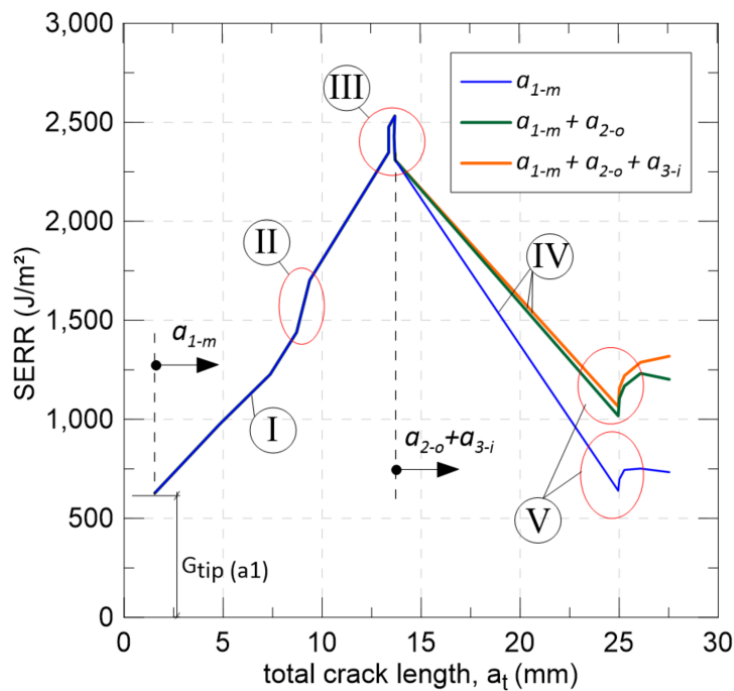


Figure 5.22. R-curve for $If-o_1$ specimen.

5.4.2.4. R-curve of If-o₂ specimen

The If-o₂ R-curve, shown in Figure 5.23, presented a typical behavior, similar to the ones usually obtained in classical fracture mechanics experiments. This may be due to the fact that this specimen presented very well-defined main cracks paths since the beginning, with less occurrence of other parallel cracks. The blue curve, related to the propagation of the main outer crack propagation (a_{1-o}), indicates an SERR for crack initiation (G_{tip}) approximately equal to 525 J/m². The presence of fiber bridging can be noticed through an increase of SERR values before reaching the steady-state value (G_{tot}) near 970 J/m². At this point, a plateau can be observed, indicating the full development of the fiber bridging. On the other hand, the green curve represents the SERR related to the sum of the cracks $a_{1-o} + a_{2-m}$, being very similar to the blue one, although shifted up approximately 230 J/m², which can be considered the value of the SERR for crack initiation of the middle crack a_{2-m} . This shifted behavior may suggest a lower contribution of fiber bridging related to the crack a_{2-m} . Likewise, the energy dissipated related to the third crack propagation a_{3-i} is apparently small.

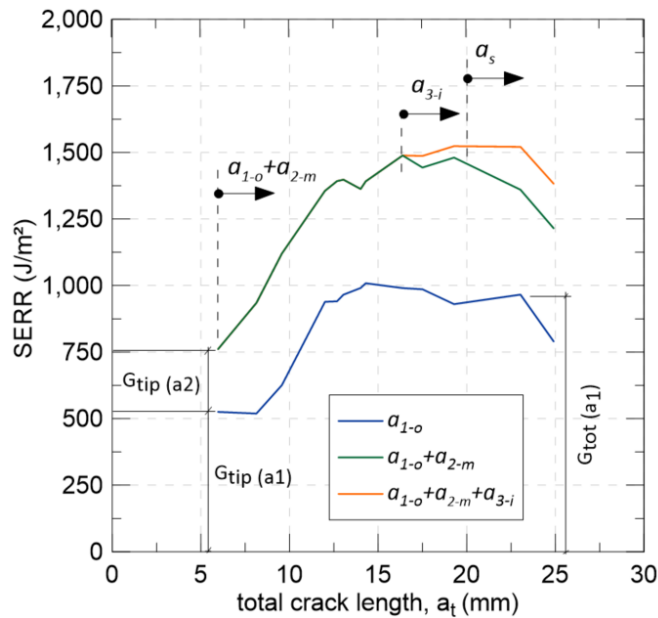


Figure 5.23. R-curve for If-o₂ specimen.

5.4.2.5. R-curve of *If-o₃* specimen

The *If-o₃* R-curve, presented in Figure 5.24, also indicates the presence of fiber bridging in the first crack a_{1-m} . The misfitting in compliance before the 5 mm of crack length, previously shown in Figure 5.21, led to the incorrect descending branch represented by the red dashed line in the R-curve. A manual adjustment on the compliance variation in relation to the total crack length resulted in the ascending branch of the blue curve, which shows the SERR for the main middle crack a_{1-m} . As observed for the specimen *If-o₁*, the curve presents a decrease in SERR values after the simultaneous initiation of the second and third main cracks a_{2-o} and a_{3-i} . Likewise, it is possible to visually identify the first crack closure, which could have led to a loss in the fiber bridging related to the crack a_{1-m} . Furthermore, a SERR of 430 J/m² was found for the crack initiation.

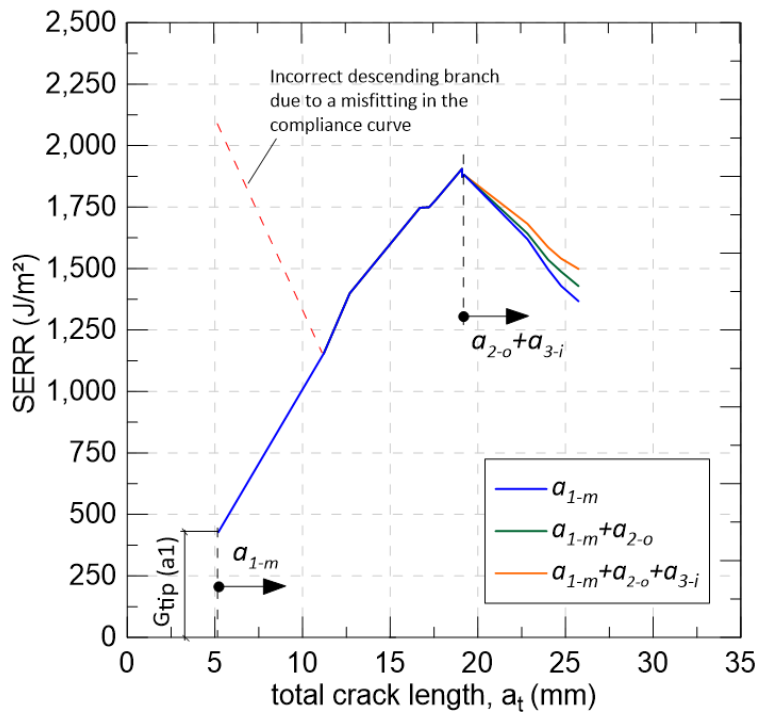


Figure 5.24. R-curve for *If-o₃* specimen.

5.4.2.6. R-curves comparison

Figure 5.25 presents the R-curves of the three specimens *If-o₁*, *If-o₂* and *If-o₃*, for comparison purposes. In all specimens, the higher SERR contribution is

provided by the first main crack, with smaller portions of energy dissipated related to the second and third cracks. The higher SERR values observed for the I_f-o_1 may have been overestimated, influenced by the misfitting in the compliance curve of this specimen, that could not be manually adjusted. It was only possible to determine the SERR for crack propagation (G_{tot}) for the I_f-o_2 experiment, which was the one that presented a typical R-curve of specimens with fiber bridging and consequent well-defined plateau. For this reason, the values found for the SERR for crack initiation and propagation of I_f-o_2 specimen were used as reference for the traction separation laws of the numerical model.

Furthermore, it can be seen that the specimens presented similar SERR for the main crack a_1 initiation, with an average value of 527 J/m^2 and a coefficient of variation (CoV) of 0.16. It is worth pointing out that this value is very similar to the average G_{tip} result found for Mode I experiments reported in Chapter 3, with approximately 5% of difference (without considering the CC_{ASTM} method due to its discrepant value). On the other hand, taking into account only the specimen I_f-o_2 , in which was possible to obtain a measurement of the SERR for crack propagation, a difference of 27% was found when comparing the results generated by the approach proposed herein and the average value found for DCB experiments, without considering the CC_{ASTM} method.

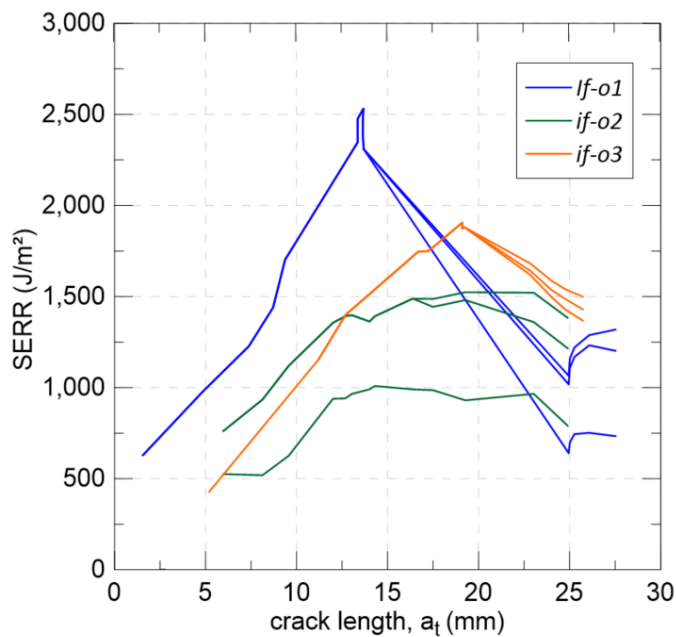


Figure 5.25. R-curves comparison.

The Appendix A reports the Tables with all the measured crack lengths and the corresponding compliance and SERR values.

5.4.3. Numerical results for DS decks multi-crack behavior

5.4.3.1. Chosen fracture parameters for Model 2

As previously mentioned, for the *Model 2*, the chosen of fracture parameters (listed in Table 5.3) were based on the *If-o₂* specimen results derived from the novel approach for the multi-crack assessment. Based on the observed plateau region of the crack *a_{1-o}*, shown in Figure 5.26, the presence of fiber bridging was taken into account through a cohesive law with bilinear-exponential shape, considering the G_{tip} and G_{tot} parameters equal to 525 J/m² and 970 J/m², respectively. Although the first experimental crack has been classified as an outer crack in the *If-o₂* specimen, this cohesive law was assigned to the middle crack in the model, based on the behavior of the other two specimens.

On the other hand, the fiber bridging was not taken into account for the second and third cracks, due to the lack of a significant SERR increase related to these cracks. Therefore, a bilinear shape was used for the outer and inner cracks, considering a SERR for crack initiation equal to 250 J/m². As presented in Figure 5.26, this value was estimated based on both the approximate G_{tip} found for the crack *a_{2-m}* and half of the difference between the curves *a_{1-o}* and *a_{1-o}+a_{2-m}+a_{3-i}* curves, considering that the energy of 500 J/m² is dissipated by two cracks (*a_{2-m}* and *a_{3-i}*). Moreover, the interfacial strength was based on preliminary numerical tests, including the results of the *Model 1*. This choice is also supported by the lower radial stresses at cracking estimated in Chapter 2 (with maximum value of 2.54 MPa, although for a different material).

Table 5.3. Parameters adopted in the cohesive laws.

| <i>Crack classification</i> | <i>Shape</i> | <i>Mode</i> | σ_c (MPa) | σ_{max} (MPa) | G_{tip} (J/m ²) | G_{tot} (J/m ²) |
|-----------------------------|----------------------|-------------|---------------------|-------------------------|----------------------------------|----------------------------------|
| Middle | Bilinear-exponential | I/II | 7 | 0.45 σ_c | 525 | 970 |
| Outer/Inner | Bilinear | I/II | 7 | - | - | 250 |

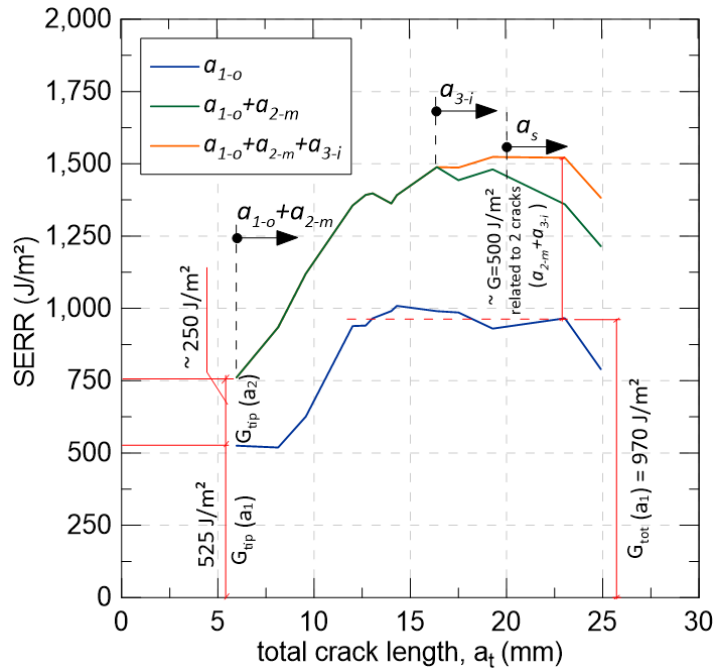


Figure 5.26. SERR values adopted for Model 2.

5.4.3.2. Load vs. displacement curves

Figure 5.27 presents the comparison between *DS* decks experimental results (illustrated through a grey envelope) and the two finite element method (FEM) models. It can be seen that the traction separation laws used in *Model 1* do not represent well the multi-cracking behavior at the junctions, leading to an incorrect peak load with unstable cracking at the post-peak region. Therefore, although the DCB and ELS specimens have been extracted from the same bridge deck as the tested junctions' specimens, the parameters previously found in Chapters 3 and 4 cannot be used to simulate the assessed junctions' behavior. This result also confirms that the R-curve and fracture parameters are dependent on the specimen's geometry in the presence of fiber bridging.

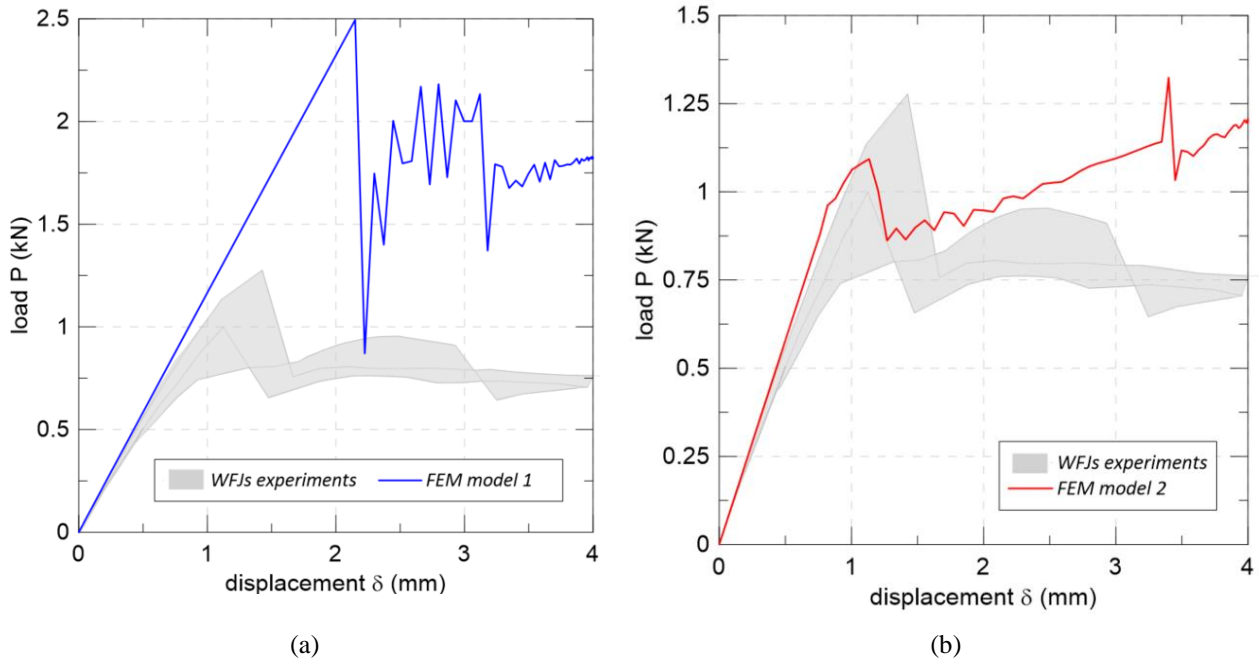


Figure 5.27. Numerical P vs. δ curves: (a) Model 1 – based on DCB and ELS results; (b) Model 2 – Based on the proposed multi-crack assessment approach.

Despite all the difficulties previously mentioned in reproducing the multi-cracking behavior of this type of material, the *Model 2* was able to simulate well the load vs. displacement curves obtained experimentally. The results indicated that the interfacial strength at the junctions is in the order of 10.7% of the tensile matrix strength. In general, preliminary tests have shown that cohesive laws with interfacial strength of this magnitude presented better agreement with experiments. Due to the high incidence of defects, it may be coherent that the interfacial strengths at the junctions are lower when compared to flat parts of the bridge decks, as observed through the low stresses calculated at the junctions in Chapter 2. In this context, it is worth pointing out the specific defects of the given WFJs specimens reported in [7], such as the inequality in triaxial fabric distribution and the resin pocket located near the roving core. Moreover, although the same interfacial strength has been adopted for all the three cracks, these values might vary between the interfaces due to the common defects.

It was also observed that all numerical load vs. displacement curves presented an upward stretch at the post peak region, in contrast with the experiment. This may be due to internal or small fractures that might have occurred during the experiments and could not be visually identified. In this scenario, it is important to

remember that, as previously mentioned, crack lengths lower than 3 mm were neglected from this analysis in order to simplify the model. Furthermore, the cracks paths were imposed on the model, assuming interlaminar trajectories between roving and fabrics, and thus, presenting some differences from what was observed experimentally, such as, for instance, the presence of crack jumps.

5.4.3.3. Crack measurement

Finally, although a good agreement has been found for the P vs. δ curves, a very small crack opening was found for the middle crack, with a maximum value of 0.012 mm. Therefore, it is difficult to estimate the respective middle crack length since an opening displacement of this magnitude could not be visually identified. Figure 5.28 shows the visual aspect of the three cracks in the FEM model. It was not possible to quantify the inner and outer crack lengths and opening displacements, due to the need of using ABAQUS default in order to apply different traction separation laws to the cracks. However, it can be seen that the inner and outer cracks visually played a greater role in the fracture process, when compared to the middle one, differently from what happened in the experiment.

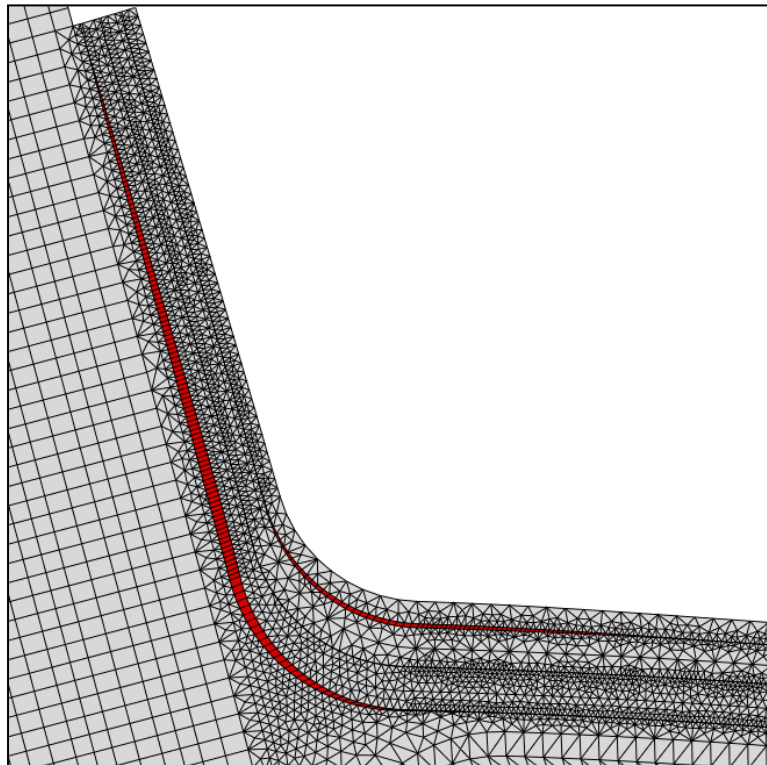


Figure 5.28. Cracks' opening displacements.

Nevertheless, considering all the complexity involved in multi-crack mechanisms, especially in a composite known for having a high variability in properties, the given approach represents a first step for a qualitative and quantitative multi-crack assessment, serving as a guideline to a good initial guess for the given fracture parameters and reducing, at a certain level, the dependency of fitting procedures. Further studies are necessary in order to evaluate all the mechanical explanation involved in this type of fracture process.

5.4.4. AS decks results and the benefits of multiple layers

The load vs. displacement curves of WFJs experiments extracted from AS decks are shown in Figure 5.29. In general, the AS deck specimens experienced a catastrophic delamination, with a sudden release of energy through a single and long crack, which presented an average of 20-mm of initial length and developed too little (approximately 2-mm), very differently from the behavior observed for DS decks. For the specimens tensioned in acute angle (AS.01 to AS.04), it is possible to separate the curves in three phases. The first stage is represented by the

typical linear elastic behavior of the material, followed by a catastrophic failure that indicates the second phase. In that stage, a sudden and sharp drop occurred caused by the occurrence of one main long crack, located near the triangular roving core region, as shown in Figure 5.30. As typically observed in brittle rupture of glass fiber-polymer profiles, the crack is accompanied by an abrupt and audible sound. Lastly, the third phase is marked by the little development of the existing crack. In the case of the specimen *AS.05*, a second and parallel crack has arisen, as abrupt as the first one, in the inner part of the junction. In this specific specimen loaded in the obtuse angle, it was possible to observe other minor cracks crossing the web with less than 6 mm of length, as shown in Figure 5.30.

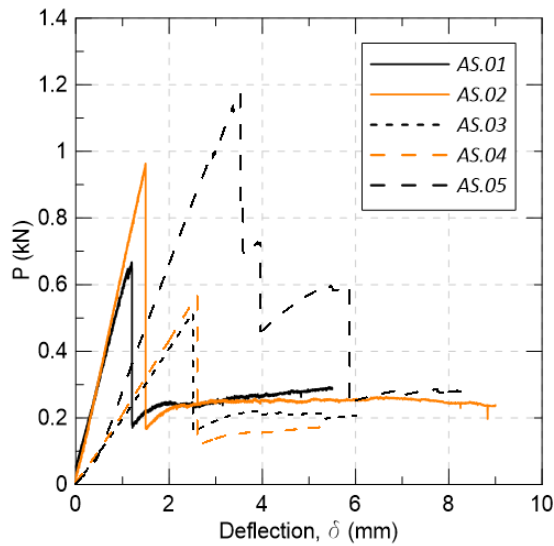


Figure 5.29. Load vs. displacements curves of AS decks.

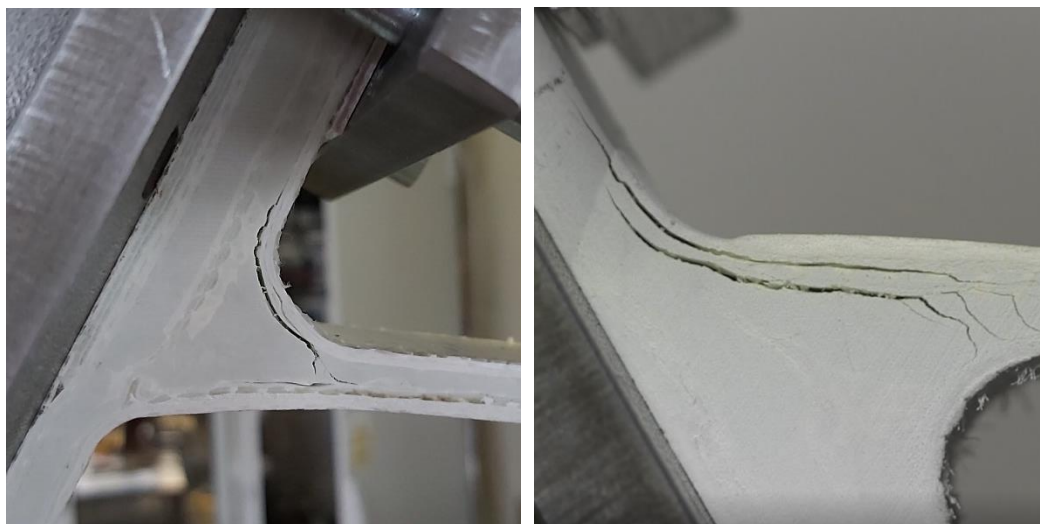


Figure 5.30. *AS* decks cracks: (a) specimen loaded on the acute angle side (AS.01); (b) specimen loaded in the obtuse angle side (AS.05).

Normalized load vs. displacement curves of both *AS* and *DS* decks specimens are shown in Figure 5.31. For comparison purposes, in the y axis, the respective loads were divided by the peak load, whereas in the x axis, the applied displacements δ were divided by the displacement corresponding to the peak load – called δ_{peak} . The benefits of having interspersed multiple layers in pultruded fiber-polymer fiber architecture can be clearly seen by comparing the behavior of *AS* and *DS* decks. The delamination may cause stress relief and delay the final failure [46] and this effect has shown to be improved in the presence of multiple cracks. In contrast to *AS* decks, the *DS* decks junctions experienced a multiple delamination, allowing the composite to undergo a gradual loss of stiffness and energy dissipation. In the latter, the cracks, in more number, started with shorter lengths (in average 2.2 mm) and develop in a more stable fashion, reaching higher lengths and opening displacements, as could be seen throughout this work. In summary, the multiple delamination has delayed the final failure, allowing higher loads to be sustained for longer and in the case of I_f^2-01 , for instance, led to a pseudo-ductile behavior.

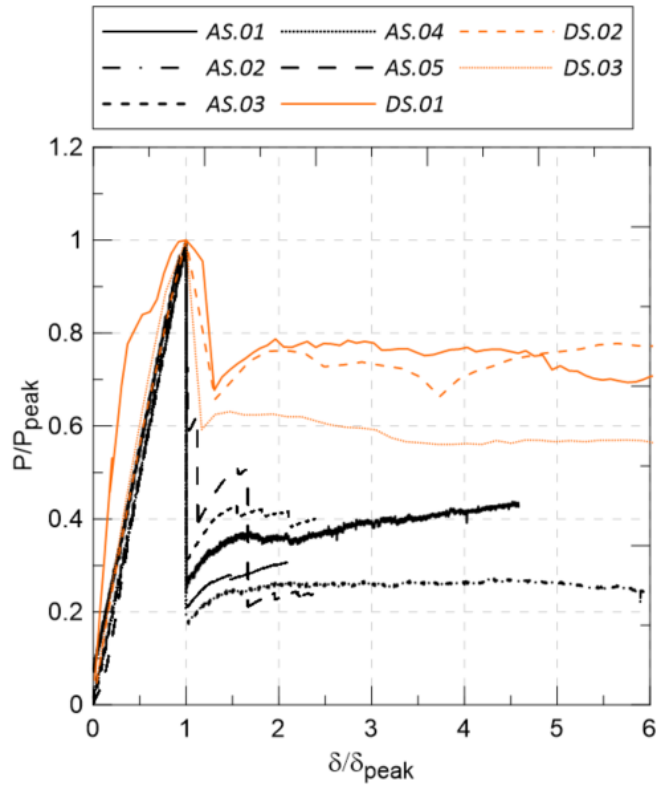


Figure 5.31. Normalized P vs. δ curves for AS and DS decks.

5.5. Conclusions

The multi-crack behavior of pultruded glass fiber-polymer WFJs extracted from a bridge deck was assessed. Three curved and parallel cracks reported in previous experiments [21] were visually measured and a numerical model simulation accounting for the junction's heterogeneity was presented. A novel approach for the multi-crack assessment using the sum of the experimental crack lengths was proposed as a first step to assess the overall behavior of composites with multiple delamination. WFJ specimens extracted from a second deck bridge, with fewer and not interspersed layers were tested and a discussion about the benefits of multiple layers was addressed.

The following conclusions can be drawn:

- The Compliance and R-curves generated from the novel approach were useful to understand the multiple delamination process, enabling to evaluate

separately the SERR related to each crack. In general, the compliance curves considering the sum of the cracks were well fitted with the function reported by Laffan *et al.* [37], presenting a typical and ascending behavior. Manual adjustments were necessary in the misfitting regions of the Compliance curves, due to its strong influence on R-curves values.

- The R-curves derived from the specimen *If-02*, which was the one that most presented well-defined crack paths, showed a typical shape similar to the ones generated from classical fracture mechanic experiments on specimens with fiber bridging and one single crack propagation. In the other specimens, *If-01* and *If-03*, it was possible to notice a descending branch in the R-curves in the case of a crack closure due to the occurrence of new ones. Very similar SERR for the first crack initiation were found between the three specimens, with an average value of 527 J/m^2 .
- Taking into account the specimens' defects, the difficulty in experimentally visualizing the crack initiation and the challenges inherent to the analysis, the load vs. displacements curves obtained through the numerical model agreed very well with experiments, considering an interfacial strength in the order of 10.7% of the tensile matrix strength, both for Mode I and Mode II. Although further studies are necessary, the approach might serve as a guideline to an initial guess for the numerical fracture parameters and reduce, at a certain level, the dependency of numerical fitting procedures.
- Although the DCB and ELS specimens have been extracted from the same bridge deck as the tested junctions' specimens, the fracture parameters previously found for these experiments were not able to simulate the multi-crack junction's behavior, confirming that the R-curve and fracture parameters are highly dependent on the specimen's geometry in the presence of fiber bridging.
- By the comparison of *AS* and *DS* decks experiments, the multiple interspersed layers have shown to contribute to a more gradual loss of stiffness and energy dissipation, besides improving the ability to sustain the load for longer. This behavior is achieved through a progressive growth of smaller multiple cracks, in contrast to the composites with lower number of

layers not interspersed, which presented very abrupt rupture due to one long and single crack.

5.6. References

- [1] BAKIS, C.E.; BANK, L.C.; BROWN, V.L.; COSENZA, E.; DAVALOS, J.F.; LESKO, J.J.; RISKALLA, S.H AND TRIANTAFILLOU, T. C. Fiber-Reinforced Polymer Composites for Construction—State-of-the-Art Review. **Journal of Composites for Construction**, v. 6, n. 2, p. 73–87, 2002.
- [2] CHEN, J. Simulation of multi-directional crack growth in braided composite T-piece specimens using cohesive models. **Fatigue and Fracture of Engineering Materials and Structures**, v. 34, n. 2, p. 123–130, 2011.
- [3] KENANE, M. L. B. & M. Measurement of mixed-mode delamination fracture toughness of unidirectional glass/epoxy composites with mixed-mode bending apparatus. **Composites Science and Technology**, v. 54, p. 439–449, 1996.
- [4] CHEN, J.; FOX, D. Numerical investigation into multi-delamination failure of composite T-piece specimens under mixed mode loading using a modified cohesive model. **Composite Structures**, v. 94, n. 6, p. 2010–2016, 2012.
- [5] LIU, P. F. et al. Finite element analysis of the influence of cohesive law parameters on the multiple delamination behaviors of composites under compression. **Composite Structures**, v. 131, p. 975–986, 2015.
- [6] W. PALMER, D.; C. BANK, L.; RUSSELL GENTRY, T. Progressive tearing failure of pultruded composite box beams: experiment and simulation. **Composites Science and Technology**, v. 58, n. 8, p. 1353–1359, 1998.
- [7] YANES-ARMAS, S.; CASTRO, J. DE; KELLER, T. Energy dissipation and recovery in web-flange junctions of pultruded GFRP decks. **Composite Structures**, v. 148, p. 168–180, 2016.
- [8] LAWRENCE, B. Progressive Failure and Ductility of FRP Composites for Construction: Review. **Journal of Composites for Construction**, v. 17, n. 3, p. 406–419, 2013.
- [9] KELLER, T.; GÜRTLER, H. Quasi-static and fatigue performance of a cellular FRP bridge deck adhesively bonded to steel girders. **Composite Structures**, v. 70,

n. 4, p. 484–496, 2005.

[10] SEBASTIAN, W. M. Fibre waviness in pultruded bridge deck profiles: Geometric characterisation and consequences on ultimate behaviour. **Composites Part B: Engineering**, v. 146, n. December 2017, p. 270–280, 2018.

[11] TURVEY, G. J.; ZHANG, Y. Shear Failure Strength Of Web-Flange Junctions In Pultruded GRP Profiles. **Advanced Polymer Composites for Structural Applications in Construction: ACIC 2004**, v. 36, p. 553–560, 2004.

[12] TURVEY, G. J.; ZHANG, Y. Tearing failure of web-flange junctions in pultruded GRP profiles. **Composites Part A: Applied Science and Manufacturing**, v. 36, n. 2 SPEC. ISS., p. 309–317, 2005.

[13] LIU, T.; HARRIES, K. A. Flange local buckling of pultruded GFRP box beams. **Composite Structures**, v. 189, n. January, p. 463–472, 2018.

[14] TURVEY, G. J.; ZHANG, Y. A computational and experimental analysis of the buckling, postbuckling and initial failure of pultruded GRP columns. **Computers and Structures**, v. 84, n. 22–23, p. 1527–1537, 2006.

[15] MOSALLAM, A. S. et al. Structural evaluation of axial and rotational flexibility and strength of web-flange junctions of open-web pultruded composites. **Composites Part B: Engineering**, v. 66, p. 311–327, 2014.

[16] LAWRENCE C. BANK AND JIANSHEN YIN. Failure of web-flange junction in postbuckled pultruded I-beams. **Journal of Composites for Construction**, v. 3, n. 4, p. 177–184, 1999.

[17] MOSALLAM, A. S. et al. Structural evaluation of axial and rotational flexibility and strength of web-flange junctions of open-web pultruded composites. **Composites Part B: Engineering**, v. 66, p. 311–327, 2014.

[18] ASCIONE, F.; MANCUSI, G. The influence of the web-flange junction stiffness on the mechanical behaviour of thin-walled pultruded beams. **Composites Part B: Engineering**, v. 55, p. 599–606, 2013.

[19] XIN, H. et al. Impact of hygrothermal aging on rotational behavior of web-flange junctions of structural pultruded composite members for bridge applications. **Composites Part B: Engineering**, v. 110, n. February, p. 279–297, 2017.

[20] TURVEY, G. J.; ZHANG, Y. Characterisation of the rotational stiffness and strength of web-flange junctions of pultruded GRP WF-sections via web bending tests. **Composites Part A: Applied Science and Manufacturing**, v. 37, n. 2, p.

152–164, 2006.

[21] YANES-ARMAS, S.; CASTRO, J. DE; KELLER, T. Rotational stiffness of web-flange junctions of pultruded GFRP decks. **Engineering Structures**, v. 140, p. 373–389, 2017.

[22] BANK, L. C., NADIPELLI, M., GENTRY, T. R., & YIN, J. S. **Local buckling of pultruded FRP beams: Theory and experiment**. Structures Congress XII. ASCE. **Anais...**1994

[23] MOSALLAM, A. S., A. A. ELSADEK, AND S. P. **Semi-rigid behavior of web-flange junctions of open-web pultruded composites**. Proceedings of the international conference on FRP composites. **Anais...**2009

[24] CINTRA, G. G. et al. Experimental investigation on the moment-rotation performance of pultruded FRP web-flange junctions. **Composites Part B: Engineering**, v. 222, n. February, p. 109087, 2021.

[25] FEO, L.; MOSALLAM, A. S.; PENNA, R. Mechanical behavior of web-flange junctions of thin-walled pultruded I-profiles: An experimental and numerical evaluation. **Composites Part B: Engineering**, v. 48, p. 18–39, 2013.

[26] CINTRA, G. G.; CARDOSO, D. C. T.; VIEIRA, J. D. Parameters affecting local buckling response of pultruded GFRP I-columns: Experimental and numerical investigation. **Composite Structures**, v. 222, n. January, p. 110897, 2019.

[27] LIU, T. Q. et al. Determining rotational stiffness of flange-web junction of pultruded GFRP I-sections. **Composite Structures**, v. 236, n. January, p. 111843, 2020.

[28] FEO, L.; MOSALLAM, A. S.; PENNA, R. Mechanical behavior of web-flange junctions of thin-walled pultruded I-profiles: An experimental and numerical evaluation. **Composites Part B: Engineering**, v. 48, p. 18–39, 2013.

[29] FASCETTI, A. et al. Web-flange behavior of pultruded GFRP I-beams: A lattice model for the interpretation of experimental results. **Composites Part B: Engineering**, v. 100, p. 257–269, 2016.

[30] YAN, S.; ZENG, X.; LONG, A. Meso-scale modelling of 3D woven composite T-joints with weave variations. **Composites Science and Technology**, v. 171, n. December 2018, p. 171–179, 2019.

[31] **AutoCAD 2020**. Disponível em: <www.autodesk.ch/>. Acesso em: 19 feb. 2020.

- [32] CAMESELLE-MOLARES, A.; VASSILOPOULOS, A. P.; KELLER, T. Experimental investigation of two-dimensional delamination in GFRP laminates. **Engineering Fracture Mechanics**, 2018.
- [33] BARBEZAT, M. et al. Fracture behavior of GFRP laminates with nanocomposite epoxy resin matrix. **Journal of Composite Materials**, v. 43, n. 9, p. 959–976, 2009.
- [34] GHASEMNEJAD, H. Interlaminar Fracture Toughness of Stitched FRP Composites. **Computers and Mathematics in Automation and Materials Science**, p. 93–96, [s.d.].
- [35] DELANEY, J. Defect Criticality in Frp Strengthening Frprcs-8. p. 1–10, 2007.
- [36] MARTIN, H. **Delamination Failure in Unidirectional Curved Composite Laminate**. Hampton, Virginia: [s.n.].
- [37] LAFFAN, M. J. et al. Measurement of the in situ ply fracture toughness associated with mode I fibre tensile failure in FRP. Part I: Data reduction. **Composites Science and Technology**, v. 70, n. 4, p. 606–613, 2010.
- [38] DÁVILA, C. G.; ROSE, C. A.; CAMANHO, P. P. A procedure for superposing linear cohesive laws to represent multiple damage mechanisms in the fracture of composites. **International Journal of Fracture**, v. 158, n. 2, p. 211–223, 2009.
- [39] **ISO (International Organization for Standardization). ISO 1172: Textile-glass reinforced plastics – Prepregs, moulding compounds and laminates – Determination of the textile-glass and mineral-filler content – Calcination methods**. . Geneva, Switzerland: [s.n.].
- [40] CINTRA, G. G. **Local Buckling Behavior of Pultruded Glass-Fiber Reinforced Polymer (pGFRP) I-Section Columns**. 2017. 2017.
- [41] YANES-ARMAS, S.; CASTRO, J. DE; KELLER, T. System transverse in-plane shear stiffness of pultruded GFRP bridge decks. **Engineering Structures**, v. 107, p. 34–46, 2016.
- [42] DASSAULT SYSTÈMES. **Abaqus**. Disponível em: <<https://www.3ds.com/support/hardware-and-software/simulia-system-information/abaqus-2021/>>. Acesso em: 19 jul. 2022.
- [43] GONZÁLEZ, E. V. et al. Simulation of delamination by means of cohesive elements using an explicit finite element code. **Computers, Materials and**

Continua, v. 9, n. 1, p. 51–92, 2009.

[44] SORENSEN, L. et al. Bridging tractions in mode I delamination: Measurements and simulations. **Composites Science and Technology**, v. 68, n. 12, p. 2350–2358, 2008.

[45] CAMESELLE-MOLARES, A. et al. Numerical simulation of two-dimensional in-plane crack propagation in FRP laminates. **Composite Structures**, v. 200, n. April, p. 396–407, 2018.

[46] SONG, K.; DAVILA, C.; ROSE, C. Guidelines and parameter selection for the simulation of progressive delamination. **2008 ABAQUS User's Conference**, p. 1–15, 2008.

6. Conclusions and suggestions for future works

6.1. Conclusions

This work aimed to investigate the delamination and multiple crack behavior of pultruded fiber-polymer composites, with emphasis on the assessment of web-flange junctions (WFJs) performance, due to its dominant role in pultruded composites' failure process. The main conclusions derived from this research are presented as follows, separated according to the main Chapters of the thesis.

6.1.1. Experimental investigation on the moment-rotation performance of pultruded fiber-polymer web-flange junctions

- A novel characterization approach using the Digital Image Correlation (DIC) technique was successfully introduced and applied to the moment-rotation characterization of the web-flange junctions (WFJs) of different I-sections and channels (tested in open- and closed mode), without the need of additional parameters or equations to determine the rotational stiffness.
- The imperfections, defects and mat wrinkling affecting the junction's performance were assessed and discussed and it was seen that I-sections presented the highest variety in the experimental rotational stiffness values, probably due the greater incidence of mat wrinkling areas at the junction region. It was shown that these defects also modify the stress trajectories significantly when located on tension regions, thus affecting the degradation in moment-rotation relations.
- Different crack behaviors were observed for channels tested in open- and close-mode: while the former presented development of interlaminar cracks produced by radial stresses with a pronounced post-cracking residual moment capacity and a slow degradation of stiffness (up to 90% of reduction in the original stiffness), the latter exhibited intralaminar cracks

due to tangential stresses and presented a higher load capacity, followed by a catastrophic failure.

- Equations based on energy principles were successfully developed to estimate the rotational stiffness for both for L- and T-shape junctions and maximum differences of 20% and 38% were observed between theoretical and experimental results for I-sections and channels, respectively. A lower bound function representing the rotational stiffness retention was also proposed and fit well with experimental results from a wide variety of profiles, although presenting greater differences for slender I-sections.

6.1.2. Mode I and Mode II Fracture Behavior in Pultruded Glass Fiber-Polymer Bridge Decks – Experimental Investigation

- Standardized testing methodologies for fracture modes I and II, usually applied to non-pultruded composites, were adopted to obtain the fracture parameters in pultruded glass fiber-polymer specimens and the introduction of starter crack via a water jet machine proved to be adequate.
- Among the six methods adopted for Mode I, the Compliance Calibration Method according to *ASTM D5528-01* (CC_{ASTM}) was the only one that presented a non-typical R-curve behavior, with a clear downward tendency in the expected plateau region. This response could possibly be caused by the absence of the parameter Δ in the formulation. However, the inclusion of the parameter in the CC_{ASTM} formulation led to SERR values for crack propagation up to 38% lower than all the other data reduction methods. The other five methods presented very similar outcomes.
- For Mode II, differences lower than 1% were obtained between the results for crack propagation SERR when comparing the Corrected beam theory using effective crack length (CBTE) and the Experimental compliance method (EMC) methods. However, the SBT method presented SERR results below the expected, lower than the results obtained for Mode I.
- Regarding the crack initiation SERR values, a higher scattering was noticed for both Modes, possibly associated with the pre-crack method and the well-

known high incidence of defects in pultruded profiles, which precludes a damage control around the crack tip.

- The ratio of SERR for crack propagation in Mode II and Mode I (G_{IIc}/G_{Ic}) ranged between 1.57 and 1.63 for crack propagation and varied from 0.78 to 1.12 for crack initiation.

6.1.3. Mode I and Mode II Fracture Behavior in Pultruded Glass Fiber-Polymers Bridge Decks – Numerical Investigation

- Numerical models were developed to investigate the most suitable cohesive laws shapes to fit experimental results obtained from fracture modes I and II. Among the three different shapes of cohesive laws tested, both the trilinear and bilinear-exponential laws provided good results in terms of the load vs. displacement curves, especially in terms of peak load. The latter presented critical strain energy release rate (critical SERR) values closer to the ones obtained experimentally, both for crack initiation and propagation, whereas the classical bilinear law generally overestimated the peak load in both fracture modes. Nevertheless, it is important to point out that it led to good agreements in terms of compliance, crack opening displacement (COD) and crack length predictions, also simulating very well the post-peak descending branch for the double cantilever beam (DCB) test (mode I).
- A parametric study performed has shown how each parameter of the three-part cohesive law has a different influence depending on the type of test. Higher values of normal interface strength (σ_c), maximum fiber bridging traction (σ_{max}) and SERR due to crack initiation (G_{tip}) mainly result in greater peak loads, whereas the total fracture toughness (G_{tot}) might lead to a general shift of the curve. The bilinear-exponential law tends to result in lower values of corresponding loads, and this effect becomes more significant as the curvature of the cohesive law softening increases.
- When comparing the simulations with the experimental techniques for Mode I, the Modified Beam Theory (MBT_{ASTM}) presented the closest results for crack propagation SERR values, with a difference as low as 4% with

respect to the numerical response. On the other hand, the Compliance Calibration Method with an alternate function (CC-f) presented the furthest results, with a difference of 8.1%. For Mode II, although a good fit was found between experimental and numerical load *vs.* displacement curves, based on the SERR values obtained through CBTE and EMC methods, none of the methods used to predict the experimental fracture toughness could fully express the R-curves, compliance behavior and crack lengths obtained through FEM models. In this context, the SBT method resulted in the furthest values when compared to the numerical model, with a difference of 20% between them.

6.1.4. Novel approach for multi-crack assessment of pultruded fiber-polymer web-flange junctions

- A novel approach was proposed to assess the multiple crack propagation behavior with respect to the total crack length. The method was applied to experimental results of multiple layered web-flange junctions (WFJs) of pultruded glass fiber-polymer deck bridge system available in literature. The Compliance and R-curves generated from the novel approach were useful to understand the multiple delamination process, enabling to evaluate separately the SERR related to each crack. The method allowed to successfully understand the apparent dominance of one crack over the others on the R-curve and to identify different fiber bridge development for each crack. Moreover, it was possible to observe that the formation of new cracks may lead to closure of existing cracks, with a significant drop on R-curve that may be associated with loss of fiber bridge.
- A numerical investigation was conducted to simulate the damage evolution and failure process observed experimentally. The fracture parameters estimated based on the proposed approach led to a very good agreement in terms of load *vs.* displacements curves between the numerical model and the experiments. Moreover, for this type of material, good results were observed considering an interfacial strength in the order of 10.7% of the

tensile matrix strength. However, it is worth pointing out that the model could not represent correctly the individual importance of each crack on the failure process.

- The fracture parameters obtained for DCB and ELS specimens – extracted from the same bridge deck as the WFJs specimens – were not able to simulate well the multi-crack junction's behavior in terms of P vs. δ curves, confirming that the R-curve and fracture parameters are dependent on the specimen's geometry in the presence of fiber bridging.
- WFJs extracted from the *ASSET* (*AS*) bridge deck system were also tested to evaluate, by comparison, the benefits provided by a multiple interspersed layered fiber architecture. The given WFJ composite, which present half of the number of layers (not interspersed) of *DS* decks, exhibited a brittle behavior, characterized by a sharp drop of load vs. displacement curves due the occurrence of one single and long crack, being unable to sustain the same load bearings for much long. In opposition, the *DS* bridge deck WFJs developed multiple cracks with progressive growth, having an initial length almost ten times smaller than the one observed for *AS* decks. The multiple delamination in the *DS* decks has delayed the final failure, allowing higher loads to be sustained for longer.

6.2. Major contributions of the Thesis

The most relevant contributions of this thesis are described as follows:

- Suggestion of a simple and direct testing set-up and methodology to characterize the rotational stiffness of WFJs of pultruded fiber-polymer composites;
- Suggestion of a simple methodology to determine the stresses on the crack initiation region based on the curved beam theory for anisotropic material [9];
- Proposition of a lower bound function to simulate the post-peak rotational stiffness retention;

- Proposition of equations to determine the theoretical rotational stiffness for both L- and T-shape specimens;
- Proposal to adapt and extend existing testing methodologies to obtain interlaminar fracture mechanics parameters of pultruded glass fiber-polymers, based on classical and standardized experiments;
- Complement the scarcity on interlaminar fracture data, especially for interlaminar fracture in Mode II;
- Evaluation of the most suitable cohesive laws shapes for the studied material through numerical simulation;
- Development of a novel approach to assess the multi-cracking behavior of pultruded fiber polymer composites.

6.3. Suggestions for future works

In order to further develop the conclusions drawn in the present thesis, suggestions for future works are described below.

Defects control

As addressed in Chapter 2, it is well known that pultruded fiber-polymer composites present many defects that are difficult to control, especially at the junction's region, such as mat wrinkling, resin-rich zones, voids and imperfections in general that can lead to an underperforming structural function. Further quantitative and qualitative investigations on the influence of these defects on the composites overall behavior and properties could help to improve the design codes in favor of security. Moreover, studies focused on suggesting improvements in fiber architectures and manufacturing could contribute to advances in pultrusion industry.

Modes I and II delamination

In the lack of standardized methods to serve as reference to experimentally determine the pultruded composites fracture parameters, further investigations on

the procedures used to insert an initial starter crack on the specimens are needed, in order to quantify how it influences on the results, for instance, on the SERR for crack initiation. Developing experimental studies on the Mode II parameters assessment, both for interlaminar, intralaminar or translaminar fracture, are also fundamental to serve as basis for numerical analyses and reduce the time-consuming experiments in the future. Likewise, the conclusions drawn in Chapter 4 of this work indicate the need to propose solutions that take into account the difficulty in measuring the crack lengths in Mode II. In parallel, due to the great differences observed for results provided by data reduction methods in Mode II, comparisons comprising a higher number of methods would be useful to evaluate which one provides the more accurate results.

Multi-crack assessment

The studies addressing the multi-crack behavior of pultruded fiber-polymer composites are an open field for new propositions in experimental, numerical and analytical analyses. There are very few works focused on the subject, despite the importance to develop research simulating the actual failure composites behavior that could lead to improvements in the existing design codes. Further investigations on the novel approach concerning the sum of the total experimental crack lengths are needed. Reducing the dependency on fitting procedures and visual crack lengths measurements could be valuable in more accurately determining the fracture mechanics parameters. Studies on multiple cracks mechanisms occurring in pultruded fiber-polymer could help to improve the SERR quantification method obtained by the novel approach proposed herein.

Benefits of multiple interspersed layers and pseudo-ductility

Parametric numerical studies focused on understanding and quantify the influence of the fiber architecture on multi-crack behavior could generate positive impacts in pultrusion industry. Further investigations on the composite's progressive failure and damage mechanisms to achieve a more pseudo-ductile behavior, especially focused on weak regions such as the junctions, could also be useful to the material structural design. Comprising different types of profiles in

this type of analysis, such as I-sections that present very few studies in this area, could help to fill in existing gaps in literature. Finally, analysis in slender profiles having large post-buckling deflections could also be investigated as an attempt to provide early warning before rupture.

7. Appendix A – Novel approach for multi-crack assessment

The Tables 7.1 to 7.3 contain the fracture parameters calculated for each WFJ specimen ($If-o_1$, $If-o_2$ and $If-o_3$), with basis on the novel approach proposed for the multi-crack assessment (see formulations presented in Section 5.2.3). The nomenclature used in the Tables is presented as follows.

| | | | |
|----------|--|------------------|--|
| P | applied load | k_i | ratio of the assessed crack length (a_i) and the sum of the crack lengths (a_t) – see Equation 5.6 |
| δ | applied displacement | | |
| a_1 | crack length of the first crack | $G(a_1)$ | SERR related to the crack length a_1 |
| a_2 | crack length of the second crack | $G(a_2)$ | SERR related to the crack length a_2 |
| a_3 | crack length of the third crack | $G(a_3)$ | SERR related to the crack length a_3 |
| a_t | sum of the length of main cracks $a_1 + a_2 + a_3$ | $G(a_1+a_2)$ | SERR related to the crack lengths a_1 and a_2 |
| C | compliance, calculated as δ/P | $G(a_1+a_2+a_3)$ | SERR related to the crack lengths a_1 , a_2 and a_3 |

7.1. *If-o₁ specimen*

Table 7.1. Fracture parameters of *If-o₁* calculated with basis on the novel approach proposed for multi-crack assessment.

| (mm) | P (kN) | a1 (mm) | a2 (mm) | a3 (mm) | C (mm/kN) | at (mm) | k1 | k2 | k3 | C fitted (mm/kN) | G (a1) (J/m ²) | G (a2) (J/m ²) | G (a3) (J/m ²) | G (a1 + a2) (J/m ²) | G (a1 + a2 + a3) (J/m ²) |
|-------|--------|---------|---------|---------|-----------|---------|------|------|------|------------------|----------------------------|----------------------------|----------------------------|---------------------------------|--------------------------------------|
| 0.920 | 0.741 | 0.0 | - | - | 1.24 | 0 | - | - | - | - | - | - | - | - | - |
| 1.121 | 0.772 | 1.6 | - | - | 1.45 | 1.55 | 1 | - | - | 0.88 | 628.2 | 0.0 | 0.0 | 628.2 | 628.2 |
| 1.314 | 0.801 | 4.8 | - | - | 1.64 | 4.82 | 1 | - | - | 1.30 | 975.4 | 0.0 | 0.0 | 975.4 | 975.4 |
| 1.521 | 0.807 | 7.4 | - | - | 1.88 | 7.38 | 1 | - | - | 1.73 | 1227.8 | 0.0 | 0.0 | 1227.8 | 1227.8 |
| 1.710 | 0.833 | 8.7 | - | - | 2.05 | 8.71 | 1 | - | - | 2.00 | 1439.7 | 0.0 | 0.0 | 1439.7 | 1439.7 |
| 1.895 | 0.886 | 9.4 | - | - | 2.14 | 9.37 | 1 | - | - | 2.14 | 1702.7 | 0.0 | 0.0 | 1702.7 | 1702.7 |
| 2.086 | 0.926 | 13.4 | - | - | 2.25 | 13.357 | 1 | - | - | 3.11 | 2347.3 | 0.0 | 0.0 | 2347.3 | 2347.3 |
| 2.287 | 0.951 | 13.4 | - | - | 2.40 | 13.36 | 1 | - | - | 3.12 | 2476.1 | 0.0 | 0.0 | 2476.1 | 2476.1 |
| 2.489 | 0.954 | 13.7 | - | - | 2.61 | 13.67 | 1 | - | - | 3.20 | 2532.0 | 0.0 | 0.0 | 2532.0 | 2532.0 |
| 2.709 | 0.935 | 13.6 | - | - | 2.90 | 13.63 | 1 | - | - | 3.19 | 2427.2 | 0.0 | 0.0 | 2427.2 | 2427.2 |
| 2.932 | 0.911 | 13.7 | 0.0 | 0.0 | 3.22 | 13.68 | 1 | - | - | 3.20 | 2310.1 | 0.0 | 0.0 | 2310.1 | 2310.1 |
| 3.246 | 0.646 | 13.7 | 10.0 | 1.2 | 5.02 | 24.95 | 0.55 | 0.40 | 0.05 | 4.87 | 640.1 | 377.8 | 46.5 | 1017.9 | 1064.4 |
| 3.452 | 0.673 | 13.8 | 10.0 | 1.2 | 5.13 | 25.01 | 0.55 | 0.40 | 0.05 | 4.89 | 698.2 | 409.1 | 50.3 | 1107.3 | 1157.6 |
| 3.665 | 0.688 | 14.0 | 10.0 | 1.2 | 5.33 | 25.26 | 0.56 | 0.40 | 0.05 | 4.96 | 744.9 | 423.3 | 52.1 | 1168.2 | 1220.3 |
| 3.879 | 0.701 | 14.1 | 10.8 | 1.3 | 5.53 | 26.08 | 0.54 | 0.41 | 0.05 | 5.15 | 751.8 | 480.7 | 55.8 | 1232.4 | 1288.2 |
| 4.077 | 0.711 | 14.1 | 10.8 | 2.7 | 5.73 | 27.53 | 0.51 | 0.39 | 0.10 | 5.31 | 733.5 | 468.4 | 117.0 | 1201.9 | 1318.9 |

7.2. *If-o₂* specimenTable 7.2. Fracture parameters of *If-o₂* calculated with basis on the novel approach proposed for multi-crack assessment.

| δ (mm) | P (kN) | a1 (mm) | a2 (mm) | a3 (mm) | C (mm/kN) | a _t (mm) | k1 | k2 | k3 | C fitted (mm/kN) | G (a1) (J/m ²) | G (a2) (J/m ²) | G (a3) (J/m ²) | G (a1 + a2) (J/m ²) | G (a1 + a2 + a3) (J/m ²) |
|---------------|--------|---------|---------|---------|-----------|---------------------|------|------|------|------------------|----------------------------|----------------------------|----------------------------|---------------------------------|--------------------------------------|
| 1.124 | 0.999 | 0.0 | 0.0 | - | 1.13 | 0.0 | - | - | - | 1.12 | - | - | - | - | - |
| 1.475 | 0.657 | 3.9 | 2.1 | - | 2.25 | 6.0 | 0.65 | 0.35 | - | 1.99 | 525.4 | 235.8 | 0.0 | 761.2 | 761.2 |
| 1.685 | 0.698 | 4.4 | 3.7 | - | 2.41 | 8.1 | 0.54 | 0.46 | - | 2.37 | 519.1 | 415.5 | 0.0 | 934.6 | 934.6 |
| 1.891 | 0.739 | 5.2 | 4.4 | - | 2.56 | 9.6 | 0.54 | 0.46 | - | 2.66 | 626.0 | 494.3 | 0.0 | 1120.3 | 1120.3 |
| 2.116 | 0.76 | 7.6 | 4.4 | - | 2.78 | 12.0 | 0.63 | 0.37 | - | 3.23 | 938.9 | 416.9 | 0.0 | 1355.8 | 1355.8 |
| 2.333 | 0.762 | 7.9 | 4.8 | - | 3.06 | 12.7 | 0.62 | 0.38 | - | 3.38 | 940.7 | 451.6 | 0.0 | 1392.3 | 1392.3 |
| 2.56 | 0.756 | 8.2 | 4.8 | - | 3.39 | 13.0 | 0.63 | 0.37 | - | 3.47 | 965.6 | 432.2 | 0.0 | 1397.8 | 1397.8 |
| 2.796 | 0.727 | 9.2 | 4.8 | - | 3.85 | 14.0 | 0.66 | 0.34 | - | 3.74 | 990.8 | 372.0 | 0.0 | 1362.8 | 1362.8 |
| 3.027 | 0.731 | 9.4 | 4.9 | - | 4.14 | 14.3 | 0.65 | 0.35 | - | 3.81 | 1008.8 | 382.8 | 0.0 | 1391.6 | 1391.6 |
| 3.252 | 0.737 | 10.0 | 6.4 | 0.0 | 4.41 | 16.4 | 0.61 | 0.39 | - | 4.32 | 990.5 | 498.1 | 0.0 | 1488.6 | 1488.6 |
| 3.483 | 0.730 | 10.5 | 6.4 | 0.6 | 4.77 | 17.5 | 0.60 | 0.37 | 0.03 | 4.55 | 985.9 | 457.4 | 43.5 | 1443.3 | 1486.9 |
| 3.739 | 0.723 | 10.9 | 7.8 | 0.6 | 5.17 | 19.3 | 0.56 | 0.41 | 0.03 | 5.01 | 930.1 | 550.6 | 43.0 | 1480.7 | 1523.7 |
| 3.961 | 0.705 | 12.8 | 7.3 | 3.0 | 5.62 | 23.0 | 0.55 | 0.32 | 0.13 | 5.87 | 965.9 | 394.1 | 161.1 | 1359.9 | 1521.0 |
| 4.197 | 0.663 | 12.8 | 8.7 | 3.4 | 6.33 | 24.9 | 0.51 | 0.35 | 0.14 | 6.32 | 790.1 | 425.1 | 167.4 | 1215.2 | 1382.6 |

7.3. *If-o₃ specimen*Table 7.3. Fracture parameters of *If-o₃* calculated with basis on the novel approach proposed for multi-crack assessment.

| δ (mm) | P (kN) | a1 (mm) | a2 (mm) | a3 (mm) | C (mm/kN) | a _t (mm) | k1 | k2 | k3 | C fitted (mm/kN) | G (a1) (J/m ²) | G (a2) (J/m ²) | G (a3) (J/m ²) | G (a1 + a2) (J/m ²) | G (a1 + a2 + a3) (J/m ²) |
|---------------|--------|---------|---------|---------|-----------|---------------------|------|------|------|------------------|----------------------------|----------------------------|----------------------------|---------------------------------|--------------------------------------|
| 1.113 | 1.136 | 0.0 | - | - | 0.98 | 0.0 | - | - | - | 0.49 | - | - | - | - | - |
| 1.425 | 1.277 | 5.2 | - | - | 1.12 | 5.2 | 1.00 | - | - | 0.99 | 427.3 | - | - | 427.3 | 427.3 |
| 1.666 | 0.757 | 11.2 | - | - | 2.20 | 11.2 | 1.00 | - | - | 1.98 | 1155.0 | - | - | 1155.0 | 1155.0 |
| 1.871 | 0.798 | 12.7 | - | - | 2.34 | 12.7 | 1.00 | - | - | 2.29 | 1399.3 | - | - | 1399.3 | 1399.3 |
| 2.098 | 0.806 | 16.7 | - | - | 2.60 | 16.7 | 1.00 | - | - | 3.27 | 1747.1 | - | - | 1747.1 | 1747.1 |
| 2.311 | 0.797 | 17.2 | - | - | 2.90 | 17.2 | 1.00 | - | - | 3.41 | 1749.7 | - | - | 1749.7 | 1749.7 |
| 2.529 | 0.797 | 17.6 | - | - | 3.17 | 17.6 | 1.00 | - | - | 3.51 | 1777.8 | - | - | 1777.8 | 1777.8 |
| 2.751 | 0.799 | 19.1 | - | - | 3.44 | 19.1 | 1.00 | - | - | 3.95 | 1906.1 | - | - | 1906.1 | 1906.1 |
| 2.974 | 0.792 | 19.1 | - | - | 3.76 | 19.1 | 1.00 | - | - | 3.95 | 1872.9 | - | - | 1872.9 | 1872.9 |
| 3.194 | 0.792 | 19.2 | 0.0 | 0.0 | 4.03 | 19.2 | 1.00 | - | - | 3.99 | 1881.3 | - | - | 1881.3 | 1881.3 |
| 3.421 | 0.780 | 19.8 | 1.1 | 1.9 | 4.39 | 22.8 | 0.87 | 0.05 | 0.08 | 4.39 | 1619.4 | 22.9 | 39.8 | 1642.3 | 1682.0 |
| 3.651 | 0.769 | 19.8 | 1.8 | 2.4 | 4.75 | 24.0 | 0.82 | 0.08 | 0.10 | 4.49 | 1496.7 | 39.1 | 50.6 | 1535.8 | 1586.4 |
| 3.879 | 0.763 | 19.8 | 2.6 | 2.4 | 5.08 | 24.8 | 0.80 | 0.10 | 0.10 | 4.55 | 1429.4 | 57.9 | 53.4 | 1487.3 | 1540.7 |
| 4.116 | 0.761 | 19.8 | 2.8 | 3.2 | 5.41 | 25.7 | 0.77 | 0.11 | 0.12 | 4.65 | 1367.2 | 61.8 | 69.5 | 1429.0 | 1498.5 |